Modelling Self-Potentials as a Predictor of Seawater Intrusion in Coastal Groundwater Boreholes

Malcolm Thomas Graham

A thesis submitted for the degree of Doctor of Philosophy
of the Imperial College London

Department of Civil and Environmental Engineering
Imperial College London
October 2018

Declaration of originality

The contents of this report are all my own work, and any quotation from, or description of, the work of others is fully acknowledged by reference to the sources, whether published or unpublished.

The following article, which forms the basis for Chapters 4 to 6 of this thesis, has been published in the journal of Water Resources Research:

Graham, M. T., MacAllister, DJ., Vinogradov, J., Jackson, M. D., and Butler, A. P. (2018). Self-potential as a predictor of seawater intrusion in coastal groundwater boreholes. Water Resources Research, 54(9):6055-6071. https://doi.org/10.1029/2018WR022972.

Copyright declaration

Abstract

Seawater intrusion is pervasive on every inhabited continent, although existing monitoring techniques typically fail to predict the timing of its occurrence in groundwater boreholes. Recent monitoring of a coastal groundwater observation borehole suggests that a nearby saline front can affect self-potential (SP) signals and could be used to predict saline intrusion.

The borehole displays a persistent SP gradient, which is absent in boreholes further inland. This gradient reduces several days before saline breakthrough, constituting a possible precursor to intrusion, and fluctuates at the same frequency as oceanic tides. The magnitude of the oscillations reduces prior to breakthrough.

A numerical model of the surrounding Chalk aquifer explains the SP gradient and precursor for the first time. The gradient requires spatial variation in the exclusion-efficiency η of the aquifer, a parameter that, in the context of seawater intrusion in the Chalk, describes the extent to which anions are excluded from the pore space and which has been linked previously to rocks with narrow pore throats. The modelled precursor is a response to seawater moving through fractures with a change in η across them. The fractures driving the precursor may either intersect the borehole or lie immediately beneath it. However, the observed reduction in SP oscillations can only be replicated in the latter scenario.

The model relies on relatively high values of η in marl horizons, a parameter that had not been measured previously in this lithology. The results of marl testing carried out as part of this project closely agree with the simulated values and provide greater confidence in the model.

These SP phenomena were observed in a single coastal groundwater observation borehole. To understand fully the applicability of SP monitoring and modelling for predicting seawater intrusion, it should now be applied to boreholes in different aquifer types, including operating abstraction boreholes.

Acknowledgements

This work was funded by the Natural Environment Research Council and the Grantham Institute for Climate Change, via the Science and Solutions for a Changing Planet Doctoral Training Partnership.

I would like to thank my supervisors, Dr. Adrian Butler and Prof. Matthew Jackson, for developing the concept for this project and for helping me pursue an answer to the many questions it has thrown up. I am also very grateful to Dr. Jan Vinogradov, who has been a sounding board for many hypotheses along the way. Although some of them were wide of the mark, he has listened patiently to them all and provided me with thoughtful and constructive criticism throughout. Along with Dr Shuai Li, he also provided valuable guidance during the laboratory component of the project. Thank you also to Graham Nash for his help in maintaining and repairing the numerous pieces of laboratory equipment required to conduct these experiments.

This project would not have been possible without the initial body of work completed by Dr Donald John MacAllister. The models described in this thesis owe a great deal to the high quality datasets he collected in the field and in laboratory experiments. Indeed, I have followed many of the procedures he developed for data collection and analysis.

I would like to thank Dr Amadi Ijioma for sharing his SP modelling code. Although I have since modified it to suit the requirements of this project, his work provided me with an excellent starting point.

I am grateful to Mike Packman and Dr Simon Cook of Southern Water, for the provision of data from the Saltdean study area and for taking such a strong interest in the progress of my work. It has been extremely useful to get insights from a key stakeholder in the outcomes of this project. I would also like to thank Jamie Tomlin of Atkins for the provision of data and for helping arrange access to the Balsdean observation borehole. In this regard, I am also very grateful to the landowner, Brighton and Hove City Council, and the tenant farmer, David Hole, for being so accommodating in allowing me to collect data on their land.

Thank you to Dr Andrew Hughes, Marianne Stuart and Mark Fellgett from the British Geological Survey for helping me to obtain key datasets for the model.

I would also like to express my appreciation for the time spent by my examiners, Dr Ian Bastow and Professor Denis Peach, in reviewing this thesis. Their comments were thoughtful and constructive throughout and helped to improve the quality of my work.

Finally, I'd like to thank my wife Gabbie and daughter Arwen for never complaining, despite the profound affect taking on this PhD has had on all our lives. Without your love and good humour, the last 4 years would have been a lonely experience.

‘The winds, the sea, and the moving tides are what they are. If there is wonder and beauty and majesty in them, science will discover these qualities. If they are not there, science cannot create them.’

Rachel Carson, 1952

Contents

List of Tables

List of Figures

List of symbols

Symbol	Description	Units
A	amplitude of the spring-neap tidal cycle	m
A_0	mean amplitude of the semidiurnal tidal component	m
$\mathbf{A}$	sparse matrix of electrical conductivity terms	N/A
$a_{\Gamma i}$	boundary element terms in sparse matrix $\mathbf{A}$	N/A
a_{Pi}	element centre terms in sparse matrix $\mathbf{A}$	N/A
b	saturated thickness of the aquifer	m
$\mathbf{B}$	sparse matrix of source terms	N/A
B_H	surface scalar horizontal component of magnetic field	T
$\mathbf{B}_H$	surface vector horizontal component of magnetic field	T
C	fluid solute concentration	kg/kg
C_i^0	molar concentration of ion i in lower salinity solution	M
$C_i^{\Delta x}$	molar concentration of ion i in higher salinity solution	M
CEC	cation exchange capacity	meq/100g
C_{ED}	electrochemical diffusion coupling coefficient at full saturation	V
C_{EE}	electrochemical exclusion coupling coefficient at full saturation	V
C_{EED}	electrochemical exclusion-diffusion coupling coefficient at full saturation	V
C_{EK}	electrokinetic coupling coefficient at full saturation	VPa^{-1}
C_f	ionic strength	M
C_s	solute concentration of fluid sources	kg/kg
C_{uEED}	electrochemical exclusion-diffusion coupling coefficient in the unsaturated zone	V
C_{uEK}	electrokinetic coupling coefficient in the unsaturated zone	VPa^{-1}
$\mathbf{D}$	dispersion tensor	$\mathrm{m}^2\mathrm{s}^{-1}$
D_i	diffusion coefficient of ion i	-
D_m	apparent molecular diffusivity	$\mathrm{m}^2\mathrm{s}^{-1}$
$\mathbf{D}_{mec}$	mechanical dispersion tensor	$\mathrm{m}^2\mathrm{s}^{-1}$
e	charge on an electron	C
$\mathbf{E}_H$	surface vector horizontal component of electric field	Vm^{-1}
F	formation factor	-
g	acceleration due to gravity	ms^{-2}
h	piezometric head above sea level	m
H_0	amplitude of tidal fluctuations at the coast	m
H_{GW}	amplitude of groundwater level fluctuations	m

h_{Nh}	measured sea level at Newhaven	mAOD
$\mathbf{I}$	identity tensor	-
j	electrical current density	Am^{-2}
J_1	smaller lunar elliptic diurnal component of tides	N/A
$\mathbf{k}$	permeability tensor	m^2
K	hydraulic conductivity	m/day
K_1	lunar diurnal component of tides	N/A
K_2	lunisolar semidiurnal component of tides	N/A
k_B	Boltzmann constant	JK^{-1}
K_i	hindrance diffusion coefficient of ion i	-
L	generic cross-coupling term for self-potential sources	-
L_{EED}	cross-coupling term for electrochemical exclusion-diffusion sources	Am^{-1}
L_{EK}	cross-coupling term for electrokinetic sources	$\mathrm{APa}^{-1}\mathrm{m}^{-1}$
m	Archie's cementation exponent	-
M_2	principal lunar semidiurnal component of tides	N/A
N_2	lunar elliptic semidiurnal component of tides	N/A
N_A	Avogadro's number	mol^{-1}
O_1	lunar diurnal component of tides	N/A
P	pressure	Pa
P_1	solar diurnal component of tides	N/A
P_n	non-hydrostatic pressure	Pa
P_T	total pressure	Pa
Q_1	larger lunar elliptic diurnal component of tides	N/A
Q_s	unit volumetric fluid mass source	$\mathrm{kgm}^{-3}\mathrm{s}^{-1}$
r	pore throat radius	m
S	aquifer storage coefficient	-
S_1	solar diurnal component of tides	N/A
S_2	principal solar semidiurnal component of tides	N/A
S_{ps}	specific pressure storativity	m^{-1}
S_w	saturation	-
T	temperature	K
t_0	period of tidal fluctuation	days
T_+	macroscopic Hittorf number	-
T_c	temperature in centigrade	°C
TDS	total dissolved solids	mg/l
TDS_s	total dissolved solids in sea water	mg/l
t_{na}	microscopic Hittorf number for sodium	-
T_{SN}	period of the spring-neap tidal cycle	days
$\mathbf{u}$	specific discharge	ms^{-1}
U	thermodynamic potential of the self-potential source mechanism	-
$\mathbf{v}$	mean pore water fluid velocity	ms^{-1}
V	electrical potential	V
V_{ED}	electrochemical diffusion potential	V

V_{EE}	electrochemical exclusion potential	V
V_{EED}	electrochemical exclusion-diffusion potential	V
V_{EK}	electrokinetic potential	V
x	distance inland from the coast	m
$\mathbf{x}$	column vector of electrical potentials	V
y	distance parallel to the coast	m
$\mathbf{y}$	column vector of source terms	N/A
z	elevation relative to ordnance datum	m
$\mathbf{Z}$	magnetotelluric response tensor	ms^{-1}
z_i	charge number of ion i	-
z_s	depth of the saline-freshwater interface below sea level	m
α_L	longitudinal dispersivity	m
α_T	transverse dispersivity	m
ΔL_1	element dimension in the direction of the first coordinate axis	m
ΔL_2	element dimension in the direction of the second coordinate axis	m
ΔL_3	element dimension in the direction of the third coordinate axis	m
ΔL_L	element dimension in the direction of flow	m
ΔV_{AC}	apparent potential difference in column experiment	V
ΔV_{AP}	apparent potential difference across test sample	V
ΔV_C	potential difference due to electrode effects	V
ϵ_w	dielectric permittivity of the pore fluid	Fm^{-1}
η	electrochemical exclusion efficiency	-
λ	Debye length	m
μ	dynamic viscosity of the pore fluid	Fm^{-1}
ϕ	porosity	-
ϕ_{frac}	volume of void space in fractures as a proportion of total fracture zone volume	-
ϕ_{mat}	volume of void space in the matrix of the fracture zone as a proportion of total fracture zone volume	-
ρ	fluid density	kgm^{-3}
ρ_f	density of fresh water	kgm^{-3}
ρ_m	mineral grain density	kgm^{-3}
ρ_s	density of seawater	kgm^{-3}
σ_f	electrical conductivity of the pore fluid	Sm^{-1}
$\sigma_{f_{FZ}}$	electrical conductivity of the pore fluid in each fracture zone	Sm^{-1}
$\sigma_{f_{FZ0}}$	initial electrical conductivity of the pore fluid in each fracture zone	Sm^{-1}
$\sigma_{f_{mat0}}$	initial electrical conductivity of the pore fluid in the matrix	Sm^{-1}

σ_s	saturated electrical conductivity of the rock	Sm^{-1}
τ	tidal lag	days
ζ	zeta potential	V

Chapter 1

Introduction

1.1 Motivation

Globally, groundwater provides the main source of water for human consumption; it is also critically important for agriculture in many countries (WWAP, 2014). The demand for groundwater is particularly high in coastal areas, where the average population density is more than three times the global average (Small and Nicholls, 2003).

Many coastal aquifers are vulnerable to seawater intrusion, with numerous incidences reported in every inhabited continent (Barlow and Reichard, 2010; Bocanegra et al., 2010; Custodio, 2010; Morgan and Werner, 2015; Shi and Jiao, 2014; Steyl and Dennis, 2010). A map of areas vulnerable to seawater intrusion in the continental United States is shown in Figure 1.1a, while known incidences of seawater intrusion in continental Europe are shown in Figure 1.1b. The risks of seawater intrusion are greatest when the water table is low relative to local sea levels and its prevalence is likely to increase as a result of climatic variability and rising demand for groundwater, leading to increased abstractions (Ferguson and Gleeson, 2012).

Traditional approaches for characterising seawater intrusion fall into three main categories (Werner et al., 2013): monitoring of hydrochemistry; monitoring of groundwater levels; and geophysical investigations. If used to protect a groundwater abstraction source, the first approach

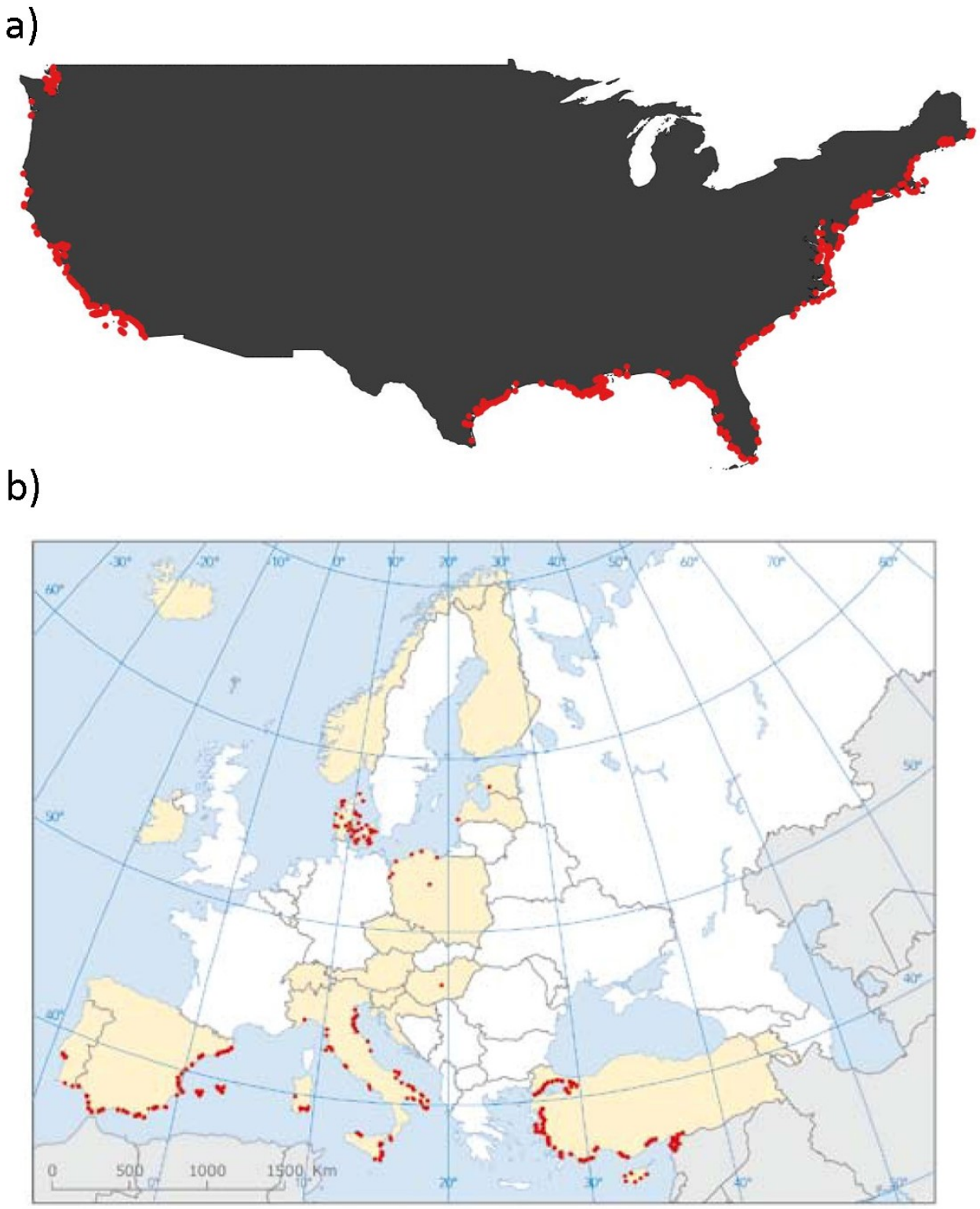

Figure 1.1: a) coastal areas vulnerable to saline intrusion in continental United States (adapted from Sawyer et al. (2016)) and b) recorded incidences of seawater intrusion in parts of continental Europe (EEA, 1999).

requires regular monitoring of fluid electrical conductivity σ_f in a nearby monitoring borehole and relies on both the monitoring borehole and abstraction point (such as a borehole, well or

trench) lying within the same flow path. Groundwater level monitoring and hydrochemistry approaches are limited in their ability to predict the timing of seawater intrusion, particularly in heterogeneous aquifers, where seawater may be transported along a small number of preferential flow paths. Time-lapse geophysical surveys using measurements of resistivity and electromagnetism have been used in various studies to investigate seawater intrusion phenomena (e.g. Comte and Banton, 2007; Fitterman, 2014; McDonald et al., 1998), although these typically require a large footprint for the long-term installation of monitoring apparatus or repeated surveys during the defined period of intrusion risk.

As concentration (or salinity) gradients are a well-known source of self-potentials (SP), through the development of an electrochemical exclusion-diffusion potential (e.g. Jackson, 2015; Jouniaux et al., 2009; Lanteri et al., 2009a; Leinov and Jackson, 2014; Martínez-Pagán et al., 2010; Revil, 1999; Westermann-Clark and Christoforou, 1986), SP may represent an alternative means of identifying a nearby saline front. The relatively low cost of the monitoring equipment, combined with a small footprint within a single borehole, represent significant advantages compared to traditional methods for identifying seawater intrusion.

Electrochemical SPs have been used to track the position of an injected saline front in both field (Jougnot et al., 2015; Sandberg et al., 2002) and laboratory (Martínez-Pagán et al., 2010) experiments, with the latter suggesting that an SP signal can be observed ahead of any increase in salinity. This is supported by modelling of saline breakthrough in hydrocarbon reservoirs, where changes in SP occurred several tens of metres ahead of the saline front (Gulamali et al., 2011; Jackson et al., 2012b).

Several studies of coastal aquifers have highlighted changes in the electrokinetic (or streaming) potential due to variations in groundwater pressure (Babu et al., 2009; Morgan and Werner, 2015; Kang et al., 2014; Schiavone and Quarto, 1984), although none of these has linked changes in SP to the position of the saline front. Studies of the electrochemical potential, arising from variations in concentration, within coastal aquifers have typically focused on the salinity of formations immediately adjacent to the borehole (e.g. Jones et al., 1999; Nativ and Fligelman, 1994; Radhakrishna, 2001).

MacAllister et al. (2016) and MacAllister (2016) were the first studies to establish a link between changes in borehole SP and remote movements of the saline front in a coastal aquifer. This was achieved by measuring tidal variations in SP and σ_f in a coastal groundwater monitoring borehole in the UK Chalk subject to regular seawater intrusion (the Saltdean Observation Borehole (OBH)). MacAllister et al. (2018) then demonstrated that the tidal signal in the Saltdean OBH was dominated by the electrochemically-induced component of SP across a remote saline front.

MacAllister (2016) and MacAllister et al. (2018) also showed that the Saltdean OBH, which has been subject to regular seawater intrusion, displays a consistent SP gradient ahead of the saline front and that this feature is absent in Chalk boreholes further inland. Moreover, a characteristic reduction in this gradient, or precursor, occurs several days prior to saline breakthrough in the borehole (MacAllister et al., 2018). Numerical modelling conducted by MacAllister (2016) and MacAllister et al. (2018) was unable to replicate the initial SP gradient and did not attempt to simulate the subsequent precursor. Consequently, the source mechanisms for these phenomena remain unexplained.

1.2 Aim and objectives

Ultimately, it is important to establish whether SP monitoring can predict seawater intrusion in operating abstraction boreholes. However, SP monitoring in these boreholes presents major challenges, which have yet to be overcome. Firstly, abstractions boreholes are sensitive, highly protected assets and water companies would require further evidence of the effectiveness of the technique before permitting the installation of SP monitoring equipment. Secondly, groundwater pumping in the vicinity of SP probes would create substantial pressure gradients within the borehole and in the surrounding aquifer, a known source of SP that would lead to additional complexity in data interpretation.

The aim of this thesis is to assess whether SP can be used to predict seawater intrusion in a coastal monitoring borehole. This represents an initial step in determining whether SP

monitoring can be used effectively in abstraction boreholes, and the findings of this research should contribute to a greater understanding of SP source mechanisms in coastal aquifers.

The research will be supported by numerical modelling, which will seek to explain observed patterns of SP in a coastal monitoring borehole, particularly in the period leading up to saline breakthrough. The model will focus on the Saltdean OBH near Brighton, where two years of SP monitoring data have already been collected, spanning multiple episodes of saline intrusion. The Saltdean OBH was formerly an abstraction borehole, although it was abandoned in the 1930s due to salinisation (Jones and Robins, 1999). It now acts as a monitoring borehole for the Balsdean Pumping Station, a major asset controlled by Southern Water that provides drinking water to the eastern part of Brighton and which has been identified as being at risk from seawater intrusion. The ability to predict seawater intrusion using SP would have major implications for how groundwater is managed at this site and potentially in numerous other coastal aquifers that are exploited for drinking water and agriculture.

The specific objectives of the model will be as follows:

- To match the SP gradient observed in the Saltdean OBH prior to seawater intrusion and, through sensitivity analysis, develop an understanding of the key mechanisms that control it.

- To replicate the changes in SP observed in the days preceding seawater intrusion and explain the factors that control this signal. In particular, the modelling will seek to establish whether there is a link between these changes and impending seawater intrusion.

- To assess how SP could be used as a predictor of seawater intrusion at Saltdean and more broadly, how SP monitoring and analysis could be applied to abstraction boreholes, both in the Chalk and in other aquifer types. This will include an appraisal of the features necessary for the observed SP phenomena to occur and the key elements of data acquisition required for any alternative site.

1.3 Outline of thesis

Chapter 2 of this thesis introduces the theory of SP and its governing equations. This demonstrates the importance of the electrokinetic potential and the exclusion-diffusion potential for generating SP in coastal aquifers, respectively caused by gradients in non-hydrostatic pressure and concentration (strictly speaking the natural logarithm of ionic strength). It also summarises previous attempts to model SP in the context of saline intrusion and introduces the possibility of SP signals being generated ahead of a saline front, a concept which underpins subsequent chapters. The models described rely on an understanding of the pressure and salinity distribution throughout the model domain, parameters which are commonly provided by hydrodynamic flow and transport models.

Chapter 3 introduces the range of conceptual and numerical models used to represent seawater intrusion in coastal aquifers. The difficulties in validating these models with adequate data from field investigations are discussed and the concept of reducing uncertainty through a combination of modelling and geophysics is introduced. Subsequently, this chapter describes various approaches to simulating complex features, such as tidal boundary conditions and the extreme heterogeneity encountered in fractured aquifers, and concludes with a summary of previous models of the Brighton Chalk Block, where the Saltdean OBH is located.

This provides context for Chapter 4, which includes a detailed characterisation of the geology, hydrogeology and electrical properties of the Chalk in the vicinity of the Saltdean OBH. This provides a basis for parameterising models of the site, which are developed in the following chapters. A description of recent SP monitoring at the site is also provided, along with a discussion of the results and their significance. The observed SP phenomena at the site may be linked to saline intrusion, but the available data and previous modelling of the site have been unable to explain the mechanisms which cause them. This sets the scene for Chapters 5, 6 and 7, where a combined hydrodynamic and electrodynamic model of the site is described, which aims to replicate the SP phenomena and investigate the factors which control them.

The first phenomenon to be simulated is the SP gradient in the Saltdean OBH, which persists

throughout the year with only minor fluctuations. In Chapter 5, a combined hydrodynamic and electrodynamic model is described that aims to simulate this gradient under steady state conditions. The structures of the element meshes for the model are introduced, along with the parameter values applied, based on the site characterisation in Chapter 4. Sensitivity analyses on the results are conducted to investigate the causes of the observed SP gradient.

In Chapter 6, the model is developed further to simulate the transient evolution of SP and replicate the precursor to saline intrusion observed in the SP field data. Tidal oscillations are implemented at the coast and recharge to the aquifer is stopped to encourage saline intrusion in the borehole. Again, sensitivity analysis is used to investigate the main controls on the precursor.

Chapter 7 focuses on the frequency component of SP in the Saltdean OBH and investigates how the power spectral density (PSD) of SP changes around the time of saline intrusion. This represents a possible alternative means of predicting saline intrusion to the precursor simulated in Chapter 6. The model is used to simulate the observed changes in PSD and investigate their cause.

The model results in Chapters 5 and 6 were found to be highly sensitive to the relative contributions of the exclusion and diffusion components of the exclusion-diffusion potential, referred to as the exclusion efficiency. The exclusion efficiency of marl horizons was found to be particularly important. Chapter 8 seeks to validate the model by testing the exclusion efficiency of marl cores in the laboratory.

Finally, in Chapter 9, the findings from Chapters 5-8 are summarised and a discussion of their implications follows. Conclusions are drawn on the applicability of SP as a predictor of saline intrusion and recommendations for further work are provided.

Chapter 2

Self-potentials and their application to saline intrusion

2.1 Introduction

The self-potential (SP) method has been in use for nearly 200 years (Jackson, 2015). Many of the earliest SP investigations were conducted for the purposes of mineral exploration (e.g. De Witte, 1948; Sato and Mooney, 1960; Yungul, 1950), although since the 1970s, the technique has been applied to a much wider variety of research areas, including numerous groundwater investigations (e.g. Ernstson and Scherer, 1986; Jardani et al., 2006; Jackson et al., 2012a).

Although review articles by Jouniaux et al. (2009) and Jackson (2015) cite numerous applications of SP, its potential application to seawater intrusion in coastal aquifers is mentioned in neither. Even when Pezard et al. (2009) measured changes in SP above the saline front in a coastal borehole, the authors attributed these variations to the flow of fresh groundwater, rather than due to any influence from the saline front itself. More recent studies by MacAllister (2016), MacAllister et al. (2016) and MacAllister et al. (2018) were the first to explicitly link changes in borehole SP to remote movements of the saline front.

To understand the nature of any possible relationship between SP and seawater intrusion, it is

important to develop an understanding of SP source mechanisms and the results of previous laboratory, field and modelling investigations. This chapter presents the equations that govern SP phenomena and describes how these have been applied to the study of seawater intrusion, including the measurement of key parameters and their use in simulating intrusion processes.

2.2 Self-potential source mechanisms

Numerous mechanisms can generate SP, including electrokinetic, electrochemical, thermoelectric, piezoelectric and redox processes (e.g. Jouniaux et al., 2009). At conditions close to thermodynamic equilibrium (Revil and Linde, 2006), the contributions of each source mechanism i can be related to total electrical current density j (Am^{-2}) via the following generalised equation (Jackson, 2015; Jackson et al., 2012b; Saunders et al., 2008; Sill, 1983):

$$j = \sigma_s \nabla V + \sum_i L_i \nabla U_i, \tag{2.1}$$

where σ_s is the effective saturated electrical conductivity of the host material including matrix and pore space constituents (Sm^{-1}), V is the electrical potential (V), U_i is the thermodynamic potential of the source mechanism (e.g. non-hydrostatic pressure, ionic strength) and L_i is the associated cross-coupling term. In the absence of SP source mechanisms, Equation (2.1) is equivalent to Ohm's law. The cross-coupling term is often expressed in terms of a coupling coefficient C_i (Jackson et al., 2012b):

$$L_i = \sigma_s C_i. \tag{2.2}$$

In coastal aquifers, gradients in the electrokinetic V_{EK} and electrochemical exclusion-diffusion potential V_{EED} are likely to be the main components of SP (MacAllister, 2016; MacAllister et al., 2016, 2018), due to variations in pressure, from oceanic tides, and in salinity, due to the presence of seawater at depth below fresher groundwater near the water table (see Section 3.2).

2.2.1 Electrokinetic potential V_{EK}

An excess of charge typically occurs at mineral-water interfaces, which is balanced by an adjoining layer of opposing charge (counterions) within the fluid (Hunter, 1981). This arrangement is often referred to as the electric double layer, as shown in Figure 2.1. The fluid layer closest to the mineral surface (the Stern layer) is characterised by strongly sorbed counterions; the layer furthest from the mineral surface is known as the diffuse layer (or Gouy-Chapman layer) and is characterised by a lower density of charge, which are loosely bound to the mineral (Hunter, 1981). The point where pore-fluid becomes mobile is known as the shear plane and this typically lies within the diffuse layer (Jackson, 2015). The electrical potential at the shear plane is referred to as the zeta potential ζ (Jackson, 2015).

In chalk aquifers saturated with seawater and groundwater, where ζ is typically negative (Jackson et al., 2012a; MacAllister, 2016), groundwater flow, driven by non-hydrostatic pressure gradients, transports positively charged ions through the diffuse layer, leading to an electrokinetic (or streaming) current (Jackson, 2015) (Figure 2.2a). A conduction current arises to maintain overall electroneutrality, and ∇V_{EK} represents the electrical potential gradient required to sustain this current (Jackson et al., 2012b). In the absence of other SP sources, Equations (2.1) and (2.2) can be used to give (Jackson, 2015):

$$j = -\sigma_s \nabla V_{EK} + \sigma_s C_{EK} \nabla P_n \tag{2.3}$$

where P_n is non-hydrostatic pressure (Pa) and C_{EK} is the electrokinetic coupling coefficient ($\mathrm{VPa^{-1}}$). For a given averaging volume with a total current density of zero, the tensor C_{EK} is defined by:

$$\nabla V_{EK} = C_{EK} \nabla P_n. \tag{2.4}$$

The magnitude of C_{EK} decreases with concentration up to the concentration of seawater; in

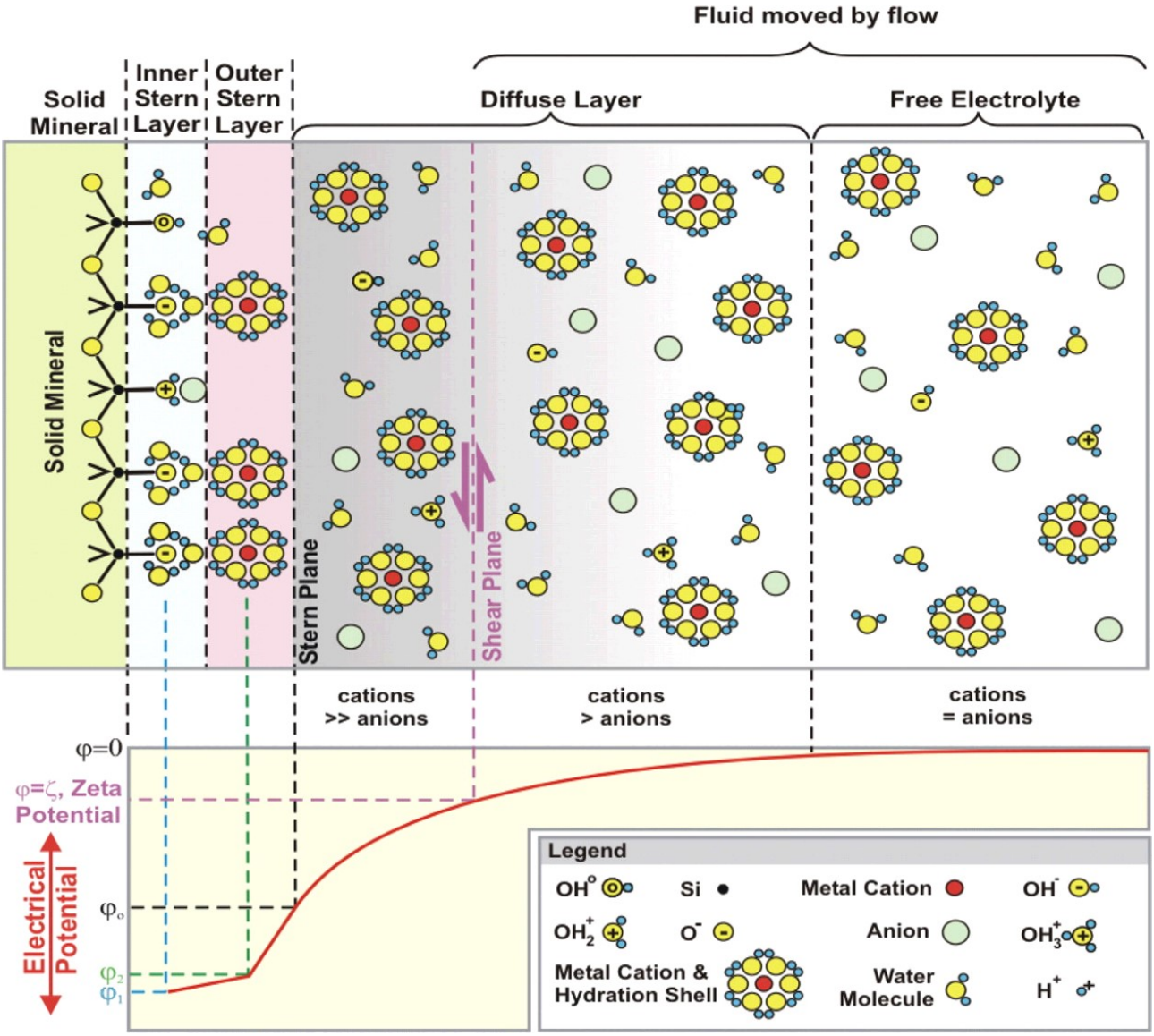

Figure 2.1: Schematic representation of the electric double layer (from Glover and Jackson, 2010).

highly saline groundwater, counterions are closer to the mineral surface on average and so a lower charge density is transported under a given (non-hydrostatic) pressure gradient (Jaafar et al., 2009; Vinogradov et al., 2010). Several authors report an empirical relationship (valid up to the concentration of seawater) between C_{EK} and the molar fluid concentration C_f of the following form, based on laboratory testing of core samples (Vinogradov et al., 2010; Jackson et al., 2010; MacAllister, 2016):

$$C_{EK} = aC_f^b. \tag{2.5}$$

Vinogradov et al. (2010) reported values of $a = -1.36 \times 10^{-9}$ and $b = -0.9123$ in sandstone, while MacAllister (2016) reported values of $a = -1.32 \times 10^{-9}$ to -7.24×10^{-10} and $b = -0.91$ to -0.76 in the Chalk of England (the Chalk). MacAllister (2016) attributed variations in the values for the Chalk to differences in ζ, which is related to C_{EK} via the Helmholtz-Smoluchowski equation (e.g. Vinogradov et al., 2010):

$$C_{EK} = \frac{\varepsilon_w \zeta}{\mu \sigma_s F}, \tag{2.6}$$

where ε_w is the dielectric permittivity of the pore fluid (Fm^{-1}), μ is the dynamic viscosity of the pore fluid (Pas), σ_s is the saturated electrical conductivity of the formation (Sm^{-1}) and F is the dimensionless formation factor. If surface conductivity is negligible (see Section 4.4.2), F is given by σ_f/σ_s, where σ_f is the electrical conductivity of the pore fluid (Sm^{-1}). An experimental procedure for measuring C_{EK} is described in Section 2.3.1.

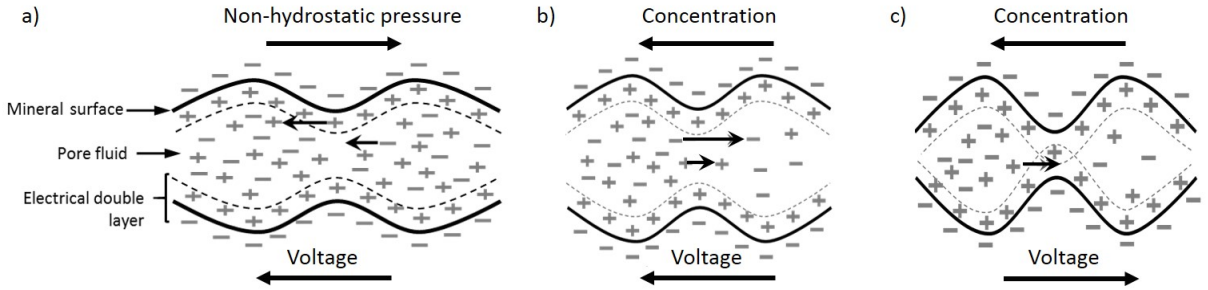

Figure 2.2: Pore-scale representation of a) ∇V_{EK}, where counterions in the diffuse layer are transported in the direction of flow b) ∇V_{ED}, where (in this example) more mobile anions migrate more easily towards fresher pore water and c) ∇V_{EE}, where (in the case of a negatively charged mineral surface) anions are excluded from the pore space and an excess of cations migrates down the concentration gradient. Adapted from Jackson et al. (2012b),© 2012, SPE. Reproduced with permission of SPE. Further reproduction prohibited without permission.

2.2.2 Exclusion-diffusion potential V_{EED}

In the absence of other SP sources, Equations (2.1) and (2.2) can be used to give the gradient of the electrochemical exclusion-diffusion potential V_{EED} (e.g. Jackson, 2015; Revil and Linde, 2006), which comprises a diffusion (or liquid junction) and an exclusion (or membrane)

component:

$$j = -\sigma_s \nabla V_{EED} + \sigma_s C_{EED} \nabla ln(C_f) \tag{2.7}$$

where C_f is the molar fluid concentration (M) and C_{EED} is the electrochemical coupling coefficient (V) (Leinov and Jackson, 2014):

$$C_{EED} = -\frac{k_B T}{e}(2T_+ - 1). \tag{2.8}$$

Here, k_B is the Boltzmann constant ($= 1.3806488 \times 10^{-23}$ JK^{-1}), T is temperature (K), e is the charge on an electron ($= 1.60217657 \times 10^{-19}$ C) and T_+ is the macroscopic Hittorf number for cations (-), which is the proportion of total current carried by cations when an electrical field is applied in the absence of concentration, temperature and pressure gradients (Revil, 1999). For a given averaging volume with a total current density of zero, Equation (2.7) can be expressed as (Leinov and Jackson, 2014; Revil, 1999):

$$\nabla V_{EED} = -\frac{k_B T}{e}(2T_+ - 1)\nabla ln(C_f). \tag{2.9}$$

In the case of a salinity gradient in an uncharged porous medium, charge separation is induced by differences in mobility between cations and anions, giving rise to a gradient in the electrochemical diffusion potential (V_{ED}) (e.g. Jackson, 2015; Revil, 1999) (Figure 2.2b). In multi-ionic solutions, such as seawater and groundwater, the potential difference between two end members with known compositions can be calculated from (Lanteri et al., 2009b):

$$\Delta V_{ED} = -\frac{k_B T}{e}\left(\frac{\sum_i K_i D_i z_i (C_i^{\Delta x} - C_i^0)}{\sum_i K_i D_i z_i^2 (C_i^{\Delta x} - C_i^0)}\right) ln\left(\frac{\sum_i K_i D_i z_i^2 C_i^0}{\sum_i K_i D_i z_i^2 C_i^{\Delta x}}\right), \tag{2.10}$$

where K_i is the hindrance diffusion coefficient (equal to one for an infinite pore volume), D_i is the diffusion coefficient for each ion (-), z_i is the charge number of ion i (-), and C_i^0 and $C_i^{\Delta x}$

are the molar concentrations of each ion in the lower and higher salinity solutions respectively.

However, simulating the mixing of these end-members due to diffusion and dispersion is not straightforward. Indeed, simulating the transport of multiple ions in solution is beyond the capabilities of most solute transport models and is computationally expensive, leading to difficulties in parameterising SP models. As Na^+ and Cl^- comprise 86% of all dissolved ions in seawater (Angelis, 2005), most SP models of seawater intrusion are simplified by representing only NaCl electrolytes (e.g. Gulamali et al., 2011; Jackson, 2015; Martínez-Pagán et al., 2010). In this scenario, T_+ is equivalent to the microscopic Hittorf number for sodium, t_{Na}. Ignoring the weak concentration dependency of t_{Na} and assuming a constant temperature gives the following expression (Jackson, 2015; Leinov and Jackson, 2014):

$$\nabla V_{ED} \mid_{(T_+=t_{Na})} = -\frac{k_B T}{e}(2t_{Na} - 1)\nabla ln(C_f). \tag{2.11}$$

The following relation can be used to represent the slight changes in t_{Na} with ionic strength (Gulamali et al., 2011; Jackson et al., 2012b; Leinov and Jackson, 2014):

$$t_{Na} = \begin{cases} 0.39, C_f < 0.09M \\ 0.366 - 2.12 \times 10^{-2}(log_{10}(C_f)), C_f > 0.09M. \end{cases} \tag{2.12}$$

From Equations (2.7) and (2.11), the coupling term for the case of pure electrochemical diffusion is given by:

$$C_{EED} \mid_{(T_+=t_{Na})} = -\frac{k_B T}{e}(2t_{Na} - 1) \equiv C_{ED}. \tag{2.13}$$

If the salinity gradient lies within a negatively charged porous medium and the electrical double layer is thick relative to the pore-throat radius, chloride ions are excluded from the pore space, leading to a gradient in the electrochemical exclusion potential V_{EE} (Figure 2.2c). Under these conditions, the sodium cations are the sole charge carriers and hence T_+=1, giving (Leinov and

Jackson, 2014; Westermann-Clark and Christoforou, 1986):

$$\nabla V_{EE} \mid_{(T_+=1)} = -\frac{k_B T}{e} \nabla ln(C_f), \tag{2.14}$$

which leads to the following coupling term for pure electrochemical exclusion:

$$C_{EED} \mid_{(T_+=1)} = -\frac{k_B T}{e} \equiv C_{EE}. \tag{2.15}$$

The relative importance of the exclusion and diffusion components can be defined by a dimensionless exclusion efficiency (Leinov and Jackson, 2014; MacAllister, 2016; Westermann-Clark and Christoforou, 1986), where:

$$\eta = -\frac{\nabla V_{EED} - \nabla V_{ED}}{\nabla V_{EE} - \nabla V_{ED}}. \tag{2.16}$$

Dividing the electrical potential gradients by $\nabla ln(C_f)$, this can be rewritten (based on Equations (2.8), (2.9), (2.11) and (2.13) to (2.15)) in terms of the coupling coefficients:

$$\eta = -\frac{C_{EED} - C_{ED}}{C_{EE} - C_{ED}}. \tag{2.17}$$

Various authors have suggested that the value of η is strongly influenced both by the zeta potential ζ and by the ratio r/λ, where r is the pore throat radius of the host rock (m) and λ is the Debye length (m), a measure of the thickness of the electrical double layer (e.g. Westermann-Clark and Christoforou, 1986; Leinov and Jackson, 2014; MacAllister, 2016). These relationships are discussed further in Sections 4.4 and 8.5.

2.2.3 Telluric currents

MacAllister et al. (2016) showed that low-frequency variations in the Earth's magnetic field

can exert a small, but measurable influence over SP in coastal aquifers. The magnetic field variations, driven by the interaction of solar plasma with the ionosphere and magnetosphere, induce electric (or telluric) currents within the Earth (Chave and Jones, 2012) which oscillate at frequencies ranging from once per day up to 100 kHz (Telford et al., 1990). The phase difference between the magnetic and electric fields is a function of period and is typically less than 45° for long period oscillations, while the magnitude of telluric currents depends on the electrical conductivity of the subsurface (Chave and Jones, 2012). A complex function, known as the magnetotelluric response tensor $\mathbf{Z}$ is used to relate the surface vector horizontal electric $\mathbf{E_H}$ and magnetic $\mathbf{B_H}$ fields and this is typically derived using complex statistical analysis (Chave and Jones, 2012). Once a reliable estimate of $\mathbf{Z}$ has been obtained, inverse modelling is used to infer the Earth's conductivity structure at a given location, although solutions to this problem are non-unique (Chave and Jones, 2012).

The apparently random fluctuations in telluric currents over a wide range of frequencies can adversely affect the interpretation of SP signals (Corwin, 1990; Jackson, 2015). However, Trique et al. (2002) were able to qualitatively infer changes in the subsurface conductivity by comparing the transient response of pairs of SP dipoles in the French Alps. Discrepancies in the paired responses were attributed to changes in telluric current distortion, due to local changes in the groundwater flow regime which affect the conductivity of the subsurface.

Another common source of telluric currents is the tidal movement of the electrically conductive oceans within the Earth's magnetic field, known as the oceanic dynamo (MacAllister et al., 2016; Rosser and Schlapp, 1990; Schlapp, 1977). These currents in turn produce an additional magnetic field, which is particularly prominent in coastal areas (Malin, 1970). Malin (1970) showed that the oceanic dynamo is dominated by the lunar semidiurnal tidal period, while magnetic fields produced in the ionosphere are greatly reduced at nighttime, giving a stronger diurnal component to the signal.

2.3 Application of SP data to saline intrusion

Although MacAllister (2016), MacAllister et al. (2016) and MacAllister et al. (2018) were the first published studies to investigate SP as an indicator of seawater intrusion in coastal aquifers, numerous authors have used SP to characterise the movement of a saline front in other media, including the modelling of SP produced by brines in hydrocarbon reservoirs (Gulamali et al., 2011; Ijioma, 2016; Jackson et al., 2012b). In several field and lab experiments, SP has been shown to respond to the movement of applied saline tracers either approaching (Martínez-Pagán et al., 2010; Revil and Jardani, 2010) or travelling beneath the measurement electrodes (Ikard et al., 2012; Sandberg et al., 2002; Bolève et al., 2011).

Interpreting the results of these studies requires knowledge of the SP coupling coefficients defined in Equations (2.4) and (2.7).

2.3.1 Measurement of coupling coefficients

Experimentally derived values of C_{EK} are obtained by applying a range of non-hydrostatic pressure differences ΔP_n across a sample and measuring the resulting differences in the electrokinetic potential ΔV_{EK}. In this one-dimensional case, there is no net current flow across the sample and hence Equation (2.4) is valid. After plotting ΔV_{EK} against ΔP_n, the value of C_{EK} is given by the gradient of the straight line through these data (e.g. Jaafar et al., 2009; Jouniaux and Pozzi, 1995; Revil et al., 2005; Vinogradov et al., 2010).

Early measurements of C_{EK} were conducted on crushed rock samples (e.g. Korpi and de Bruyn, 1972; Somasundaran and Kulkarni, 1973), but more recently, experimental set-ups have been developed to measure intact rock cores (e.g. Jaafar et al., 2009; Jouniaux and Pozzi, 1995; Revil et al., 2005; Vinogradov et al., 2010) and give a more reliable estimate of in situ behaviour. The apparatus shown in Figure 2.3 is typical of these experiments, in which the rock core is connected to reservoirs of contrasting pressure at each end. In this example, synthetic oil is used to drive brine through the system, as it prevents electrical current from flowing along a

path parallel to the core and captures any air bubbles passing through the brine (Jaafar et al., 2009).

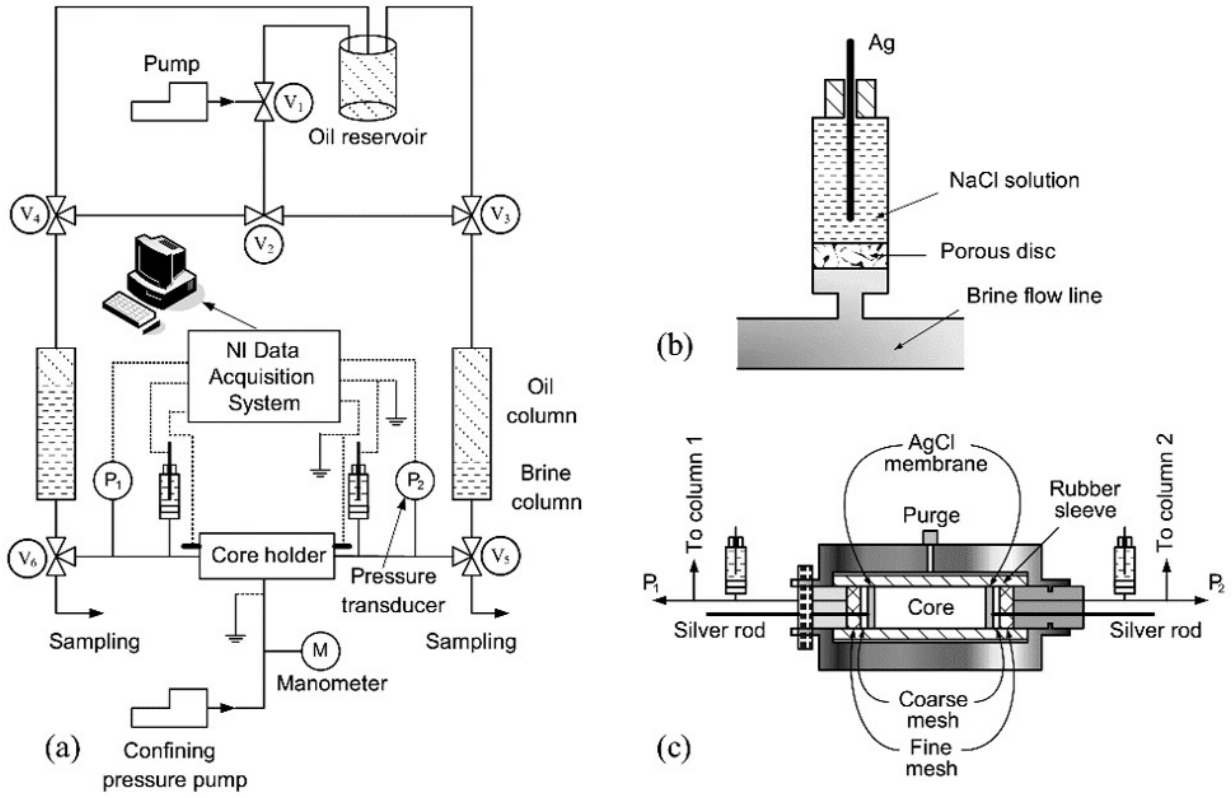

Figure 2.3: Experimental apparatus for measuring C_{EK} a) pressure control and data acquisition system, showing flowlines (solid lines), electrical connections (dashed lines) and pressure vessel containing the rock core sample, with valves V1-V6 used to adjust differential pressures and flow direction b) close-up of non-polarising Ag/AgCl electrode and c) core holder (Jaafar et al., 2009).

Values of C_{EED} can be derived from Equations (2.11) to (2.17), assuming ΔV_{EED} is known, although obtaining measurements of ΔV_{EED} is not straightforward. In a typical experiment, solutions of differing ionic strength, such as seawater and groundwater, are applied to each side of a core sample and the electrodes are filled with a solution of similar ionic strength to the adjacent reservoir, thereby minimising the development of a diffusion potential at the electrode-reservoir interface.

Applying a concentration gradient across the sample does not yield ΔV_{EED} directly, as the different ionic strengths within each electrode produce an additional voltage ΔV_C. ΔV_C must be subtracted from the measured voltage to obtain ΔV_{EED}. A detailed description of the experimental method for deriving ΔV_{EED} is given in Chapter 8.

Once ΔV_{EED} is known for a given pair of solutions, the exclusion efficiency η and hence the coupling coefficient C_{EED} can be calculated using Equations (2.16) and (2.17).

2.3.2 SP modelling of saline intrusion

Previous simulations of SP during saline intrusion can be divided into inverse models, which use SP measurements to characterise current sources, such as groundwater flow (Jardani et al., 2008) or advancing saline fronts (Martínez-Pagán et al., 2010), and forward models, which take an inferred distribution of temperature, salinity or pressure and use it to predict the resultant distribution of SP (e.g. Gulamali et al., 2011; Jackson et al., 2012b; MacAllister, 2016; Ikard et al., 2012).

The inverse problem is complicated by the non-uniqueness of the solution and typically requires an initial estimate of the source terms in conjunction with a minimised cost function. Using this approach, Martínez-Pagán et al. (2010) modelled the current sources generated by a plume of NaCl brine entering a sandbox and found that the observed SP signal was generated in advance of the saline front. Forward SP models typically rely on an initial hydrodynamic simulation to produce the required distribution of current sources (Gulamali et al., 2011; Ijioma, 2016; Jackson et al., 2012b; MacAllister, 2016).

SP models typically assume that there are no external current sources or sinks, giving no current flow across the model boundaries and hence:

$$\nabla . j = 0. \tag{2.18}$$

Combining this with Equations (2.1) and (2.2) gives:

$$\nabla . (\sigma_s \nabla V) = -\sum_i \nabla . (L_i \nabla U_i), \tag{2.19}$$

where ∇U_i represents a series of known source terms. Forward models typically use experi-

mental measurements of the coupling coefficients (see previous section) to derive the coupling terms L_i and solve Equation (2.19). This generates a distribution of electrical potentials across the model domain, so that the effective SP signal between two points can be extracted.

Early SP simulations of hydrocarbon reservoirs used forward modelling to estimate only the ∇V_{EK} component of SP, based on an initial hydrodynamic model (Jackson et al., 2010; Saunders et al., 2008; Wurmstich and Morgan, 1994). More recent studies by Gulamali et al. (2011), Jackson et al. (2012b) and Ijioma (2016) used a 3D hydrodynamic model developed in Eclipse (Schlumberger, 2010) to simulate the distribution of pore pressure, salinity and temperature produced by the injection of saline brine in a conceptualised hydrocarbon reservoir and an electrodynamic model was subsequently used to simulate the contributions of ∇V_{EK}, ∇V_{EED} and the thermoelectric potential gradient ∇V_{TE}, which arises in response to temperature gradients (Leinov and Jackson, 2014).

A common feature of these models is the change in the SP signal at production wells several hundred days prior to saline breakthrough. Jackson et al. (2012b) conceptualised the injected water front as a current source, leading to voltages that dissipate on either side of it and allowing the start of the anomaly to be detected in advance of the front. Changes in ∇V_{EK} are the largest contributors to these signals, although the results suggest that there is also a significant contribution from ∇V_{EED} (Figure 2.4). By contrast, the ∇V_{TE} component of the SP signal was found to be negligible in advance of the saline front, despite temperature differences of up to 50°C between formation fluids and the injected brine. In coastal aquifers, where variations in temperature are minimal by comparison, the contribution of ∇V_{TE} to the SP signal is likely to be even less significant.

MacAllister et al. (2018) used a similar approach to simulate SP in a coastal groundwater monitoring borehole, although their 2D model of the borehole and surrounding aquifer did not simulate the observed changes in SP prior to seawater intrusion (described further in Section 4.5.2). However, the model did produce tidal variations in SP with a similar magnitude to those observed in the field. This follows earlier work by MacAllister et al. (2016) that linked semidiurnal SP oscillations in the borehole to tidally induced movements of the saline front.

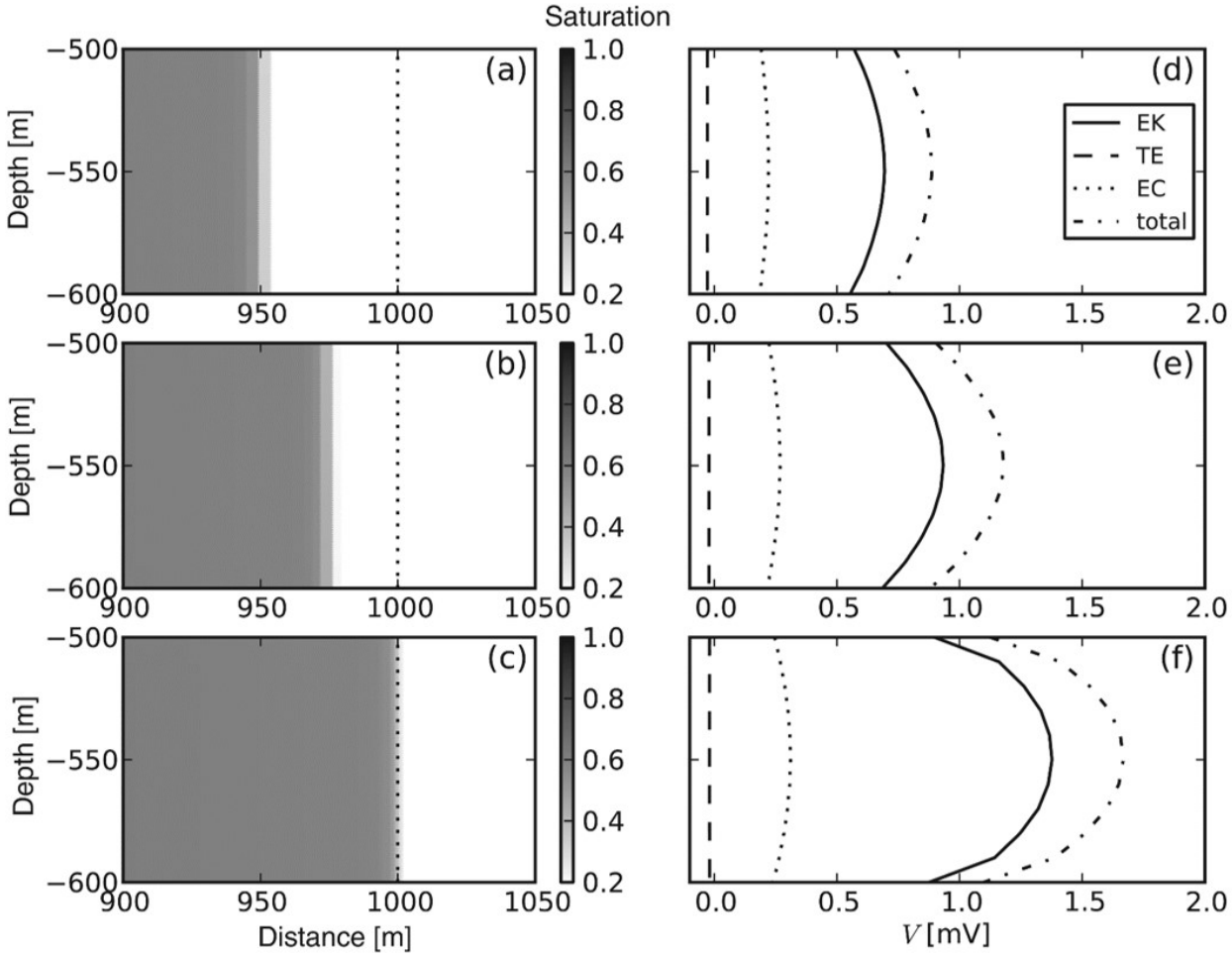

Figure 2.4: Modelling of SP precursors in a homogeneous hydrocarbon reservoir, where the initially oil-filled pore space becomes saturated with saline brine. The cross-section through the reservoir shows water saturation when the front is a) 50 m away from the production well b) 25 m from the well and c) at breakthrough. The corresponding SP signals produced by the model are shown in d) to f) (from Jackson et al. (2012b), © 2012, SPE. Reproduced with permission of SPE. Further reproduction prohibited without permission.).

Tidal variations in SP at Saltdean are discussed further in Sections 4.5.2 and 7 of this thesis.

In all of these models, temperature dependent effects were either ignored or shown to be insignificant in comparison to pressure and concentration related phenomena. Telluric currents were omitted in each case; this is probably due to the small magnitude and transient nature of these sources, as well as the obvious difficulty in parameterising the source term (Section 2.2.3).

Previous SP models typically allow the coupling coefficients C_{EK} and C_{EED} to vary with pore saturation and salinity, but commonly ignore changes in these parameters due to geological

heterogeneity. Wurmstich and Morgan (1994) and Jardani et al. (2008) are the only previous models to systematically link geological variations to changes in coupling coefficients, although neither include ∇V_{EED}.

In the models described by Gulamali et al. (2011), Jackson et al. (2012b) and Ijioma (2016) the coupling terms are unaffected by heterogeneity within a sandstone reservoir, while the mudstone layers which bound the reservoir are assumed to contain no current sources (hence $C_{EK} = C_{EED} = 0$). The models reported by Jackson et al. (2010), MacAllister (2016), MacAllister et al. (2018) and Saunders et al. (2008) assume that coupling coefficients are insensitive to changes in geology.

As discussed in Section 2.2.2, η (and therefore C_{EED}) is influenced by the pore-throat diameter of the host rock and hence, spatial variations in this parameter may be significant in heterogeneous aquifers. This issue is discussed further in Section 4.4.

2.4 Conclusions

Numerous studies indicate that SP signals can vary ahead of an advancing saline front and it has been possible to model this effect in both laboratory studies and simulations of hydrocarbon reservoirs. Although the equations which underpin these models are well understood, model parameterisation requires data from both laboratory experiments and hydrodynamic simulations. In coastal aquifers, variations in pressure and salinity are likely to be important sources of SP and accurately representing both spatial and temporal changes in these parameters requires a reliable conceptual model of the site to underpin any hydrodynamic model. A summary of approaches to hydrodynamic modelling is presented in Chapter 3, while characterisation of the Saltdean study area, which constitutes the test site for the model described in this thesis, is presented in Chapter 4.

Chapter 3

A review of groundwater modelling in coastal aquifers

3.1 Introduction

In Chapter 2, it was shown that distributions of pore water pressure and concentration are required for parameterising self-potential (SP) models and that these distributions are commonly obtained from hydrodynamic models. In the context of SP as a predictor of seawater intrusion, the hydrodynamic modelling of coastal aquifers is of particular interest.

The importance of coastal aquifers has led to numerous attempts to model and predict seawater intrusion over several decades. It is not the intention of this chapter to provide an in-depth description of these studies, as Diersch and Kolditz (2002), Simmons et al. (2010) and Werner et al. (2013) provide useful summaries of the history of research in this area. Instead, this chapter will present an overview of how the interactions of groundwater and seawater in coastal aquifers are conceptualised and modelled. In doing so, consideration will be given to the challenges of heterogeneity and time-varying boundary conditions, factors which are particularly relevant to the Chalk aquifer on the south coast of England.

All models are a simplification of reality; it is important therefore to understand what these

simplifications are and how they might affect the findings of the current study. This provides useful context for the approach to modelling described in later chapters of this thesis.

As highlighted by Butler (1994), Diersch and Kolditz (2002) and Simmons (2005), the nonlinear nature of density-dependent flow means that analytical solutions to saline intrusion problems invoke major simplifying assumptions. The assumption of a sharp interface between two immiscible fluids, the reduction of the system to one dimension and the use of steady state boundary conditions are amongst the most common simplifications. In most cases, these solutions are inadequate for investigating real-world systems, where the evolution of a dispersed front in two or three dimensions is of interest and a range of numerical approaches have been developed as a result.

The extreme heterogeneity present within fractured aquifers such as the Chalk of England presents further challenges for modelling these systems at an appropriate level of complexity. The hydrogeological properties of the Chalk are discussed in detail in Section 4.3 but in essence, the variation of key parameters such as hydraulic conductivity, by many orders of magnitude, often over distances of only a few millimetres, represents a major challenge for any groundwater model. This challenge manifests firstly as one of uncertainty, given the lack of data on the location of every hydraulically significant fracture within the Chalk. Secondly, there is the issue of resolution; even if the locations of fractures were known, constraints on the number of grid cells within a model would preclude their inclusion as explicit features and an acceptable method of spatial averaging must be found. In modelling seawater intrusion, representing the complex interactions of saline water between fractures and the surrounding matrix of the Chalk constitutes a further challenge.

In coastal aquifers, in addition to spatial variations in aquifer properties, there are complex boundary conditions driven by periodic changes in sea level, due to waves and tidal oscillations. The importance of these factors depends on the overall objectives of the study and many models, particularly those concerned with the long-term behaviour of the system, do not include these oscillations. However, the importance of semidiurnal changes in SP at Saltdean, as recently highlighted by MacAllister et al. (2016), suggests that tidal phenomena cannot be ignored in

the current study.

In this chapter, standard conceptual models for seawater and groundwater interactions will be presented, followed by an overview of the most common approaches to simulating seawater intrusion. This will be followed by examples of recent attempts to model fractured coastal aquifers, approaches to simulating tidal phenomena in groundwater models and finally, a description of groundwater models previously developed for the Brighton Chalk Block, where the Saltdean OBH is located.

3.2 Conceptualising groundwater-seawater interactions

The standard conceptual model of coastal aquifers is of a wedge of fresh groundwater overlying a body of denser saline groundwater in connection with the sea (Figure 3.1a). This concept was first proposed by DuCommun (1828), who suggested that the depth z below sea level of the interface between the two water types (in metres) could be inferred from their respective densities, a relation now commonly known as the Ghyben-Herzberg equation, following later studies by Badon-Ghyben (1889) and Herzberg (1901):

$$z = \frac{\rho_f}{\rho_s - \rho_f} h, \tag{3.1}$$

where ρ_f is the density of fresh water (1000 kgm^{-3}), ρ_s is the density of seawater (1025 kg/m^{-3}) and h is the elevation of the water table above sea level (m).

Numerous researchers have pointed out the major simplifying assumptions inherent in this relationship, including those of a sharp interface (and hence no mixing of groundwater and seawater), a homogeneous aquifer, static water bodies and the absence of vertical flow (the Dupuit assumption). More recent conceptual models, such as the one proposed by Jones and Robins (1999) for the fractured Chalk on the south coast of England show how radically the interface may change when these assumptions are not satisfied (Figure 3.1b).

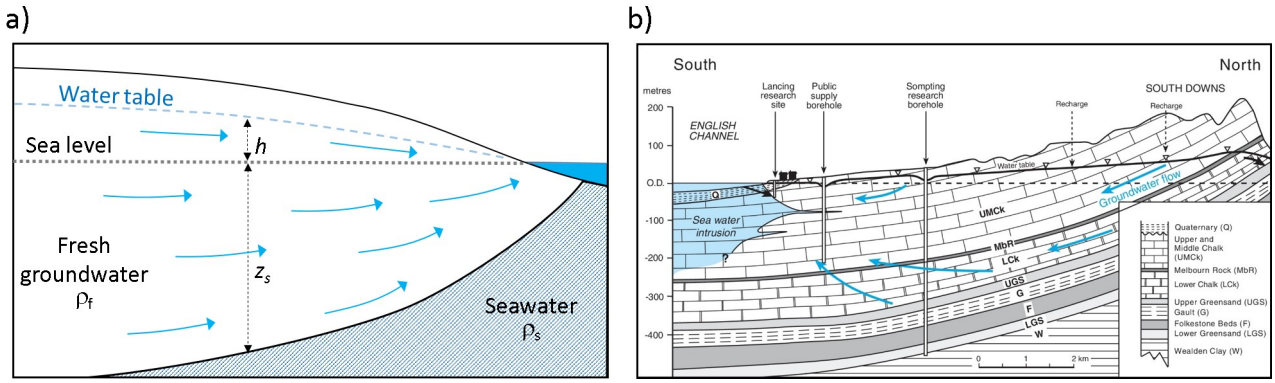

Figure 3.1: Differing conceptual models of groundwater and seawater interactions: a) the classic 'wedge-shaped' geometry of the saline-fresh water interface, showing the depth of the interface below sea level z_s, the elevation of the water table above sea level h and the densities of fresh groundwater ρ_f and seawater ρ_s (adapted from USGS, 1999) b) a conceptual model of the saline-fresh water interface in a fractured chalk aquifer on the south coast of England (Jones and Robins, 1999).

However, the Ghyben-Herzberg approach is still applied in many studies, sometimes with modifications, to give a first-pass estimate of the depth to the interface (e.g. Essaid, 1986; Nunes et al., 2003; Pool and Carrera, 2011). It also provides a useful insight into the potential effects of pumping near the coast, where a small amount of drawdown of the water table can lead to rapid upconing of saline water beneath an abstraction borehole (Figure 3.2).

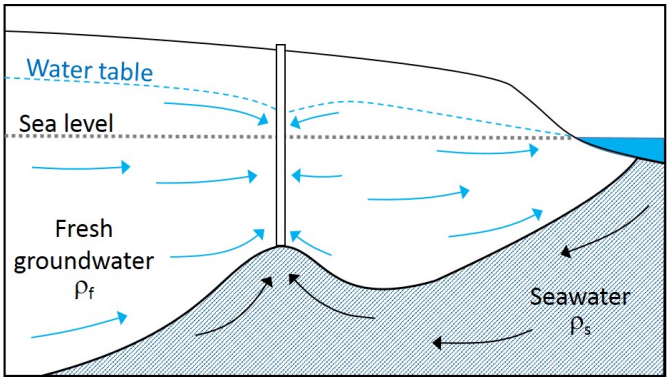

Figure 3.2: Conceptual model of upconing saline water due to pumping from a coastal abstraction borehole (adapted from USGS, 1999).

Validating any conceptual model presents an obvious challenge, particularly as many of the earliest studies relied on water levels and salinity profiles in boreholes to infer the location and extent of the interface in three dimensions. More recently, geophysical surveys have been used to assist in this regard. The results of these surveys suggest that the classic wedge-shaped interface cannot be applied to many environments, particularly where the subsurface is highly

heterogeneous (e.g. McDonald et al., 1998; Sutter and Ingham, 2017).

Unfortunately, the non-uniqueness of geophysical interpretations means that much uncertainty remains. A further development in this field has been to constrain the solution by combining geophysical observations with groundwater modelling (Figure 3.3). Although Comte and Banton (2007) used electrical resistivity tomography for this purpose, it has been applied more recently to SP data by MacAllister et al. (2018).

3.3 Modelling software packages

Groundwater flow is typically described using Darcy's law (Darcy, 1856), which can be written in the following generalised form (e.g. Povich et al., 2013):

$$\mathbf{u} \equiv \phi \mathbf{v} = -\frac{\mathbf{k}}{\mu}(\nabla P + \rho g \nabla h), \tag{3.2}$$

where $\mathbf{u}$ is the specific discharge (ms^{-1}), often referred to as the Darcy velocity, ϕ is the porosity of the aquifer (-), $\mathbf{v}$ is the mean pore water fluid velocity (ms^{-1}), $\mathbf{k}$ is the permeability tensor of the aquifer (m^2), μ is the dynamic viscosity of the groundwater (Pas), P is pressure (Pa), ρ is fluid density (kgm^{-3}) and g is the acceleration due to gravity (ms^{-2}).

In coastal aquifers subject to seawater intrusion, density varies as a result of changes in salinity and Darcy's law is insufficient to characterise the groundwater flow system accurately. Numerical groundwater models of seawater intrusion must therefore solve the variable-density groundwater flow equation (e.g. Povich et al., 2013):

$$\nabla.(\rho\phi\mathbf{v}) = Q_s - \phi\frac{\partial\rho}{\partial C}\frac{\partial C}{\partial t} - \rho S_{ps}\frac{\partial P}{\partial t}, \tag{3.3}$$

where S_{ps} is specific pressure storativity (m^{-1}), t is time (s), Q_s is the unit volumetric fluid mass source ($\mathrm{kgm}^{-3}\mathrm{s}^{-1}$) and C is solute concentration in the fluid (kg/kg). Given the interde-

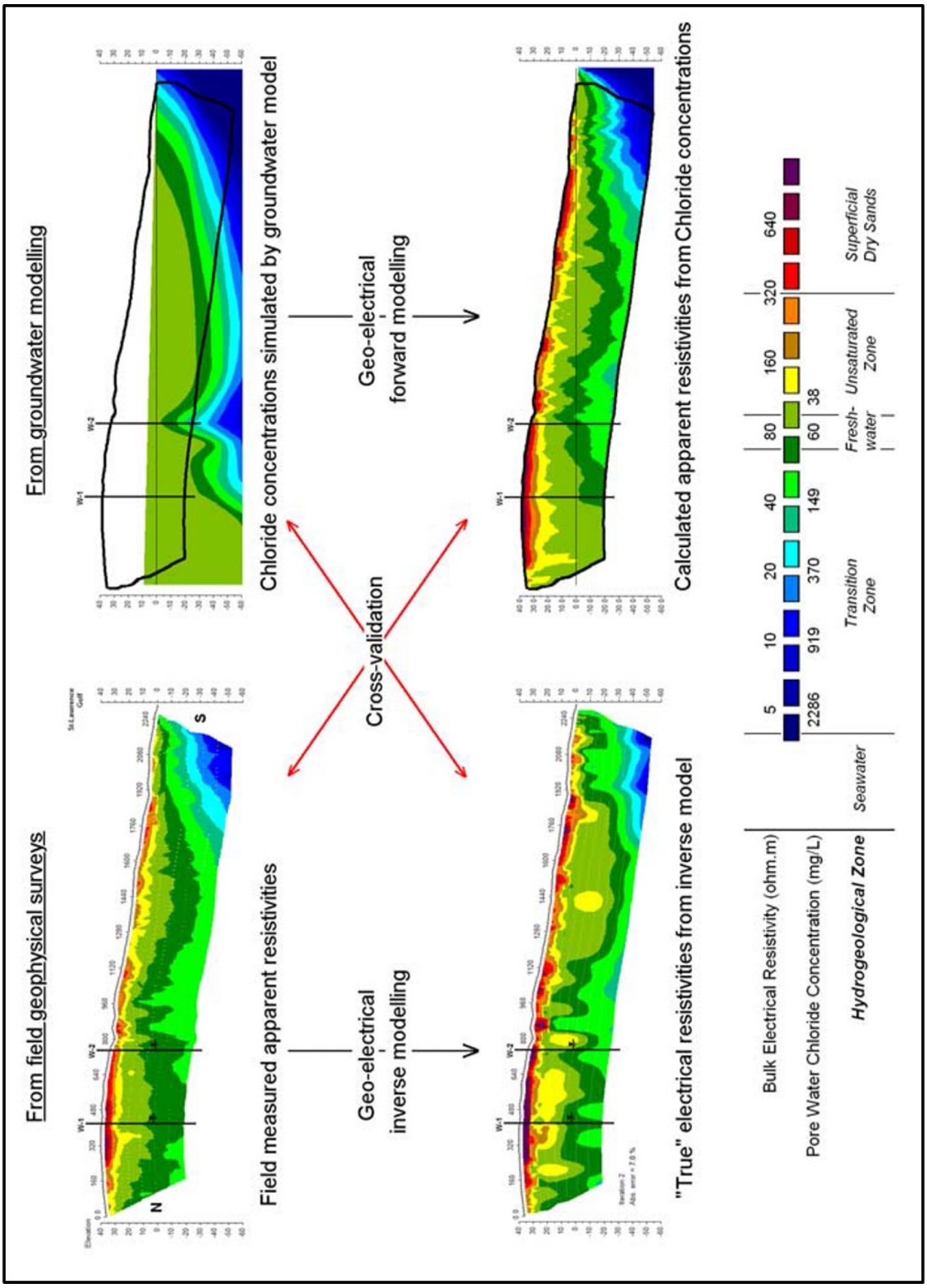

Figure 3.3: Conditioning geophysical observations of seawater intrusion with hydrodynamic modelling (Comte and Banton, 2007).

pendency of pressure and concentration, these models also must solve the advective-dispersion equation for each time step (assuming a conservative solute) (e.g. Povich et al., 2013):

$$\frac{\partial(\phi\rho C)}{\partial t} = \nabla.(\phi\rho\mathbf{D}\nabla C - \phi\rho C\mathbf{v}) + C_s Q_s, \tag{3.4}$$

where C_s is the solute concentration of fluid sources (kg/kg) and $\mathbf{D}$ is the dispersion tensor (m^2s^{-1}), given by:

$$\mathbf{D} = \phi D_m \mathbf{I} + (\alpha_L - \alpha_T)\frac{\mathbf{u}\times\mathbf{u}}{|\mathbf{u}|} + \alpha_T|\mathbf{u}|\mathbf{I}, \tag{3.5}$$

where D_m is the apparent molecular diffusivity of the solute in solution within the aquifer (m^2s^{-1}), $\mathbf{I}$ is the identity tensor and α_L and α_T are the respective longitudinal and transverse values of dispersivity (m). The second and third terms on the right hand side of Equation (3.5) constitute the mechanical component of dispersion $\mathbf{D}_{mec}$, which represents the net effect of pore-scale variations in travel time between different flow paths (Fetter, 2001).

Most groundwater modelling packages solve these equations in discretised form by applying a fixed grid over the model domain and calculating pressure and concentration for each grid cell. This technique, known as the Eulerian method, tends to offer greater computational efficiency and improved mass balance compared to the alternative Lagrangian approach, which solves the groundwater flow and transport equations for a discrete number of moving particles (Zheng and Bennett, 2002). However, Eulerian methods may suffer from excess numerical dispersion, particularly in advection dominated systems (Zheng and Bennett, 2002). Mixed Eulerian-Lagrangian methods, such as the Method of Characteristics (MOC), give an improvement in the results for a given grid-resolution, but require greater computational effort than a pure Eulerian approach (Werner et al., 2013). The trade-off between accuracy and computational effort is a theme which runs through many aspects of solute transport modelling.

Simmons et al. (2010) and Werner et al. (2013) list more than 20 different numerical modelling codes for simulating variable density groundwater flow, but there is no consensus in the litera-

ture as to which of these is the optimal method for simulating seawater intrusion problems, as each offers a different range of advantages and drawbacks. For example, finite element methods typically offer greater accuracy and more flexibility in representing complex geometries than finite difference models, but with greater computational expense (Zheng and Bennett, 2002). The issue of model accuracy is further complicated by the absence of reliable benchmarks for these codes, with sufficient complexity to be representative of real-world seawater intrusion problems (Werner et al., 2013). For example, the commonly used Henry problem (Henry, 1964) represents diffusion, but not hydrodynamic dispersion of salt (Werner et al., 2013), while van Reeuwijk et al. (2009) showed that another commonly used benchmark, the Elder problem (Elder, 1967), has multiple steady state solutions that depend on the choice of initial conditions.

SUTRA (Voss and Provost, 2002) is perhaps the most widely used package for simulating seawater intrusion (Simmons et al., 2010) and it offers several advantages within the context of the current study. Its finite element formulation allows for the complex interactions between dipping strata, fracture zones and borehole voids to be represented, while the freely available source code can be modified for the implementation of complex boundary conditions, such as those encountered when modelling tidal pressure variations at the coast. It has been tested successfully against several standard benchmarks for seawater intrusion modelling, including the Henry, Elder and HYDROCOIN (OECD, 1988) problems (Werner et al., 2013), while its longevity has allowed for numerous upgrades and auxiliary software packages to be developed.

3.4 Modelling of fractured aquifers

Simmons et al. (2010) note that the treatment of heterogeneity, and more particularly fractures, in coastal groundwater models has been far from rigorous to date. This is driven both by the difficulties in determining the locations of hydraulically significant fractures and by the challenge of representing them adequately in regional models, where the small scale of fracture apertures contrasts with relatively large model domains.

Uncertainty over the distribution of hydraulically significant fractures can be approached through

stochastic modelling. This was first applied to a coastal groundwater system by Cherubini et al. (2013), who generated 100 possible realisations of cavity distributions within a karst aquifer and used these to parameterise a steady state groundwater model in MODFLOW. However in this case, the limited model extent (180 × 180 × 35 m) did not reach the coast and the simulation did not incorporate density-dependent flow.

By contrast, Xu and Hu (2016) developed a discrete continuum model to represent density-dependent flow within a single fracture network and surrounding matrix. This involved simulating a relatively simple test case in two dimensions, with only 140 columns and 37 rows and involved a run-time of more than 15 hours to simulate a single day of groundwater flow. Clearly, this precludes the use of stochastic modelling and has yet to be applied to a real-world scenario, where there is typically a high degree of uncertainty over the extent of any fracture network and its geometry is likely to be far more complex.

These examples highlight the trade-off between accurately representing heterogeneous physical processes within coastal aquifers and capturing the inevitable uncertainty in parameterising real-world systems. At present, computational cost precludes doing both. Models that represent density-dependent flow in fracture systems with a high degree of accuracy have been applied to relatively simple test cases only (e.g. Graf and Therrien, 2008; Grillo et al., 2010; Sebben et al., 2015), while stochastic models that characterise the uncertainty of real-world systems require simplifying assumptions, such as an absence of density-driven flow (e.g. Cherubini et al., 2013) or the assignment of equivalent porous media (EPM) (e.g. Hassan et al., 2001), in which single parameter values are used to represent the combined properties of fractures and matrix.

As a result of these difficulties, published models of fractured coastal aquifers typically implement an EPM approach or include a small number of fracture zones within an EPM aquifer. Although Sebben et al. (2015) found that a small number of widely spaced fractures can radically alter the shape of the saline front, the authors noted that the errors associated with an EPM approach were reduced when the density of fractures is high and suitable values of dispersivity were assigned (Figure 3.4).

These findings support the combined EPM and discrete fracture network approach implemented

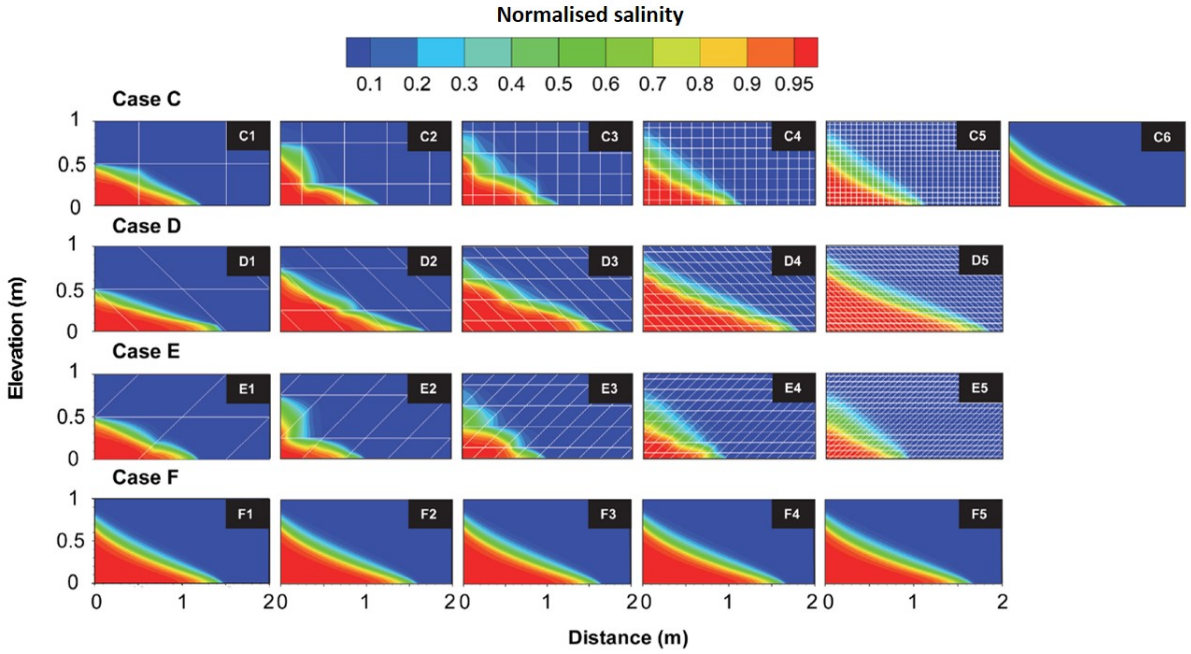

Figure 3.4: The effects of various densities and orientations of fracturing on modelled saline fronts. The EPM model C6 is compared to the orthogonal fracture scenarios (C1-C5), while EPM models F1-F5 accompany the inclined fracture sets D1-D5 and E1-E5 (adapted from Sebben et al., 2015).

by Dokou and Karatzas (2012), who used FEFLOW to model seawater intrusion in an unconfined karst aquifer. Their initial model superimposed field observations of likely fracture locations on an otherwise equivalent porous medium. Subsequent fractures were added during model calibration to match anomalously high chloride concentrations. MacAllister et al. (2018) implemented a similar method for the Saltdean study area, using Eclipse 100 (Schlumberger, 2010). The authors used geophysical logging of the Saltdean OBH to define a single fracture zone at its base and simulated this within an otherwise homogeneous Chalk aquifer.

3.5 Wave and tidal simulations

Whilst most regional models of seawater intrusion ignore the impacts of waves and tidal variations (e.g. Dokou and Karatzas, 2012; Gingerich and Voss, 2005; Werner and Gallagher, 2006), some studies have managed to incorporate detailed representations of these features over fairly limited model domains (Bakhtyar et al., 2012; Xin et al., 2010). There is some evidence to suggest that the implementation of both tides and wave action in models substantially increases

the amount of saline intrusion and that the dissipation of wave energy can lead to an effective increase in mean sea level near the coast, known as wave set-up (Xin et al., 2010). Whilst the implementation of waves appears to strongly influence saline intrusion within a few metres of the shoreline, Xin et al. (2010) and Bakhtyar et al. (2012) found these effects to be negligible at larger scales when compared to the effects of changes in water table elevation and tidal variations respectively.

These detailed representations of wave and tidal processes typically involve short time steps and relatively small model domains. The model of Bakhtyar et al. (2012) simulated a period of only 15 minutes, using time steps of 5×10^{-3} seconds to simulate a 50 m long transect perpendicular to the coast. The model produced by Xin et al. (2010) used 10 second time steps to simulate a period of up to 600 days for a 180 m long transect.

Regional models of coastal groundwater systems typically invoke simpler representations of tidal processes and ignore the action of individual waves (Ataie-Ashtiani et al., 1999; Li et al., 2009; Zhou et al., 2013), thereby saving on computational expense. In each case, tidal forcing has been shown to exert a major influence on the coastal groundwater system. For example,Li et al. (2009) used a SEAWAT model to show that increased tidal amplitudes increase both the inland extent of seawater intrusion and the volume of groundwater discharged at the coast.

Recent work by MacAllister et al. (2016) has shown an important link between tidal oscillations at the coast and observed variations in SP. MacAllister et al. (2016) showed that several components of oceanic and ionospheric tides (Table 3.1) could be seen in the SP dataset and that their relative amplitudes were similar to those seen in sea-level variations at the coast. The semidiurnal M_2 mode was found to be particularly prominent.

Subsequent hydrodynamic modelling of the system by MacAllister (2016) and MacAllister et al. (2018) implemented a tidal boundary condition with both M_2 and fortnightly oscillations, the latter representing the effects of the spring-neap tidal cycle. This allowed observed variations in pressure and salinity within the borehole to be simulated accurately and provided the basis for SP modelling, as discussed in Section 2.3.2.

Table 3.1: Semidiurnal and diurnal components of ionospheric and oceanic tides (adapted from Bindoff et al., 1988 and Doodson, 1921).

Component	**Description**	**Period (hours)**	**Frequency (cpd)**	**Relative amplitude**
M_2	principal lunar semidiurnal	12.421	1.932	1.000
S_2	principal solar semidiurnal	12.000	2.000	0.466
N_2	lunar elliptic semidiurnal	12.658	1.896	0.191
K_2	lunisolar semidiurnal	11.967	2.005	0.127
K_1	lunar diurnal	23.934	1.003	0.573
O_1	lunar diurnal	25.819	0.930	0.415
P_1	solar diurnal	24.066	0.997	0.193
Q_1	larger lunar elliptic diurnal	26.868	0.893	0.079
J_1	smaller lunar elliptic diurnal	23.098	1.039	0.032
S_1	solar diurnal	24.000	1.000	0.005

3.6 Modelling of the Brighton Chalk Block

The earliest published groundwater model of the Brighton Chalk Block was developed by Nutbrown et al. (1975) to investigate the impacts of variable recharge and abstractions on groundwater flow. As the model assumes an absence of vertical flow within the aquifer (the Dupuit assumption), it is limited in its ability to simulate seawater intrusion processes accurately. Simulated values of hydraulic head for the end of each year were used to estimate the depth of the saline-freshwater interface within the model. The authors note that this is unlikely to be suitable in the most permeable parts of the coastal aquifer, where seasonal movements of the saline front can be rapid. However, an important finding of the model developed by Nutbrown et al. (1975) is that transmissivity values in excess of 2,500 m^2/d were required for calibration to observed head values in several dry valleys, including in the vicinity of the Saltdean OBH.

A more recent model of the Brighton and Worthing Chalk Blocks, developed in MODFLOW by AMEC (2016), also required increased transmissivity between Saltdean and the coast during calibration in order to match observed groundwater levels. The primary aim of the model

was to assess the impacts of Southern Water's groundwater abstraction boreholes on flows and ecology in the Lewes Winterbourne stream, although the study also considered the potential impacts of abstractions on saline intrusion. Transport modelling was not conducted as part of this exercise, although unsurprisingly, its analysis of fluid electrical conductivity σ_f data from the Balsdean Pumping Station found that the timing of saline intrusion events was linked to spring high tides at the coast and low groundwater levels.

Focusing specifically on the issue of saline intrusion at Saltdean, MacAllister et al. (2018) used a hydrodynamic model developed in Eclipse 100 (Schlumberger, 2010) to simulate pressure and salinity variations near the Saltdean OBH; these were subsequently used to parameterise an electrodynamic model of the area. The hydrodynamic model assumed that advection is the sole mechanism for solute transport and since molecular diffusion and mechanical dispersion were ignored, a narrow saline front was produced, with a classic 'wedge-shape' geometry.

Although MacAllister et al. (2018) included a single discrete fracture near the base of the Saltdean OBH, the rest of the aquifer was modelled as an EPM, thereby ignoring the effects of differing rates of transport in the numerous fractures and matrix blocks known to exist throughout the Chalk. While each component may contain a relatively sharp transition zone, at a large scale, the offset between them can be considered equivalent to a relatively dispersed saline front, as highlighted by Konikow (2011). The mechanical dispersion term applied in most solute transport models accounts for this phenomenon in EPMs, although it is less appropriate for explicitly representing specific hydrogeological flow features, such as fractures, where there is less variation in flow path length and groundwater velocity.

3.7 Discussion and conclusions

It is clear that no model can simulate the full range of complex physical processes that occur within a fractured coastal aquifer. A pragmatic approach is therefore required to prioritise the features most likely to affect the overall modelling objectives, based on a conceptual model of the study site. A detailed description of the study area is presented in Chapter 4.

As discussed in Sections 2.3.2 and 4.5.2, previous hydrodynamic and electrodynamic modelling has failed to replicate some of the most important SP phenomena at the study area. It is important to ascertain whether the model can be improved by implementing more physically-based mechanisms for solute transport, such as molecular diffusion. Although the locations and characteristics of some fractures may be known, there is a need to invoke an EPM approach across the majority of any coastal aquifer. In doing so, mechanical dispersion may be required to represent the effects of small-scale heterogeneity on the saline front.

Previous work by MacAllister et al. (2018) suggests that the implementation of complex, tidal boundary conditions is also important in simulating the pressure, salinity and SP variations observed in a coastal Chalk groundwater observation borehole.

SUTRA is a commonly used density-dependent flow package that can incorporate these features, while its finite element structure provides flexibility in representing complex geometries. It is well known within the scientific community and is open source, such that modelling results can be replicated easily by others and developed further. For these reasons, SUTRA has been chosen as the platform for hydrodynamic modelling in this project.

Chapter 4

Characterising the Saltdean study area: geology, hydrogeology and self-potentials

4.1 Introduction

As discussed in Section 2.3.2, previous modelling studies suggest that changes in self-potential (SP) within oil wells may occur ahead of an advancing saline front (e.g. Gulamali et al., 2011; Jackson et al., 2012b; Ijioma, 2016), while similar phenomena have been reported in laboratory experiments (e.g. Martínez-Pagán et al., 2010). Until recently however, there have been no studies on the use of SP to predict seawater intrusion in coastal groundwater boreholes.

To address this, MacAllister (2016), MacAllister et al. (2016) and MacAllister et al. (2018) carried out nearly 2 years of SP monitoring in the Saltdean OBH near Brighton (Figure 4.1). The Saltdean OBH, which lies 1.8 km from the coast, was formerly used as an abstraction borehole, but was abandoned in 1936 because of repeated saline intrusion (Jones and Robins, 1999). It now acts as a monitoring borehole for the Balsdean Pumping Station (PS), around 1.2 km further inland. Southern Water, which operates the Balsdean PS, is concerned about

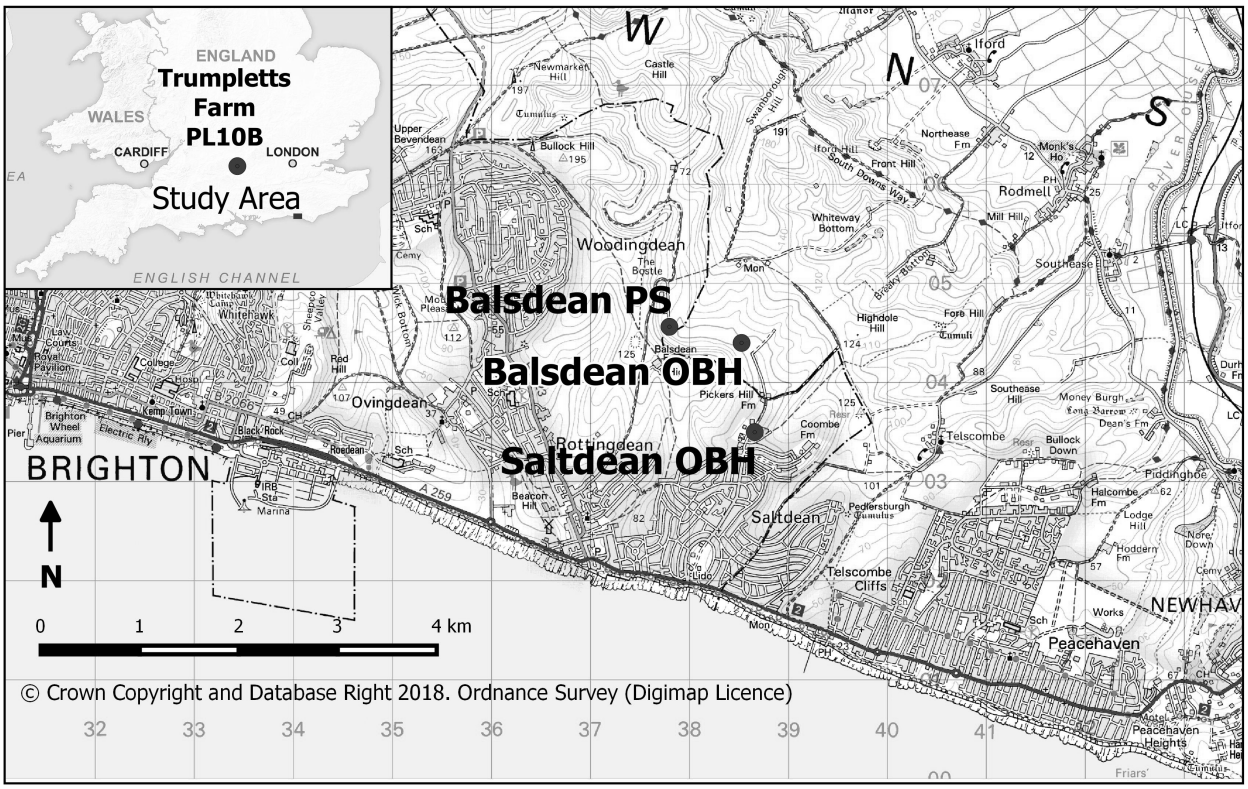

Figure 4.1: Map of the Saltdean study area and location of the Trumpletts PL10B borehole.

the ongoing risks of seawater intrusion to this key asset, making the Saltdean OBH a suitable choice for SP monitoring.

An array of SP electrodes was installed in the Saltdean OBH in May 2013, along with temperature T, pressure P and fluid electrical conductivity σ_f probes, to investigate possible changes in SP prior to saline breakthrough (MacAllister, 2016) (Figure 4.2). SP profiles were also taken in the Trumpletts PL10B borehole in Berkshire in July 2013 (MacAllister, 2016) and in the Balsdean OBH in December 2015, as part of this project. These boreholes intersect similar geological units and allow the results from the Saltdean OBH to be compared with those obtained further inland.

This chapter summarises what is already known from the literature about the geology, hydrogeology and petrophysics of the Saltdean area and analyses the data obtained from the SP monitoring programme. The numerical modelling described in subsequent chapters aims to explain the key features of the SP data, based on the parameter values presented herein.

4.2 Geology

The Saltdean OBH (Figure 4.2) lies within a dry valley in the South Downs, an area dominated by chalk strata that form part of the wider Chalk Group (the Chalk), a lithostratigraphic unit covering the southeast portion of England. The majority of the Chalk comprises very pure limestone units, although these are frequently interrupted by horizons of marl, flint and hardgrounds (Jones and Robins, 1999). The matrix of the pure limestone units comprises a mixture of coccoliths, foraminifera and shell fragments, separated by narrow pores, with a typical throat diameter of around 1 μm (Price, 1987).

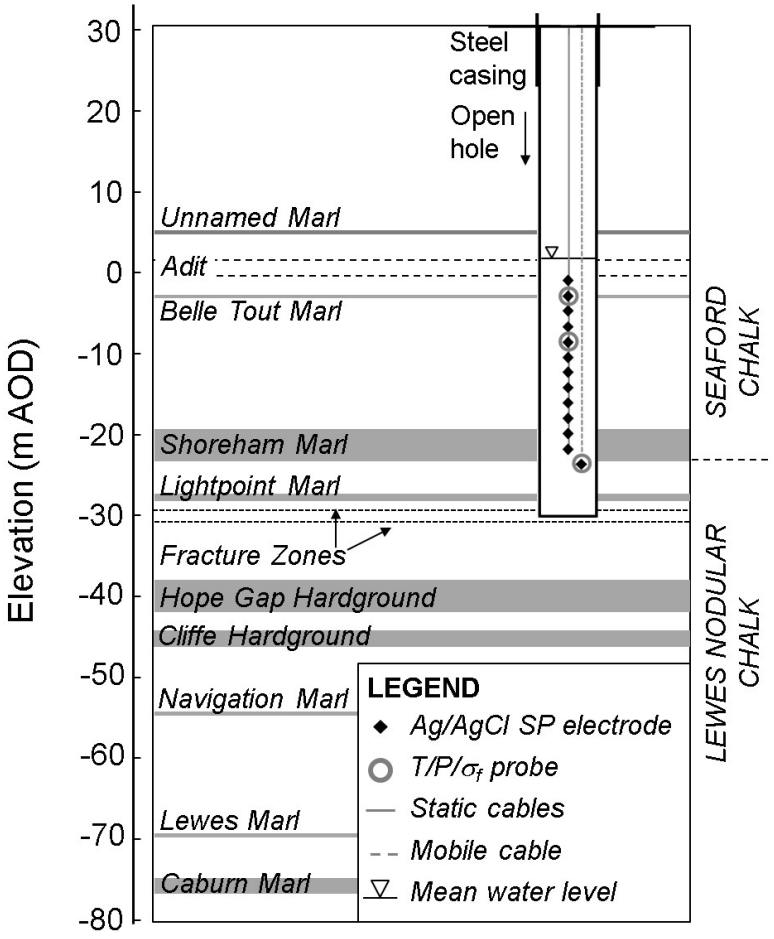

Figure 4.2: Schematic of the Saltdean OBH. The stratigraphy has been inferred from: geophysical logs of the Victoria Gardens and St Peter's Church boreholes, c. 7 km along strike to the west (Jones and Robins, 1999); descriptions of the depths of the upper fracture zone and adit (BGS, 2018a; Jones and Robins, 1999); and a 3D geological model of the area developed by AMEC (2012). The presence of the lower fracture zone was inferred during calibration of the model described in Chapters 5 to 7.

The Chalk strata near Saltdean dip gently towards the coast (Jones and Robins, 1999) at an angle of approximately 5°, based on the inferred depth of the Seaford-Lewes Nodular Chalk contact in the Saltdean OBH (AMEC, 2012) and at the Balsdean PS (MWH, 2006). The Saltdean OBH extends to 60 m below ground level, intersecting a series of chalk, marl and hardground layers within the Seaford and Lewes Nodular Chalk Members of the White Chalk Subgroup (Figure 4.2). Previous logging of the Saltdean OBH indicates a hydraulically significant fracture zone at its base (Jones and Robins, 1999; MacAllister, 2016), while a second, deeper fracture zone, which is also shown in Figure 4.2, has been inferred during development of the numerical model in Chapter 6.

Borehole logs from the area indicate that an adit with a diameter of 1.4 m intersects the Saltdean OBH at -2 m above Ordnance Datum (AOD) and that this extends 32 m to the northwest, connecting the Saltdean OBH to two other groundwater boreholesnearby (BGS, 2018a). This is discussed further in Section 4.3.1.

4.3 Hydrogeology

4.3.1 Groundwater levels

Water levels in the Saltdean OBH were measured at 5 minute intervals from 24 May 2013 to 23 February 2015 using the $T/P/\sigma_f$ probes (MacAllister, 2015b). They vary seasonally, from a maximum of > 3 mAOD towards the end of the winter recharge season, to around 0.5 mAOD in late summer, when seawater intrusion typically occurs (Figure 4.3).

Borehole water levels are also strongly influenced by oceanic tides and to a lesser extent, abstractions from the Balsdean PS (Figure 4.4). The amplitude of tidal fluctuations in the Saltdean OBH is 0.37 m on average, compared to an average amplitude of 2.4 m at Newhaven, which lies on the coast 7 km to the southeast. The average lag between tidal maxima at Newhaven and in the Saltdean OBH is 3.67 hours (0.153 days).

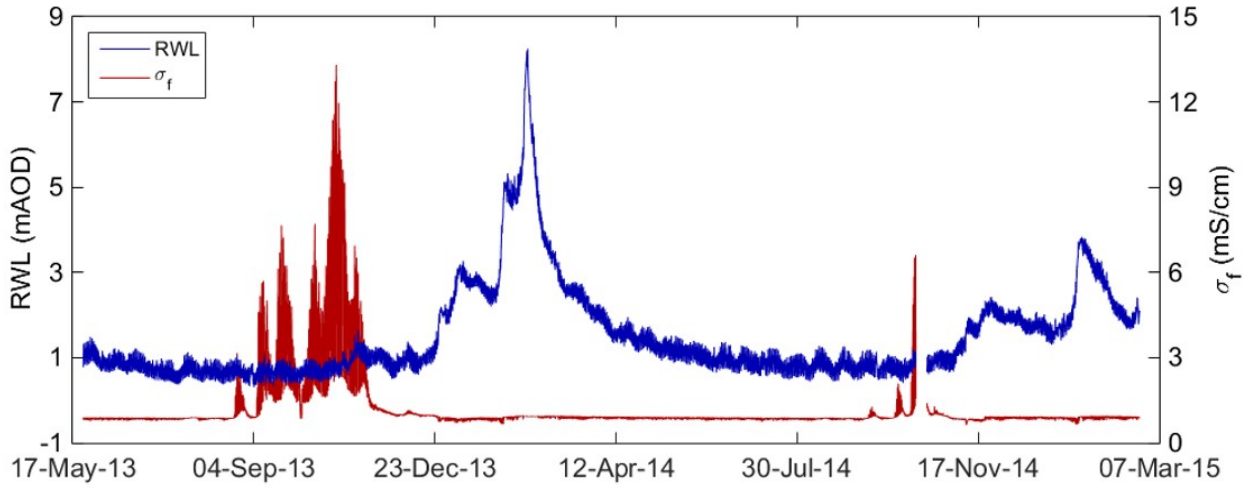

Figure 4.3: Reduced water levels (RWL) and σ_f in the Saltdean OBH, based on data provided by MacAllister (2015b).

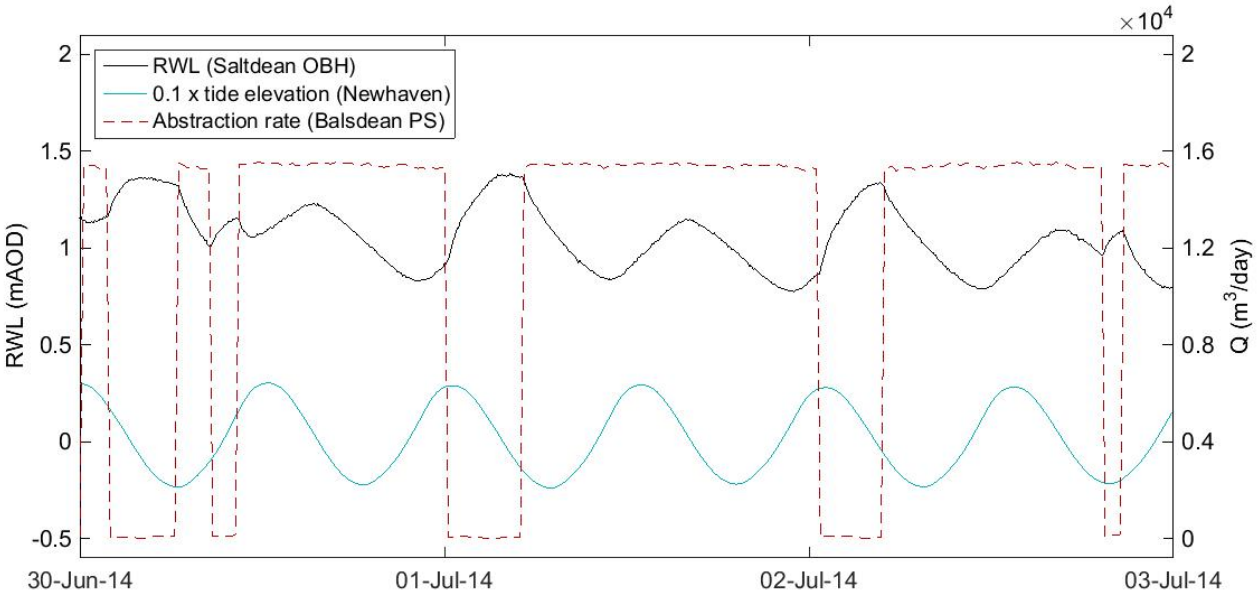

Figure 4.4: Influence of marine tides and Balsdean PS abstractions on water levels in the Saltdean OBH. The magnitude of marine tides at Newhaven has been reduced by a factor of 10 for display purposes. Based on data provided by MacAllister (2015b), BODC (2015) and Southern Water (2015).

From spectral analysis, using the Lomb-Scargle power spectral density (PSD) method to account for gaps in the data (Lomb, 1976; Scargle, 1982), water levels were found to vary with a dominant frequency of 1.932 cycles per day (CPD) (Figure 4.5a). This is consistent with the frequency of the M_2 lunar semidiurnal tidal component (Table 3.1) and corresponds to a period of 0.518 days. A smaller peak, consistent with the S_2 tidal mode, can be seen also. The same

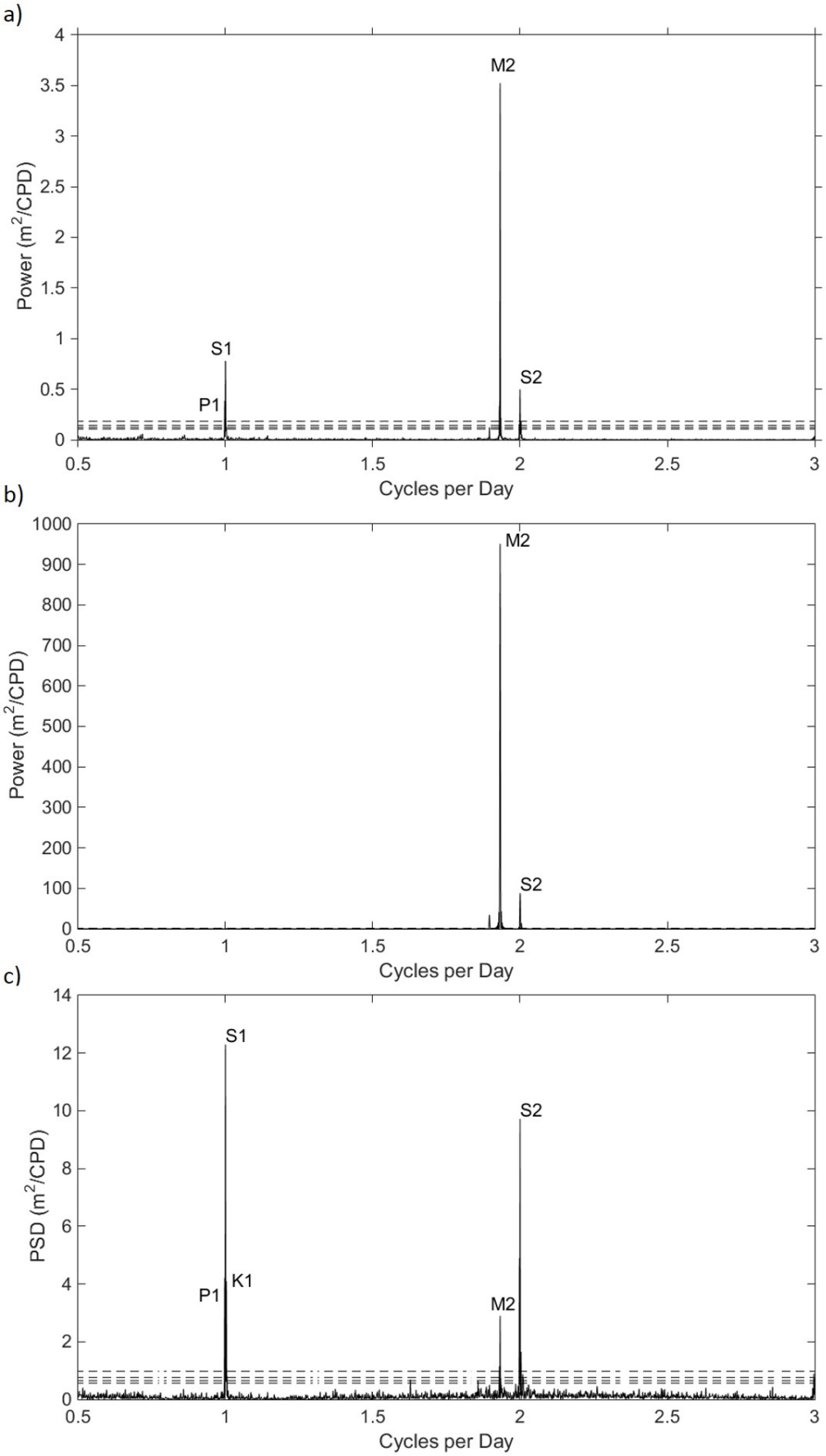

Figure 4.5: Lomb-Scargle PSD estimates from May 2013 to February 2015 for a) water levels in the Saltdean OBH b) tidal observations at Newhaven and c) water levels at the Balsdean PS. Ionospheric and oceanic tidal components are also shown, based on Bindoff et al. (1988). The 50%, 90%, 99% and 99.99% significance levels are plotted as dashed lines on each graph, although in the case of Newhaven, these coincide with the x-axis at the scale plotted.

semidiurnal components occur in the PSD of tidal variations at Newhaven and with the same relative magnitudes (Figure 4.5b). This suggests a strong influence from marine tides on water levels at Saltdean, a phenomenon previously described by MacAllister et al. (2016).

The PSD of the Saltdean OBH also includes diurnal fluctuations, which are not present in the Newhaven data. The PSD for the Balsdean PS is dominated by diurnal fluctuations, with the largest peak occurring at 1.000 cycles per day, consistent with the frequency of the S_1 tidal component (Figure 4.5c). The size of this peak relative to other tidal modes is inconsistent with the relative magnitudes of oceanic and ionospheric tides shown in Table 3.1 and it appears more likely to be caused by a daily abstraction regime than by any natural phenomenon. Taken together, the PSDs in Figure 4.5 indicate that marine tides are the biggest influence on water levels in the Saltdean OBH, while abstractions at the Balsdean PS exert a smaller, but still significant, impact.

As stated in Section 4.2, the Saltdean OBH is intersected by a shallow adit that connects it to two nearby groundwater monitoring boreholes. No water level data are available from these boreholes and they are not accessible for monitoring. As such, it is unknown what effect this hydraulic connection with nearby boreholes has on water level variations in the Saltdean OBH.

4.3.2 Groundwater flow

The majority of groundwater flow in the Chalk occurs within fractures (Allen et al., 1997; Bloomfield, 1996; MacDonald and Allen, 2001), where the hydraulic conductivity is typically several orders of magnitude higher than that of the surrounding matrix (Butler et al., 2012; Jones and Robins, 1999). Fractures may exist as faults, joints or bedding planes, although the latter are considered to be the most pervasive and the most significant conduits for flow (Bloomfield, 1996).

Numerous, laterally-extensive marl seams have been logged within the Chalk, which typically act as barriers to flow, although their relatively low hydraulic conductivity may concentrate groundwater flow on their margins, leading to enhanced dissolution and the enlargement of

fractures (Gallagher et al., 2012; Molyneux, 2012; Zaidman et al., 1999). Hardgrounds are often considered flow conduits, due to their brittle nature and enhanced fracturing (Schurch and Buckley, 2002; Soley et al., 2012), although they may also be barriers to flow when fracturing is minimal (Jones and Robins, 1999).

In general, the hydraulic conductivity of the Chalk decreases with depth and the most significant flow horizons typically occur within 50 m of the water table (Butler et al., 2009; Jones and Robins, 1999; Williams et al., 2006). Within the South Downs, the Seaford Chalk is considered to be the major water-bearing unit (Jones and Robins, 1999). Laterally, the Chalk is significantly more permeable in valleys than in interfluves (Jones and Robins, 1999; MacDonald and Allen, 2001).

AMEC (2016) reported a high density of dissolution features beneath the dry valley near Saltdean, which it attributed to enhanced degradation from the mixing of seawater and groundwater. In calibrating a groundwater flow model of the Brighton and Worthing Chalk Blocks, AMEC (2016) found that hydraulic conductivity values were up to 4 orders of magnitude larger in dry valleys than in nearby interfluves.

According to Jones and Robins (1999), logging of the Saltdean OBH has indicated a hydraulically significant fracture at its base, which constitutes the main conduit for saline intrusion. This was later supported by MacAllister (2016), who showed, through a series of σ_f profiles, that saline water enters near the base of the borehole and exits via the adit near the top of the water column. This agrees with regional trends reported by AMEC (2016), who indicated that seawater intrusion into boreholes in the Worthing and Brighton Chalk Blocks typically occurs through fractures and is particularly prevalent during autumn spring tides.

Recharge estimates vary across the South Downs, although in the Brighton Block, where the Saltdean OBH is located, Jones and Robins (1999) report a mean value of around 480 mm/yr. The majority of recharge occurs during the winter months, with limited recharge between May and September (Ireson et al., 2009; Wellings, 1984). Despite the minimal flow occurring in the unsaturated zone during this period, the narrow pore-throat diameters in the Chalk matrix mean that it remains almost entirely saturated within 30 m of the water table (Price, 1987),

although dewatering of the fractures occurs, typically accounting for less than 1% of the total rock volume (Butler et al., 2012; Mathias, 2005; Price, 1987). Recharge mechanisms within the Chalk comprise rapid bypass flow through fractures and slower piston flow, which occurs through the matrix (Jones and Robins, 1999).

4.3.3 Hydrochemistry

The composition of seawater from the English Channel near Saltdean and groundwater from the Balsdean PS was reported by MacAllister (2016) and is shown in Tables 4.1 and 4.2. Unsurprisingly, the seawater samples were dominated by Na^+ and Cl^- ions, which contribute to an ionic strength that is nearly two orders of magnitude greater than that of groundwater. Although Na^+ and Cl^- are also prominent in the groundwater samples, Ca^{2+} and HCO_3^{2-} are the dominant ions, reflecting the chemistry of the chalk host rock.

Table 4.1: Composition of seawater in the English Channel near Saltdean (MacAllister, 2016). The errors reflect the range in laboratory results from 15 analyses.

Chemical Species	**Concentration (mg/l)**	**Molarity (mM/l)**
Ca^{2+}	423.13 ± 43.07	10.56 ± 1.07
K^+	453.39 ± 177.11	11.60 ± 4.53
Mg^{2+}	1227.90 ± 197.90	50.52 ± 8.14
Na^+	10262.21 ± 529.39	446.4 ± 23.03
Sr^{2+}	8.27 ± 1.17	0.09438 ± 0.013
F^-	6.13 ± 1.44	0.3227 ± 0.076
Cl^-	19008.53 ± 1948.29	536.2 ± 54.95
Br^-	107.00 ± 57.59	1.339 ± 0.72
SO_4^{2-}	2485.07 ± 502.70	25.87 ± 5.23
HCO_3^-	131.60 ± 14.60	2.157 ± 0.24
TDS (mg/l)	34113.23 ± 3473.26	
Ionic Strength (mM)	673.06 ± 70.70	
pH	7.59 ± 0.60	

Table 4.2: Composition of groundwater taken from the Balsdean PS (MacAllister, 2016). The errors shown reflect the range in laboratory results from 24 analyses.

Chemical Species	**Concentration (mg/l)**	**Molarity (mM/l)**
Ba^{2+}	0.01 ± 0.002	$8.16\times10^{-5} \pm 1.5\times10^{-5}$
Ca^{2+}	62.76 ± 13.29	1.57 ± 0.33
K^{+}	1.88 ± 0.74	0.048 ± 0.019
Mg^{2+}	4.02 ± 1.11	0.17 ± 0.046
Na^{+}	28.66 ± 5.60	1.25 ± 0.24
Si^{4+}	3.62 ± 0.27	0.13 ± 0.01
Sr^{2+}	0.20 ± 0.006	0.002 ± 0.0001
F^{-}	0.09 ± 0.026	0.005 ± 0.001
Cl^{-}	46.87 ± 8.85	1.32 ± 0.25
Br^{-}	0.28 ± 0.1	0.0035 ± 0.001
NO_3^{-}	27.87 ± 4.108	0.45 ± 0.07
SO_4^{2-}	16.80 ± 2.82	0.17 ± 0.03
HCO_3^{-}	158.18 ± 23.18	2.59 ± 0.38
CO_3^{2-}	24.71 ± 0.05	0.41 ± 0.0008
TDS (mg/l)	375.94 ± 60.15	
Ionic Strength (mM)	8.51 ± 1.37	
pH	7.79 ± 0.58	

σ_f measured in the Saltdean OBH ranges from 0.8-1.0 mS/cm throughout most of the year (∼500-700 mg/l), reaching maximum values of nearly 10 mS/cm (∼7,000 mg/l) due to seawater intrusion in late summer (Figure 4.3). A smaller increase in σ_f occurs in conjunction with major recharge events, indicating the presence of elevated salinity above the water table (Figure 4.6). This influx of more saline water is preceded by a sharp reduction in σ_f of short duration, which may reflect distinct contributions from two separate recharge mechanisms in the Chalk (see Section 4.3.2). Rapid bypass flow in the fractures appears to deliver relatively fresh recharge to the borehole, while piston flow may be responsible for more mineralised recharge, as a result of prolonged interactions between percolating rainwater and the rock matrix.

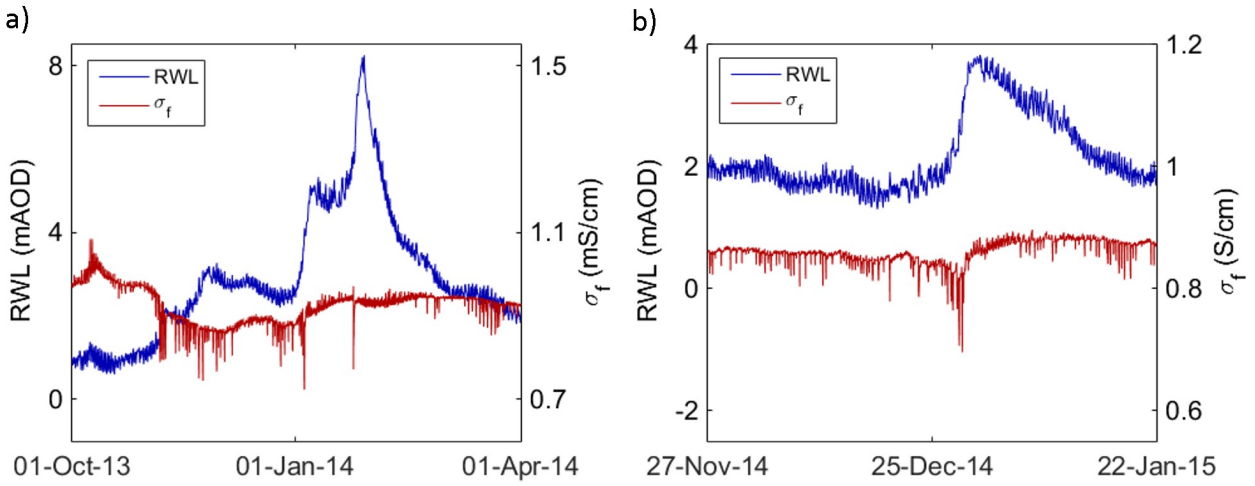

Figure 4.6: Fluctuations in σ_f at the top of the Saltdean OBH water column during major recharge events.

Pore-water chemistry within the unsaturated zone at Saltdean has not been analysed, although national datasets obtained from the British Geological Survey (Stuart, 2005) suggest that Cl^- concentrations in unsaturated Chalk near the coast can exceed 1,000 mg/l (Figure 4.7).

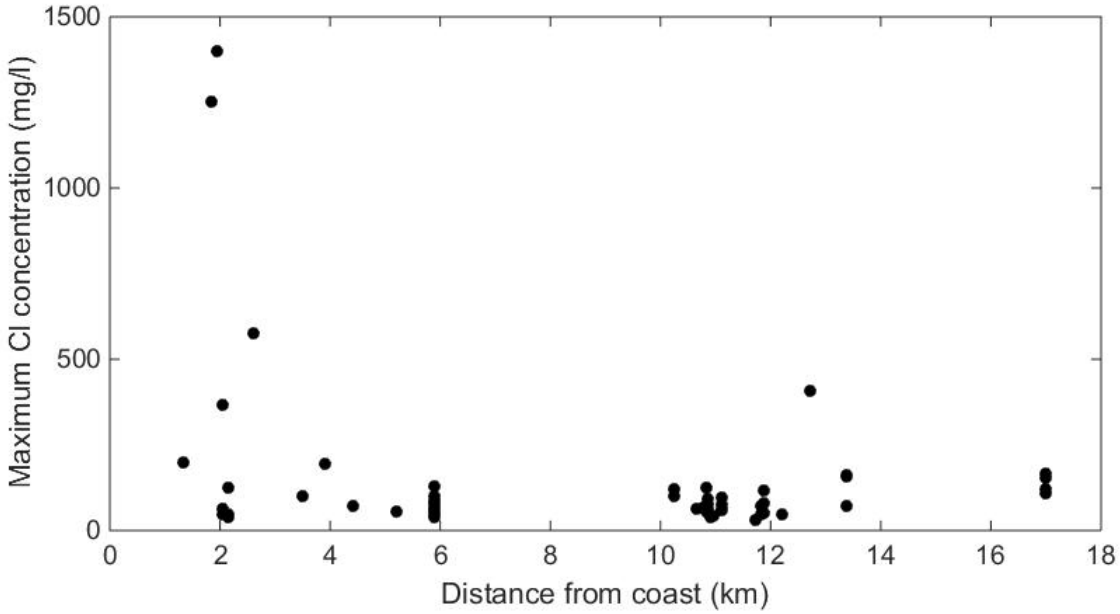

Figure 4.7: Maximum pore water chloride concentration in the unsaturated zone of the Chalk versus distance from the coast (based on data provided by Stuart, 2005)).

Elevated Cl^- (and hence salinity) in the unsaturated zone near the coast is normally attributed to a combination of chloride inputs from precipitation and dry deposition and concentration

through evapotranspiration (Bresciani et al., 2014). In the context of SP monitoring, the presence of saline water is likely to increase the electrical conductivity of the unsaturated zone, while salinity gradients in the unsaturated zone may be an important source of SP (Equation (2.7)).

4.3.4 Aquifer properties

The median storage coefficient in the South Downs Chalk is 0.0022 (MacDonald and Allen, 2001), although this value appears to neglect the drainage of fractures under gravity. The mean porosity of the White Chalk Subgroup in the south of England is 0.39 (Bloomfield et al., 1995).

Based on observed drawdown at the Balsdean PS, MWH (2006) calculated a transmissivity of 6,050 m^2/day for the 16 m interval of the Chalk intersected by the abstraction boreholes. MWH (2006) used this to infer a hydraulic conductivity of 900 m/day for the surrounding aquifer, significantly higher than the median value of 9 m/day for the South Downs as a whole (based on the median transmissivity of 880 m^2/day reported by MacDonald and Allen (2001) and an assumed aquifer thickness of 50 m (Butler et al., 2009; Jones and Robins, 1999; Williams et al., 2006)).

An alternative method for constraining the aquifer properties in this area is to consider the amplitude and lag of tidally induced pressure variations within the Saltdean OBH, compared to observed oceanic tides at the coast. This method, first reported by Jacob (1950) (as cited by Fetter (2001)) relates the lag τ and amplitude of groundwater level fluctuations H_{GW} to hydraulic conductivity K via the following expressions:

$$K = \frac{t_0 S x^2}{4\pi b \tau^2}, \tag{4.1}$$

$$K = \frac{\pi S x^2}{b t_0 ln(\frac{H_{GW}}{H_0})^2}, \tag{4.2}$$

where t_0 is the period of tidal fluctuation (days), S is the aquifer storage coefficient (-), x is the distance of the observation borehole from the coast (1800 m), b is the saturated thickness of the aquifer (m) and H_0 is the amplitude of tidal fluctuations at the coast (m). Assuming an aquifer thickness of 50 m, a storage coefficient of 0.0022 and incorporating parameter values from Section 4.3.1 gives respective K values of 247 m/day and 254 m/day. The portion of the aquifer characterised by this method, and the close agreement between these two estimates, suggests that a K value of around 250 m/day is the most appropriate for simulating seawater intrusion processes in the Saltdean OBH (see Section 5.2.3). Although this is significantly lower than the 900 m/day inferred by MWH (2006) for the upper 16 m of the aquifer, it is comparable to the values assigned by AMEC (2016) from the water table to the base of the Lewes Nodular Chalk, both in the lower part of the dry valley near Balsdean (100-190 m/day) and, more broadly, to Chalk valleys within the Brighton Block (0.31-465 m/day).

4.4 Electrical parameters

4.4.1 SP sources and coupling coefficients

As discussed in Section 2.2.2, saline intrusion models of SP are often simplified by assuming that the system is dominated by NaCl electrolytes of varying concentrations. Based on the reported concentrations of groundwater and seawater near Saltdean (Tables 4.1 and 4.2), this gives an estimate of 26.76 mV for the change in electrochemical diffusion potential ΔV_{ED} across the saline front (Equation (2.11)), compared to a value of 27.31 mV for multi-ionic solutions (Equation (2.10)). In the case of a perfect membrane, in which all anions are excluded from the pore space, the change in electrochemical exclusion potential V_{EE} across the saline front would be -111.35 mV for both a multi-ionic solution and for an NaCl solution.

The relative influence of these two end members is described by the exclusion efficiency η (Equations (2.16) and (2.17)), which is related to the pore-throat diameter of the host rock (see Section 2.2.2). Measurements of η can then be used to evaluate the coupling term C_{EED}, which

links the gradient in ionic strength to the gradient of the combined exclusion-diffusion potential ∇V_{EED} (Equations (2.7) to (2.9)). Rearranging Equations (2.8), (2.13), (2.15) and (2.17) and assuming no current flow gives the following expression for C_{EED} in a porous medium saturated with NaCl electrolytes in solution:

$$C_{EED} = -\frac{k_B T}{e}\Big[\big(\eta + 1\big)\big(2t_{na} - 1\big) - \eta\Big]. \tag{4.3}$$

The exclusion efficiency η of Seaford (0.01-0.12) and Lewes Nodular Chalk (0.02-0.06) cores saturated with local groundwater and seawater was measured by MacAllister (2016). Although MacAllister (2016) also measured η for shale (0.24) to understand the effects of clay minerals and hence, smaller pore-throat diameters, no direct measurements of η are available for marls and hardgrounds, which lie beneath the Saltdean study area. These values can be inferred based on observed changes in σ_f and SP with depth in the Victoria Gardens borehole (Figure 4.8), 7 km west of Saltdean. An experimental method for deriving η values in the marl is described in Chapter 8 and is used to validate the parameterisation of the model described in Chapters 5 to 7 and the field method described below.

Firstly, σ_f values from the borehole log, in mS/cm, are converted to total dissolved solids (TDS) in mg/l, using the following relation (Walton, 1989), which is broadly consistent with TDS and σ_f values for local seawater and groundwater (Table 4.3):

$$TDS = 700\sigma_f. \tag{4.4}$$

The average ratio of ionic strength C_f to TDS from laboratory analyses (Table 4.3) is used to convert these data via:

$$C_f = 2.12 \times 10^{-5} TDS. \tag{4.5}$$

Distinct, monotonic changes in both SP and σ_f occur adjacent to the Shoreham Marl, the Hope Gap Hardground and the Navigation Marl, as well between the two Lightpoint Marls. Applying the calculated changes in C_f to Equations (2.11), (2.14) and (2.16) and assuming the

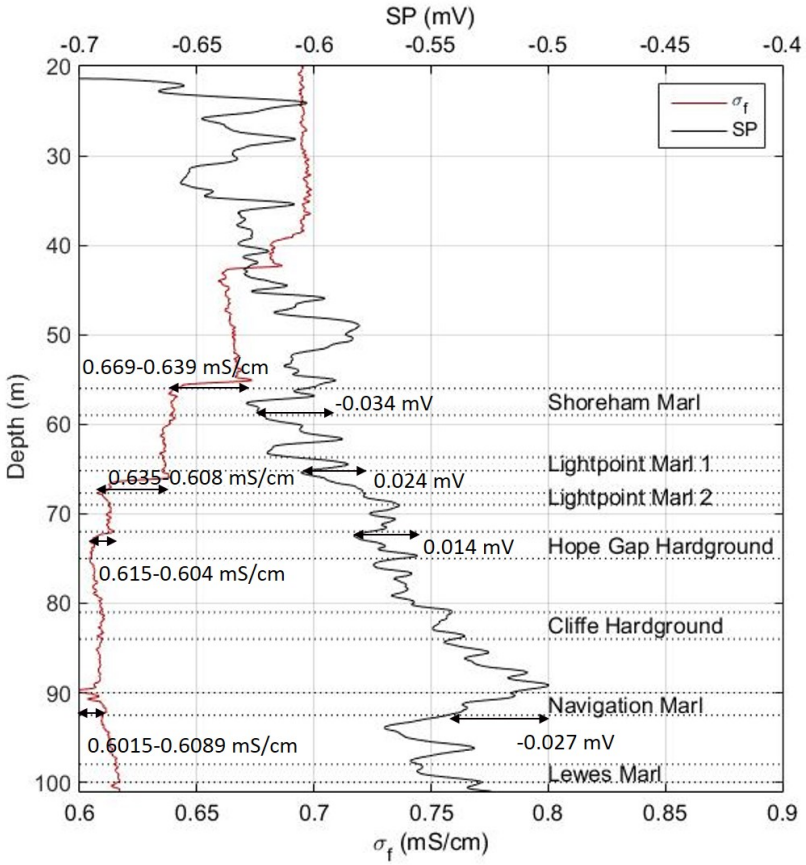

Figure 4.8: σ_f and SP with depth in the Victoria Gardens Borehole in Brighton. Monotonic changes in σ_f and SP across specific horizons are highlighted, based on data provided by BGS (2017) and stratigraphic interpretation by Jones and Robins (1999).

Table 4.3: Laboratory σ_f, TDS and C_f for seawater and groundwater near Saltdean (MacAllister, 2015a).

Source	σ_f **(mS/cm)**	**TDS (mg/l)**	C_f **(M)**	C_f**/TDS**
Seawater (Saltdean)	50.34	34,113	0.673	1.97×10^{-5}
Groundwater (Balsdean OBH)	0.463	376	0.00851	2.26×10^{-5}

variations in SP within the borehole are representative of ∇V_{EED} within the adjacent formation gives estimates of η for the Shoreham Marl (0.16), the Hope Gap Hardground (0.21) and the Navigation Marl (0.25), as well as for the strata between the Lightpoint Marls (0.20). The estimates for the marl and hardground horizons are consistent with several previous studies (Leinov and Jackson, 2014; MacAllister, 2016; Westermann-Clark and Christoforou, 1986) that show an inverse relationship between η and the ratio of pore-throat diameter r to the Debye length λ, a measure of the thickness of the electric double layer (see Section 2.2.2). Simply

put, lithologies with relatively narrow pore-throat diameters, such as marls and hardgrounds (Fay-Gomord et al., 2016) can be expected to have higher values of η, as a thick electric double layer relative to the pore-throat diameter facilitates the exclusion of chloride ions from the pore-space (see Figure 2.2 and Section 2.2.2). It is unclear whether the high value of η in the vicinity of the Lightpoint Marls also reflects the presence of clay minerals and this data point has been omitted from further analysis. Given the level of uncertainty associated with this method, the exclusion-efficiency of marl is investigated further in Chapter 8.

The relationship between η and r/λ for the lithologies encountered at Saltdean is shown in Figure 4.9. Data for r in the Chalk are taken from MacAllister (2016). Geometric mean values of r for marls and hardgrounds (Fay-Gomord et al., 2016) and shale (Nelson, 2009) were combined with values of λ, which is given by (e.g. Leinov and Jackson, 2014):

$$\lambda = \left(\frac{\epsilon_f k_B T}{2000 N_A C_f e^2}\right)^{0.5}, \tag{4.6}$$

where the value of C_f applied is the average ionic strength across each marl or hardground band, as given by Equations (4.4) and (4.5), N_A is Avogadro's number ($6.022140857 \times 10^{23}$ mol^{-1}) and ϵ_f is the dielectric permittivity of the electrolyte in solution (F/m), which can be approximated by (e.g. Leinov and Jackson, 2014):

$$\epsilon_f = 8.85 \times 10^{-12}(80 - 13C_f + 1.065C_f^2 - 0.03006C_f^3). \tag{4.7}$$

Errors in r/λ for the field-derived data points in Figure 4.8 are based on the range in r values for marls and hardgrounds reported by Fay-Gomord et al. (2016) and variations in λ given by Equations (4.4) to (4.7). Errors in field-derived values of η are not shown, as the level of uncertainty associated with this method is unknown. Errors in r/λ reported by MacAllister (2016) for chalk and shale are dominated by uncertainties in the composition of the fluids applied during testing, leading to errors in λ; errors in η reflect uncertainties in the experimental measurement of voltages (see Chapter 8).

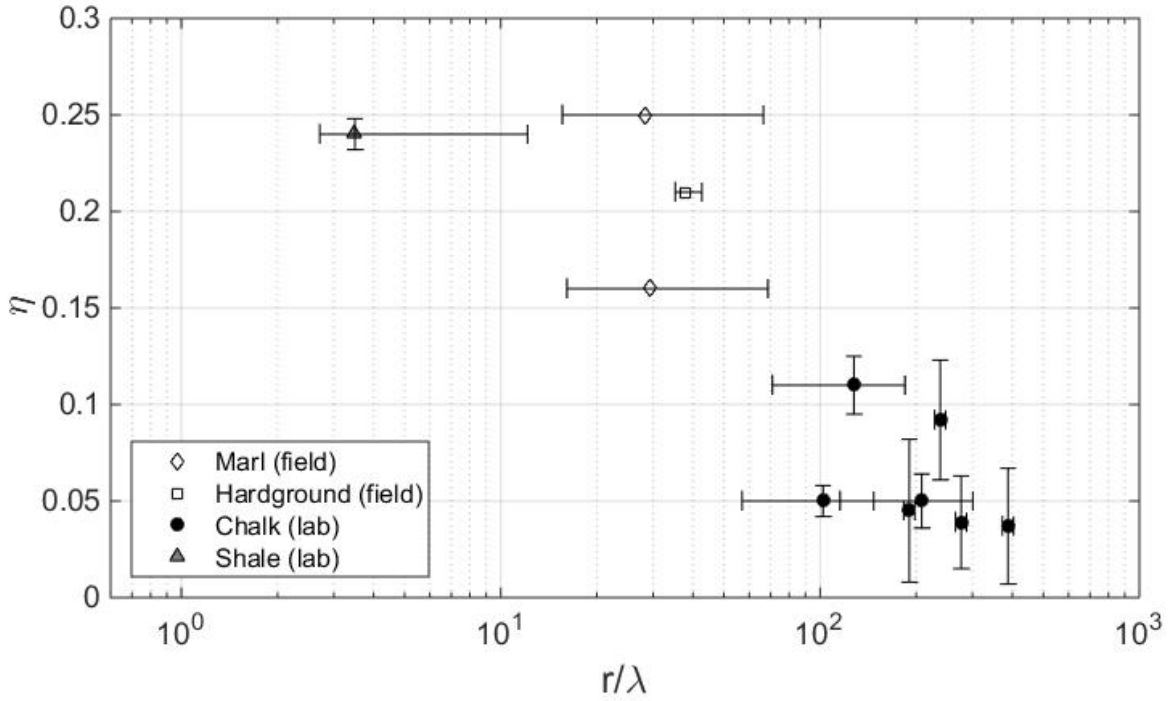

Figure 4.9: Plot of η versus r/λ for lithologies encountered at Saltdean. A laboratory value for shale is shown for comparison with field estimates of η for clay-rich units. Based on data from BGS (2017) (bore logs for field estimates of η), Fay-Gomord et al. (2016) (pore-throat diameters of marls and hardgrounds), MacAllister (2016) (η in chalk and shale) and Nelson (2009) (pore-throat diameters in shale).

Vinogradov et al. (2010) showed that $|ln(C_{EK})|$ varies linearly with $|ln(C_f)|$ up to the concentration of seawater in fully saturated sandstone core samples. Using the approach described in Section 2.3.1, MacAllister (2016) measured C_{EK} for Chalk samples saturated with groundwater from the Balsdean PS (Table 4.2) and seawater (Table 4.1). Regression of these data, shown in Figure 4.10, gives the following relation:

$$C_{EK} = -1.013 \times 10^{-9} C_f^{-0.85}. \tag{4.8}$$

4.4.2 Electrical conductivity

As shown in Equations (2.1) and (2.2), the current generated by SP sources is proportional to the electrical conductivity σ_s of the host material. For the Chalk aquifer, σ_s can be estimated

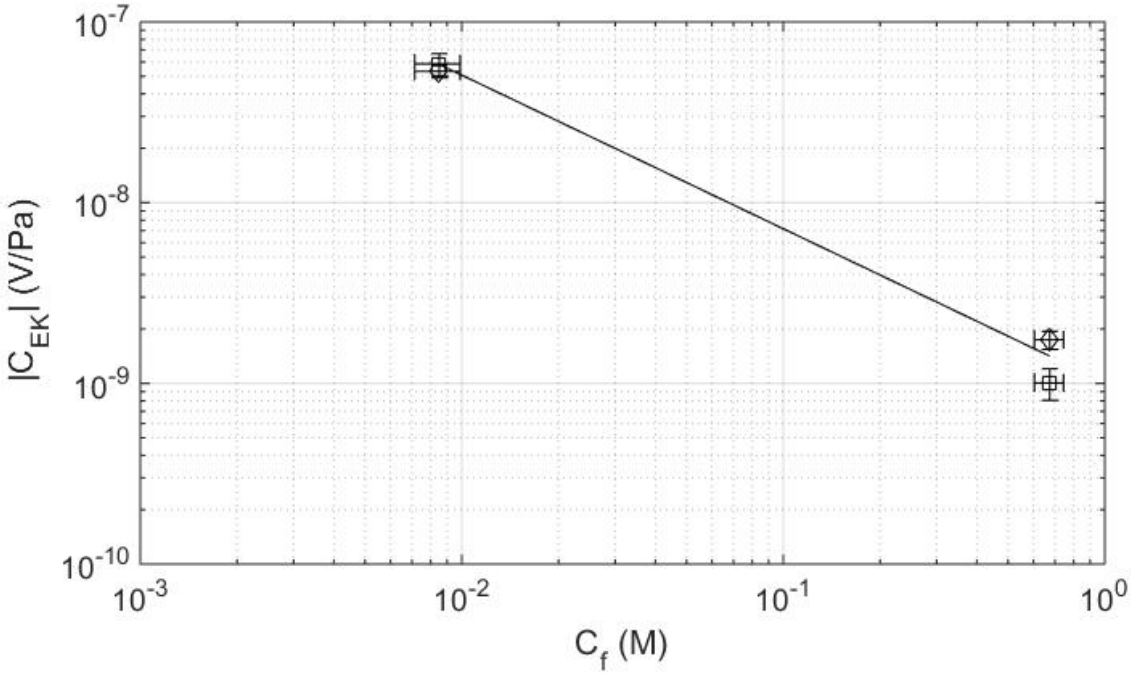

Figure 4.10: Logarithmic plot of $|C_{EK}|$ and C_f for Chalk samples tested by MacAllister (2016).

using Archie's law, which neglects the conductivity of rock grains (Telford et al., 1990):

$$\sigma_s = \phi^m \sigma_f S_w^2, \tag{4.9}$$

where m is the cementation exponent (-) and S_w is saturation (-). MacAllister (2016) derived values for m of 2.1-2.6 from core samples of Seaford and Lewes Nodular Chalk. As pore fluid is the only conductor in this model, Equation 4.9 effectively relates σ_s to the connectedness of the pore space. As discussed in Section 4.3.2, the Chalk matrix remains almost entirely saturated above the water table, with dewatering of fractures accounting for less than 1% of the total rock volume; as such, S_w is likely to exceed 0.99 throughout the unsaturated zone.

Archie's law is unsuitable for representing marl seams, which contain a high proportion of clay minerals and display low resistivity values in geophysical logs (Jones and Robins, 1999). The presence of clay minerals increases σ_s due to conduction within the electric double layer, which occurs as a result of rapid exchange of cations between the pore fluid and hydrated clay minerals (Jin et al., 2007). This effect can be accounted for using the empirical Waxman-Smits equation

(Darling, 2005), originally developed for shaly sands:

$$\sigma_s = \phi^m \sigma_f S_w^2 \Big(1 + B\frac{\rho_m CEC}{100\phi\sigma_f S_w}\Big), \tag{4.10}$$

where ρ_m is the mineral grain density (Fay-Gomord et al. (2016) report values of 2.7 g/cm for marl), CEC is the cation exchange capacity (averaging 9.5 mEq/100g for a typical marl (Cornell and Aksoyoglu, 1991)) and:

$$B = (-1.28 + 0.255T_c - 0.00004059T_c^2)/(1 + \frac{0.04T_c - 0.27}{\sigma_f^{-1.23}}), \tag{4.11}$$

where T_c is temperature (°C), which was consistently around 11°C in the Saltdean OBH.

4.5 Self-potential monitoring

4.5.1 Monitoring apparatus and data processing

An array of 13 non-polarising Silvion Ag/AgCl WE300 electrodes was installed in the Saltdean OBH from May 2013 to February 2015 by MacAllister (2016) (Figure 4.2). The shallowest of these was installed at -2.8 mAOD and used as a reference electrode throughout, with the remaining electrodes spaced at 2 m intervals below it. The deepest electrode was installed separately from the others at -26.8 mAOD, along with an AquaTroll 200 $T/P/\sigma_f$ probe; several vertical profiles of SP and σ_f were collected over the monitoring period using this 'travelling electrode'. Two further $T/P/\sigma_f$ probes were installed at -4.8 mAOD and -10.8 mAOD respectively to record vertical changes in these parameters. The monitoring apparatus was connected to a Campbell Scientific CR3000 data logger, which collected data at 5 minute intervals. Further details on the equipment used and data collection methods are given by MacAllister (2016).

Power spectral density analysis shows that the SP signal is dominated by semidiurnal oscillations, consistent with the M_2 component of oceanic tides (MacAllister, 2016). A first-order Savitsky-Golay (SG) moving average filter, with a sampling window of 2.2 days, was applied

to the data to assist in identifying longer-term trends in SP. The SG filter has been used previously for SP analysis (e.g. MacAllister, 2016; Maineult et al., 2008) and has the advantages of maintaining the shape and amplitude of lower frequency oscillations, without introducing phase delay (MacAllister, 2016; Maineult et al., 2008; Savitsky and Golay, 1964).

In addition to the long-term monitoring conducted at the Saltdean OBH, vertical SP profiles were collected from borehole PL10B at Trumpletts Farm in Berkshire (Figure 4.1), more than 60 km from the coast (MacAllister et al., 2018) and from the Balsdean OBH as part of this study, which lies around 1 km inland from the Saltdean OBH. All three boreholes intersect the Seaford and Lewes Nodular Chalk, allowing a comparison of SP profiles in a similar geological setting, at varying distances from the coast.

4.5.2 SP gradients

A key finding from the data collected by MacAllister (2016) is the presence of a persistent SP gradient across the water column in the Saltdean OBH. This gradient occurs when the water column comprises only fresh groundwater and it is modified only slightly by tidal variations in water level, despite the reversal in flow direction that would be expected during a tidal cycle (Figure 4.11). This reversal in flow direction was confirmed by MacAllister et al. (2018), based on a series of σ_f profiles in the borehole following saline breakthrough.

The potential gradient across the water column (based on vertical profiles taken by the travelling electrode) remained close to 0.2 mV/m throughout the monitoring period (Figure 4.12) and this suggests the presence of a persistent current source near the borehole. The consistency of the SP gradient, despite semidiurnal and seasonal fluctuations in water level, suggests that electrokinetic effects are unlikely to be the main driver of this phenomenon. As noted by MacAllister (2016), electrochemical sources of SP, due to exclusion-diffusion potentials from a nearby saline front, are a more likely explanation.

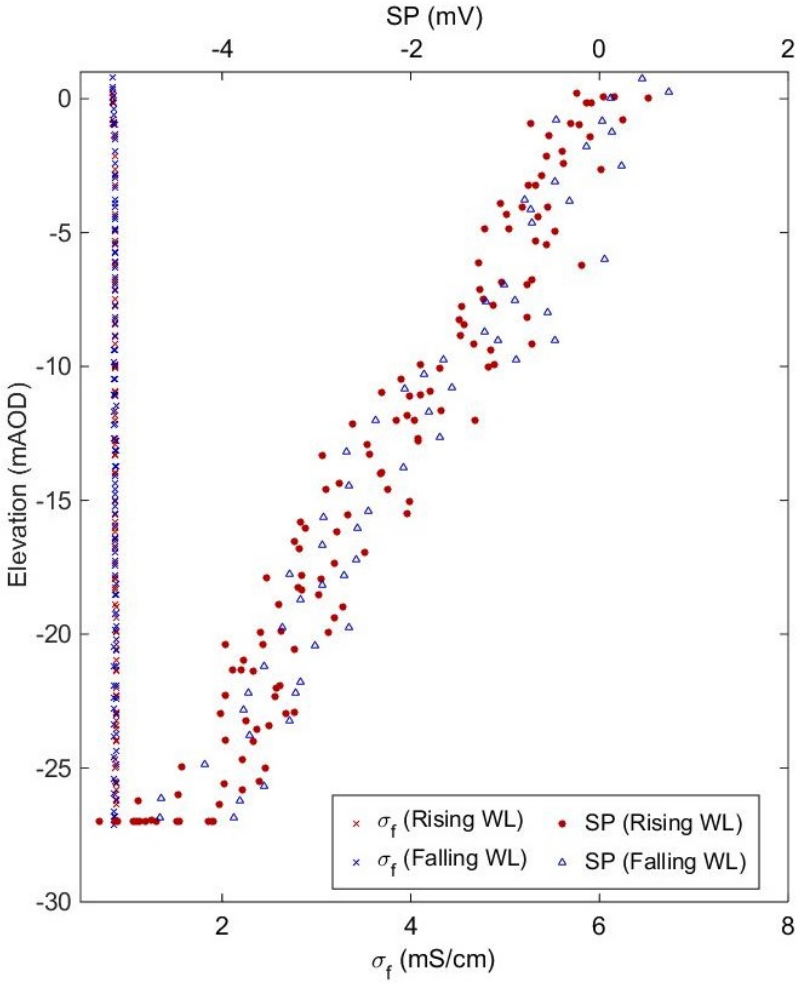

Figure 4.11: SP and σ_f profiles of the Saltdean OBH during periods of rising and falling water levels (WL) on 8 August 2013 (adapted from MacAllister, 2016).

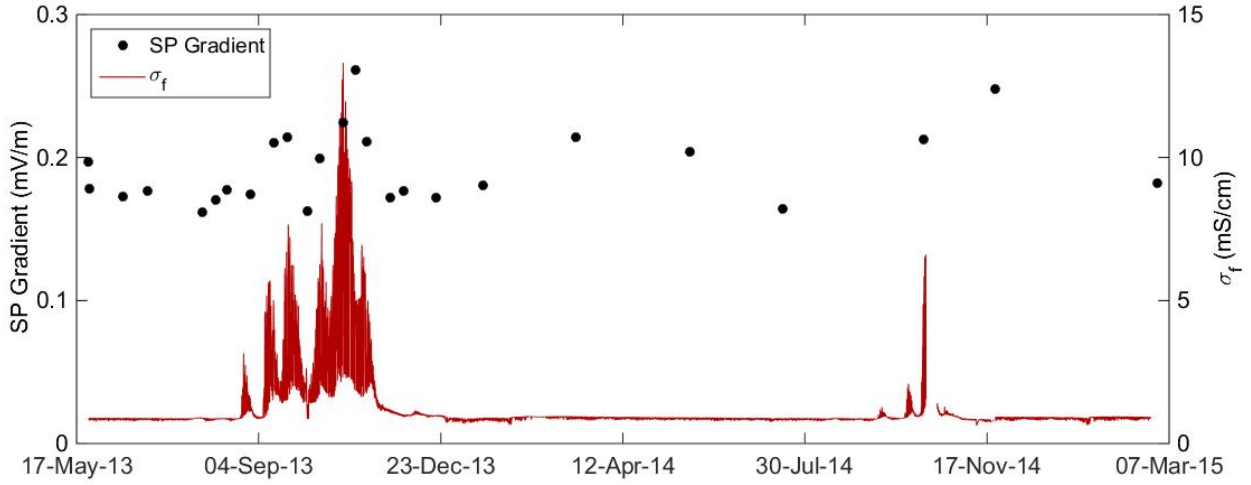

Figure 4.12: SP gradients within the Saltdean OBH, calculated from vertical profiles taken with the travelling electrode and referenced to the shallowest borehole electrode, plotted alongside σ_f from the base of the borehole (data from MacAllister (2015b)).

This hypothesis is supported by comparing the Saltdean OBH profile with those from boreholes further inland. MacAllister et al. (2016) showed that the respective SP gradients in the Balsdean OBH and Trumpletts borehole, which respectively lie 1 km and 60 km further from the coast (Figure 4.1), are minimal by comparison (Figure 4.13).

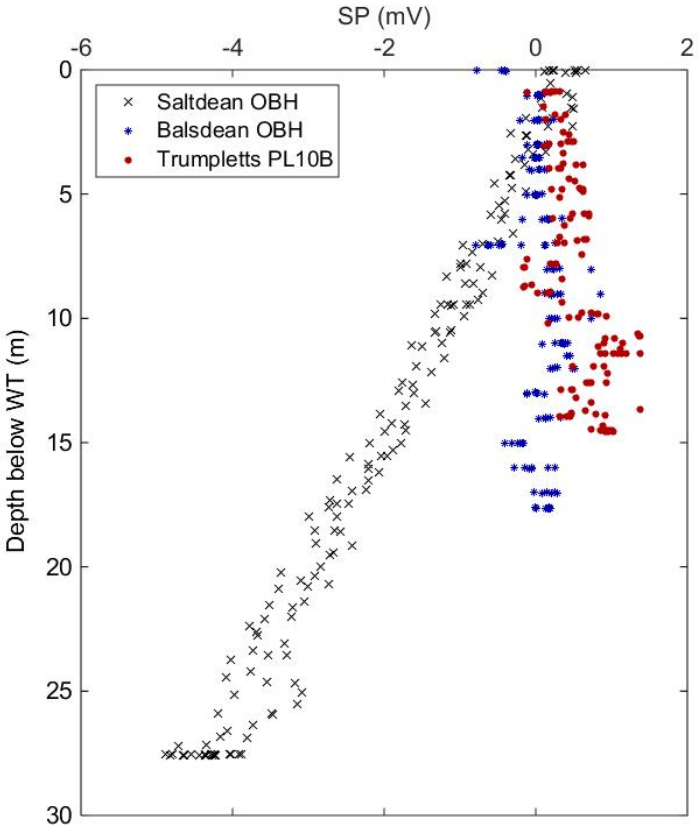

Figure 4.13: SP profiles from the Saltdean OBH, Balsdean OBH and Trumpletts PL10B borehole (data from the Saltdean OBH and Trumpletts provided by MacAllister, 2015b).

While this suggests that a nearby saline front may be responsible for the observed gradient in the Saltdean OBH, it should be noted that the front does not intersect the borehole for most of the year. For example, when the profiles shown in Figure 4.11 were collected, σ_f was approximately 0.87 mS/cm throughout the water column (equivalent to 609 mg/l, based on Equation (4.4)). However, the proximity of the front is demonstrated by the intrusion events that occur in late summer of 2013 and 2014 (Figure 4.3).

Perhaps of greater importance for SP as a predictor of seawater intrusion, the potential dif-

ference across the water column decreased by 0.2-0.3 mV several days prior to breakthrough (Figure 4.14); this 'precursor' is most apparent in the 2013 data. These precursors can also be seen in the 2014 data, although the occurrence of what appear to be two minor intrusion events prior to more obvious saline breakthrough on 12 September leads to a more complex pattern of both salinity and SP.

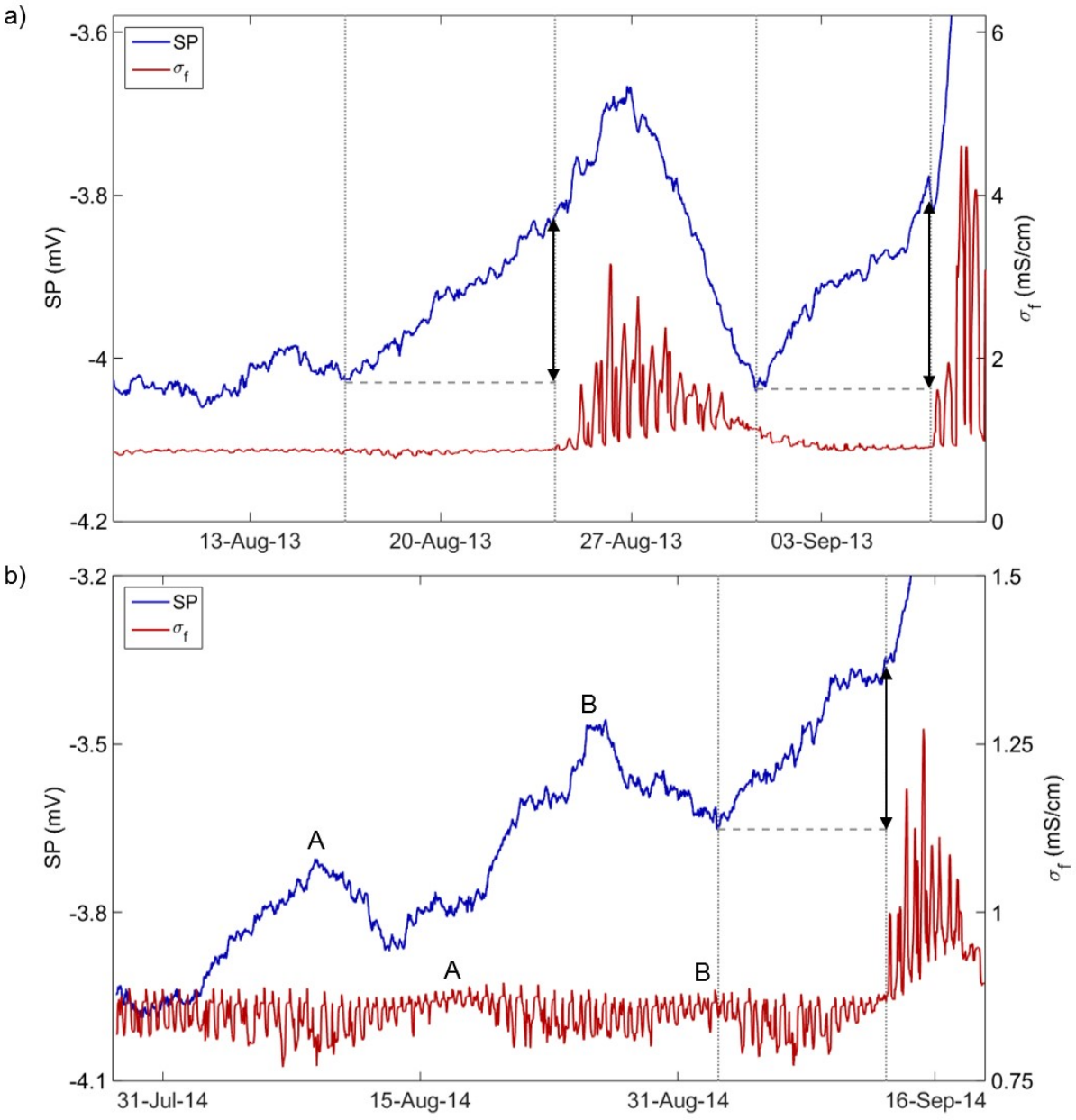

Figure 4.14: Transient SP and σ_f in the Saltdean OBH around the time of saline intrusion in a) 2013 and b) 2014. All data were collected from -26.8 mAOD. Characteristic increases in SP prior to intrusion are highlighted by vertical lines and arrows. In b), similar SP responses can be seen prior to minor intrusion events; these are marked 'A' and 'B' (data from MacAllister, 2015b).

Previous modelling of these phenomena

As described in Section 2.3.2, MacAllister (2016) developed a 2D electrodynamic model to investigate possible sources of the SP gradient. The results, shown in Figure 4.15, appear to confirm that V_{EK} does not make a significant contribution to the observed gradient.

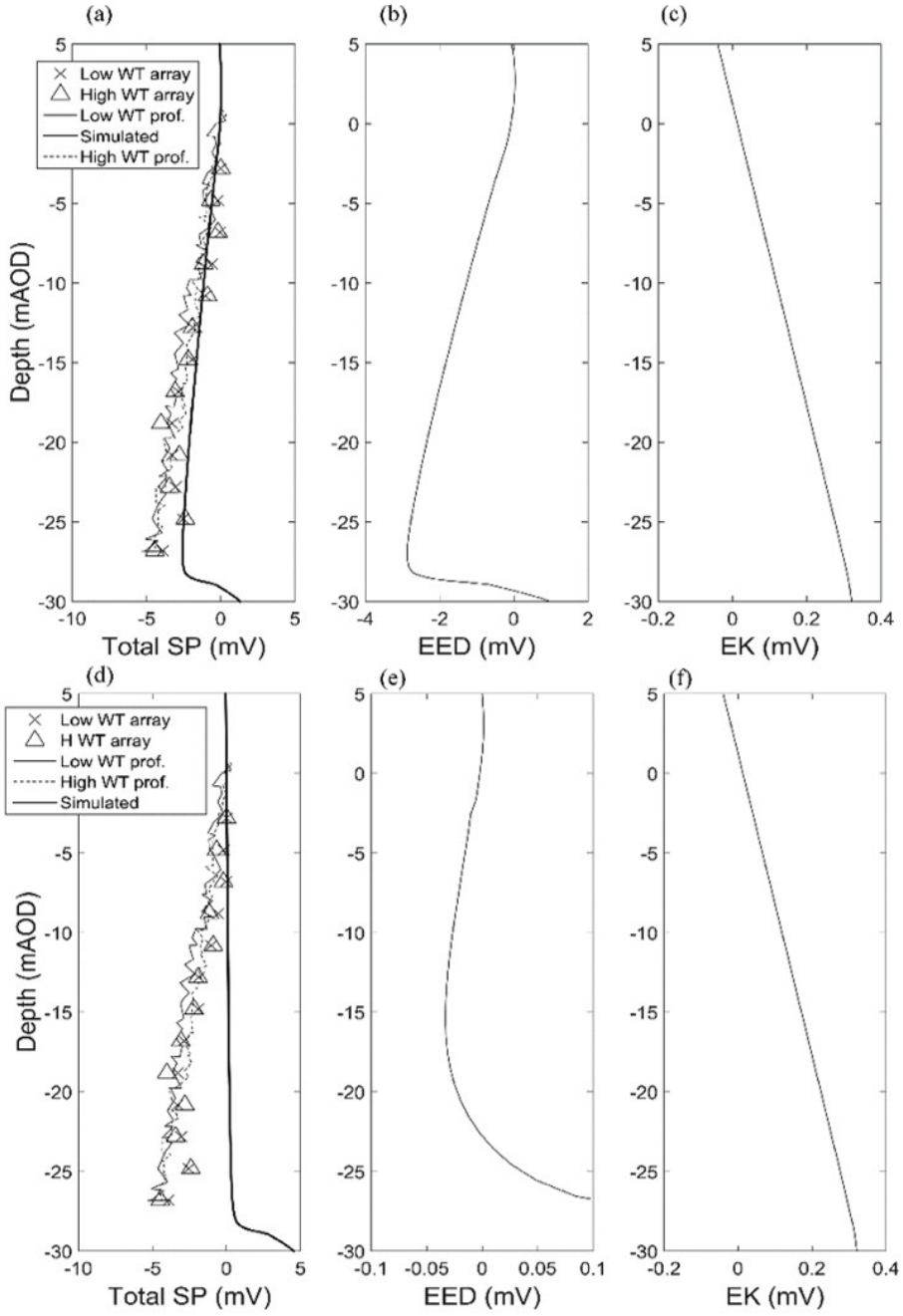

Figure 4.15: a) simulated total SP plotted against field SP observations, using a model solver tolerance of 1×10^{-5} V b) V_{EED} and c) V_{EK} components from the same simulation d) simulated versus observed SP using a model solver tolerance of 1×10^{-7} V e) V_{EED} and f) V_{EK} components from the same simulation (MacAllister, 2016).

The significance of the V_{EED} component is harder to interpret however, as the solution appears to be highly sensitive to the chosen tolerance in the iterative model solver. With a tolerance of 1×10^{-5} V, the model produces an SP gradient of the correct polarity, although it underestimates the magnitude by around 40 %. With a tighter model tolerance, which might be expected to produce a more accurate result, this gradient disappears.

As noted in Section 2.3.2, a single value of exclusion efficiency η was applied by MacAllister (2016) throughout the model domain. However, the description of the local hydrogeology (Section 4.3) suggests that the Chalk aquifer is extremely heterogeneous and, as discussed in Section 4.4, η is likely to vary substantially across different marl, hardground and chalk units. Given the failure of the model to replicate the observed SP gradient, this omission may be significant and further modelling is required to assess the importance of heterogeneity. A new model of the Saltdean site is described in Chapter 5, which employs spatially variable values of η and aims to replicate the observed SP gradient.

To date, no attempt has been made to simulate the precursors shown in Figure 4.14. This is addressed in Chapter 6.

4.5.3 Tidal variations in SP

Although periodic changes in the SP gradient are relatively small in the Saltdean OBH, MacAllister et al. (2016) showed using PSD analysis that they occur at a distinct set of frequencies, which are largely consistent with the main components of oceanic tides (Table 3.1). In common with oceanic tides, the M_2 component is particularly prevalent (Figure 4.16a). Similar patterns can be seen in the PSDs of borehole water level (Figure 4.16b) and σ_f (Figure 4.16c). MacAllister et al. (2016) suggested that tidal oscillations of the saline front in the nearby Chalk aquifer was likely to be the ultimate control on these phenomena. To test this hypothesis, it is important to determine whether observed SP changes can be explained by changes in pressure and salinity within the borehole itself.

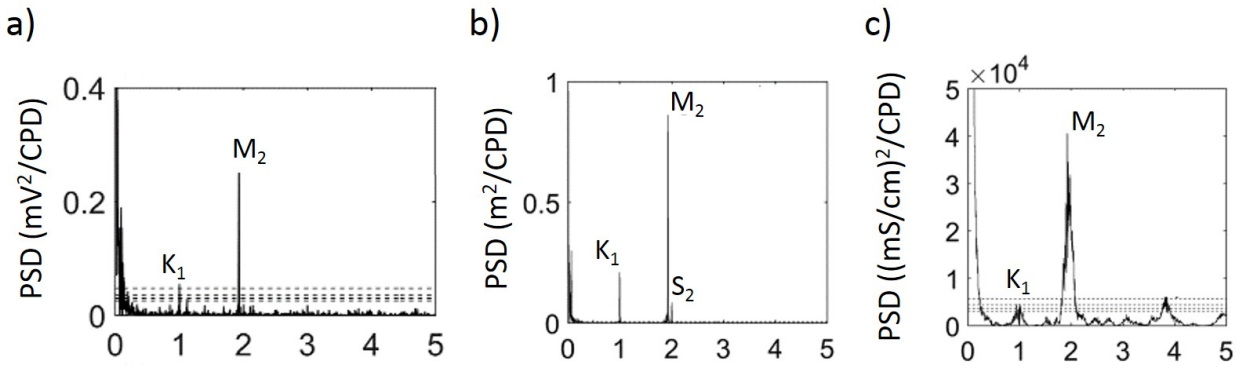

Figure 4.16: Power spectral density plots of a) SP across the water column b) water level variations and c) σ_f variations in the Saltdean OBH from May to August 2013 (adapted from MacAllister et al., 2016).

While there is an apparent relationship between SP, water levels and σ_f in the frequency domain, the coupling of these phenomena in the time domain is less clear. MacAllister et al. (2016) suggested that SP is anti-correlated with hydraulic head in the borehole and indeed, this is supported by variations in these parameters about one month before the major intrusion event in 2013 (Figure 4.17a). MacAllister (2016) argued, based on Equation (2.4), that this is consistent with a negative value of C_{EK}, although this would indicate that the maximum negative pressure gradient in the borehole occurs in conjunction with water level maxima; intuitively, the maximum negative pressure gradient should occur during a falling tidal cycle. MacAllister (2016) also suggested that there is a positive correlation between borehole σ_f and SP, a hypothesis supported to some extent by Figure 4.17b.

A closer inspection of the field data suggests that the relationship between these parameters is more complex than that proposed by MacAllister (2016). During spring time in 2014, when water levels are higher and the saline front is expected to be further from the borehole, the situation is reversed: SP is positively correlated with hydraulic head (Figure 4.18a)) and in the main, is anti-correlated with σ_f (Figure 4.18b)).

It is apparent from Equations (2.4), (2.11) and (2.14) that the SP signal is related to gradients in these parameters, rather than their absolute values, and that any correlation between these parameters should account for this. No direct measurements of P_n were taken, although pressure measurements were taken near both the top and base of the water column (Figure 4.2). The

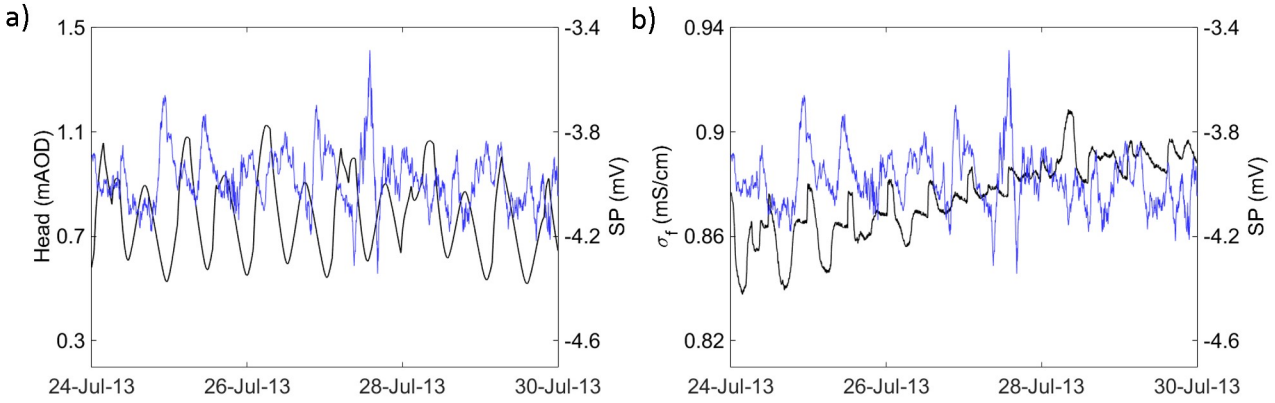

Figure 4.17: Variations in SP (blue lines) with a) hydraulic head (black line) and b) σ_f (black line) in July 2013, around 1 month prior to seawater intrusion. SP data (provided by MacAllister, 2015b) have been smoothed using an S-G filter with a 125 minute sampling window.

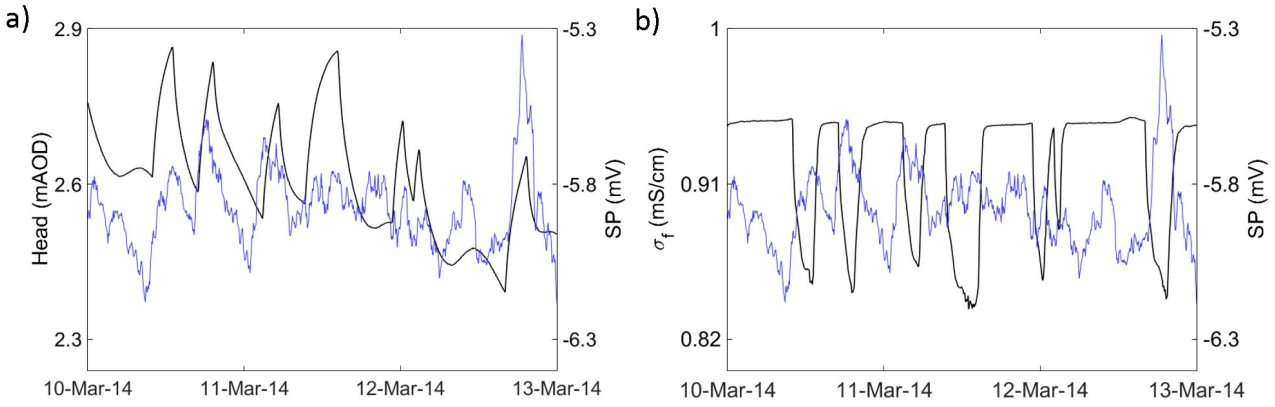

Figure 4.18: Variations in SP (blue lines) with a) hydraulic head (black line) and b) σ_f (black line) in March 2014. SP data (provided by MacAllister, 2015b) have been smoothed using an S-G filter with a 125 minute sampling window.

change in non-hydrostatic pressure can be estimated from:

$$\Delta P_n = \Delta P_T - \bar{\rho} g \Delta z, \tag{4.12}$$

where P_T is total pressure (Pa), Δz is the vertical distance between the two probes (m) and $\bar{\rho}$ is the mean fluid density between the probes (kg/m^3), which is derived from:

$$\bar{\rho} = \rho_f + \frac{(\rho_s - \rho_f) TDS}{TDS_s}, \tag{4.13}$$

where ρ_0 is the density of fresh water (1000 kg/m^3), ρ_{SW} is the density of sea water (1025 kg/m^3), TDS_{SW} is the concentration of sea water (35,000 mg/l) and TDS is estimated from Equation (4.4). Uncertainty in the absolute depth of each probe ($\pm$1 cm) is likely to be significant in comparison to the absolute value of P_n, although changes in P_n can be calculated relative to a fixed starting condition.

Plotting changes in $\frac{\Delta P_n}{\Delta z}$ against SP shows a positive correlation in some parts of the data and a negative correlation in others (Figure 4.19a). Essentially, there appears to be a phase lag between the signals which varies throughout the dataset. For the most part, SP remains positively correlated against the vertical σ_f gradient within the borehole (Figure 4.19b).

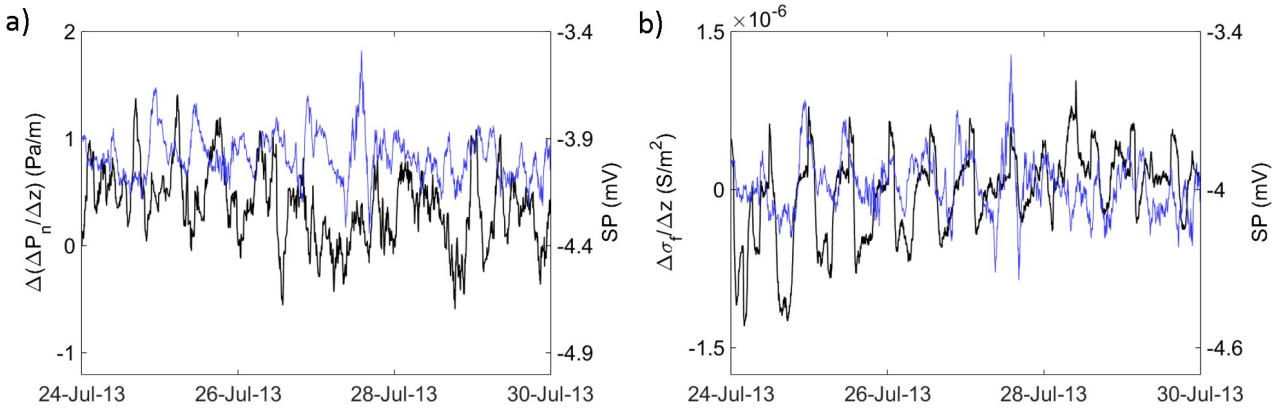

Figure 4.19: Variations in SP (blue lines) with a) $\Delta(\frac{\Delta P_n}{\Delta z})$ (black line) and b) $\frac{\Delta \sigma_f}{\Delta z}$ (black line) in July 2013. SP data have been smoothed using an S-G filter with a 125 minute sampling window.

From inspection of the 2014 data, there also appears to be a varying lag between the SP signal and $\Delta(\frac{\Delta P_n}{\Delta z})$ (Figure 4.20a), while SP is now anti-correlated with $\frac{\Delta \sigma_f}{\Delta z}$ (Figure 4.20b).

4.6 Discussion

Based on the data presented in Figures 4.19 and 4.20, there is no systematic relationship between current sources that occur within the borehole (i.e. gradients in non-hydrostatic pressure and ionic strength) and measurements of borehole SP. This lends further weight to the hypothesis that SP in the borehole is responding to external sources. If, following the discussion

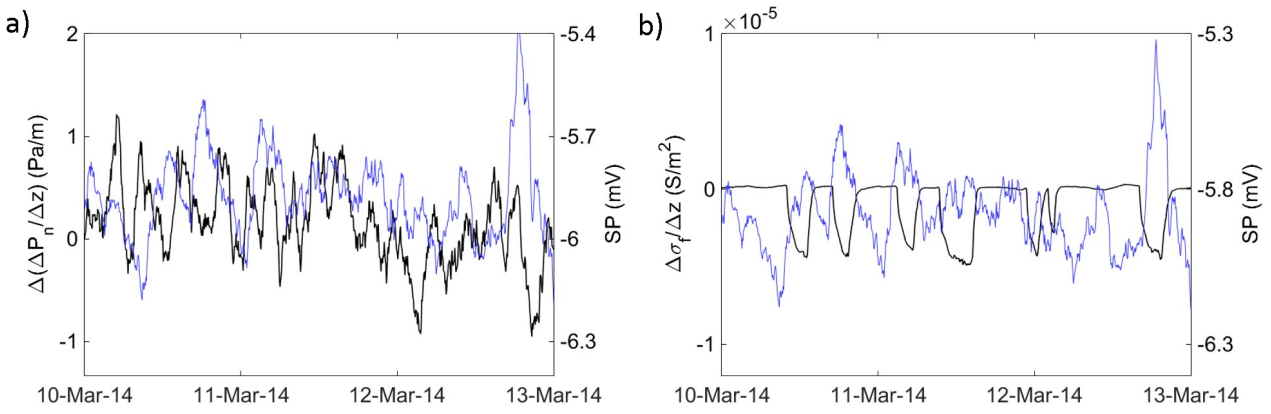

Figure 4.20: Variations in SP (blue lines) with a) $\Delta(\frac{\Delta P_n}{\Delta z})$ (black line) and b) $\frac{\Delta\sigma_f}{\Delta z}$ (black line) in March 2014. SP data have been smoothed using an S-G filter with a 125 minute sampling window.

in Section 4.5.2, electrokinetic effects make only a minor contribution to the signal, this again suggests that remote movements of the saline front are responsible for the observed phenomena.

Given the extreme variations in permeability known to exist in the Chalk, a phase lag between tidal oscillations in the fractures and in the matrix is to be expected and this may explain some of the features described above. Furthermore, analysing vertical gradients in parameters neglects important three-dimensional phenomena, such as gradients in pressure and salinity between the borehole and the adjacent aquifer. Although the persistent SP gradient in the Saltdean OBH strongly suggests that SP is affected by variations in salinity outwith the borehole, it is unclear to what extent temporal variations in SP may be influenced by pressure and salinity gradients across the borehole walls. To gain a more complete understanding of the system, it is clear that three-dimensional modelling is required and this is addressed in Chapters 5 to 7.

For reasons of practicality, the model presented in these chapters represents the response of the saline front to modern sea levels. However, it is recognised that there have been numerous, significant changes in sea level since the Chalk was formed, more than 60 million years ago. Over the course of the last 3 million years alone, global sea levels have varied by several tens of metres, reaching maxima of around 50 m above present day elevations (Rohling et al., 2014). From Equation (3.1), an increase in sea levels of only 1 m might be expected to reduce the depth of the saline-fresh water interface by 40 m in coastal aquifers, leading to salinisation

of the shallow subsurface. In the case of the Chalk in the South Downs, where the hydraulic conductivity of the matrix is typically 10^{-4} to 10^{-2} m/day (Jones and Robins, 1999), pore-water salinity may remain for extended periods and this may constitute a persistent source of SP. Further investigations, such as the analysis of pore-water from core samples at various depths within the Chalk, would be required to test this hypothesis.

4.7 Conclusions

The Saltdean OBH is strongly influenced by the sea. Its water levels exhibit tidal oscillations with the same frequency as oceanic tides and it is subject to repeated seawater intrusion events. Spatial and time-varying SP trends within the borehole also appear to be controlled by the presence and movement of a nearby saline front.

The hydrogeology of the surrounding Chalk aquifer is undoubtedly complex, due to extreme heterogeneity that arises from fracturing and lithological variations. As discussed in Section 4.4, these factors are likely to exert a strong influence on the generation of SP and the propagation of associated electrical currents.

Previous electrodynamic models of the Saltdean OBH, which fail to replicate the observed SP gradient and the associated precursor, neglect much of this heterogeneity. It is also notable that these models were two-dimensional and this may affect their ability to simulate pressure and salinity variations around the borehole accurately.

Based on the characterisation of the site described in this chapter, a new model of the Saltdean OBH and surrounding aquifer is described in Chapters 5 and 6 to address these shortcomings. The ultimate aim of the model is to replicate the observed SP phenomena in a coastal groundwater observation borehole and develop a clearer understanding of the mechanisms that control them.

Chapter 5

Modelling the baseline self-potential gradient

5.1 Introduction

Self-potential (SP) monitoring of the Saltdean OBH near Brighton has revealed several phenomena that may be caused by a nearby saline front, including the presence of a persistent SP gradient in the water column (Figures 4.11 to 4.13), even when there is no measurable salinity gradient, and a slight reduction in the SP gradient several days prior to saline intrusion (Figure 4.14). These phenomena are described in Chapter 4.

The primary objective of this chapter is to replicate the SP gradient in the Saltdean OBH using an electrodynamic model, and in doing so, to develop an understanding of possible source mechanisms for the phenomenon, which was not seen in boreholes further inland (Figure 4.13). A hydrodynamic model will be used to generate the pressure and salinity distributions required to simulate the main components of SP in a coastal aquifer, V_{EK} and V_{EED} (Section 2.2).

A previous model of the site, developed by MacAllister et al. (2018) and MacAllister (2016), was unable to replicate the observed SP gradient. Several features of the model may be responsible for this and are worthy of further investigation. Firstly, the hydrodynamic component of

the model, produced in Eclipse 100, neglects diffusion and dispersion of salt and MacAllister (2016) recommended that future simulations implement a more physically-based mechanism for representing solute transport. Secondly, in common with numerous previous models of SP (e.g. Jackson et al., 2010; Saunders et al., 2008), variations in exclusion efficiency η due to changes in lithology were not implemented in the model. Finally, the iterative solver used to derive the electrochemical component of SP, V_{EED}, was found to be unstable and the results were highly sensitive to changes in the solver tolerance (Figure 4.15).

A further objective of this chapter is to investigate the importance of these factors, using a more physically-based solute transport model, coupled with an electrodynamic model utilising a direct (i.e. non-iterative) solver and implementing variations in η to reflect changes in lithology.

5.2 Hydrodynamic model construction

5.2.1 Overview

Hydrodynamic simulations were conducted using SUTRA3D (or SUTRA) (Voss and Provost, 2002), one of the most widely used models for simulating density-driven flow and transport (Werner et al., 2013). As discussed in Chapter 3, SUTRA represents advection, diffusion and mechanical dispersion of solutes within a finite element mesh, which allows complex geometries to be represented.

Three model domains were used to simulate salinity and pressure at a variety of scales while minimising computational expense. This approach allows simulation of sea level fluctuations at the coast, as well as a detailed representation of changes in lithology, salinity and pressure near the Saltdean OBH. In particular, the requirement for fine mesh discretisation is driven by the Peclet number, which in simple terms governs the ratio of longitudinal dispersivity α_L relative to the element dimension ΔL_L in the direction of flow to ensure model stability (e.g. Simmons et al., 2010; Voss and Provost, 2002). To approximate the observed rate of seawater intrusion (Figure 4.6) in the model, a narrow transition zone is required. This necessitates

minimal dispersion in the model and hence, small elements.

5.2.2 Finite element mesh

The first of the three hydrodynamic models simulates the aquifer in 2D at a regional scale (Figure 5.1a), allowing the pressure and salinity distribution both at the coast and in the vicinity of the Saltdean OBH (at $x = 1800$ m) to be represented. The finite element mesh was generated in ModelMuse (Winston, 2014), using the default parameters for generating an irregular mesh and the Cuthill and McKee method for renumbering nodes and elements. This provides pressure and salinity boundary conditions for a local 2D model (Figure 5.1b), which includes a more detailed representation of stratigraphy near the borehole and aligns the regular model mesh with the inferred dip of the strata (5.1° towards the coast). This in turn provides pressure and salinity boundary conditions for a 3D local model (Figure 5.1c), comprising the plane of the borehole and the upper fracture zone shown in Figure 4.2.

5.2.3 Input parameters

The stratigraphy shown in Figure 4.2 was used to define the distribution of aquifer properties within the model. The parameter values assigned to the model domain are shown in Tables 5.1 to 5.3 and are based on the available data for the site, as described in Chapter 4. The borehole and adit were simulated only in the 3D model, with the adit extending from $0 \leq y \leq 32.5$ m and for elements entirely within the range $-0.7 \geq z \geq -2.3$ m.

The high value of hydraulic conductivity K applied to the fracture zones in Figure 4.2 was found to be necessary during model calibration to ensure that, under steady state conditions, the saline front is prevented from intersecting the borehole by the flow of fresh groundwater from further inland. The tendency for the inland edge of the front to intersect the borehole is exacerbated by mechanical dispersion, a parameter that is commonly exaggerated in solute transport models (Konikow, 2011). In reality, a sharper front may exist near the borehole and as a result, the hydraulic conductivity of the fracture zones may be lower.

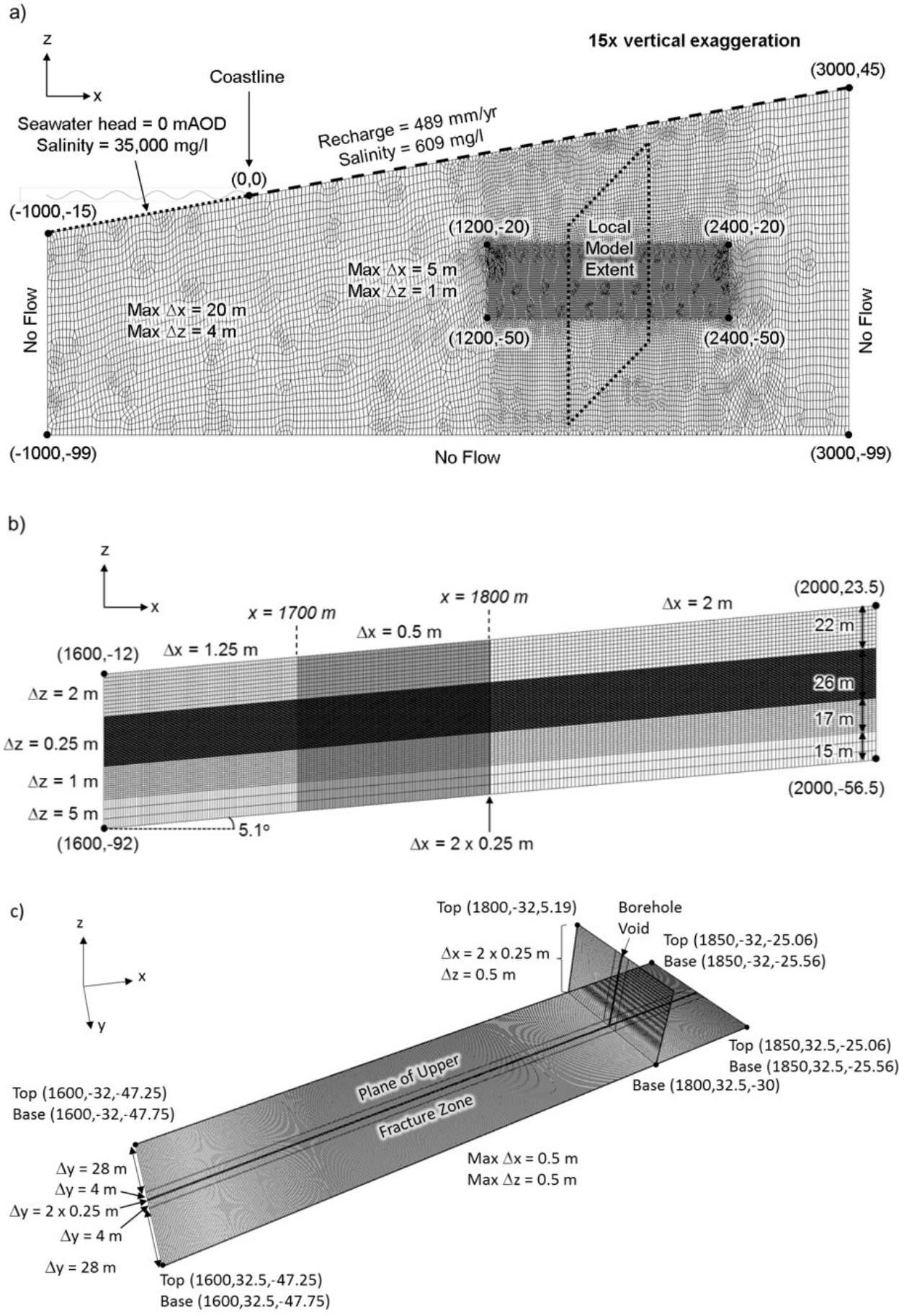

Figure 5.1: Finite element meshes for a) the 2D regional model, including steady state boundary conditions b) the 2D local model and c) the 3D model of the borehole and fracture plane.

Table 5.1: Assigment of hydraulic conductivity K and porosity ϕ.

Parameter	**Chalk Above** -50 mAOD	**Chalk Below** -50 mAOD	**Marls & Hardgrounds**	**Fracture Zones**[1]	**Borehole & Adit**[2]
K (m/day)	254	25.4	25.4	1.68×10^5	6.71×10^6
$\phi(-)$[3]	0.39 (0.001)	0.39 (0.0001)	0.39 (0.0001)	0.1 (0.1)	1 (-)

[1] To maintain the same fracture zone transmissivity between models with different element sizes, fracture zone K in the 2D regional model is 8.38×10^4 m/day.
[2] The borehole and adit are represented within the 3D model only.
[3] ϕ values applied to the 2D local model (see Section 5.2.4) are shown in parentheses.

Table 5.2: Model values of longitudinal dispersivity α_L and transverse dispersivity α_T

Parameter	**2D Regional**	**2D Local**	**3D Model**
α_L(m)	$0.5\Delta L_L$ for $\lvert x\rvert < 250 \cap z \geq -30$ $0.25\Delta L_L$ elsewhere	$0.25\Delta L_L$	$0.5\Delta L_L$ for $1799.75 < x < 1800.25 \cup 0 < z < 0.5$ $0.25\Delta L_L$ elsewhere
α_T(m)	0.01 inside refined area 0.1 elsewhere	0.01	0.01

To aid convergence, the SUTRA models were run in saturated mode, which allows negative pressures to occur above the water table but maintains constant values of permeability and saturation. Parameterisation of the unsaturated zone was carried out subsequently within the electrodynamic model, as described in Section 5.3.3.

5.2.4 Simulations

The models were run to steady state with constant boundary conditions, based on long-term averages of sea level and recharge, as shown in Figure 5.1. An initial solute concentration of 35,000 mg/l (with a density of 1025 kg/m^3) and a hydraulic head of 0 mAOD was applied throughout the 2D regional model.

To aid model convergence for a highly heterogeneous system, an initial model run was performed with K = 1,680 m/day (equivalent to 2.5×10^{-9} m^2) in both fracture zones, comprising 100,000

Table 5.3: Additional model parameters

Parameter	**Value**
Upstream weighting	0
Pressure boundary condition factor for regional/local models (ms)	0.01/1
Concentration boundary condition factor for regional/local models (ms)	0.01/1
Maximum number of non-linearity iterations for transient models	100
Pressure convergence tolerance (CG solver) (Pa)	1×10^{-13}
Concentration convergence tolerance (GMRES solver) (kg/kg)	1×10^{-13}
Maximum number of solver iterations for pressure and concentration	5000
Fluid compressibility (Pa^{-1})	4.4×10^{-10}
Molecular diffusivity of seawater in chalk (m^2/s)	5.5×10^{-10}
Density of fresh water (kg/m^3)	1000
Coefficient of fluid density change with concentration (kg/m^3)	714.2857
Fluid viscosity (Pas)	0.001
Solid matrix compressibility (Pa^{-1})	7.05×10^{-9}
Acceleration due to gravity (m/s^2)	9.81

time steps, each of 100,000 seconds (giving a total simulated period of 318 years). This provided the initial conditions for a further run with a fracture zone K of 83,800 m/day (1.25×10^{-7} m^2), covering a period of 174 days with time steps of 250 seconds.

The final pressure and concentration values for the regional model were applied to the boundary nodes in the 2D local model. An initial groundwater concentration of 609 mg/l and a head of 0 mAOD was applied throughout.

The chosen time steps ensure a grid Courant number of less than 1 throughout, thus preventing groundwater from travelling across more than the dimension of a mesh element in a single time step. This is a challenge in highly heterogeneous models, where the high groundwater velocities within fractures force the adoption of extremely small time steps compared to the time required for parts of the matrix to reach equilibrium. To overcome this problem, the porosity was modified as shown in Table 5.1 to reduce the contrasts in groundwater velocity and normalise the grid Courant number across the model domain. This approach does not affect the model

results, as the steady state solution to the groundwater flow equation is insensitive to storage. The 2D local model simulated a nominal period of 7 days, using 10 second time steps.

The final pressure and concentration values for the 2D local model provide boundary conditions for the 3D model. To help simulate the magnitude of salinity oscillations observed following breakthrough (Figure 4.6) and address the well-known challenges in accurately simulating narrow transition zones (e.g. Konikow, 2011; Simmons et al., 2010), a MATLAB code was written to compress the saline front within the upper fracture zone. The modelled salinity from $x = 1600 - 2000$ m was redistributed over a 200 m interval centred around the mean isohaline (17,800 mg/l); seawater (35,000 mg/l) and groundwater concentrations (609 mg/l) were applied to the seaward and inland sides of this interval respectively. The resultant salinity distribution provided boundary conditions for each node within the fracture plane of the 3D model. Pressure values from the 2D local model were assigned only to nodes at the seaward and coastal edges of the 3D model and to the shallowest nodes in the y-z plane of the borehole shown in Figure 5.1c. Values of P_n were maintained at these nodes by accounting for changes in density arising from front compression.

An initial groundwater concentration of 609 mg/l and a head of 0.85 mAOD was applied to the 3D model. The initial time step was 0.1 seconds, with a 50% increase applied every 1000 time steps up to a maximum length of 10 seconds. The model was run for 40,000 time steps (covering 3.5 days) in order to reach equilibrium.

5.3 Electrodynamic model construction

5.3.1 Numerical method

The electrodynamic model was written in MATLAB, using the control volume finite difference (CVFD) method. It is based on the approach described by Ijioma (2016) for modelling SP in hydrocarbon reservoirs and solves a discretised form of Equation (2.19) for V_{EK} and V_{EED} across the model domain, assuming no external current source or sinks and hence, no current

flow across the model boundaries.

A detailed description of the numerical method employed by the electrodynamic model is given in Appendix A. However, in simple terms the model solves a sparse matrix equation to simulate the electrokinetic potentials V_{EK} and exclusion-diffusion potentials V_{EED} throughout the model domain:

$$\mathbf{Ax} = \mathbf{By}, \tag{5.1}$$

where $\mathbf{x}$ is an $mno \times 1$ column vector of electrical potentials (V_{EK} or V_{EED}) for the m rows, n columns and o layers of the model and $\mathbf{y}$ is an $mno \times 1$ column vector of source terms (P_n for V_{EK} and $ln(C_f)$ for V_{EED}). $\mathbf{A}$ is an $mno \times mno$ sparse matrix comprising terms of the form:

$$a_{\Gamma i} = -\frac{\sigma_s \Delta L1_i \Delta L2_i}{0.5(\Delta L3_i + \Delta L3_{i+1})} \tag{5.2}$$

for each boundary Γ of element i, where $\Delta L1 - 3_i$ are the element dimensions in the directions of the coordinate axes, σ_s represents the bulk electrical conductivity of the aquifer and:

$$a_{Pi} = -\sum_{\Gamma=1}^{6} a_{\Gamma i} \tag{5.3}$$

for the centre of each element. Similarly, $\mathbf{B}$ represents an $mno \times mno$ sparse matrix where the σ_s terms are replaced by a coupling term (L_{EK} for V_{EK} and L_{EED} for V_{EED}).

In each case, a direct solution is found for $\mathbf{x}$ using the *mldivide* function in MATLAB and the total electrical potential is found by adding the solution vectors for V_{EK} and V_{EED}. As the SP signal is a potential difference between two points, the modelled SP (effectively ΔV_{EK} and ΔV_{EED}) is the difference in potentials (V_{EK} and V_{EED}) between a given location and that of a reference electrode (in this case, at an elevation of -2.8 mAOD within the Saltdean OBH).

5.3.2 Initial data processing

The SP modelling begins by mapping pressures and concentrations from the 2D local model onto the logically rectangular mesh shown in Figure 5.2 using the *griddata* function in MATLAB and assuming no variation in the y-direction (i.e. parallel to the coast). It then incorporates data for the region covered by the 3D hydrodynamic model in Figure 5.1c. The top 40 elements in Figure 5.2 lie above the extent of the 2D local and 3D hydrodynamic models; parameterisation of this region is described in Section 5.3.4.

Hydrostatic pressure P_h was inferred throughout the model domain by taking the nodal pressure values at the base of the 40^{th} element P_{40}, calculating the arithmetic mean of fluid density ρ between each element below them and invoking:

$$\Delta P_h = \rho g \Delta z, \tag{5.4}$$

where g is the acceleration due to gravity (9.81 m/s^2), Δz is the change in elevation between elements (m) and ρ is linearly interpolated from the density of fresh water (1000 kg/m^3 for 0 mg/l) and sea water (1025 kg/m^3 for 35,000 mg/l). The non-hydrostatic pressure component P_n was obtained by subtracting P_h from the total pressure at the centre of each element.

Spuriously low or high salinities produced by numerical oscillations in the SUTRA model were removed by limiting minimum and maximum concentrations to 609 mg/l and 35,000 mg/l respectively. To mimic the relatively sharp salinity gradient at the toe of the front indicated by Figure 4.14 and avoid minor fluctuations in borehole salinity ahead of this, all salinity values below 700 mg/l were set equal to 609 mg/l.

Modelled porosity was 0.39 throughout the model domain, except in the borehole and adit, where a value of 1 was applied.

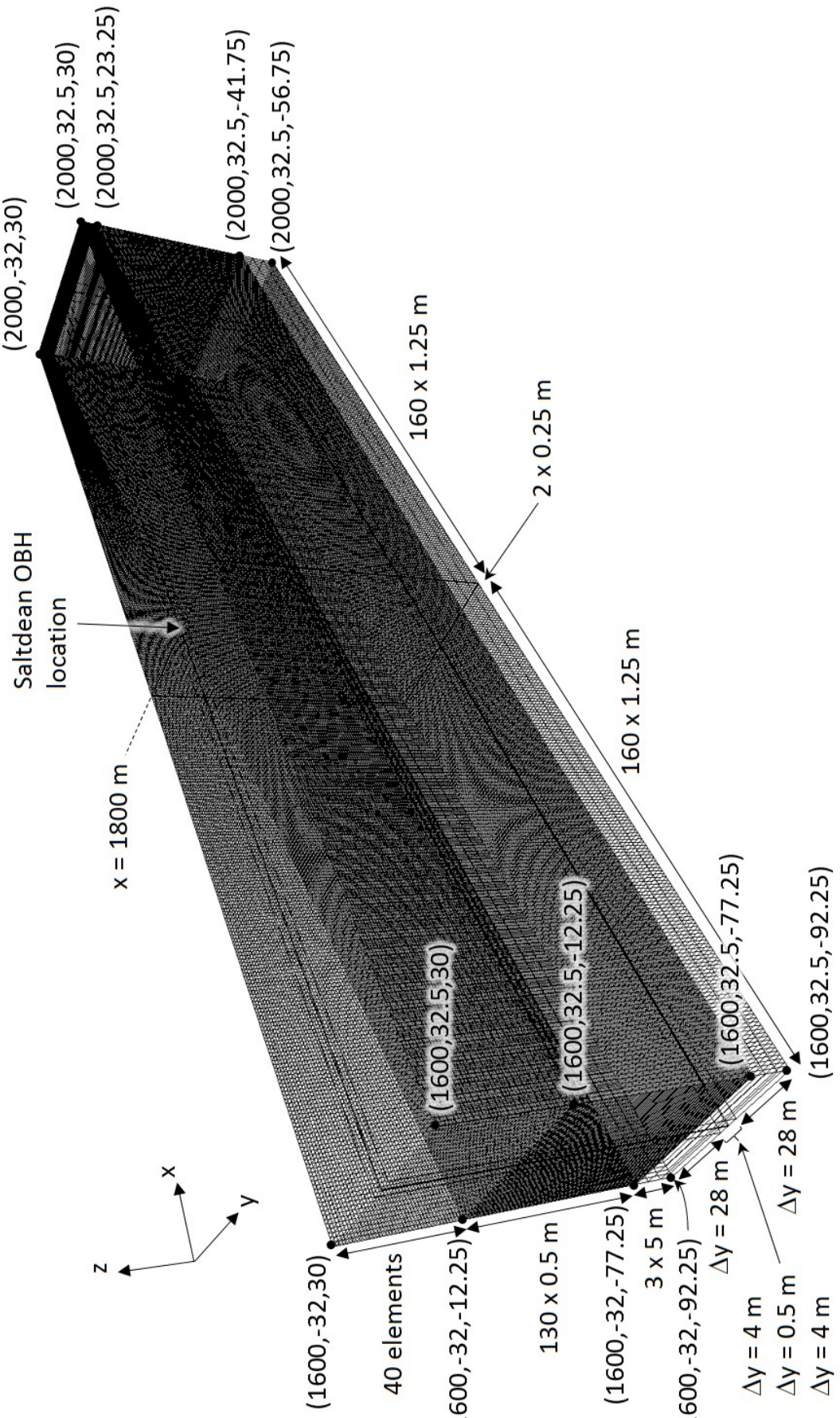

Figure 5.2: Finite element mesh for the electrodynamic model.

5.3.3 Representing the unsaturated zone

Where the water table lies above the top of the SUTRA local model, its elevation was inferred from Equation 5.4 and values of P_{40}, assuming hydrostatic conditions and a constant fluid density of 1000.435 kg/m^3 (consistent with a fluid concentration of 609 mg/l). Saturation was reduced linearly from 1 to 0.995 over the 2 elements immediately above the water table to reflect dewatering of fractures (e.g. Ireson et al., 2009; Mathias, 2005) and concentration was increased linearly to 2,200 mg/l over a further 2 elements above this, reflecting the presence of elevated salinity in the unsaturated zone (Figure 4.6). Constant values of saturation (0.995) and concentration (2,200 mg/l) were maintained above this.

5.3.4 Electrical parameters

The TDS concentrations simulated by SUTRA were converted to σ_f and C_f using Equations (4.4) and (4.5).

The bulk electrical conductivity of the aquifer σ_s was simulated using Archie's law (Equation (4.9)), with a value of 2.5 for the cementation exponent m below the unnamed marl in Figure 4.2 and m=1.5 above this, reflecting an increased degree of fracturing at shallow depths and hence, greater connectedness of the pore and fracture network (Glover, 2009; Roubinet et al., 2018). For marl seams, Equation (4.10) was applied, reflecting the contribution of surface conductance in clay minerals.

The values of the coupling coefficients at full saturation C_{EED} and C_{EK} were obtained from Equations (4.3) and (4.8); the values of the exclusion efficiency η (Section 2.2.2) below the water table are shown in Table 5.4. This parameterisation, which was refined during model calibration, is based on the range of values for each lithology presented in Figure 4.9 and reflects the relationship between η and the pore-throat diameter r of the host rock proposed by Westermann-Clark and Christoforou (1986), Leinov and Jackson (2014) and MacAllister (2016). The values of $\eta = 0$ in the fracture zones, borehole and adit reflect the negligible

influence of charged mineral surfaces in these regions.

Table 5.4: Modelled exclusion efficiencies η

Feature	η
Seaford Chalk	0.09
Lewes Nodular Chalk (above lower fracture zone)	0.03
Lewes Nodular Chalk ($\leq$ 3.5 m below lower fracture zone)	0.01
Lewes Nodular Chalk (>3.5 m below lower fracture zone)	0.05
Shallow marls (above base of borehole)	0.15
Deep marls and hardgrounds (below base of borehole)	0.24
Fracture zones, borehole and adit	0

Above the water table, these coupling coefficients were reduced to reflect slightly lower saturation values. Following Jackson et al. (2012b) and (MacAllister, 2016), values of the electrokinetic coupling coefficient in the unsaturated zone (C_{uEK}) were obtained from:

$$C_{uEK} = C_{EK} S_w^{0.6} \tag{5.5}$$

and modified values of the electrochemical exclusion-diffusion coupling coefficient for the unsaturated zone (C_{uEED}) from:

$$C_{uEED} = (1 - S_w)^3 C_{EED}. \tag{5.6}$$

5.4 Model results and discussion

5.4.1 Salinity and SP

A 2D plot of modelled σ_f within the vertical plane running perpendicular to the coast and intersecting the borehole is shown in Figure 5.3a, alongside the modelled SP distribution (Figure 5.3b). The saline front lies only 4.5 m from the base of the borehole in the x-direction and 0.25 m below the base of the borehole (1 grid cell) in the z-direction.

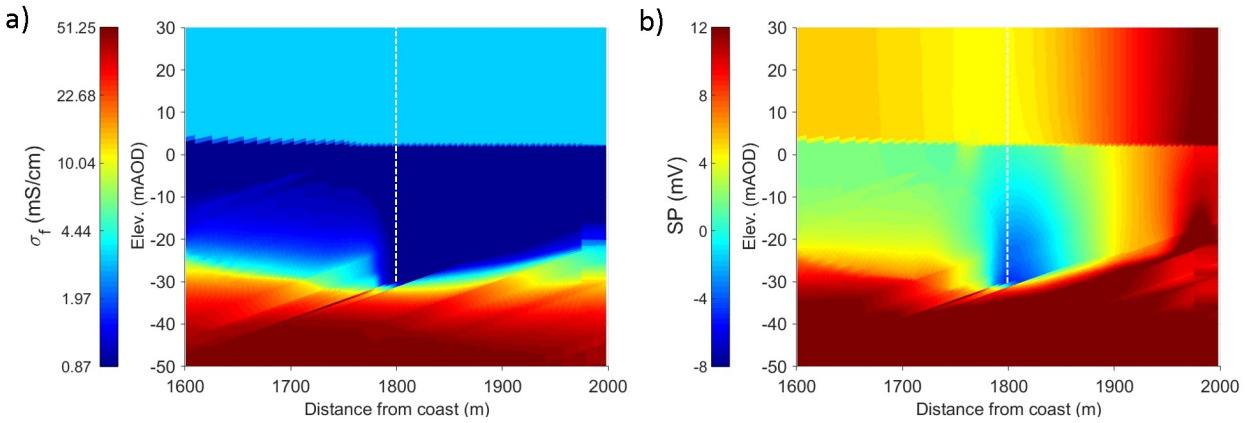

Figure 5.3: Model distribution of a) σ_f and b) SP within the vertical plane of the borehole (y=0) at steady state. The borehole location is shown as a dashed white line.

The results show a clear negative SP gradient in the z-direction in the vicinity of the borehole; the simulated SP gradient in the borehole is plotted next to an observed profile in Figure 5.4a. As well as closely matching the observed profile, an interesting aspect of the results is the dominance of V_{EED} in comparison to V_{EK}. This supports the hypothesis (proposed by MacAllister et al. (2018) and discussed in Section 4.5.2) that the insensitivity of the SP gradient to tidal and seasonal pressure changes is evidence of an electrochemical, rather than an electrokinetic source mechanism.

The sensitivity of the SP gradient to multiple input parameters is shown in Figure 5.4b. The elevated electrical conductivity of clay minerals in the marl bands does not greatly affect the magnitude of the SP gradient, although inspection of line 1 suggests it is responsible for the deviation in observed SP adjacent to the Shoreham Marl, just below -20 mAOD (see Figure 4.2). The removal of elevated salinity (and hence electrical conductivity) in the unsaturated zone lowers the modelled gradient significantly (line 2). Increasing recharge by 25% produces a deeper saline front and reduces the SP gradient substantially (line 3). The greatest impact on the SP gradient is achieved by removing variations in η (lines 4 and 5) and in the case of a constant value of η throughout the model domain, the SP gradient ahead of the front disappears (line 5).

A further aspect of model sensitivity concerns the chosen hydrodynamic model and by extension, the hydrogeological conceptual model. Simulations conducted by MacAllister (2016)

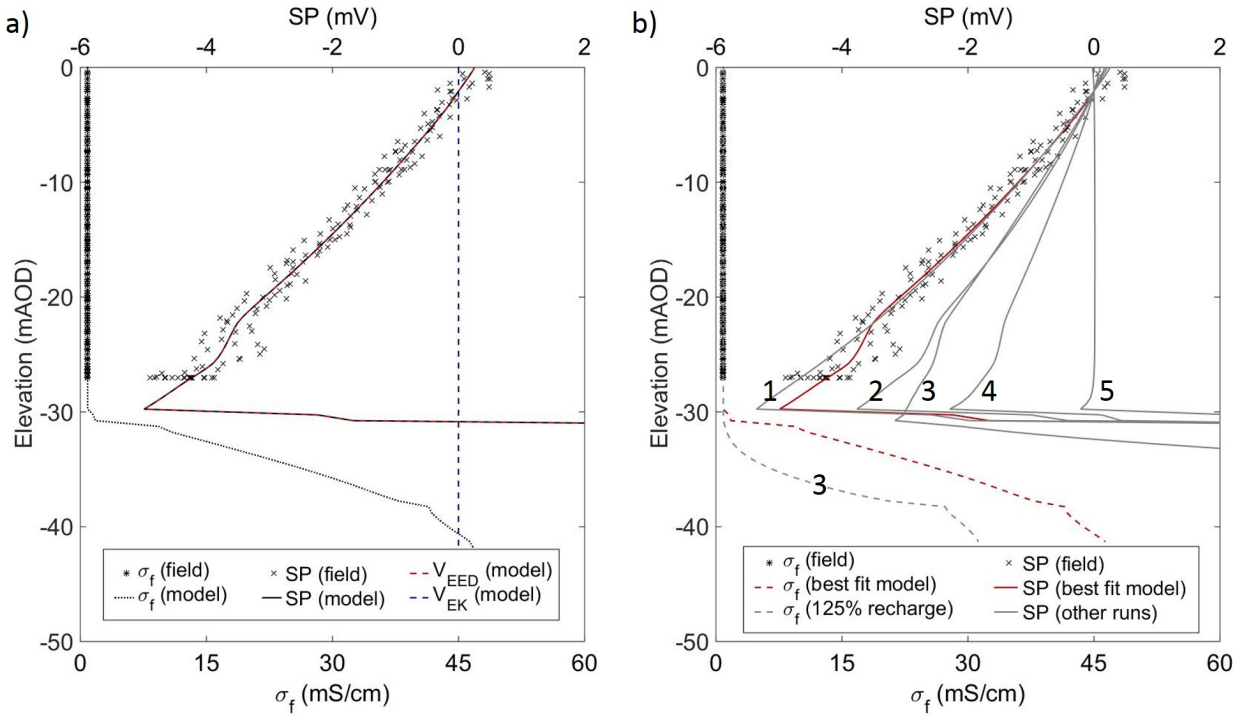

Figure 5.4: Comparison of observed and simulated SP and σ_f gradients. a) Best-fit model results, showing the contribution of V_{EED} and V_{EK} components. b) Sensitivity analysis showing the effects of: 1) representing formation electrical conductivity in the marl horizons using Archie's law (cf. Waxman-Smits) 2) applying a fluid concentration of 609 mg/l throughout the unsaturated zone 3) increasing steady state recharge by 25% 4) applying η=0.04 for all chalk layers (excluding marls and hardgrounds) 5) applying η=0.04 for all chalk, marl and hardground layers.

and MacAllister et al. (2018) were based on a hydrodynamic model produced by Eclipse 100, which ignores both Fickian diffusion and mechanical dispersion. This produced a sharp saline front for the Saltdean model (Figure 5.5a) and resembles the classic conceptual model proposed by DuCommun (1828), Badon-Ghyben (1889) and Herzberg (1901) (Figure 3.1). MacAllister (2016) noted that the Eclipse 100 model oversimplifies the transport of salt and recommended that future models invoke a more physically-based approach in this regard. For comparison, the more dispersed and complex front produced by the current SUTRA model (with post-processing to sharpen the front within the upper fracture zone) is shown in Figures 5.5b and 5.5c.

To assess the importance of the hydrodynamic model in simulating the observed SP gradient, a highly simplified and relatively narrow saline front was applied to the electrodynamic model. The front is completely horizontal across the model domain, with concentrations varying linearly

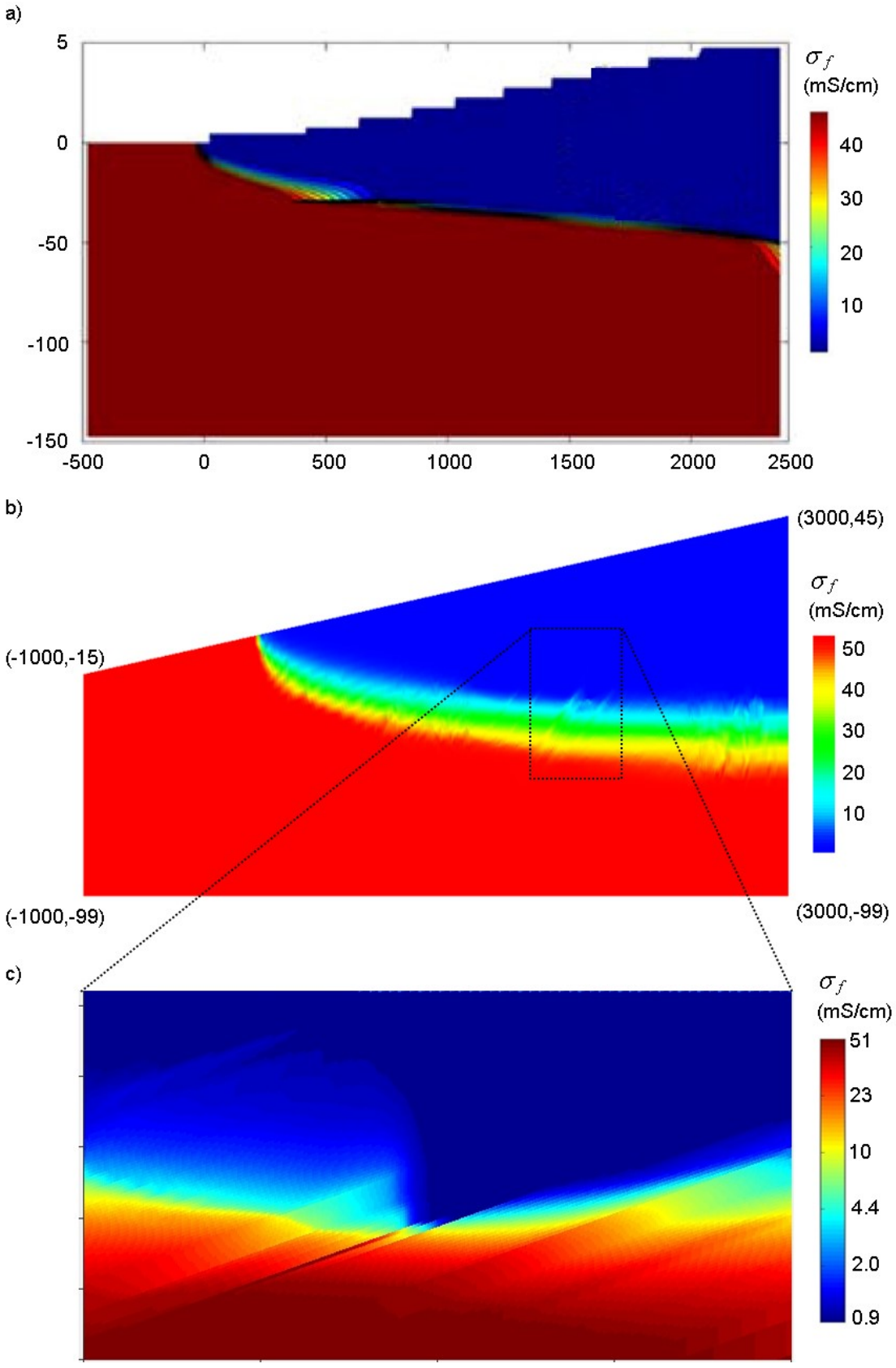

Figure 5.5: Comparison of simulated saline fronts for the Saltdean study area, comprising: a) the regional model of MacAllister (2016) and MacAllister et al. (2018) produced by Eclipse 100, b) the regional model described in this chapter, produced in SUTRA and c) the area surrounding the Saltdean OBH, following post-processing and with logarithmic colour scale to highlight the shape of the front at low σ_f.

from 609 mg/l (0.87 mS/cm) at -32 mAOD to 35,000 mg/l (51.25 mS/cm) at -37 mAOD (Figure 5.6a). The shape of the SP profile is similar to the original SUTRA model, although the narrower extent of the front has doubled the SP gradient. In Figure 5.6b, the vertical extent of the simple front is doubled, giving a front that is comparable to the SUTRA model and a similar SP gradient as a result. These results suggest that the SP results are fairly insensitive to the type of small-scale variations in the shape of the front shown in Figure 5.5c.

A more striking effect is achieved by lowering the narrow front in Figure 5.6a by 5 m (Figure 5.6c). From inspection of Figure 4.2, it is clear that the deeper front coincides with the location of electrochemically exclusive hardgrounds ($\eta = 0.24$), leading to a reversal of the original SP gradient. This also provides an interesting insight into the results for Figure 5.6a, where the front lies entirely within more electrochemically diffusive chalk strata ($\eta = 0.05$) and produces a much stronger SP gradient, with the same polarity as that observed in the Saltdean OBH.

A final comparison between conceptual models is presented in Figure 5.6d, where the narrow front in Figure 5.6a is applied to a homogeneous electrodynamic model. Replicating the approach of MacAllister (2016) and MacAllister et al. (2018), no variations in η are included, although the results are derived using a direct, rather than iterative solver. The absence of an SP gradient is comparable to the results achieved by MacAllister (2016) when a lower tolerance of 1×10^{-7} V was applied to the iterative solver (Figure 4.15d) and suggests that the best-fit model of MacAllister (2016) (Figure 4.15a), based on a solver tolerance of 1×10^{-5} V, is adversely affected by solver error.

Discussion

The results suggest that the observed SP gradient relies both on a nearby saline front and local variations in η. Given the extremely low permeability of the chalk matrix, the presence of a nearby saline front may reflect historical saline intrusion from prolonged droughts or periods when sea levels were significantly higher than they are currently, as discussed in Section 4.6. While these historic events may suggest a high risk of future intrusion, it is difficult to infer the timing of future events from a single SP profile. To this end, the evolution of the SP gradient

over time could provide a better indication of imminent saline intrusion and this is investigated further in Chapter 6.

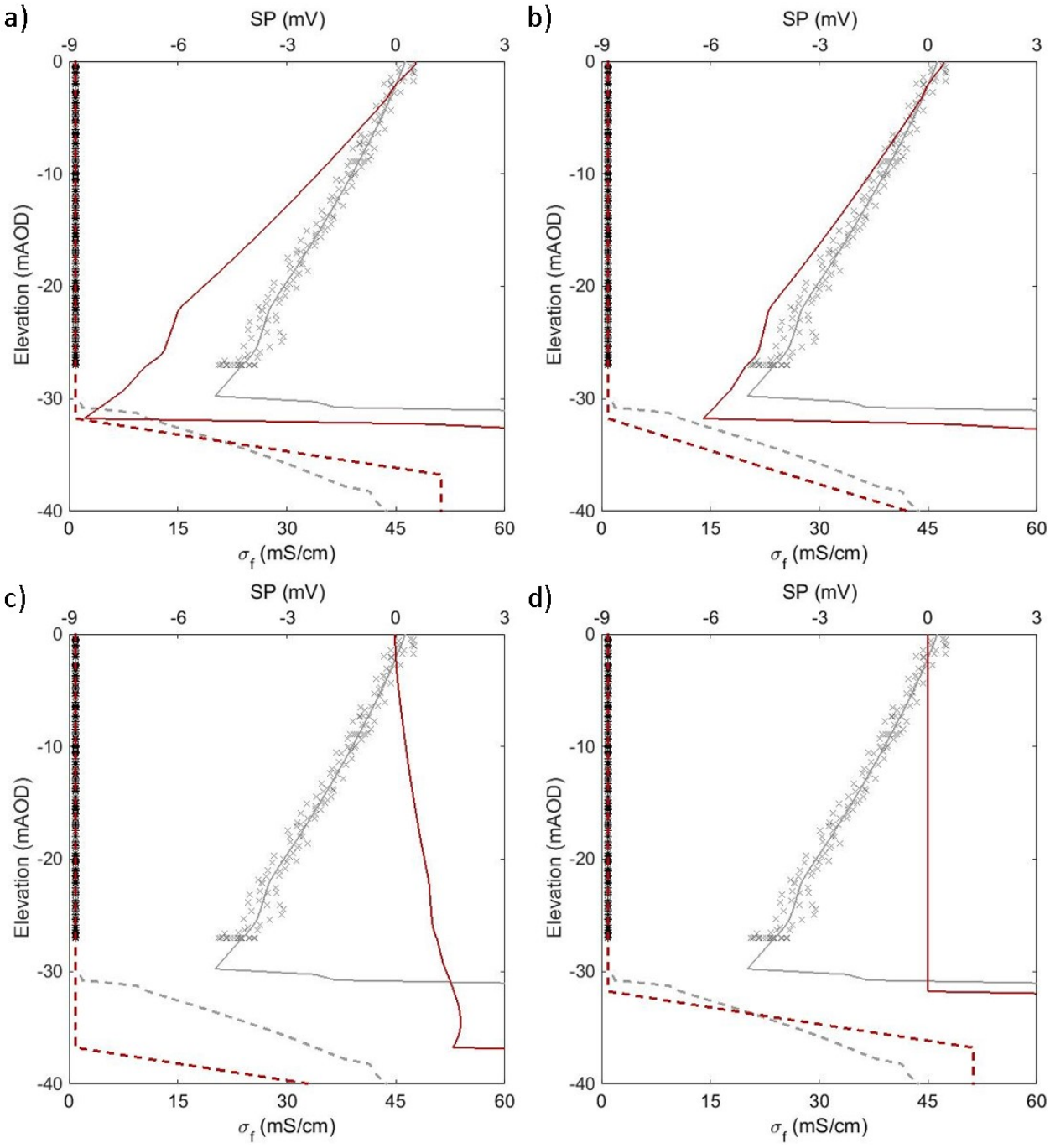

Figure 5.6: The effects of depth and dispersion of modelled fronts (red dotted lines) on the borehole SP gradient (red solid lines). Simulated fron.ts using the best-fit electrodynamic parameters extend from a) -32 mAOD to -37 mAOD b) -32 mAOD to -42 mAOD c) -37 mAOD to -42 mAOD. In d), the front extends from -32 mAOD to -37 mAOD with a constant $\eta = 0.04$ throughout the model domain and no elevated salinity in the unsaturated zone. All modelled fronts are horizontal, with linearly varying σ_f (or salinity). The saline front (dotted grey line) and SP profile (solid grey line) for the best-fit model are shown for comparison along with field observations of σ_f (black asterisks) and SP (grey crosses).

5.4.2 Borehole water levels

Based on simulated pressures, the effective borehole water level in the steady state model is 1.02 mAOD, which is 0.14 m higher than the maximum water level in the Saltdean OBH on 15 August 2013. However, it is apparent from Figures 5.3a and 5.4 that even a slight lowering of the water table would lead to salinisation of the borehole under steady state conditions. This suggests that the saline front within the model is significantly wider than the one which occurs beneath the Saltdean OBH, despite efforts to minimise dispersion through implementation of a fine element mesh, as described in Section 5.2.1.

As is commonly the case in solute transport models, SUTRA represents mechanical dispersion as a Fickian process (Konikow, 2011; Voss and Provost, 2002). Although the solute transport mechanisms invoked by SUTRA are a closer approximation to real-world phenomena than the simple approach employed by Eclipse, this method of representing mechanical dispersion is non-physically based and, as Konikow (2011) demonstrates, it is likely to exaggerate spreading of the front. Given that SP signals are related to concentration gradients (strictly $\nabla ln(C_f)$), this has clear implications for model calibration. In matching field observations of the borehole SP gradient (Figure 5.4), the degree of heterogeneity in other input parameters, such as η, may have been overestimated in order to compensate for excessive dispersion of the saline front and this suggests a degree of non-uniqueness in the model.

As discussed in Section 5.2.1, the width of the front in SUTRA (and other hydrodynamic models that include molecular diffusion and mechanical dispersion) is controlled by the model's mesh dimensions. However, strictly speaking, this only applies to cells in the vicinity of the front. It is possible that adaptive meshing techniques could be used to implement small cells in a more computationally efficient manner, based on the location of the front in any given time step and local groundwater velocities.

5.4.3 Grid design

Although implementation of a finer mesh in the hydrodynamic model would be likely to reduce the width of the saline front, this would necessitate a reduction in the length of model time steps to minimise grid Courant numbers, and an increase in the computational effort required to solve each time step. Given that the hydrodynamic model described herein had a run time of around 2 weeks using a 3.4GHz Intel Core processor with 16.0 GB of RAM, the use of a finer mesh would have made the process of model calibration impractical.

The sensitivity of hydrodynamic transport models to grid refinement is well known (e.g. Diersch and Kolditz, 2002; Konikow, 2011), although relatively few studies have been done on the effect of grid dimensions in electrodynamic models of solute transport and none of these focused on coastal aquifers. However, in simulating SP within a hydrocarbon reservoir, Ijioma (2016) showed that additional grid refinement affected the results significantly.

A formal assessment of model sensitivity to domain extent and grid refinement is given in Appendix B. The results suggest that the domain boundaries do not affect modelled SP within the borehole, although further refinement of the model grid leads to a slight dampening of the SP gradient. In common with the hydrodynamic model, the number of additional model cells associated with even a modest level of refinement would lead to a substantial increase in run times; in the case of the electrodynamic model, a halving of cell dimensions throughout the x-z plane of the model increases the time required to solve each time step by a factor of 15.

While grid refinement in the electrodynamic model appears to dampen the SP gradient, conversely (from Equation (2.9)) the sharper saline front associated with smaller grid cells in a more refined hydrodynamic model could lead to steeper SP gradients (a hypothesis supported by the sensitivity analysis in Figure 5.6). This raises questions over the benefit of continued discretisation. Although similar assessments have not been completed for SP models, grid refinement studies for solute transport test cases reported by Diersch and Kolditz (2002) and Simmons et al. (1999) suggest that the results continue to evolve even at very fine levels of grid refinement, and in some cases, the results produced by coarser grids more closely match

observed values. Given these uncertainties and the large computational expense involved, refining the grid until further discretisation no longer affects the results is beyond the scope of this study.

5.5 Discussion and conclusions

The model described in this chapter demonstrates that the observed SP gradient within the Saltdean OBH can be replicated using plausible values for the wide range of input parameters that exist. Although the model presented is not a unique solution to the problem, the results and accompanying sensitivity analysis allow several important conclusions to be drawn.

Firstly, the model strongly suggests that the observed SP gradient is dominated by the electrochemical component of SP, ∇V_{EED}. As such, it relies on the presence of a nearby saline front, although the precise depth and extent of this front is uncertain. Based on the sensitivity analyses presented in Figures 5.4 and 5.6, there are likely to be a suite of solutions that fit the observed data. As a general rule, reductions in the SP gradient relating to a deeper front may be offset by increases in gradient arising from a sharper front. Unfortunately, in most hydrogeological investigations, neither the depth or extent of the saline front below any borehole is known with any certainty.

Secondly, the SP gradient is insensitive to small-scale variations in the shape of the front. This has implications for the underlying conceptual and hydrodynamic models and it may be that, for steady state solutions, a fairly simple approach may suffice. However, the importance of the hydrodynamic model is likely to increase when simulating the transient evolution of the saline front and the entry of saline water into the borehole. This aspect is addressed in the following chapter.

Finally, variations in the exclusion efficiency η are essential for producing a significant SP gradient. Unfortunately, few data are available for this parameter and for most lithologies, there are no direct measurements from laboratory experiments. For the current model, values of η have been inferred for marls and hardgrounds from theoretical work and field data, although

they remain subject to considerable uncertainty. As such, along with the depth and extent of the saline front, uncertainties in η represent another source of non-uniqueness in the model results. However, unlike in situ characterisation of the saline front beneath a borehole, η values for the local geology are measurable and this is addressed in Chapter 8.

Chapter 6

Modelling the evolution of self-potentials prior to saline intrusion

6.1 Introduction

Recent monitoring of the Saltdean OBH by MacAllister (2016) revealed a persistent self-potential (SP) gradient ahead of the saline front that was absent in boreholes further inland (Figures 4.12 and 4.13). In Chapter 5, a combined hydrodynamic and electrodynamic model was described that matches the observed SP gradient prior to saline breakthrough (Figure 5.4).

A slight reduction in the observed gradient prior to seawater intrusion (Figure 4.14) suggests that SP monitoring could be used as a predictive tool, although the mechanisms that control this phenomenon have not been identified to date. To mimic the evolution of SP in the lead up to saline intrusion, the steady state model described in Chapter 5 was used to provide the initial conditions for a transient simulation. This transient model represents the advancing saline front and its entry into the borehole, induced by the application of tidal oscillations at the coast and the removal of recharge after 1 week of the simulation.

The primary objective of this chapter is to replicate the observed precursor and through a process of sensitivity analysis, develop an understanding of the key factors that control this

phenomenon. This represents an important step in understanding the potential for precursors to exist at other sites and their likely characteristics. It should also help to inform the data requirements for any future laboratory and field investigations.

6.2 Model description

The parameters in Tables 5.1 to 5.3 were applied to the transient model with the following modifications. Porosity values in the 2D local model were modified in the steady state simulations to accelerate convergence (see Section 5.2.4); this can be justified on the basis that the steady state solution is insensitive to storage parameters. In the transient version of this model, porosity values were set to be consistent with those applied to the other model domains, thus ensuring that pressure and salinity evolve at an appropriate rate.

As SUTRA does not provide an option to simulate dual porosity systems, the choice of porosity in the fracture zones (0.1) (see Figure 4.2) is a compromise to represent a combination of rapid flow through fractures (comprising less than 1% of the aquifer volume (Butler et al., 2012; Price, 1987)), slower flow through the matrix (comprising approximately 39% of the aquifer volume (Bloomfield et al., 1995)) and diffusion of salinity between the two. Previous studies by Jones and Robins (1999) and MacAllister (2016) confirm the presence of the shallower fracture shown in Figure 4.2, although the presence of the lower fracture zone was inferred during model calibration. The importance of the lower fracture zone is discussed in Section 6.3.2.

Given the importance of non-linear behaviour in the transient model, a non-linearity convergence criterion of 1 Pa was applied to the pressure solution and 1×10^{-5} kg/kg to the concentration solution.

The 2D regional model was run over 33 semidiurnal tidal cycles (17.1 days), comprising 8,448 time steps of 174.66 seconds ($\frac{\pi}{128}$ radians, based on a period of 0.518 days). To characterise the spring-neap tidal variation, a regression was performed on the sea-level data from Newhaven (BODC, 2015) over the period of monitoring, using the $fminsearch$ function in MATLAB and the following equation:

$$h_{Nh} = A\left[cos(\frac{2\pi t}{T_{SN}}) + A_0 + 1\right]\left[cos(\frac{2\pi t}{0.518})\right], \tag{6.1}$$

where h_{Nh} is measured sea level at Newhaven in mAOD, A is the amplitude of the spring-neap tidal cycle (0.641 m), t is time in days since the first data point, T_{SN} is the period of the spring-neap tidal cycle (14.8 days) and A_0 is the mean amplitude of the semidiurnal tidal component (2.44 m).

The results of the regression are plotted against sea level observations at Newhaven in Figure 6.1. Although it is apparent that Equation (6.1) does not capture monthly variations in the amplitude of spring and neap tides, the model reasonably approximates the period and amplitude of semidiurnal and fortnightly tidal variations. As such, it was considered to be appropriate for representing the key elements of seawater intrusion in the Saltdean OBH. Variable pressures based on the regression were applied to the sea floor nodes shown in Figure 5.1a.

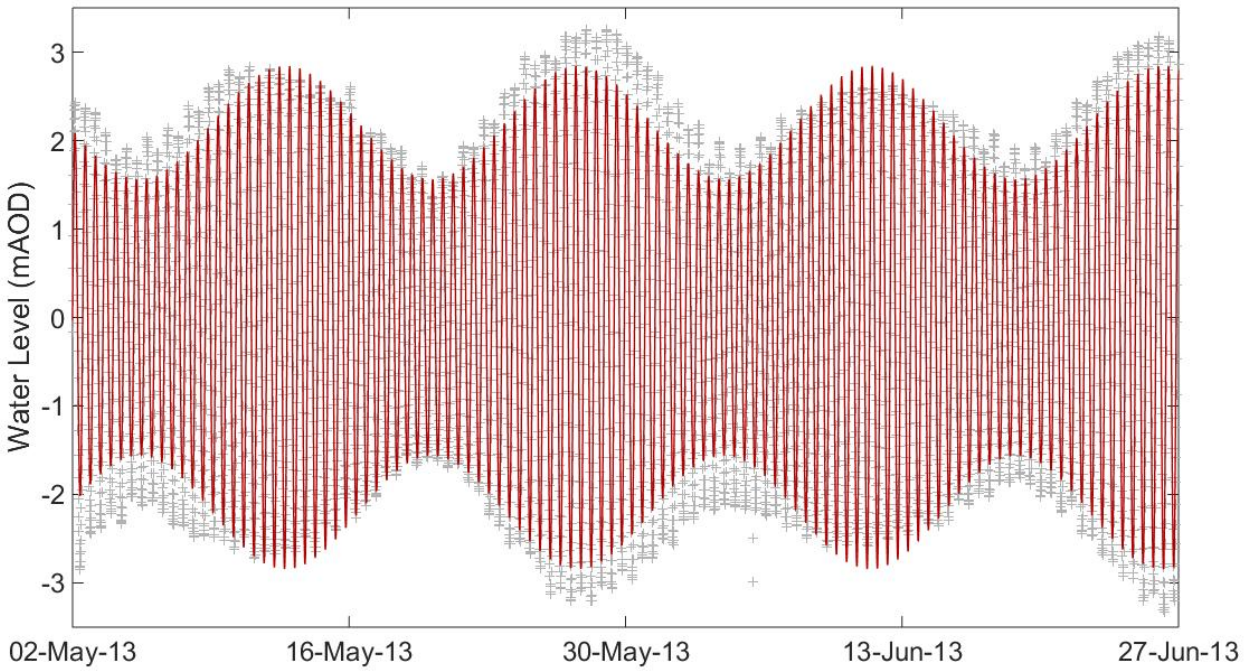

Figure 6.1: Comparison of modelled (red line) and observed (grey crosses) tidal oscillations at Newhaven.

Pressure and concentration values were saved every 698.63 seconds ($\frac{\pi}{32}$ radians) of the simulation and applied to all nodes at the boundaries of the 2D local model. The 2D local model was run

for 33,920 time steps, the first 256 of which were 21.83 seconds long ($\frac{\pi}{2048}$ radians), followed by uniform time steps of 43.66 seconds, simulating a total period of 17.1 days. This allowed the output files, printed every 256 time steps, to capture values close to the modelled tidal maxima and minima at $x = 1800$ m, based on a simulated tidal lag of 0.13 days ($\frac{\pi}{2}$ radians) (compared to an observed tidal lag of 0.15 days, as shown in Section 4.3.1). In addition, pressures and concentrations for the boundaries of the 3D model were saved every 698.63 seconds.

These values were processed to compress the front as described for the steady state simulation in Section 5.2.4 and applied to the 3D model. Boundary conditions were applied to the same nodes as in the steady state run, with the exception of concentration boundary conditions from within the fracture zone, to avoid artificially constraining interactions between the fracture zone and the highly permeable borehole. The 3D model simulated 33 tidal cycles (17.1 days) over 135,679 time steps, with an initial duration of 1.82 seconds ($\frac{\pi}{12288}$ radians). After every 384 time steps, their duration was multiplied by a factor of 3, reaching a maximum of 10.92 seconds ($\frac{\pi}{2048}$ radians). This ensured that the results, output every 1,024 time steps, were synchronised with those of the 2D local model.

The electrodynamic model, described in Section 5.3, was run for each time step output by the SUTRA model, solving for SP four times per tidal cycle.

For the purposes of calibration, the transient model has a nominal start time of 10:02 am on 10 August 2013, at the mid-point of a rising tide at Newhaven. This allows for 7 days of continuous recharge and tidal oscillations in the model prior to the observed start of the SP precursor (Figure 4.14) and the cessation of model recharge on 17 August.

6.3 Model results

6.3.1 Water levels

As shown in Figure 6.2, the frequency, phase and amplitude of tidal water level fluctuations in the model match observations from the Saltdean OBH, although as discussed in Section

5.4.2, modelled water levels are higher to account for greater dispersion of the front and avoid salinisation of the borehole under steady state conditions. In addition, the effects of abstractions at the Balsdean PS, which were not implemented in the model, can be seen in the observed data as sharp departures from the otherwise sinusoidal variations in water level.

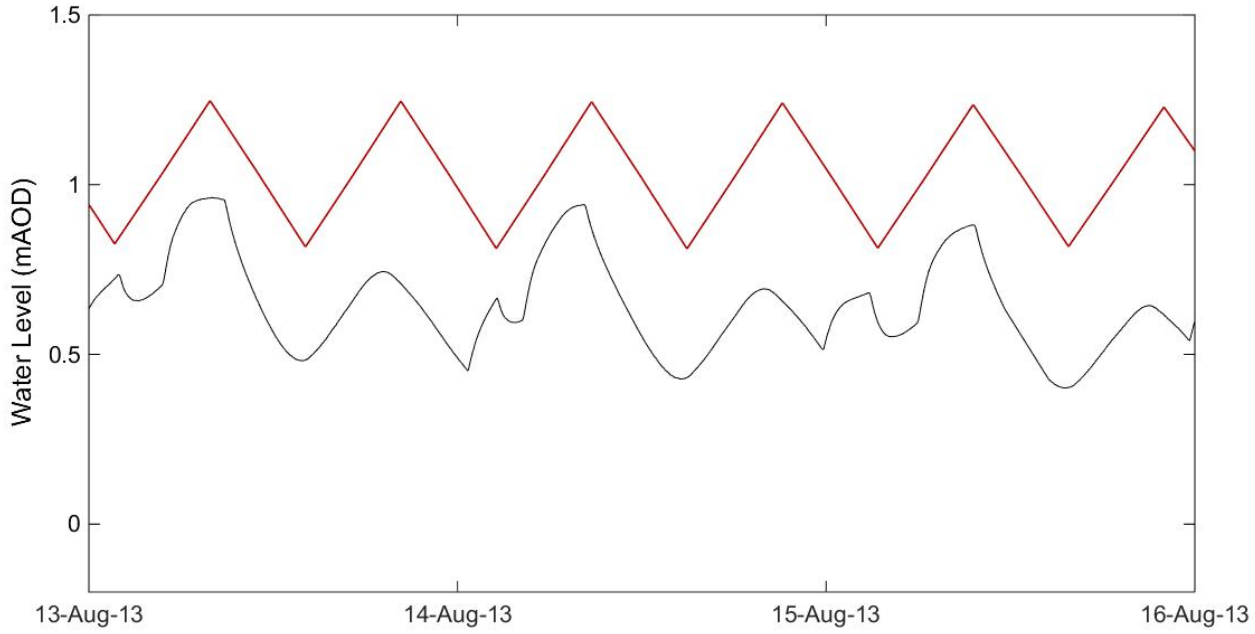

Figure 6.2: Comparison of modelled (red line) and observed (black line) tidal oscillations in the Saltdean OBH.

6.3.2 Self-potentials

The model results are assessed by comparing them to field observations of SP and σ_f around the time of saline intrusion in August 2013. The model in Figures 6.3c-d closely matches the observed data (Figures 6.3a-b), particularly once the field data have been smoothed to remove tidal oscillations and other, higher frequency components. The smaller magnitude of σ_f peaks following breakthrough in comparison to those shown in Figure 4.14 highlights the highly dispersed front produced by SUTRA (even after post-processing), a feature common to numerical models that simulate diffusion and mechanical dispersion of solutes (Konikow, 2011).

Sensitivity analysis in the model provides an important insight into the likely mechanisms

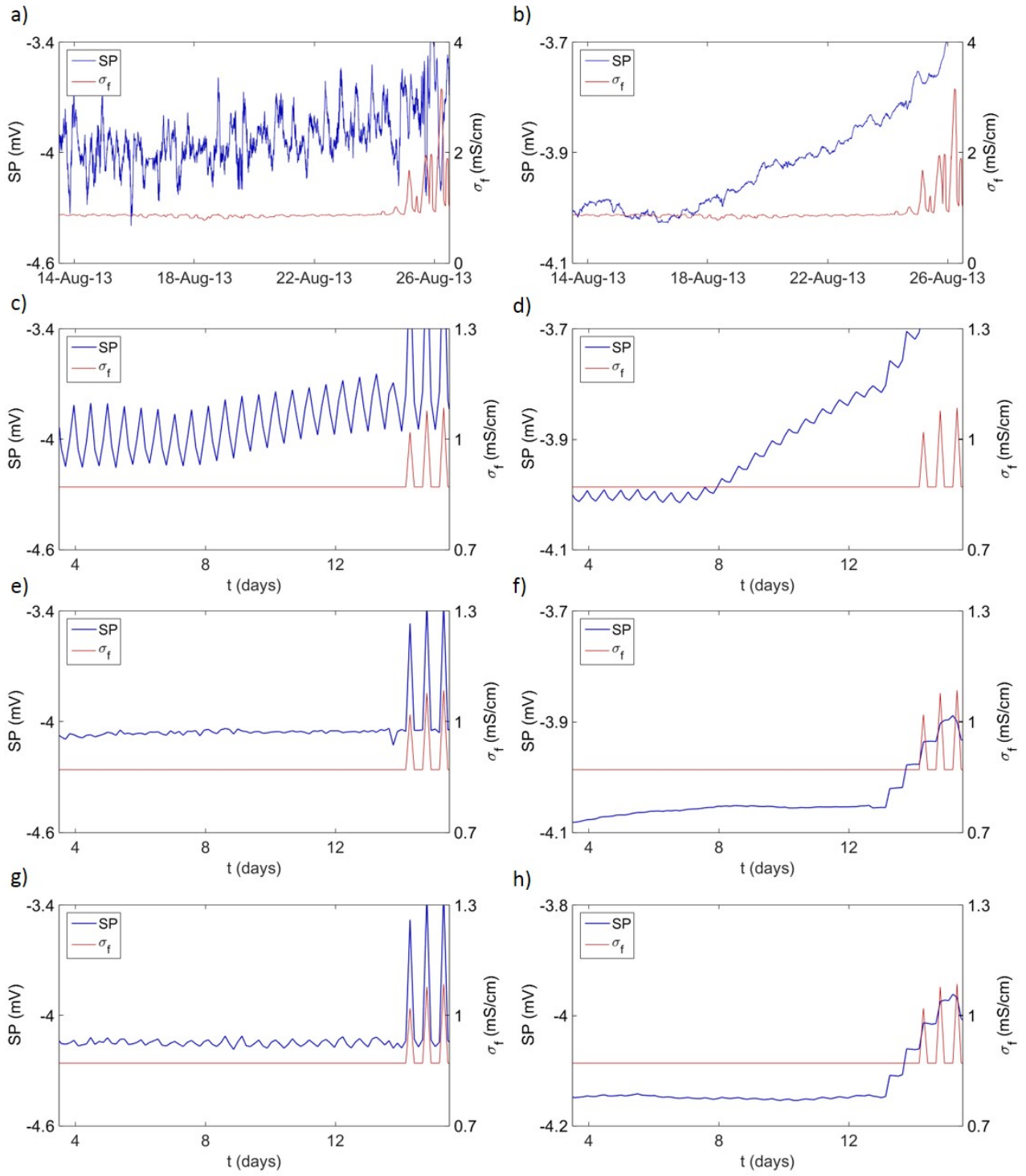

Figure 6.3: Comparison of observed and simulated SP precursors in the Saltdean OBH. a) field SP and σ_f data, smoothed using an SG filter with a sampling window of 105 minutes to reduce high frequency noise b) field SP and σ_f data, using an SG filter sampling window of 2.2 days c) best-fit model SP and σ_f (unfiltered) d) best-fit model results, using an SG filter sampling window of 2.2 days e) model sensitivity analysis, applying a fixed salinity distribution in the lower fracture zone throughout (unfiltered) f) as e), but using an SG sampling window of 2.2 days g) model sensitivity analysis, with η=0.01 above and below the lower fracture zone (unfiltered) h) as g), but using an SG sampling window of 2.2 days. SP values represent the potential difference from -2.8 to -26.8 mAOD; σ_f values are taken from -26.8 mAOD.

that drive the precursor. The first analysis investigates the contribution of the inferred lower fracture zone in Figure 4.2 to the evolution of SP. This is achieved by treating the lower fracture zone as a region of low permeability, unfractured chalk and modelling the initial salinity distribution in this layer throughout the transient model (while allowing the saline front to evolve freely throughout the rest of the model domain). As shown in Figures 6.3e-f, this completely removes any precursor to intrusion and also removes tidal SP oscillations.

However, movement of salinity beneath the borehole is not sufficient by itself to produce a precursor. Applying η=0.01 within 2.5 m of the lower fracture zone (i.e. both above and below it) also removes the modelled precursor (Figures 6.3g-h). The precursor therefore reflects the movement of salinity through a heterogeneous geoelectric environment.

More specifically, under steady state conditions, the front predominantly spans the lower plane of the lower fracture zone (Figure 6.4a). From Table 5.4, the front interacts with η values of 0 (within the fracture zone) and 0.01 (immediately below the fracture zone). Immediately prior to intrusion, the front spans the upper plane of the top fracture zone (Figure 6.4b), with η values of 0 (within the fracture zone) and 0.03 (immediately above the fracture zone). From Equation (2.16), this increase in the effective value of η across the front can be linked to a reduction in ∇V_{EED} and the dampening of the initial SP gradient which consitutes the precursor.

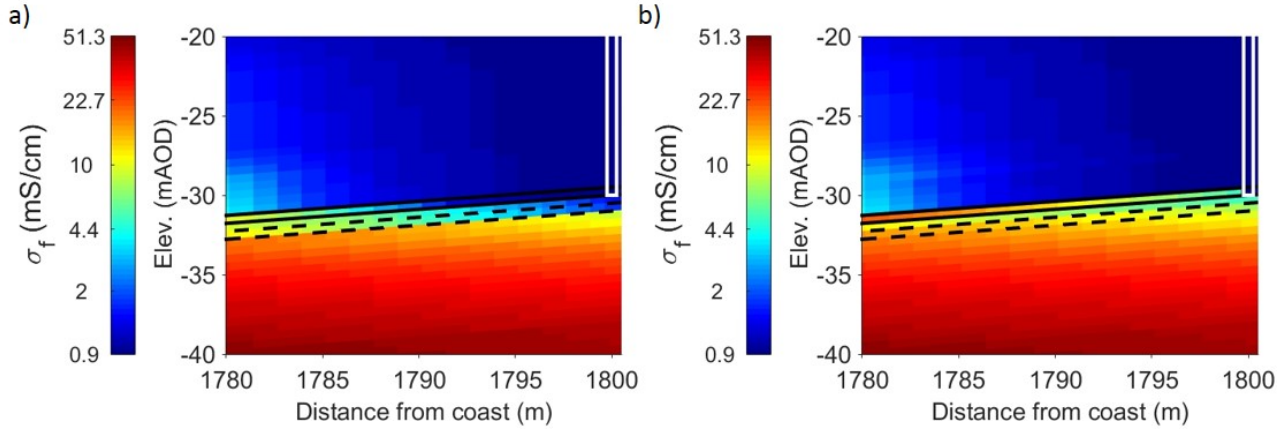

Figure 6.4: Modelled salinity distribution in the best-fit model near the Saltdean OBH at a) 0 days b) 14.2 days (immediately prior to saline breakthrough). The outlines of the borehole (solid white lines), the upper fracture zone (solid black lines) and the lower fracture zone (dashed black lines) are also shown.

A precursor is also obtained by applying the change in η values (from 0.01 below to 0.03 above) across the upper fracture zone instead (Figure 6.5). In this scenario, a static front was maintained in the lower fracture zone, thus demonstrating that movement of saline water within the upper fracture zone is the source of the modelled precursor. Although the smoothed precursor is similar to that observed in the borehole, tidal oscillations are notably smaller in magnitude than those observed in the field and in the best-fit model.

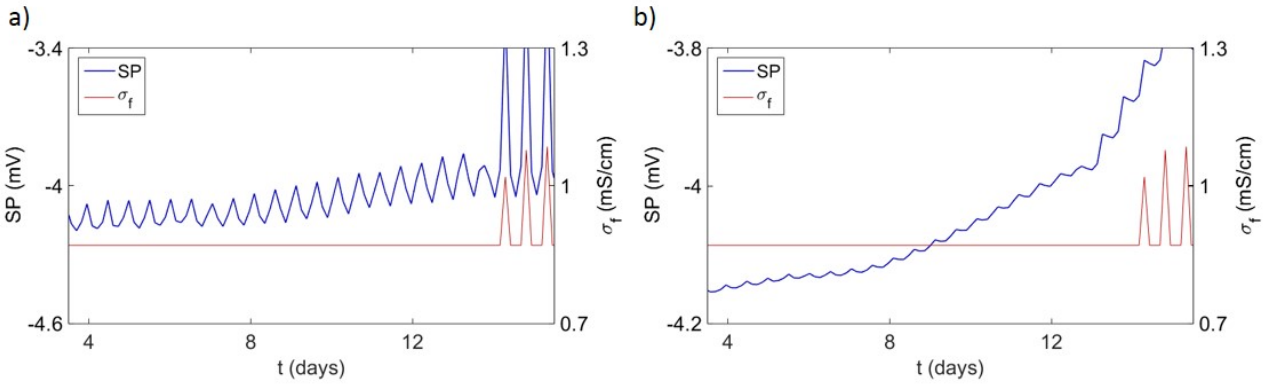

Figure 6.5: Simulated precursor when the boundary between $\eta = 0.03$ and $\eta = 0.01$ in Table 5.4 is applied on either side of the upper fracture zone. a) σ_f and SP with no smoothing filter and b) raw σ_f and smoothed SP, using an SG filter sampling window of 2.2 days.

The results of the sensitivity analysis are explored further in Figure 6.6, which shows the saline front near the borehole and changes in SP (relative to the steady state model) immediately prior to seawater intrusion. In each case, the saline front within the upper fracture zone lies $<$ 1 m laterally from the base of the borehole, on its seaward side. Figures 6.6a-b, which represent the initial, best-fit model, show how the SP gradient in the borehole is affected ahead of the saline front within the upper fracture zone. When a static front is then applied to the lower fracture zone, changes to the vertical SP gradient occur directly above the saline front within the upper fracture zone, with minimal changes ahead of it (Figures 6.6c-d), thereby giving no clear precursor (as shown in Figures 6.3e-f). When the best-fit model is modified by applying a constant value of η across the lower fracture zone, changes in the vertical SP gradient lag behind the saline front in the upper fracture zone (Figures 6.6e-f). Finally, by applying a change in η across the upper instead of lower fracture zone and implementing a static front in the lower fracture zone, the changes in SP are almost identical to those seen in the best-fit model.

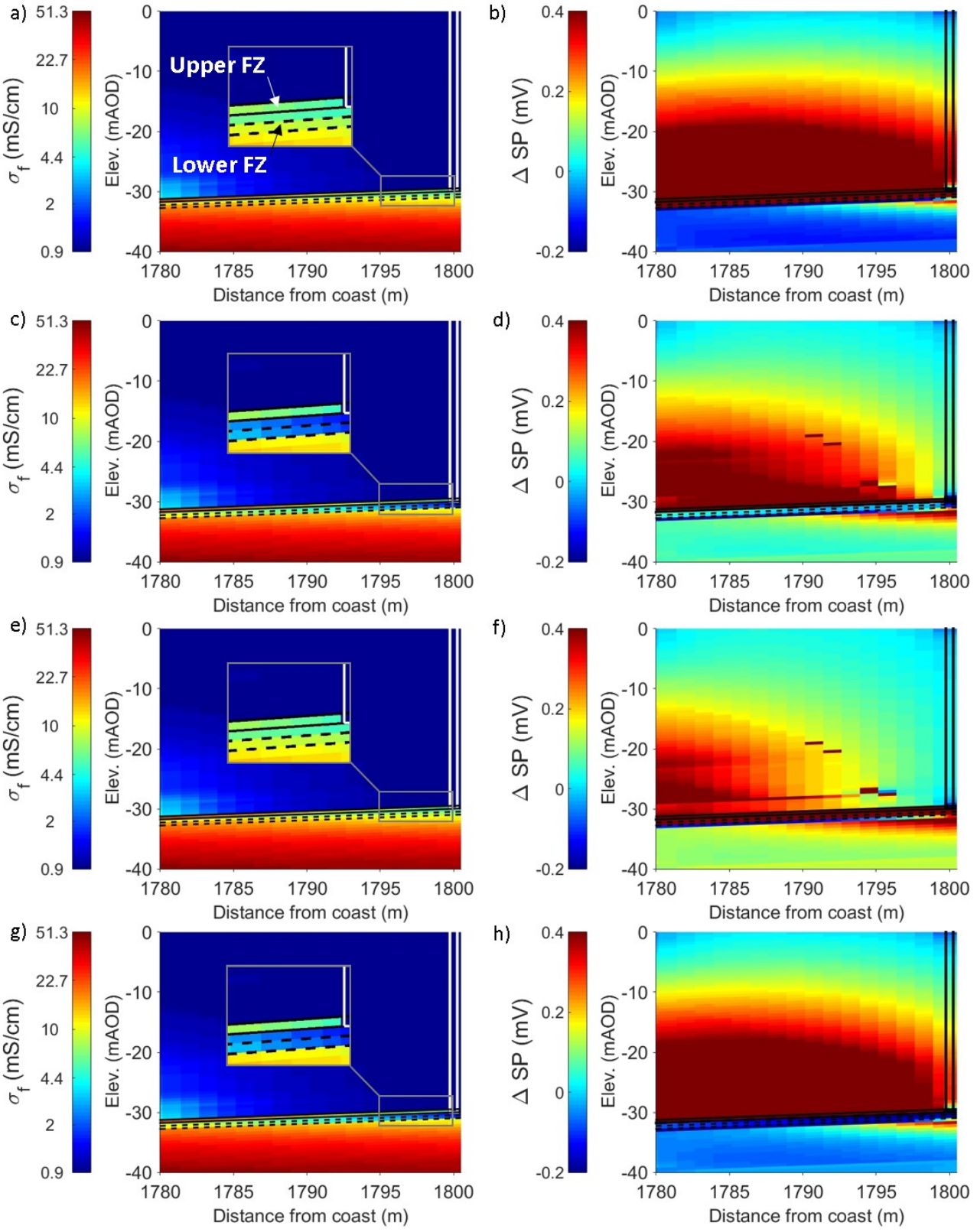

Figure 6.6: Modelled distributions of σ_f (a,c,e,g) and changes in SP relative to initial conditions (b,d,f,h) immediately prior to saline breakthrough (t = 14.2 days). a-b) best-fit model, with a dynamic lower fracture zone intersecting strata of differing η; c-d) as a-b), with a static saline front in the lower fracture zone; e-f) as a-b) with $\eta = 0.01$ on both sides of the lower fracture zone; and g-h) as a-b), with static lower fracture zone and change in η across upper fracture zone. The outlines of the borehole (solid lines), the upper fracture zone (solid lines) and the lower fracture zone (dashed lines) are also shown. The limits of the ΔSP colour scale have been curtailed to emphasise changes in SP within the borehole.

Interestingly, local changes to η near each fracture zone have little effect on the initial SP gradient (Figure 6.7), despite their obvious importance for the precursor.

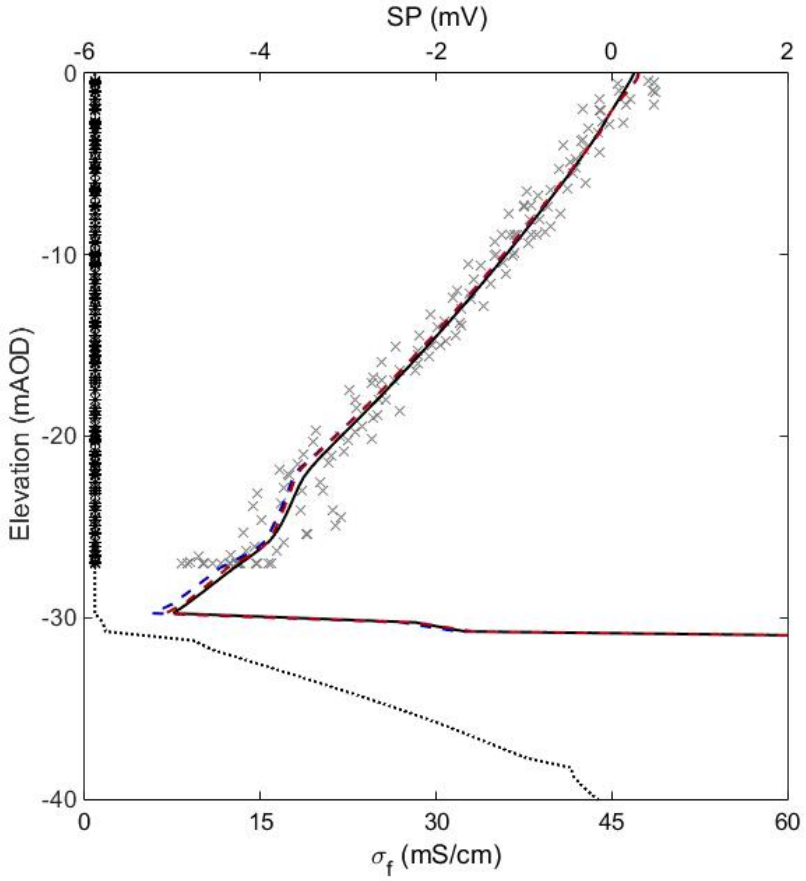

Figure 6.7: Comparison of initial SP gradients in the model when applying different values of η across the lower fracture zone (black line), different values of η across the upper fracture zone (dashed red line) and a single value of $\eta = 0.01$ across both fracture zones (dashed blue line). Modelled σ_f (dotted black line), observed SP (grey crosses) and observed σ_f (black asterisks) on 15 August 2013 are also shown.

6.4 Discussion and conclusions

Based on the model results in this chapter, the precursor reflects the interaction of the saline front with different η values as it moves through the aquifer. As shown in Figure 6.5, the source of the precursor could be the main conduit for seawater entering the borehole. However, the precursor may also be a response to the movement of seawater beneath the borehole (Figure 6.3). It is notable that only the latter scenario replicates the observed magnitude of tidal SP fluctuations.

In the latter scenario, the precursor does not directly reflect an advancing saline front that will enter the borehole. However, geophysical logging and hydraulic testing (e.g. Butler et al., 2009; Gallagher et al., 2012; Jones and Robins, 1999) suggest that there are typically numerous hydraulically significant fractures within the upper 100 m of the Chalk. Saline intrusion in the Chalk (and other fractured coastal aquifers) may therefore be characterised by saline water filling progressively shallower fracture zones. Thus, the arrival of higher salinity groundwater immediately beneath the borehole would be a strong, although indirect, indicator of imminent breakthrough into the borehole itself. Although this model has been developed to simulate SP in the vicinity of a coastal groundwater observation borehole, the upconing of saline water that typically occurs prior to intrusion in abstraction boreholes (see Figure 3.2) lends greater significance to this latter scenario.

The key factor in both cases is the exclusion efficiency η on either side of hydraulically significant fractures that transport seawater inland. By contrast, the baseline SP gradient discussed in Section 5 is not affected significantly by such local variations in η (Figure 6.7). This has profound implications for SP monitoring as a predictor of saline intrusion, as it suggests that the likely existence and nature of a precursor cannot be established in advance through profiling of the borehole. As such, alternative methods would be needed to understand whether a precursor will occur. An obvious strategy would be to monitor the SP response during an initial intrusion event and use this to indicate future occurrences. However, this may not be feasible for sensitive abstraction boreholes where the intention is to avoid intrusion in the first place. Another approach may be to characterise the likely distribution of η values adjacent to and immediately beneath the borehole, based on a broader understanding of the local lithostratography and with a particular focus on the locations of hydraulically significant fractures. In the case of an abstraction borehole, where upconing of saline water is likely to occur (Figure 3.2), estimates of η may be required over a greater depth range beneath the borehole.

At present, there are very few data on η across all aquifers, and each measurement of η in the Chalk has been taken from a different location; hence, the prevalence and magnitude of small-scale variations in η near a single borehole is unknown. Other parameters, such as clay content and permeability, are highly variable in the Chalk (and in many other aquifers) over

distances of only a few mm. Consequently, there are grounds for optimism that variations in η are also common and so SP precursors to seawater intrusion may indeed be widespread. Clearly, further data collection is required to assess how η varies with depth and with changes in lithology and ultimately, to understand the likelihood of precursors being present in other boreholes. To address some of the current data gap, the first measurements of η in marl samples are described in Chapter 8.

The focus in this chapter has been on the time-varying response of SP to impending seawater intrusion. However, as discussed in Section 4.5.3, analysis of SP in the frequency domain may contribute to a greater understanding of movements of the saline front, a concept initially proposed by MacAllister et al. (2016). The tidal component of SP is of particular interest in this regard, given the differing magnitudes of tidal oscillations produced under different model scenarios. Tidal SP oscillations are investigated further in the following chapter.

Chapter 7

Changes in the SP power spectrum prior to saline intrusion

7.1 Introduction

In Section 4.5.2, it was shown that the self-potential (SP) gradient within the Saltdean OBH reduces several days prior to saline water entering the borehole and that this may represent an early warning system for saline intrusion. By focusing on a period of a few weeks around the time of intrusion, this precursor signal can be seen clearly (Figure 4.14). Although this can be done in retrospective analysis of intrusion events, using SP as a predictive tool would require analysis of longer-term datasets, with a focus on SP changes throughout any given summer, when the water table is typically low and the risks of seawater intrusion are greatest.

Viewed within a longer-term dataset of this type, the precursor is not apparent in the raw SP data (Figure 7.1a), although it can be distinguished more clearly after applying a Savitsky-Golay smoothing filter (Figure 7.1b). However, given the fluctuations in SP over the course of a typical summer, due to electrode drift and contributions from a variety of current sources, it may prove difficult to distinguish the precursor 1 day prior to intrusion, as shown by Figure 7.1c. The motivation for this chapter is to assess whether other aspects of the SP data from the Saltdean OBH may be clearer indicators of impending seawater intrusion.

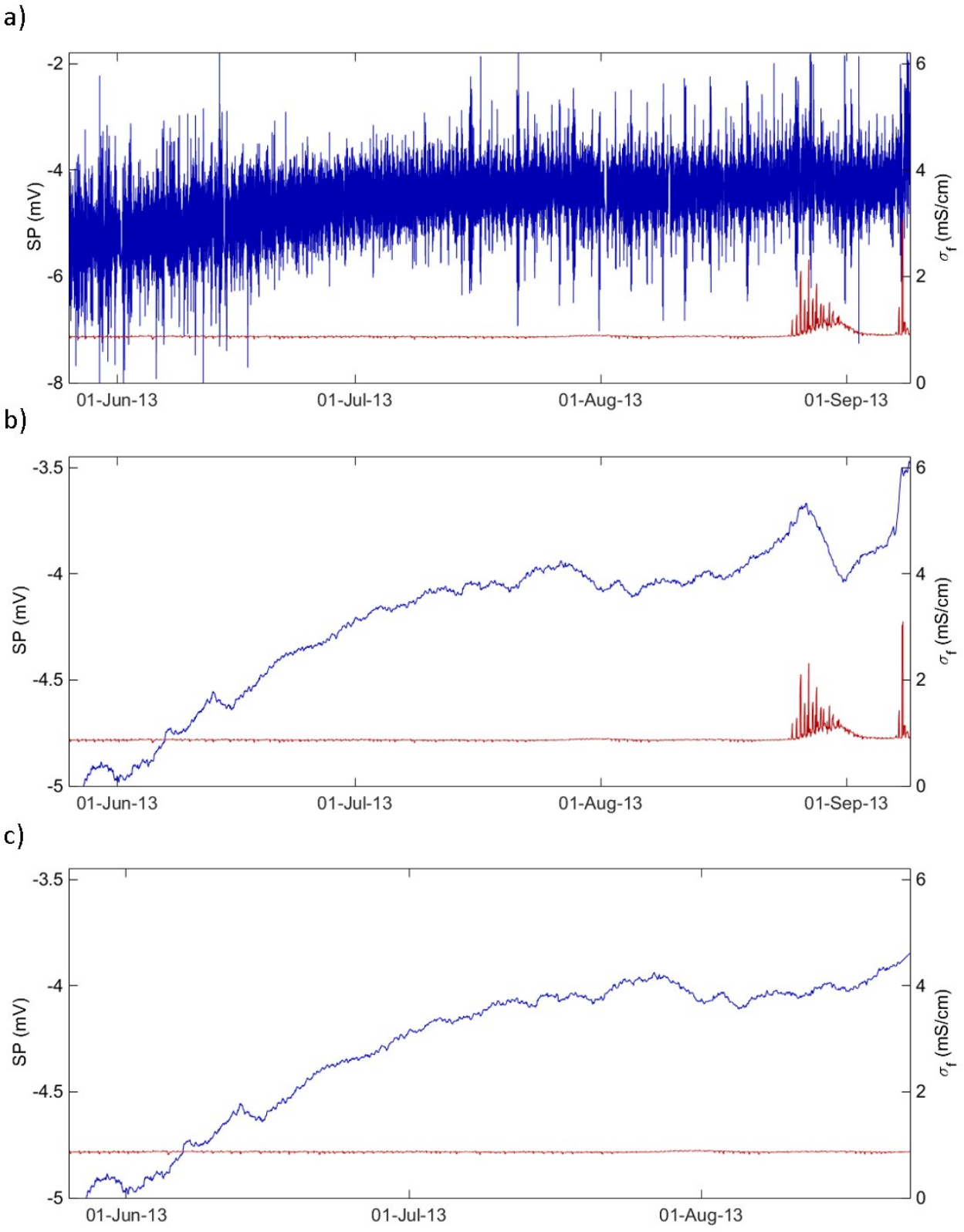

Figure 7.1: Variations in SP (blue lines) within the Saltdean OBH plotted against σ_f (red lines) in summer 2013, shown as a) raw SP data b) filtered using an SG filter with a 2.2 day sampling window and c) filtered using an SG filter with a 2.2 day sampling window and curtailed 1 day prior to seawater intrusion.

MacAllister et al. (2016) showed that the power spectrum of SP at Saltdean (covering a single period of 3 months) closely matches the power spectrum of oceanic tides measured at Newhaven, including a dominant peak corresponding to the semidiurnal M_2 tidal mode (see Sections 3.5 and 4.5.3). This was the first published study to show that oceanic tides can exert a measurable influence on SP in coastal boreholes. However, MacAllister et al. (2016) did not investigate temporal changes in the Saltdean OBH power spectrum and, to date, there has been no assessment of whether the characteristics of the borehole power spectrum change in the lead up to saline intrusion. This chapter will analyse the evolution of the SP power spectrum in the Saltdean OBH during the summers of 2013 and 2014. Numerical modelling will be used to investgate the cause of any changes in SP prior to saline breakthrough.

7.2 Observed changes in SP power spectra in the Saltdean OBH

From Figure 4.5 it is apparent that marine tides at the coast strongly influence water levels in the Saltdean OBH and there is a significant semidiurnal peak in both power spectra. Figure 6.1 shows that the amplitude of marine tides varies over the course of each spring-neap tidal cycle, with a period of 14.8 days, although smaller variations over a 29.6 day cycle are also evident.

To assess trends in SP prior to intrusion and remove the effects of periodic fluctuations, the Lomb-Scargle method (Lomb, 1976; Scargle, 1982) was used to analyse the power spectral density (PSD) of SP for a series of spring-neap tidal cycles throughout the summer of 2013 and 2014, each with a duration of 14.8 days (Figure 6.1). As an example, the PSD of the spring-neap cycle ending on 8 September 2014 (immediately prior to the first major intrusion event in Figure 4.14b), is compared to the PSD from 14.8 days earlier in Figure 7.2. Given the short timeframe for each PSD, there is insufficient resolution to pick out individual tidal components (Table 3.1). However, there is a clear reduction in the magnitudes and significance of semidiurnal SP oscillations, accompanied by a slight reduction in the magnitude and significance of diurnal oscillations.

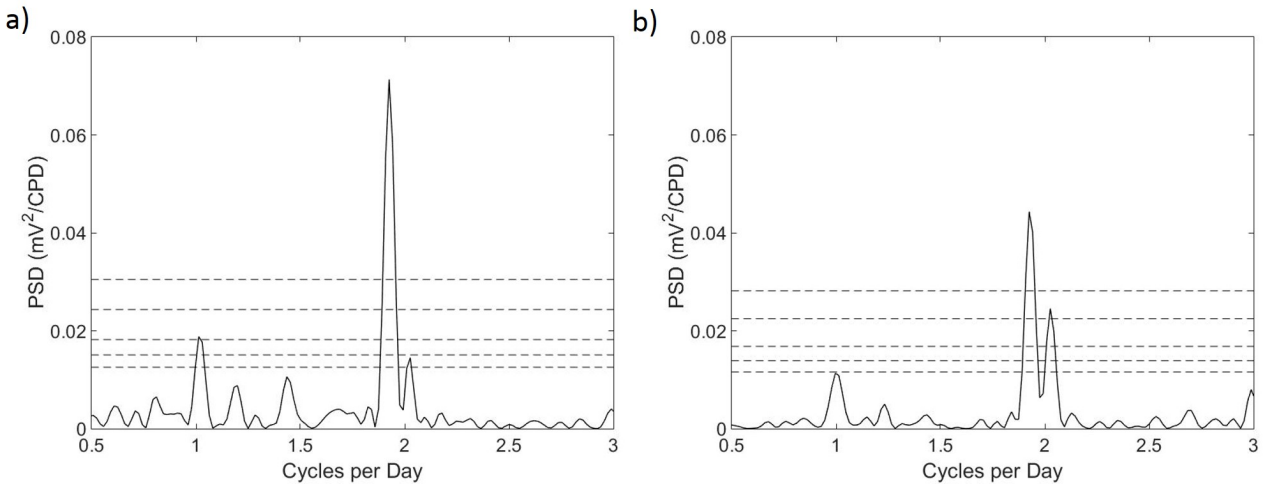

Figure 7.2: Lomb-Scargle PSD of SP during the spring-neap tidal cycle ending a) on 24 July and b) prior to intrusion on 8 September 2014. Dashed lines show the probabilities of detection at 50%, 90%, 99.99% and 99.9999% significance.

Plotting the magnitude of semidiurnal fluctuations over time, there is a sharp reduction in SP oscillations immediately prior to the major intrusion events in both 2013 and 2014, while there is also a decrease in magnitude before the minor intrusion event in August 2014 (Figure 7.3).

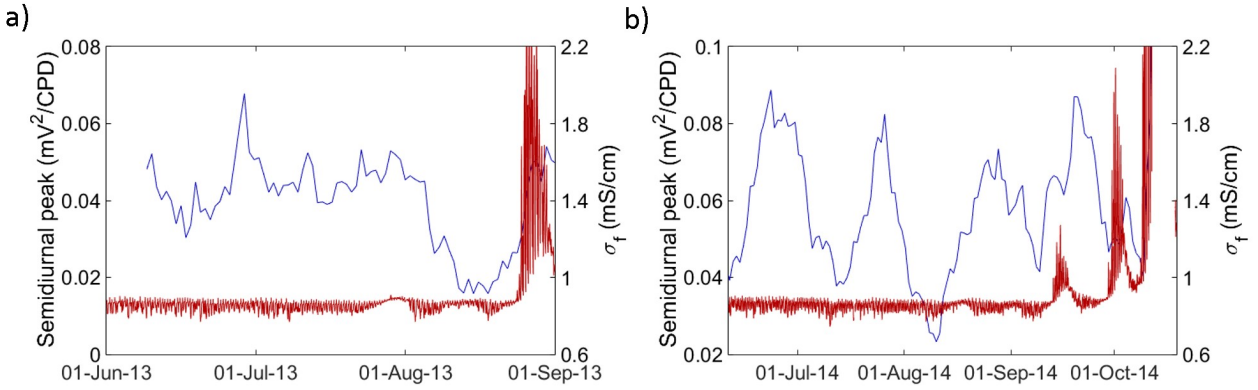

Figure 7.3: Variations in the magnitude of the semidiurnal PSD peak of SP in the Saltdean OBH (blue lines) and variations in borehole σ_f (red lines) in a) 2013 and b) 2014.

It is also important to note the presence of reductions in semidiurnal oscillations earlier in 2014 and these cannot be linked to an impending intrusion event. Given the wide range of source mechanisms for SP (Jouniaux et al., 2009) (see Section 2.2), the transient variations shown in Figure 7.3 are likely to represent the contribution of multiple processes. In order to understand the role that impending saline intrusion might play, it is important to consider the range of possible sources that exist.

7.2.1 Possible sources

Changes in borehole salinity could be considered the most obvious source of SP fluctuations in a coastal borehole, although the transient SP model described in Chapter 6 suggests that tidal SP oscillations can occur in the absence of variations in borehole σ_f. As shown by the PSD plots in Figure 7.4, semidiurnal σ_f oscillations in the borehole increased prior to intrusion in 2014, despite a clear reduction in semidiurnal SP fluctuations over this period. If the apparent reduction in semidiurnal SP oscillations is a reliable indicator of impending seawater intrusion, it cannot be attributed to changes in borehole σ_f.

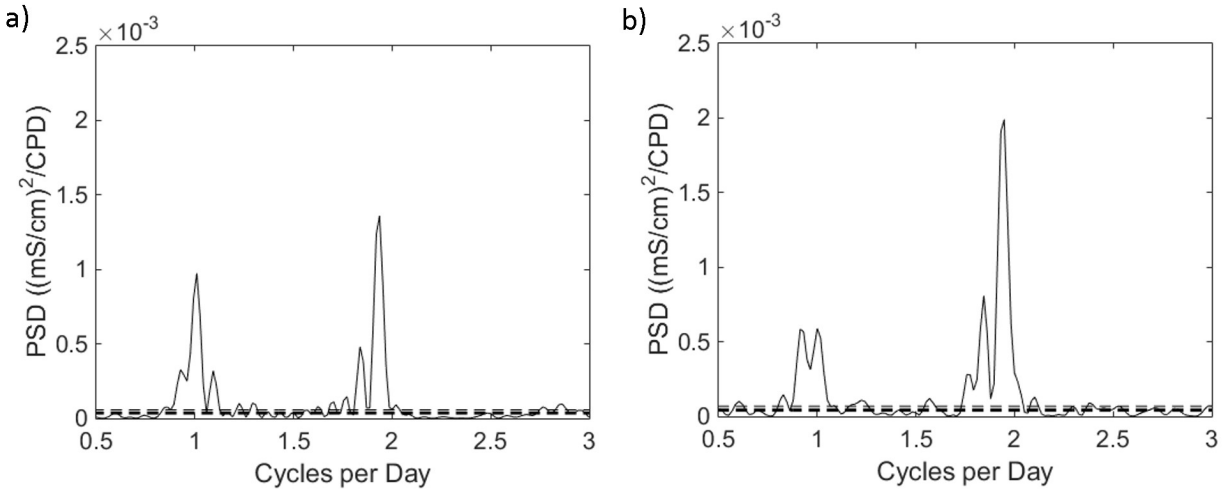

Figure 7.4: Lomb-Scargle PSD of σ_f in the Saltdean OBH during the spring-neap tidal cycle ending a) on 24 August 2014 and b) prior to intrusion on 8 September 2014. Dashed lines show the probabilities of detection at 50%, 90%, 99.99% and 99.9999% significance. These plot on top of each other at the scale shown.

Groundwater level fluctuations represent another possible source of the semidiurnal and diurnal SP signals and the PSD of water levels in the Saltdean OBH (Figure 4.5a) shows peaks at both frequencies. As well as pressure variations driving a ∇V_{EK} signal, associated movement of the saline front could generate a significant contribution from ∇V_{EED}, as discussed by MacAllister et al. (2016) (see Section 4.5.3).

Prior to the 2014 intrusion event, there was a slight reduction in semidiurnal water level fluctuations in the Saltdean OBH (Figures 7.5a-b) and this appears to be linked to a similar decrease in tidal oscillations at the coast (Figures 7.5c-d). However, the magnitude of these

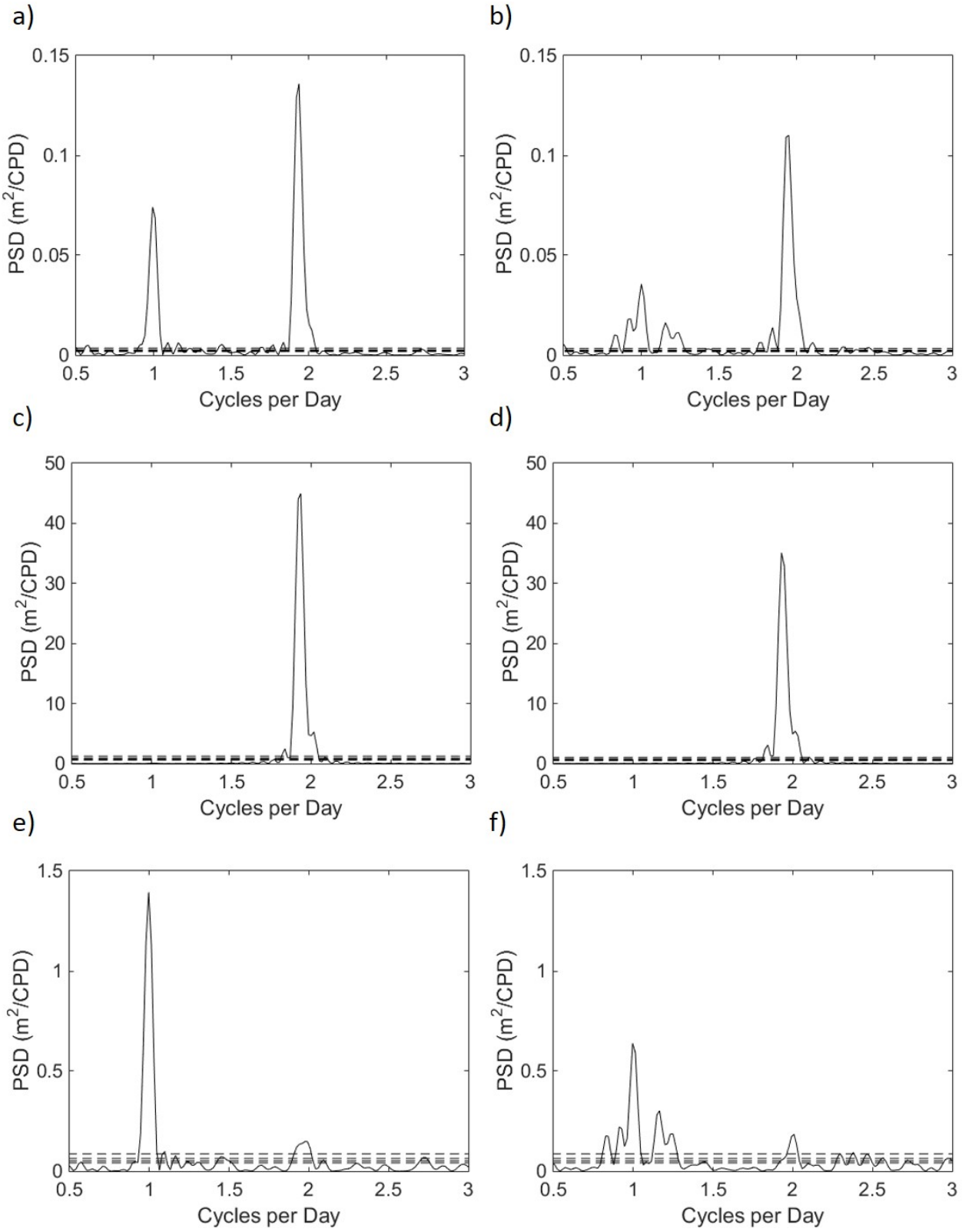

Figure 7.5: Lomb-Scargle PSD of water level variations during the spring-neap tidal cycle ending a) in the Saltdean OBH on 24 August 2014 and b) prior to intrusion on 8 September 2014 c) at Newhaven on 24 August 2014 and d) prior to intrusion on 8 September 2014 and e) at the Balsdean PS on 24 August 2014 and f) prior to intrusion on 8 September 2014. Dashed lines show the probabilities of detection at 50%, 90%, 99.99% and 99.9999% significance. These plot on top of each other at the scale shown.

changes appears small compared to the reduction in semidiurnal oscillations seen in the SP data (Figure 7.2). The reduction in the diurnal component of the signal appears to be driven by similar changes at the Balsdean PS (Figures 7.5e-f) and is likely due to changes in the daily abstraction regime.

Figure 7.6 shows variations in the magnitude of the semidiurnal peak for water level and SP variations in the Saltdean OBH. There is a particularly strong correlation between the two datasets in late summer, prior to seawater intrusion occurring. The weaker correlation in early summer suggests that water level variations are not the sole cause of the observed changes in the SP power spectra, although it is likely that they contribute to changes in other sources of electrical current in the vicinity of the borehole.

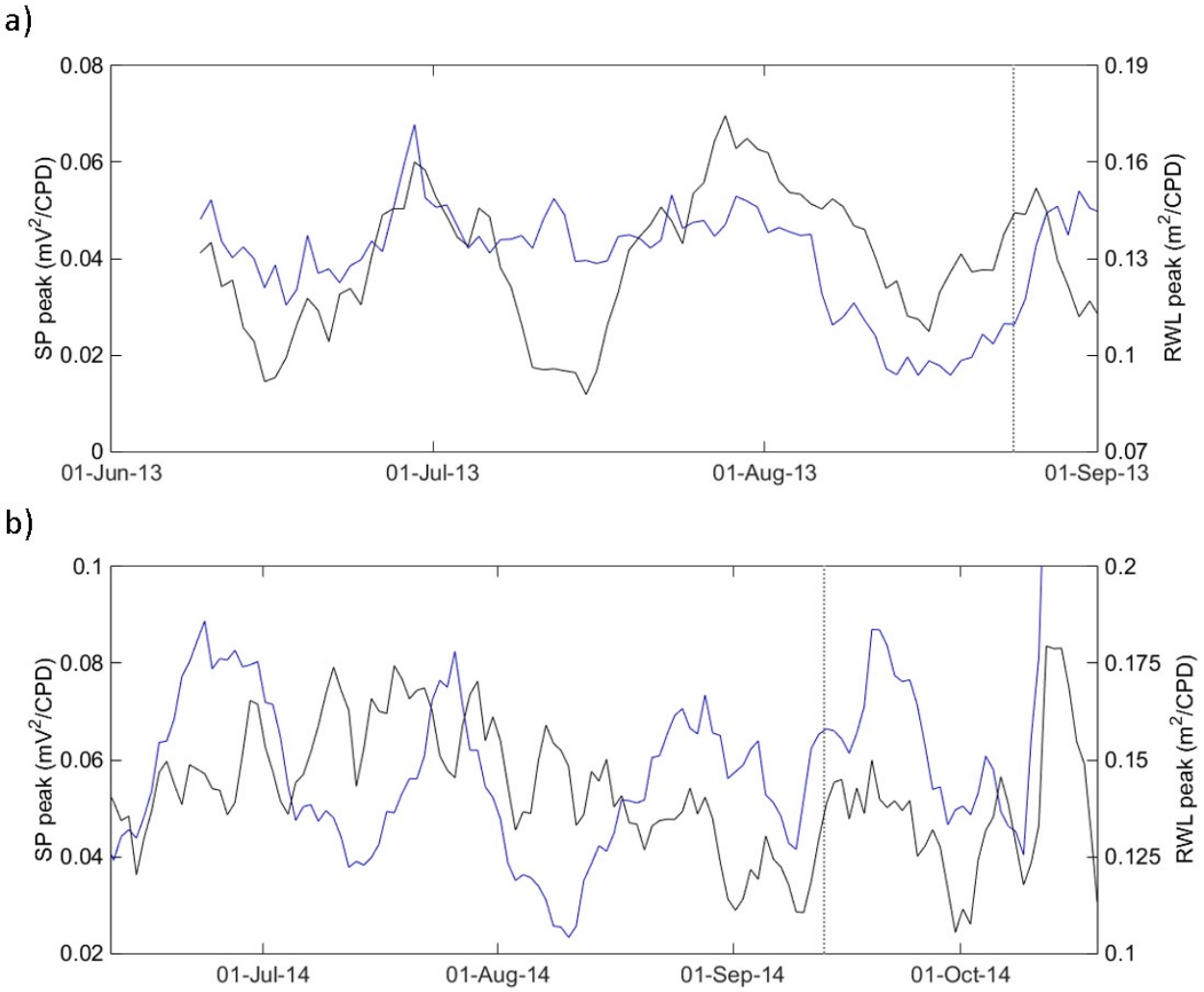

Figure 7.6: Magnitude of the semidiurnal PSD peaks in water level (black lines) and SP (blue lines) in the Saltdean OBH during a) summer 2013 and b) summer 2014. Vertical grey lines mark the onset of the first saline intrusion events in each summer.

MacAllister et al. (2016) showed that telluric currents, driven by changes in the earth's magnetic field, exert a measurable influence on the long-term SP power spectra at Saltdean, although these effects were only evident when referencing electrical potentials within the borehole to near-surface soil electrodes. Variations in the geomagnetic field measured at the Hartland observatory in Devon (BGS, 2018b), which is the closest geomagnetic observatory to Saltdean, are shown in Figure 7.7. The strength of semidiurnal oscillations reduces substantially prior to seawater intrusion in the horizontal component of the magnetic field B_H and this may contribute to the observed changes in the SP power spectra in Figures 7.2 and 7.3.

Figure 7.8 shows how the magnitude of the semidiurnal and diurnal peaks in B_H at Hartland and SP in the Saltdean OBH vary over time. There appears to be a weak correlation in some parts of the dataset, and at times the SP signal seems to lag behind the geomagnetic data. As discussed in Section 2.2.3, phase differences of up to 45° typically occur between magnetic fields and the resulting electrical fields that are induced in the subsurface. There also appears to be a greater degree of correlation between the signals around the time of intrusion, although this effect is less clear than the apparent link between SP and water levels in the borehole, shown in Figure 7.6.

It is interesting to note that both the Saltdean and Hartland sites lie close to the coast (Figure 7.9) and, as suggested by MacAllister et al. (2016), the geomagnetic field measured at Hartland is likely to be influenced by the ocean dynamo effect (see Section 2.2.3), which contributes significantly to the semidiurnal component of the magnetic field (Malin, 1970). It is clear that marine tidal oscillations, as measured at Newhaven (7 km to the southeast of the Saltdean OBH), strongly influence water levels in the Saltdean OBH, which in turn are strongly correlated with variations in SP. As such, it is perhaps unsurprising that there is an apparent link between the semidiurnal oscillations in magnetic field at Hartland and semidiurnal oscillations in SP within the Saltdean OBH. As discussed in Section 2.2.3, the relationship between geomagnetic and electrical fields is highly complex and quantifying the effect of telluric currents on SP is beyond the scope of this thesis.

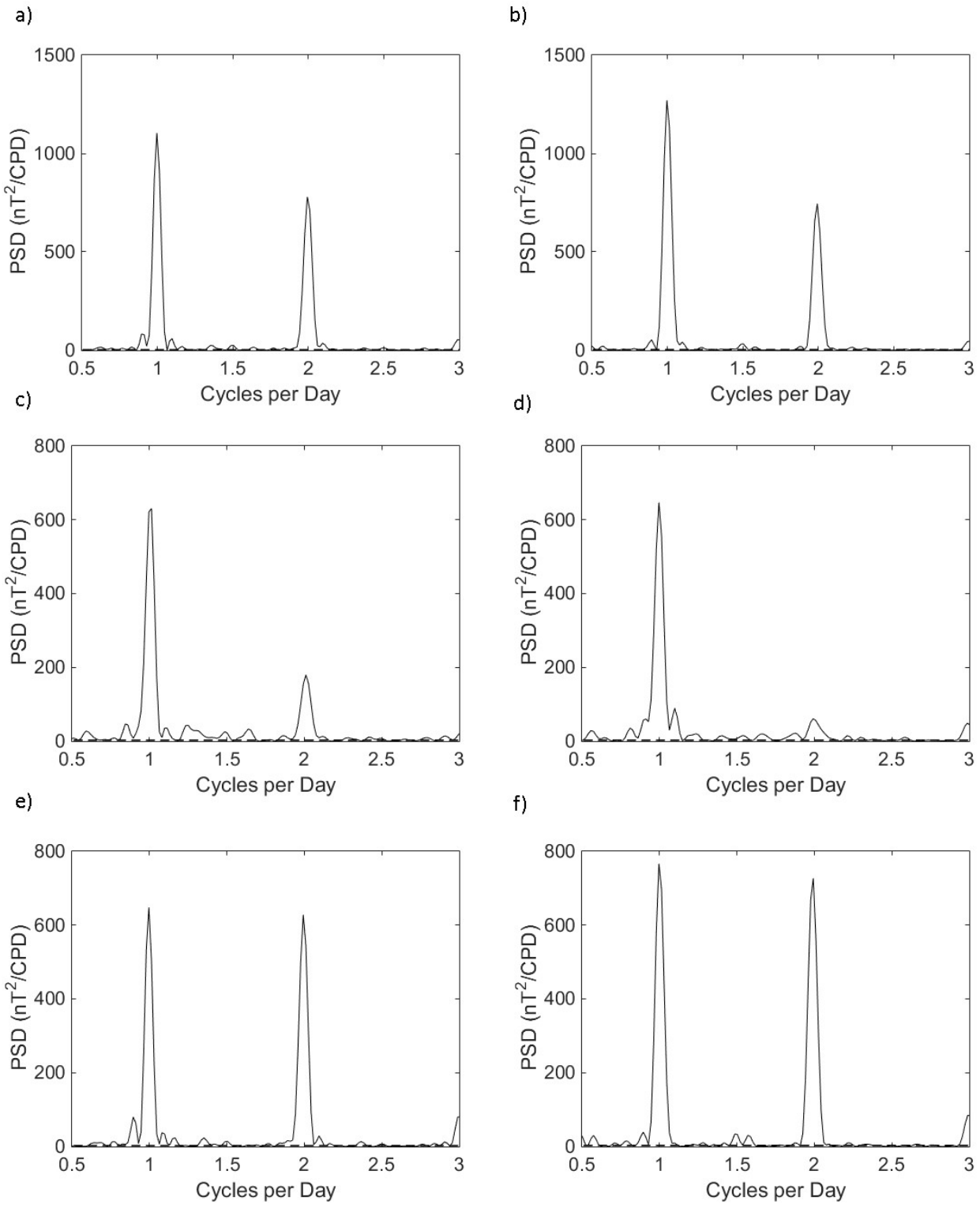

Figure 7.7: Lomb-Scargle PSD of a) total geomagnetic field during the spring-neap tidal cycle ending on 24 August 2014 and b) prior to intrusion on 8 September 2014 c) the horizontal component of the geomagnetic field during the spring-neap tidal cycle ending on 24 August 2014 and d) prior to intrusion on 8 September 2014 and e) the vertical component of the geomagnetic field during the spring-neap tidal cycle ending on 24 August 2014 and f) prior to intrusion on 8 September 2014. Dashed lines show the probabilities of detection at 50%, 90%, 99.99% and 99.9999% significance. These plot on top of each other, close to the x-axis, at the scale shown.

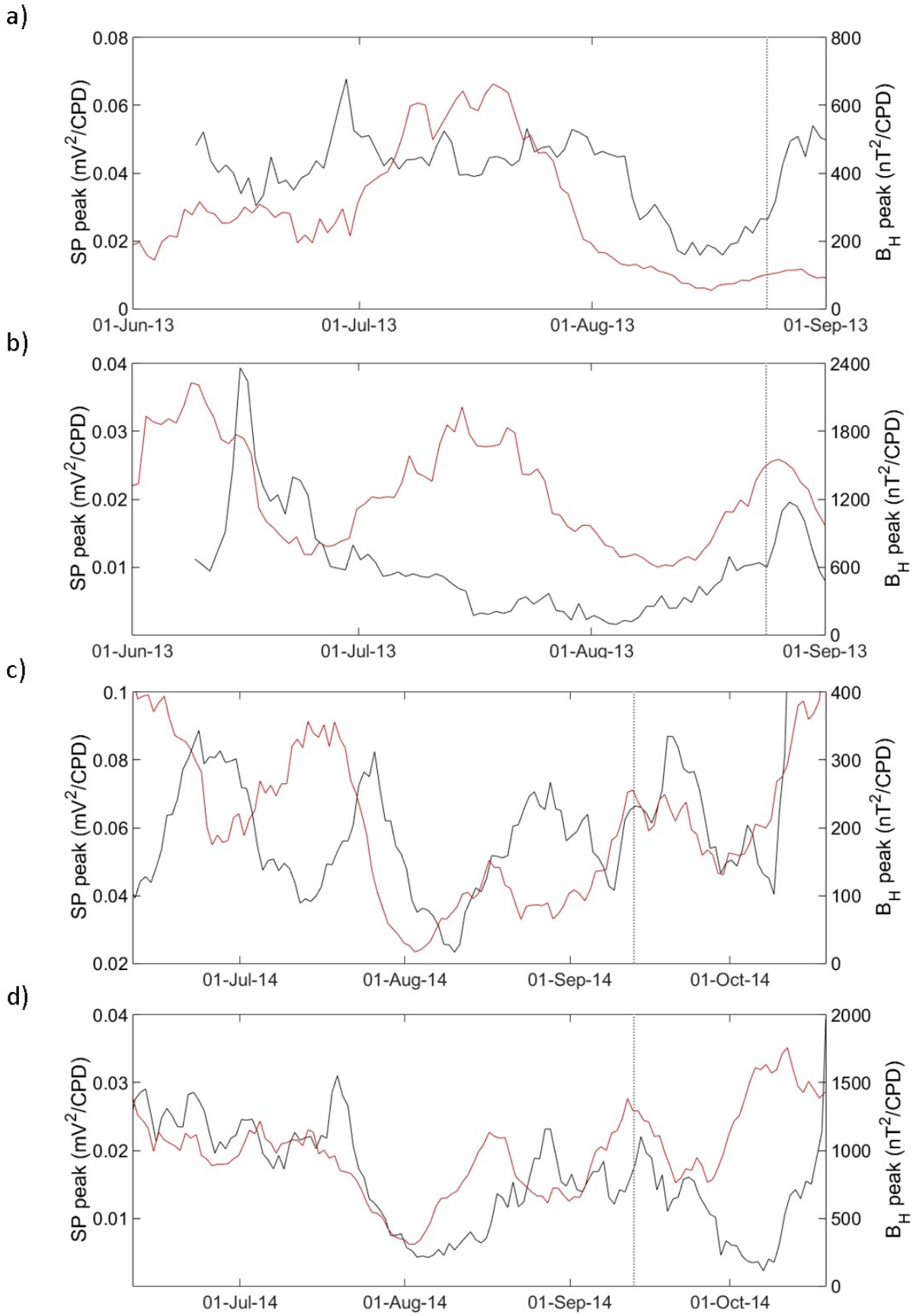

Figure 7.8: Magnitude of the a) semidiurnal and b) diurnal PSD peaks in summer 2013 and c) the semidiurnal and d) diurnal PSD peaks in summer 2014 for B_H at Hartland (solid red lines) and SP in the Saltdean OBH (solid black lines). The onset of the first saline intrusion events in each summer are marked by vertical dotted grey lines.

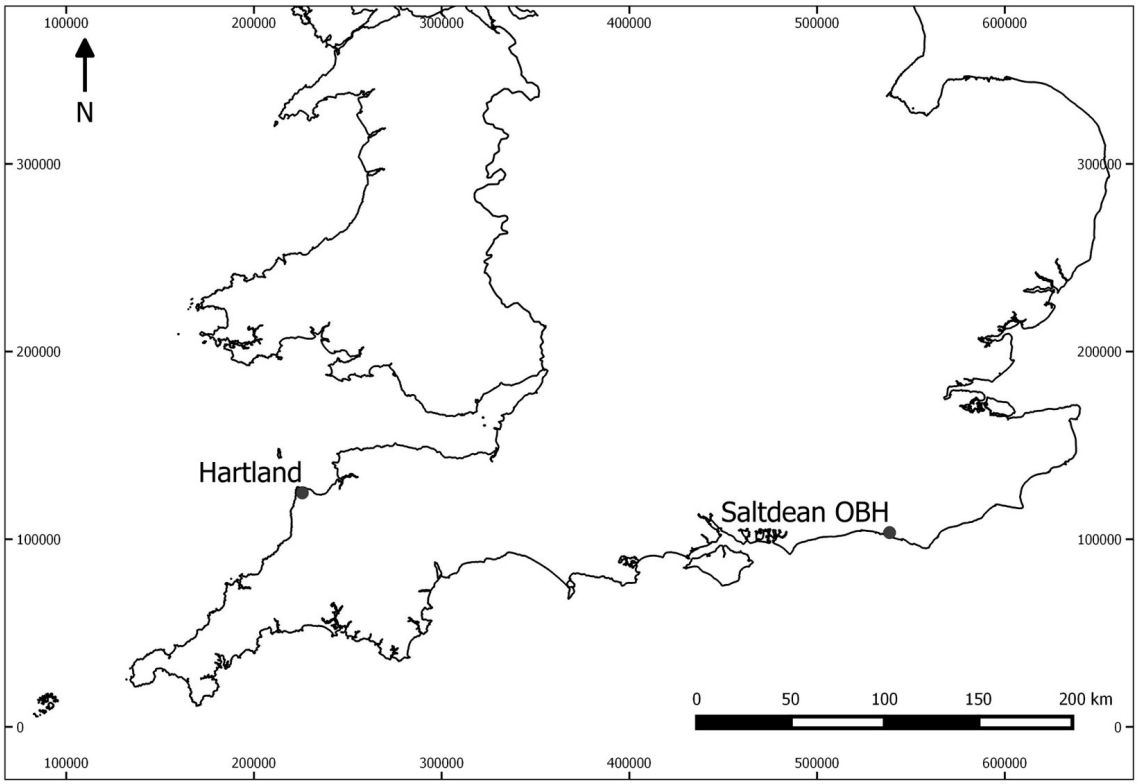

Figure 7.9: Map showing the locations of the Saltdean OBH and the Hartland Geomagnetic Observatory relative to the coast.

Temperature is another known source of SP (e.g. Jouniaux et al., 2009; Leinov and Jackson, 2014), although the changes in the semidiurnal part of the temperature PSD (Figure 7.10) are minimal compared to the changes observed in Figure 7.2.

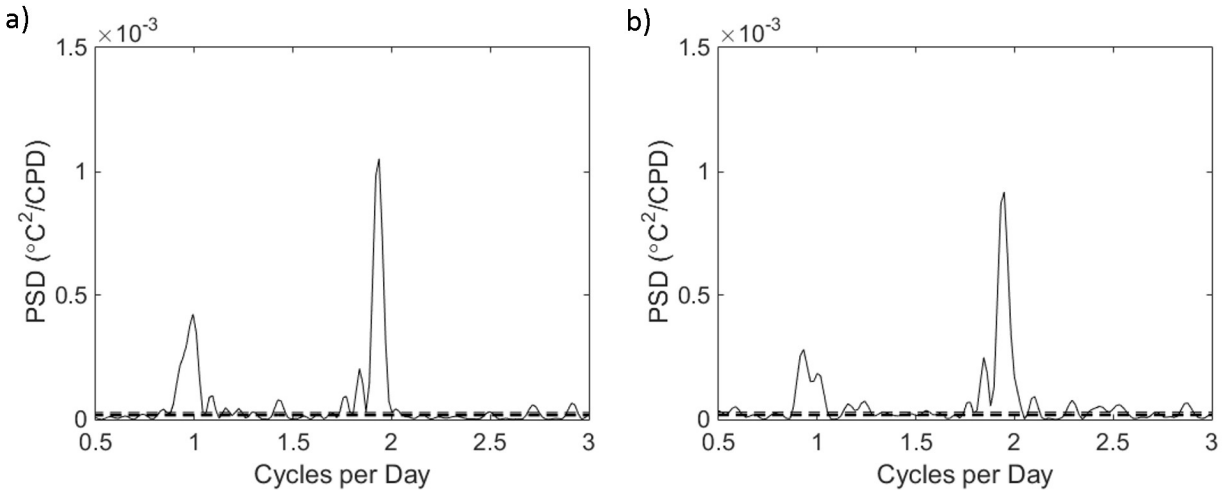

Figure 7.10: Lomb-Scargle PSD of temperature in the Saltdean OBH during the spring-neap tidal cycle ending a) on 24 August 2014 and b) prior to intrusion on 8 September 2014. Dashed lines show the probabilities of detection at 50%, 90%, 99.99% and 99.9999% significance. These plot on top of each other at the scale shown.

Temperature is unlikely to contribute significantly to the changes in SP power spectra observed prior to intrusion and this is consistent with previous findings by MacAllister et al. (2016), who found that temperature variations did not significantly influence the long-term SP power spectrum at Saltdean.

Discussion

Based on the above analysis of possible sources, water levels in the borehole are most closely correlated with the observed pattern of SP in Figure 7.3. The fact that this correlation is strongest around the time of saline intrusion in late summer suggests that tidal movements of the nearby saline front, driven by water level fluctuations, may be the ultimate driver of the observed changes in the SP power spectrum. To develop a greater understanding of whether this mechanism could be responsible for the observed changes in SP, the model described in Chapters 5 and 6 is revisited.

7.3 Modelling tidal oscillations in SP

7.3.1 Introduction

The model results in Figures 6.3 and 6.5 indicate that semidiurnal oscillations in SP at the Saltdean OBH are controlled by the movement of saline water within fractures near the borehole. As the movement of saline water is ultimately driven by variations in groundwater head, this may also explain why there is such a strong correlation between semidiurnal fluctuations in water level and SP in the borehole prior to intrusion.

In Chapter 6, two models were presented that match the observed reduction in SP gradient, or precursor, prior to saline breakthrough. These models require a change in the exclusion efficiency η (Section 2.2.2) across either the upper or lower fracture zones shown in Figure 4.2. The results for the former case, the *upper FZ model* (Figure 6.5a) appear to show an increase

in tidal SP oscillations prior to breakthrough, in contrast to the observed reduction indicated by Figures 7.2 and 7.3. As such, the primary focus of the analysis will be on the latter *lower FZ model*, in which SP changes are controlled by the movement of saline water in the lower fracture zone, due to local changes in η.

From Equation (2.7) and assuming a minimal contribution from ∇V_{EK} (as indicated by Figure 5.4a), SP variations are controlled by changes in $\nabla ln(C_f)$. A plot of $ln(C_f)$ along the lower fracture zone of the steady state model described in Chapter 5 suggests that the magnitude of $\nabla ln(C_f)$ decreases towards the coast (Figure 7.11). As the saline front moves inland beneath the borehole (at x = 1800 m), the magnitude of tidal SP oscillations might be expected to decrease as a result.

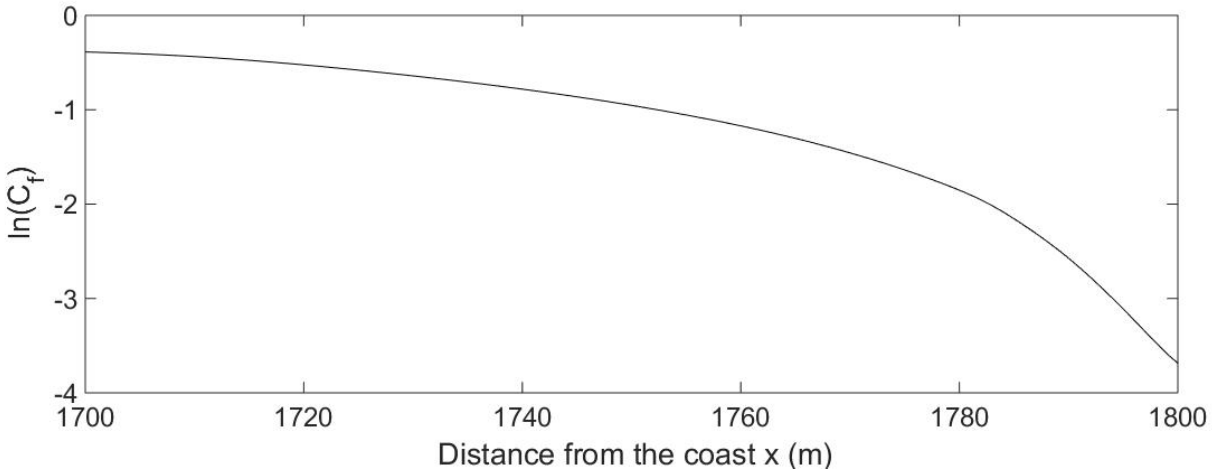

Figure 7.11: Plot of $ln(C_f)$ along the lower fracture zone for the steady state model.

7.3.2 Model description

To investigate the effects of saline intrusion on the SP power spectrum in more detail, the lower FZ model described in Chapter 6 was rerun. As the focus of the investigation is on changes in the power of the SP response to semidiurnal tidal fluctuations, spring-neap variations in the tidal cycle were removed from the model, giving the following equation for temporal variations in head h_{Nh} at the coast (based on Equation (6.1)):

$$h_{Nh} = 2.44\left[cos(\frac{2\pi t}{0.518})\right]. \tag{7.1}$$

For comparison, the same procedure was applied to the upper FZ model.

7.3.3 Results and sensitivity analysis

To assess the power of the semidiurnal SP fluctuations under normal conditions, a Lomb Scargle PSD was produced covering the first 14 tidal cycles in the upper and lower FZ models, from t = 0.19-7.44 days (Figure 7.12a). Model time steps prior to this were ignored, as there is a lag of 0.13 days between tidal oscillations at the coast and those in the borehole. As the first high tide at the coast occurs 0.06 days into the simulation, the first modelled tidal maximum in the borehole occurs at t = 0.19 days. A second PSD was produced for the 14 tidal cycles immediately prior to intrusion, from t = 6.40-13.65 days, as shown in Figure 7.12b.

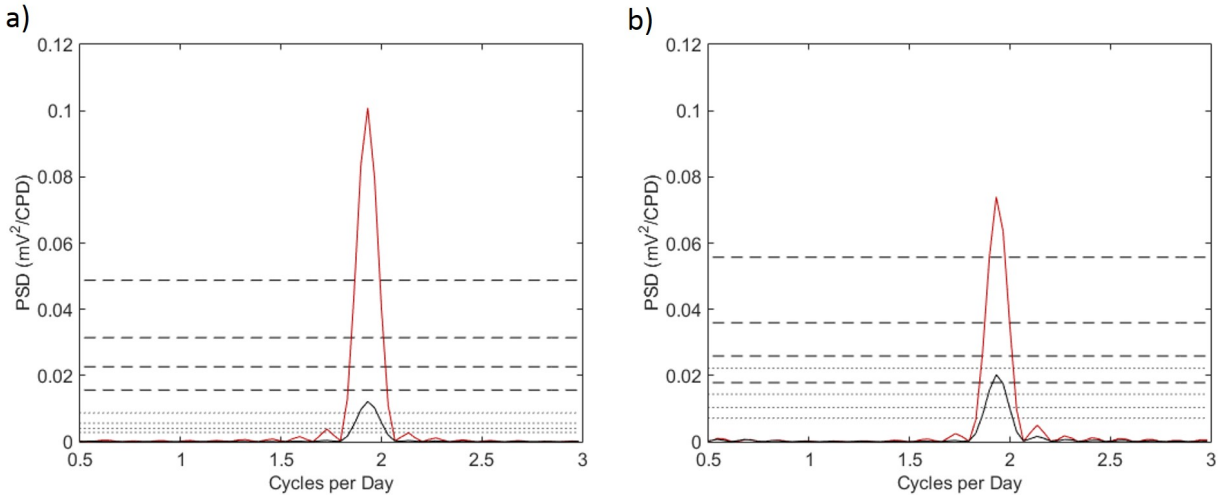

Figure 7.12: Lomb-Scargle PSD of SP for the upper (black lines) and lower (red lines) FZ models: a) t = 0.19-7.44 days and b) t = 6.40-13.65 days. Dashed lines show the probabilities of detection at 50%, 90%, 99.99% and 99.9999% significance for the lower FZ model; dotted lines show these significance levels for the upper FZ model.

As previously suggested by the results in Figure 6.5a, semidiurnal oscillations increase prior to intrusion in the upper FZ model. Furthermore, the magnitude of the semidiurnal peak is significantly lower than that shown in Figure 7.2. For the lower FZ model, there is a clear

reduction in the magnitude of the semidiurnal peak prior to intrusion, although the effect is less pronounced than that seen in the field data (Figure 7.2).

A possible source of error in the electrodynamic model relates to the dual porosity nature of the Chalk. The model described in Section 6 approaches the problem by assuming a low porosity within fracture zones in the hydrodynamic component ($\phi = 0.1$) to induce the rapid advance of the saline front associated with fracture flow, but a higher porosity ($\phi = 0.39$) in fracture zones within the electrodynamic component, to allow for sufficient electrical conductance within the relatively porous aquifer. However, this assumes that the high salinity water entering the fractures immediately fills the surrounding matrix and is likely to overestimate the bulk electrical conductivity in this part of the model domain.

To assess the impact of this assumption, a revised version of the model was produced, in which the fluid electrical conductivity within each fracture zone $\sigma_{f_{FZ}}$ is calculated using:

$$\sigma_{f_{FZ}} = \frac{\phi_{frac}\sigma_{f_{FZ0}} + \phi_{mat}\sigma_{f_{mat0}}}{\phi_{frac} + \phi_{mat}} \tag{7.2}$$

where ϕ_{frac} is the volume of void space due to fractures divided by the total volume of the fracture zone (0.1), $\sigma_{f_{FZ0}}$ is the original fluid electrical conductivity within the fracture zone derived from the hydrodynamic model for any given time step, ϕ_{mat} is the volume of void space in the matrix divided by the total volume of the fracture zone (0.39) and $\sigma_{f_{mat0}}$ represents fluid electrical conductivity in the matrix for the initial steady state model. This assumes that over the timescale of the transient model, there is negligible dispersion of salinity from the fractures to the adjacent matrix.

Semidiurnal oscillations in the upper FZ model still increase when the dual porosity approach is applied, as shown in Figure 7.13. However, the dual porosity formulation leads to a greater reduction in semidiurnal oscillations in the lower FZ model. Despite this, the initial SP gradient in the borehole is largely unaffected by applying the dual porosity method (Figure 7.14), as is the precursor (Figures 7.15a-b), which in both cases follows a similar pattern to that observed in the Saltdean OBH (Figures 7.15c-d).

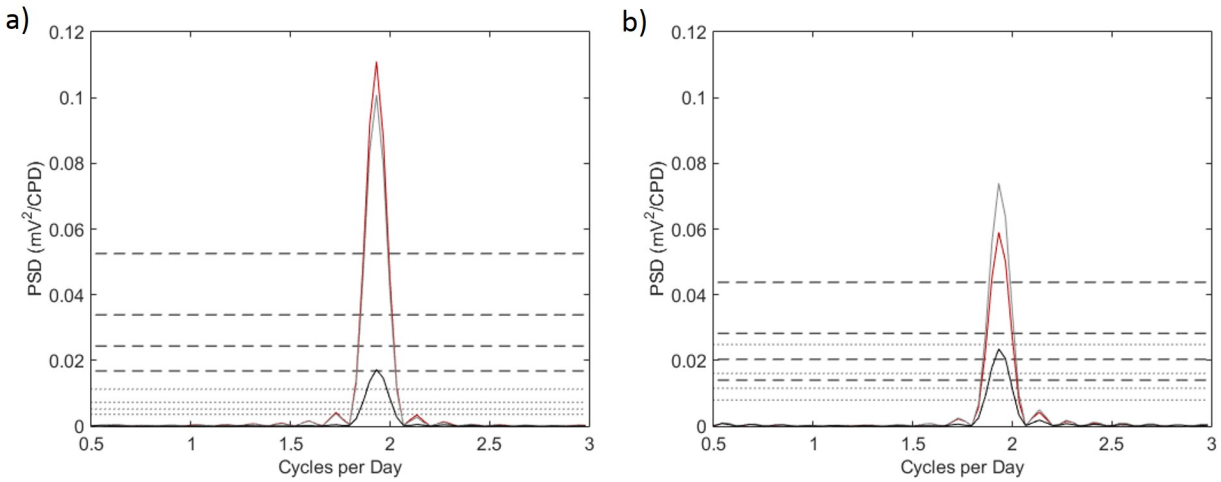

Figure 7.13: Lomb-Scargle PSD of modelled SP invoking dual porosity behaviour within both fracture zones for the upper (black lines) and lower (red lines) FZ model, compared to the original lower FZ model where a single value of σ_f is applied (grey lines) for: a) t = 0.19-7.44 days and b) t = 6.40-13.65 days. Dashed lines show the probabilities of detection at 50%, 90%, 99.99% and 99.9999% significance; dotted lines show these significance levels for the upper FZ model.

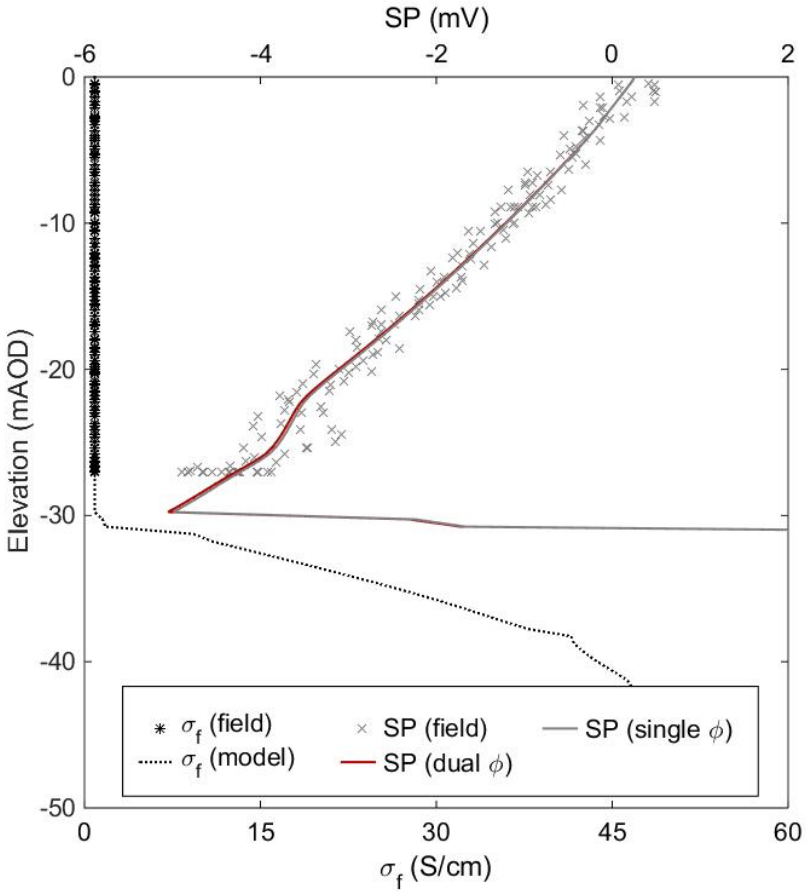

Figure 7.14: Comparison of initial SP gradients in the borehole for the single and dual porosity lower FZ models. Field SP measurements are also shown alongside field and modelled σ_f profiles.

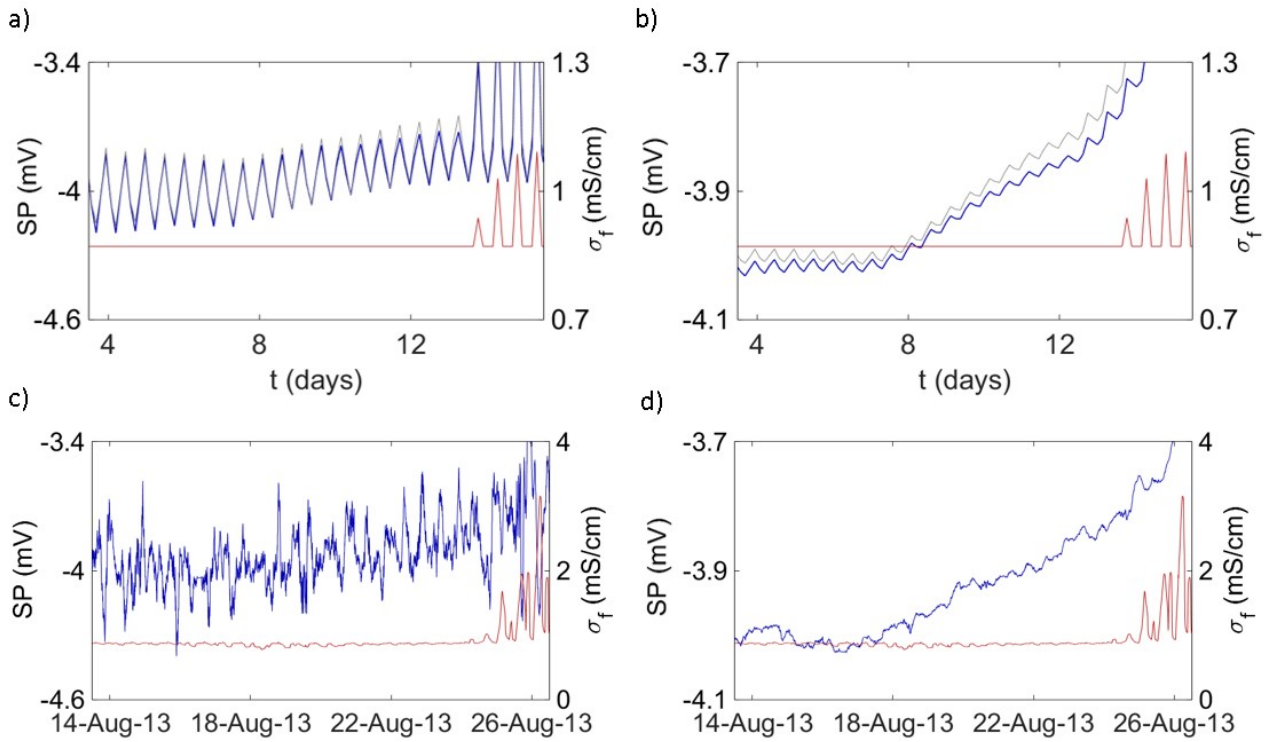

Figure 7.15: Transient SP prior to intrusion and σ_f (red lines) for a) the dual porosity (blue line) and single porosity (grey line) lower FZ models, including semidiurnal tidal variations b) the dual porosity (blue line) and single porosity (grey line) lower FZ models, smoothed using an SG filter with a sampling window of 2.2 days c) field SP data (blue line), smoothed using an SG filter with a sampling window of 105 minutes to reduce high frequency noise and d) field SP data (blue line), smoothed using an SG filter with a sampling window of 2.2 days.

7.4 Discussion and conclusions

Previous modelling results, shown in Figure 6.3, suggest that the movement of saline water within fracture zones near the Saltdean OBH is the main source of semidiurnal SP oscillations observed within the borehole. However, based on the results in Chapter 6, it is unclear whether the precursor is generated by the movement of saline water towards the borehole in the upper fracture zone, or beneath the borehole in the lower fracture zone. By investigating the tidal response of two separate models, it can be shown that the lower fracture zone is the more likely source of the observed changes in SP at Saltdean.

From Figure 7.11, one can infer that the strongest current source for this effect lies at the inland edge of the saline front. As the front progresses further inland, this source moves further from

the borehole and the model shows that the magnitude of semidiurnal oscillations reduces as a result. Sensitivity analysis on the model indicates that the size of this reduction is controlled by the electrical conductivity of the fracture zone. In other words, if the electrical conductivity in the fracture zone is reduced, the influence of the strongest source of SP oscillations on the borehole wanes.

It is apparent that several factors may contribute to the observed changes in the SP power spectrum for the Saltdean OBH, including changes in the pumping regime at the Balsdean PS, which is the most obvious control on diurnal fluctuations. However, the results of PSD analysis and modelling suggest that an approaching saline front can contribute to changes in the power of the semidiurnal SP signal prior to intrusion, as long as the front passes through regions of varying η (see Figures 6.3c and g). If the modelled front encounters varying η as it approaches the borehole, there is a slight increase in semidiurnal SP oscillations. If it intersects varying η as it passes beneath the borehole, a significant reduction in semidiurnal oscillations occurs, although the magnitude of this change depends on the rate at which saline water in fracture zones enters the surrounding matrix of the Chalk.

While PSD analysis may prove to be an effective and easily identifiable means of predicting seawater intrusion, its effectiveness remains uncertain due to the limited dataset available. This uncertainty may be reduced by conducting similar analyses at additional sites in the future. Another way to reduce uncertainty would be to collect additional data on likely variations in η near the borehole. In common with the simulations presented in Chapters 5 and 6, the spatial distribution of η is a significant control on the SP signal.

The experiments in Chapter 8 seek to address some of this uncertainty, by measuring η values in marl cores for the first time and developing a greater understanding of the link between η and the pore-throat diameter of the host rock.

Finally, it is important to note that PSD analysis of this type has been applied to a groundwater observation borehole only. If the method were applied to an abstraction borehole, the extent to which changes in pumping rate may affect the PSD analysis is unclear. For a given site, numerical modelling could be carried out to investigate the impacts of pumping on SP and this

may indicate whether longer time periods (i.e. greater than 14.8 days) would be required to resolve the semidiurnal component of the signal.

Chapter 8

Laboratory measurements of η for marl cores

8.1 Introduction

Self-potential (SP) monitoring of the Saltdean OBH conducted by MacAllister (2016) has revealed several phenomena that appear to indicate the proximity of a saline front and the timing of saline intrusion in the borehole. The model described in Chapters 5 to 7 matches these phenomena for the first time and sensitivity analyses on the model reveals the likely mechanisms that control them.

A key feature of the model is the variations in exclusion efficiency η (see Section 2.2.2) with lithology. The values assigned to chalk strata are in close agreement with previous laboratory measurements (MacAllister, 2016), but to date there have been no direct measurements of η for the various marl layers and hardgrounds that exist adjacent to and beneath the Saltdean OBH, within the Seaford Chalk and Lewes Nodular Chalk formations. Instead, these values have been inferred from SP theory (e.g. Leinov and Jackson, 2014; Westermann-Clark and Christoforou, 1986), SP and σ_f profiles in the nearby Victoria Gardens borehole (Section 4.4.1) and calibration of the model.

Marl core samples from the Lewes Nodular Chalk and Seaford Chalk formations were obtained from the National Geological Repository, administered by the British Geological Survey, although it was not possible also to obtain hardground samples. The primary objective of this chapter is to derive the first laboratory measurements of η in marl cores. This will be an important step in validating the model described in previous chapters and constraining uncertainty in what is a relatively large parameter space.

8.2 Description of samples

As shown in Figure 8.1, the core samples comprised a mixture of chalk and anastomosing bands of marl. Strict protocols were followed for cleaning and saturating the cores prior to testing, as described in Section 8.3.2.

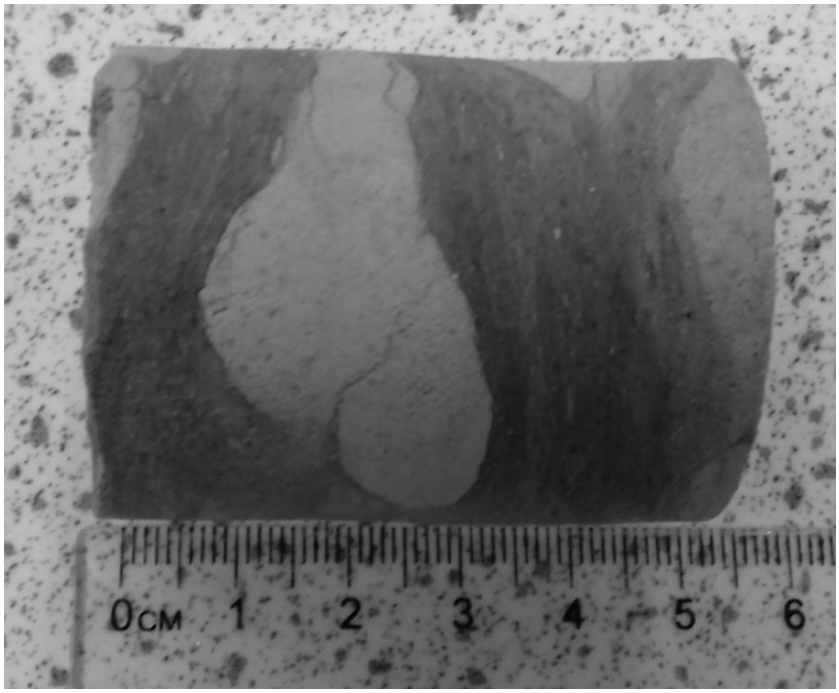

Figure 8.1: Photograph of Core 74505, showing anastomosing marl bands.

Each of the cylindrical marl core samples were 37 mm in diameter, with a length of 40-50 mm. As shown in Table 8.1, the stratigraphy of these cores is consistent with the formations intersected by the Saltdean OBH (Figure 4.2).

Table 8.1: Description of marl core samples.

BGS Core ID	Borehole Name	Depth Range (mbgl)	Stratigraphy
74496	Trumpletts PL10A, Berkshire (SU57NW72)	31.87 - 31.91	Seaford Chalk Formation
74505	Knockhall School, Greenhithe, Kent (TQ57SE/550)	101.54 - 101.59	Lewes Nodular Chalk Formation

8.3 Method

8.3.1 Overview

The method used to derive η in the marl core samples is consistent with the approach described by MacAllister (2016), who applied seawater to groundwater-saturated chalk samples and 5M NaCl solutions to the same samples when saturated with deionised water. The approach is similar to an earlier experimental technique described by Leinov and Jackson (2014), which was applied to sandstone cores.

As described in Section 2.3.1, η can be calculated from Equation (2.16) for a given pair of solutions (e.g. seawater and groundwater), although this requires values for changes in the electrochemical diffusion potential ΔV_{ED}, the electrochemical exclusion potential ΔV_{EE} and the overall electrochemical exclusion-diffusion potential ΔV_{EED} across the front. If the compositions of the solutions are known, ΔV_{ED} and ΔV_{EE} can be calculated from Equations (2.10) and (2.14) respectively. However, ΔV_{EED} must be derived experimentally, by applying a concentration gradient across the core sample of interest (Figure 8.2a).

The electrodes in Figure 8.2a are filled with a solution of similar ionic strength to the adjacent reservoir, to minimise the development of a diffusion potential at the electrode-reservoir interface. As discussed in Section 2.3.1, the different ionic strengths within each electrode produce an additional voltage ΔV_C, which contributes to the measured, or apparent electrical potential difference ΔV_{AP} across the sample as follows (Leinov and Jackson, 2014; MacAllister, 2016):

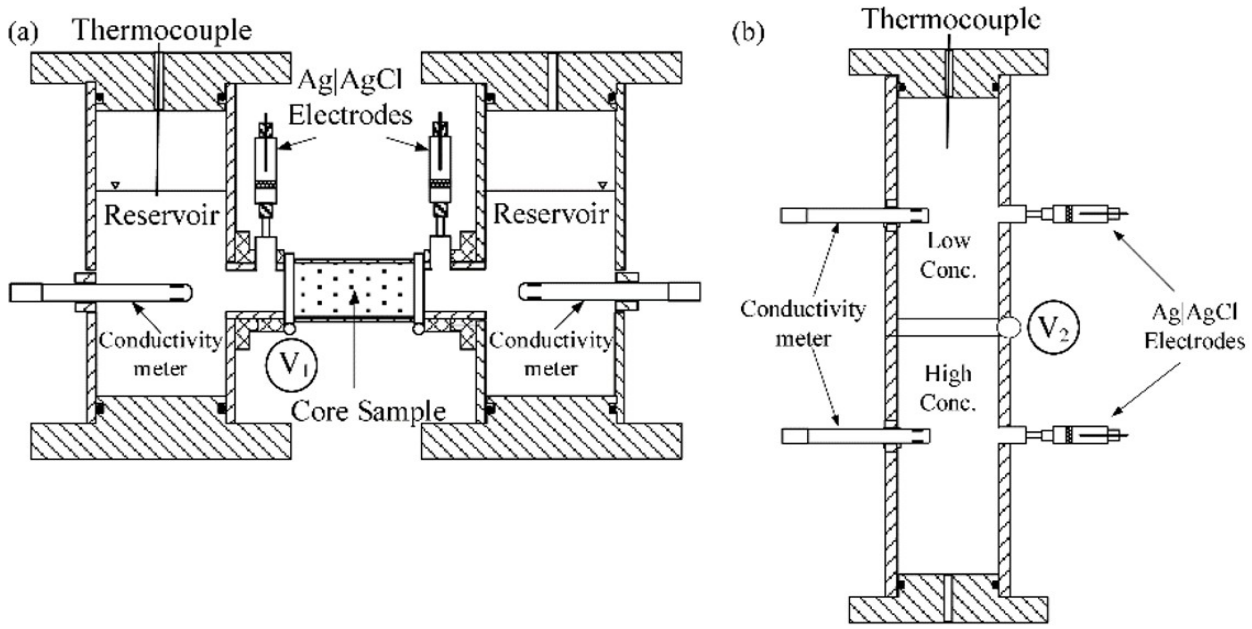

Figure 8.2: a) Experimental apparatus for measuring ΔV_{EED} across a core sample adjacent to seawater on the left hand side and groundwater on the right hand side b) experimental apparatus for measuring the combined effects of ΔV_{ED} and ΔV_C (MacAllister (2016), adapted from an original setup designed by Leinov and Jackson (2014)).

$$\Delta V_{AP} = \Delta V_{EED} + \Delta V_C. \tag{8.1}$$

Leinov and Jackson (2014) and MacAllister (2016) derived values of ΔV_C from a separate column experiment, using the same solutions as those applied to either end of the core sample in Figure 8.2a. In these column experiments, the electrical potential between the lower chamber, filled with high salinity water, and the upper chamber, filled with low salinity water, was measured in the absence of any core sample (Figure 8.2b). Although a valve separating the two chambers was opened, convection-driven flow between the two solutions was minimised by the greater density of the solution in the lower chamber. The apparent electrical potential measured in the column experiment ΔV_{AC} is related to ΔV_C by (Leinov and Jackson, 2014; MacAllister, 2016):

$$\Delta V_{AC} = \Delta V_{ED} + \Delta V_C. \tag{8.2}$$

where ΔV_{ED} is given by Equation (2.10) for multi-ionic solutions (e.g. MacAllister, 2016) and by Equation (2.11) for NaCl solutions (e.g. Leinov and Jackson, 2014).

8.3.2 Detailed description of the experimental method

The marl experiments used the same composition for each reservoir (groundwater and seawater) as MacAllister (2016), shown in Tables 4.2 and 4.1. The groundwater, extracted from the Balsdean PS by MacAllister (2016) (Figure 4.1), was filtered and treated with ultra-violet (UV) light prior to use in the experiments. Seawater samples were not available and synthetic seawater was produced in the laboratory, with the same composition as that shown in Table 4.1, using a combination of de-ionised water and inorganic salts of each constituent.

The average ΔV_{AC} obtained by MacAllister (2016) from 15 repeated column experiments using these solutions is shown in Table 8.2, along with the associated error $\epsilon_{V_{AC}}$, which is given by the range in observed values. The maximum and minimum diffusion potentials ΔV_{ED} were calculated by applying the range in analyte concentrations in Tables 4.2 and 4.1 to Equation (2.10), giving the error $\epsilon_{V_{ED}}$ around the mean of these values. The error in the electrode potential ϵ_{V_C} is given by the sum of $\epsilon_{V_{AC}}$ and $\epsilon_{V_{ED}}$.

Table 8.2: Average measurements of the electrode potential ΔV_C for seawater and groundwater from the Balsdean OBH (adapted from MacAllister (2016)).

ΔV_{AC} **(mV)**	ΔV_{ED} **(mV)**	ΔV_C **(mV)**
-80.93 ± 2.6	27.29 ± 3.2	-108.82 ± 5.8

Prior to the experiments commencing, the cores were cleaned with methanol in a Soxhlet extractor for approximately 48 hours to remove dissolved salts from the pore space. They were subsequently placed in an oven at 82 °C for 48 hours, before being submerged in filtered and UV-treated groundwater from the Balsdean PS. The submerged samples were then placed in a vacuum oven for approximately 24 hours, at a pressure of -900 to -1000 mbar. Saturation with groundwater prior to applying a salinity gradient is intended to mimic the process of intrusion that occurs in coastal aquifers, where seawater invades a pore space initially saturated with

lower salinity groundwater. Following saturation, the sides of each core were wrapped in PTFE tape to help maintain a watertight seal when placed in the apparatus shown in Figure 8.2a. The reservoirs on either side of the core were filled with synthetic seawater and groundwater.

In order to maintain stability, the measurement electrodes were filled with an NaCl solution (as opposed to a multi-ionic solution) to prevent ion exchange reactions occurring on the AgCl coating of the Ag rods shown in Figure 8.2. To minimise the development of diffusion potentials between the multi-ionic groundwater and seawater reservoirs and the adjacent electrodes, the chloride content in the electrodes was increased relative to that of the adjacent reservoirs to compensate for the absence of other ionic species. A porous ceramic disc was placed in the electrode to prevent convective flow between the two solutions. The chloride concentration in the electrode on the seawater side of the apparatus was 24,160 mg/l and 241 mg/l on the groundwater side, consistent with the compositions used by MacAllister (2016), who found from empirical testing that these concentrations were required to maintain stable measurements of the electrode potential. In this way, the higher concentrations of chloride within the NaCl electrodes compensate for the presence of other species within the multi-ionic reservoirs, as discussed in Section 8.3.1. Measurements of potential difference across the core were taken at 1 second intervals throughout the experiment, along with measurements of σ_f and pressure in each reservoir.

To demonstrate repeatability, a total of 3 experiments were conducted on each core. In contrast with the experiments reported by MacAllister (2016), the cores were oriented in the same direction each time, to prevent variations in lithology across the sample from affecting the repeatibility of the results.

8.4 Results

As shown in Figure 8.3 and Appendix C, the apparent voltages obtained from the marl experiments were lower than those reported by MacAllister (2016) for chalk cores saturated with groundwater and seawater, although the shape of each curve is similar. In each case, volt-

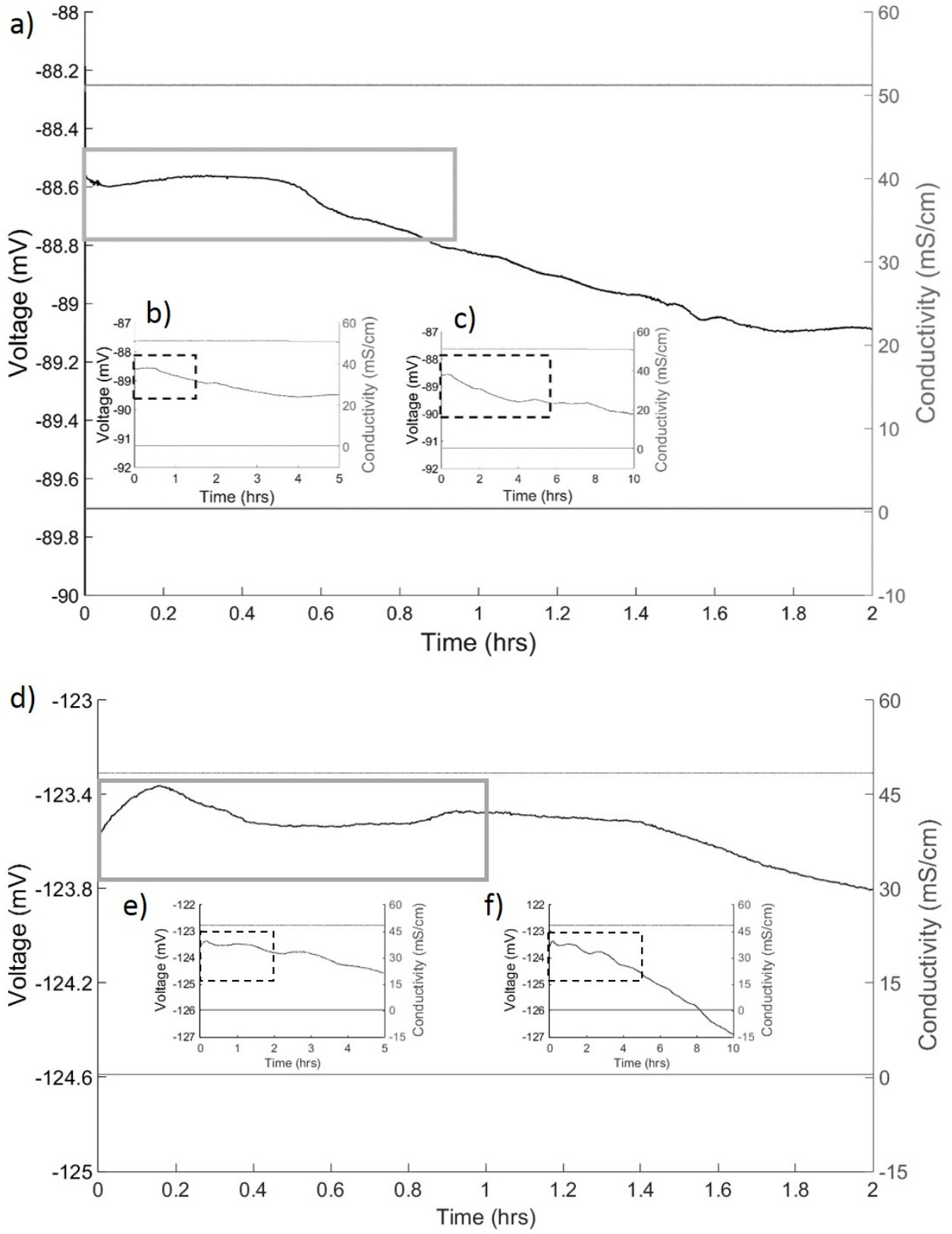

Figure 8.3: Typical results over a range of timescales for (a-c) testing of chalk cores by MacAllister (2016) and (d-f) testing of marl cores. The period used to calculate the apparent voltage ΔV_{AP} is shown by a grey box.

ages are relatively stable during the first 0.5-2 hours, typically followed by a gradual decrease. MacAllister (2016) attributed this phenomenon to pore water in the core samples reducing the salinity of the seawater reservoir near the AgCl electrode. However, as shown in Appendix C, the fluid electrical conductivity in both reservoirs remains constant over a period of at least 10 hours and this explanation seems unlikely.

Movement of ions from the multi-ionic reservoirs to the NaCl electrodes is a more plausible explanation for the observed changes in voltage, although both hypotheses indicate that the early time data are more likely to be reliable.

The most stable voltages were achieved in the third experimental run on each core. The values obtained during these experiments are in closest agreement with the early time data from the first two runs in each case and this further supports the hypothesis that the early time data are most representative of the core's exclusion efficiency.

As a result, ΔV_{AP} was taken as the average voltage during the first hour of each experiment (Table 8.3), consistent with the method employed by MacAllister (2016) for chalk cores. Equation (8.1) was then used to calculate the maximum and minimum values of ΔV_{EED} for each core sample, based on the reported errors in ΔV_C (Table 8.2) and the range in observed ΔV_{AP}. The reported value of ΔV_{EED} represents the mean of the maximum and minimum values.

It is notable that ΔV_{EED} is negative in each case for the marl cores (notwithstanding the highest possible values indicated by the errors for Core 74996), indicating a dominance of electrochemical exclusion. This contrasts with the results reported by MacAllister (2016) for chalk cores, where ΔV_{EED} was consistently positive.

The values of ΔV_{EED} were used to derive η and the associated errors reported in Table 8.3 from Equation (2.16). The range in η values was calculated based on the range of analyte concentrations for groundwater and seawater in Tables 4.2 and 4.1. These were used to calculate

Table 8.3: Summary of results from the marl core experiments.

Core ID	ΔV_{AP} **(mV)**	ΔV_C **(mV)**	ΔV_{EED} **(mV)**	ΔV_{ED} **(mV)**	ΔV_{EE} **(mV)**	η
74996	-119.90	-108.82 ± 5.8	-7.91 ± 9.0	27.29 ± 3.2	-111.54 ± 6.8	0.258 ± 0.060
	-116.59					
	-113.55					
74505	-118.53	-108.82 ± 5.8	-12.19 ± 8.3	27.29 ± 3.2	-111.54 ± 6.8	0.289 ± 0.057
	-122.91					
	-123.49					

the values of ΔV_{ED} (from Equation (2.10)) and ΔV_{EE} (from Equation (2.14)) in Equation (2.16). In each case, the lowest η values were given by the maximum concentration difference and the highest (least negative) value for ΔV_{AP}. Similarly, the highest values of η were given by the lowest value of ΔV_{AP}, combined with values of ΔV_{ED} and ΔV_{EE} produced by the lowest concentration difference across the sample.

8.5 Discussion

8.5.1 Effect of lithology on ΔV_{EED} and η

Figure 8.4 shows how the presence of clay minerals can profoundly affect measured values of ΔV_{EED}. Clean sandstone and chalk samples produce consistently positive values of ΔV_{EED}, indicating electrochemical diffusion as the dominant source of SP. By contrast, shale, marl and shaly sands commonly display negative values of ΔV_{EED}, suggesting that electrochemical exclusion is dominant in these lithologies. The pore-throat radius, which is typically smaller in the presence of clay minerals (Fay-Gomord et al., 2016; Molyneux, 2012), is clearly an important factor in this regard, although the mineral surface charge is also a significant control on exclusion (Leinov and Jackson, 2014).

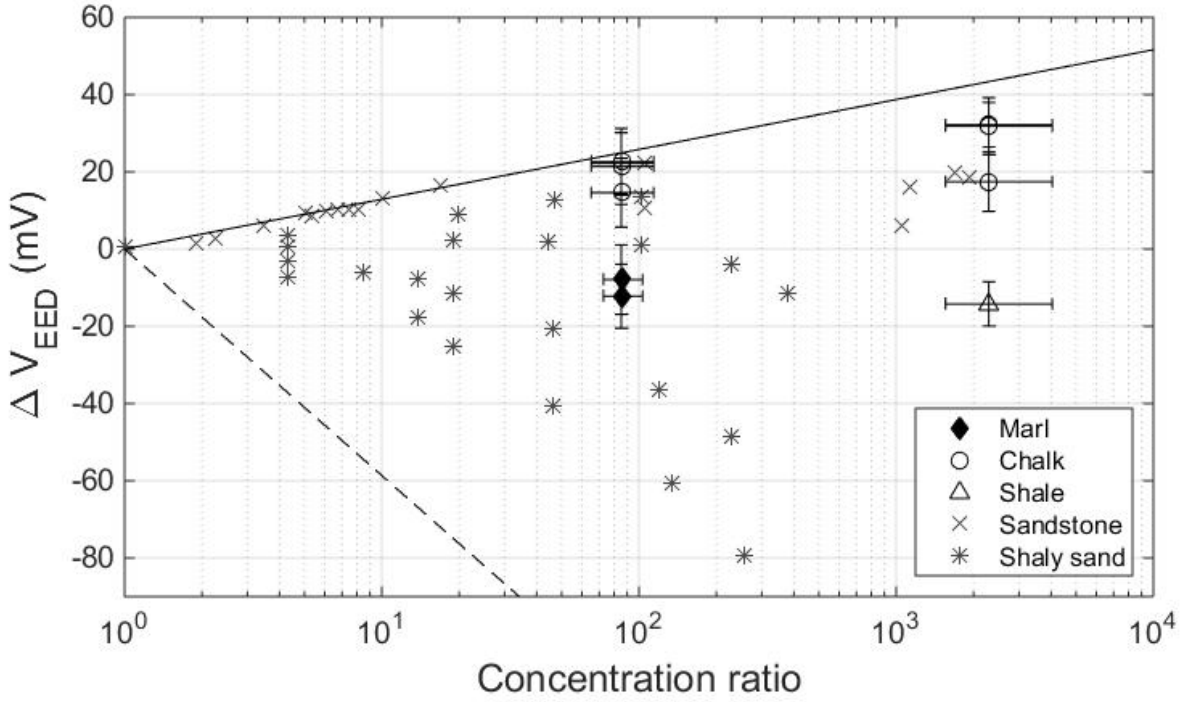

Figure 8.4: Measurements of ΔV_{EED} for a range of lithologies and concentration ratios. The limits of electrochemical diffusion (solid black line) and exclusion (dashed black line) are shown for NaCl solutions, based on Equations (2.11) and (2.14) and $t_{Na} = 0.39$. Chalk measurements are taken from MacAllister (2016), sandstone measurements from Leinov and Jackson (2014) and shaly sand measurements from Hill and Millburn (1956) (as presented in Leinov and Jackson (2014)).

As demonstrated by Leinov and Jackson (2014) and MacAllister (2016), the simple model proposed by Westermann-Clark and Christoforou (1986) that relates η to the ratio of pore-throat radius to Debye length (see Sections 2.2.2 and 4.4) is supported by measurements of chalk and sandstone, where surface charge is largely unaffected by the presence of clay minerals. The highly variable results shown in Figure 8.4 for clay-rich lithologies suggests that more complex models that relate ΔV_{EED} to surface charge (e.g. Revil and Jougnot, 2008) should also be investigated, although the required input parameters for these models, such as the mobility of counterions at the mineral surface are more difficult to determine (Leinov and Jackson, 2014). This is likely to be a particular challenge in heterogeneous lithologies, such as the marl core shown in Figure 8.1.

The η values from laboratory testing of the marl cores are compared to experimental results for chalk samples and field estimates of marl η (described in Section 4.4) in Figure 8.5 (based on Figure 4.9, which did not include laboratory results for marl). Despite uncertainty in

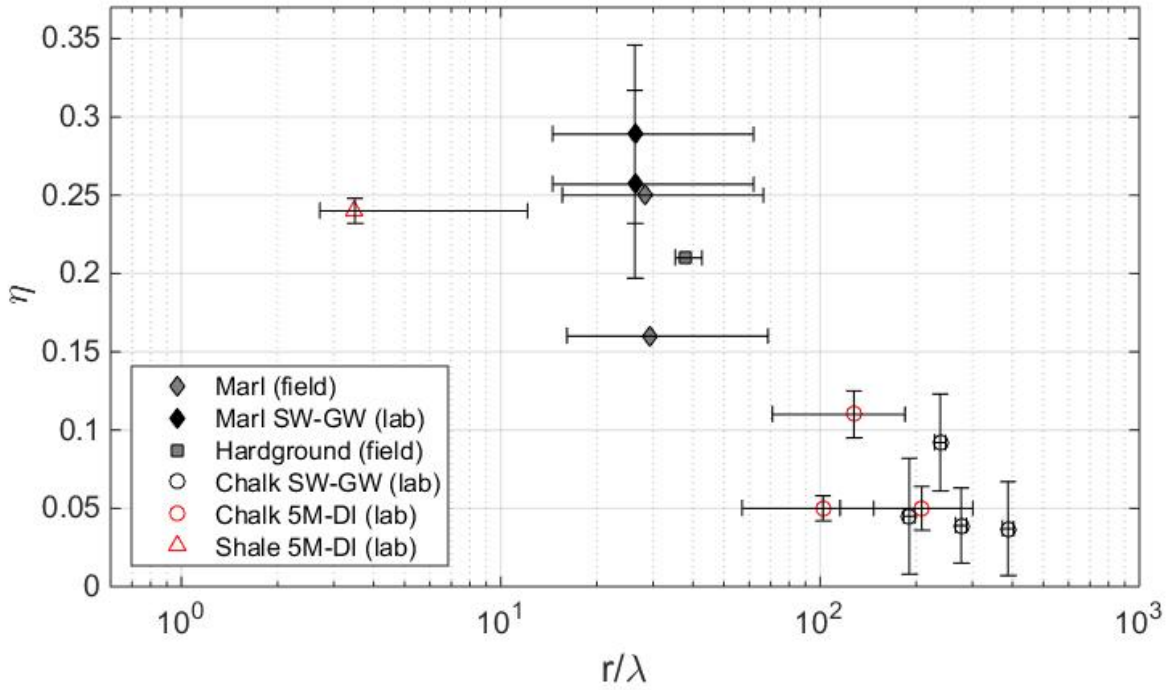

Figure 8.5: Exclusion efficiency η as a function of pore throat radius r and the Debye length λ. Samples saturated with seawater and groundwater are labelled 'SW-GW'; samples saturated with 5M NaCl solution and deionised water are labelled '5M-DI'. Errors in η for the laboratory marl samples are taken from Table 8.3, while errors in r/λ for marls and hardgrounds are given by the range of pore throat diameters reported by Fay-Gomord et al. (2016). The error in field values of η could not be quantified, due to the range of uncertainties in deriving these estimates. Chalk and shale results are taken from MacAllister (2016).

the surface charge of clay-rich lithologies discussed above, the inverse relationship between η and pore throat diameter r in Figure 8.5 remains consistent with the theoretical work of Westermann-Clark and Christoforou (1986) and experimental results reported by Leinov and Jackson (2014) for sandstone cores. It also supports parameterisation of the model presented in Chapters 5 to 7.

The slightly higher values of η found in the laboratory can be partially attributed to the scale of measurement. The samples selected for laboratory analysis represented the 4-5 cm intervals with the highest proportion of marl, based on visual inspection of core from multiple boreholes at the National Geological Repository. The marl horizons used to infer field values of η in Figure 4.8 span depth intervals of 1-2 m and similar marl thicknesses were simulated in the numerical model. In reality, these larger intervals comprise a mixture of chalk and marl bands and their effective η values are likely to lie between the values for marl and chalk shown in

Figure 8.5.

In field estimates of η, it was assumed that changes in SP and σ_f with depth in the borehole are representative of ∇V_{EED} and $\nabla ln(C_f)$ respectively in the adjacent formation. The enhanced electrical conductivity of the water column relative to the surrounding formation, as well as mixing within the borehole is likely to have a dampening effect on these parameters and is a clear source of uncertainty in the values of η obtained, although it is not possible to quantify the likely magnitude of this error. However, the limited discrepancy between the field and laboratory values for marl suggests that borehole data may give a reasonable first-pass estimate of η in the absence of experimental results. Although hardground samples could not be obtained for laboratory testing, the field-derived hardground values may therefore provide a reasonable basis for model parameterisation.

8.5.2 Errors

Although the errors in ΔV_{EED} for the marl cores ($\pm$8.3 to $\pm$9.0) are similar to those reported by MacAllister (2016) for chalk samples saturated with groundwater and seawater ($\pm$7.9 to $\pm$9.8, as shown in Figure 8.4), calculated errors in η for the seawater and groundwater experiments are roughly twice as large in the marl ($\pm$0.057 to $\pm$0.060, compared to $\pm$0.024 to $\pm$0.037 for chalk (MacAllister, 2016)). However, the maximum error in ΔV_{AP}, as given by the range in measured voltages across the core samples (halved), is similar in the marl ($\pm$3.2) and chalk experiments ($\pm$2.4 (MacAllister, 2016)).

The remaining discrepancy can be attributed to the method of calculation, which leads to higher errors as η increases. For example, applying a single value of ΔV_{AP} = -120 mV to the range in ΔV_{ED} and ΔV_{ED} values shown in Table 8.3 gives η = 0.286 $\pm$0.050, while applying ΔV_{AP} = -85 mV (reported by MacAllister (2016) from testing of chalk) gives η = 0.035 $\pm$0.036.

8.6 Conclusions

The results from the first laboratory tests of marl η show negative values for ΔV_{EED} and indicate (based on Equations (2.11), (2.12) and (2.14)) that electrochemical exclusion is the dominant source of SP in this lithology. These results go some way to validating the model described in Chapters 5 to 7 of this thesis, which requires elevated values of η in known marl horizons to explain the SP phenomena observed in the Saltdean OBH.

Given the large parameter space required to model SP in coastal aquifers, measurements of η for the full range of lithologies at the site is an important step in reducing uncertainty and for other sites may permit *a priori* characterisation of SP precursor signals. Further recommendations for developing SP as a reliable predictor of seawater intrusion are presented in Chapter 9.

Chapter 9

Summary and conclusions

9.1 Research context

Groundwater is the most significant source of drinking water worldwide. However, there is abundant evidence of seawater intrusion into groundwater sources on every inhabited continent. This situation is exacerbated by the high demand for groundwater in densely populated coastal areas, leading to lowering of the water table and upconing of the saline front. The challenge of managing groundwater in these areas is further compounded by climatic variability and rising sea levels.

Traditional geophysical methods for characterising seawater intrusion can sometimes delineate the spatial extent of the saline front, but they are not well suited to understanding the advance of the front over time. Alternatively, monitoring of water levels and salinity in individual boreholes can provide long-term datasets with a high degree of temporal resolution, but they are not effective at predicting the timing of breakthrough into individual boreholes, particularly in heterogeneous aquifers where groundwater flow paths remain poorly understood.

Recent research in the fields of petroleum geoscience and hydrogeology suggests that self-potential (SP) signals could be used to predict the arrival of saline water in boreholes. If proven, the low cost and practical installation of SP monitoring arrays, coupled with the ability

to collect data at a high frequency (for example, once per second) over a period of several years could have profound implications for groundwater management in coastal aquifers.

While this technique would be most relevant to abstraction boreholes, water companies would be unwilling to trial an unproven monitoring method in these sensitive assets. As an initial step in understanding the processes that control SP in coastal aquifers, the focus to date has been on collecting SP data from coastal groundwater monitoring boreholes.

MacAllister (2016), MacAllister et al. (2016) and MacAllister et al. (2018) were the first to investigate SP monitoring as a predictive tool in coastal groundwater observation boreholes and the data reported in these studies suggest a possible link between SP and movements of a nearby saline front. Firstly, the data show a persistent SP gradient in a coastal groundwater observation borehole, which was not seen in boreholes further inland. Secondly, there is a reduction in this gradient several days prior to seawater intrusion, subsequently referred to as a precursor. Thirdly, tidal oscillations in SP were found to match the main semidiurnal tidal component of marine tides and through power spectral density analysis, MacAllister et al. (2016) showed that these oscillations are controlled by remote fluctuations in the position of the saline front.

Despite efforts to model hydrodynamic and electrodynamic processes in the surrounding coastal aquifer, these studies were unable to explain in detail the mechanisms that control the first two phenomena, while the associated power spectral density analysis did not establish a link between SP power spectra and the timing of saline intrusion events. As a result, the research did not prove that SP could be a viable method to predict seawater intrusion.

9.2 Main findings

Through the use of numerical modelling, this thesis explains the first two SP phenomena reported by MacAllister (2016) and through a combination of modelling and data analysis, proposes an alternative technique for predicting seawater intrusion using SP power spectral density analysis.

The first phenomenon is a persistent positive SP gradient within the water column of a coastal groundwater observation borehole, which intersects the Chalk of England aquifer. The model described in Chapter 5 of this thesis matches the observed gradient for the first time and indicates that the electrochemical exclusion-diffusion potential V_{EED} is the dominant source. Sensitivity analyses show that the gradient is sensitive to the sharpness and proximity of the saline front, as well as spatial variations in the exclusion-efficiency η of the aquifer, a parameter that describes the importance of electrochemical exclusion (caused by thick electric double layers relative to the pore throat diameter) relative to diffusion (which dominates in uncharged porous media, or where the pore throat diameter is large).

The second phenomenon is a reduction in the SP gradient approximately one week prior to seawater intrusion. The model described in Chapter 6, which replicates this behaviour for the first time, suggests that this precursor is driven by an advancing front in a fracture zone either below or intersecting the base of the borehole and that there is a slight reduction in η with depth across this fracture zone. In essence, as the front begins to interact with more exclusive strata on the upper plane of the fracture, the magnitude of ∇V_{EED} near the base of the borehole is reduced, giving an associated reduction in the SP gradient.

The model suggests that the changes in SP reported by MacAllister (2016) constitute a genuine precursor to seawater intrusion. However, inspection of the data suggests that this precursor may be difficult to distinguish from numerous other small changes in SP throughout the monitoring period. In Chapter 7 the power spectral density of SP in the borehole is investigated, which may provide a clearer indication of an approaching saline front. The power of semidiurnal fluctuations in SP is shown to reduce substantially prior to seawater intrusion in 2013 and 2014, a phenomenon which is replicated by the model, although only when the main source of SP fluctuations lies within a fracture zone below the base of the borehole, due to a change in η across this fracture. As the modelled saline front advances inland through this fracture zone, the gradient of $ln(C_f)$ (where C_f is the ionic strength of fluid) beneath the borehole also reduces, giving a reduction in the SP source term. In the scenario when SP fluctuations are generated within a shallower fracture that intersects the base of the borehole, the power of semidiurnal oscillations increases prior to intrusion.

The model suggests that between them, these three SP phenomena may be used to indicate both the proximity of a saline front and the timing of its entry into a coastal groundwater observation borehole. In each case, the results are highly sensitive to the spatial distribution of η adjacent to and beneath the borehole. For abstraction boreholes, where upconing of saline water often occurs prior to intrusion, the distribution of η beneath the borehole is likely to be even more significant.

The model described in Chapters 5 to 7 invokes high values of η in marl and hardground layers within the Chalk, which have not been measured previously in laboratory experiments. In Chapter 8, the first measurements of η for marl cores are reported. These measurements were found to slightly exceed modelled values of η, although model discretisation means that individual grid cells are likely to include alternating layers of chalk and marl. As such, the laboratory experiments validate the intermediate values of η applied to these depth intervals in the model and furthermore, go some way to validating the overall findings of the model.

9.3 Future work

The findings presented above suggest that SP can be used to characterise the risks and timing of seawater intrusion in a single coastal groundwater observation borehole within the Chalk of England. The applicability of the described methods to abstraction boreholes and to boreholes in other locations remains uncertain however. As such, there is a clear need to monitor SP in additional boreholes prone to seawater intrusion, ideally in different aquifer types or in laboratory experiments that replicate the main elements of these aquifers. Ultimately, SP monitoring of abstraction boreholes would be required to demonstrate the full applicability of the technique.

The measurement of η for the range of lithologies encountered should accompany any future monitoring program, as accurately parameterising a model of the site with these data could facilitate simulation of SP phenomena in advance of seawater intrusion. Establishing whether SP phenomena are reliable and predictable indicators of seawater intrusion is fundamental to

the utilisation of this technique and successful *a priori* simulations of these phenomena would constitute an important piece of evidence in this regard.

While it has been possible to match retrospectively the observed changes in SP gradient and power spectra prior to intrusion, *a priori* characterisation of these precursor phenomena at a new site is likely to represent a major challenge for the technique. The model in Chapters 5 to 7 of this thesis relies on small changes in η across specific fracture zones and these changes appear to dictate the trend and amplitude of the changes in the SP gradient and power spectra. It is notable that the changes in η are less than the experimental errors shown for marl and chalk layers in Chapter 8.

It may be possible to reduce experimental errors by constraining more effectively the ionic strengths of seawater and groundwater solutions used to test rock samples. However, relating even well-constrained laboratory measurements to specific strata near a borehole of interest is another key challenge to be addressed. Until these problems are overcome, predicting seawater intrusion with SP may require an initial intrusion event at each site to characterise the precursor phenomena, before they can be used to indicate future events.

The hydrodynamic component of modelling could be improved by more accurately representing dispersion of the saline front. Currently available software packages either ignore dispersive processes entirely or require a large number of small grid elements in the vicinity of the front to prevent excessive dispersion. In transient simulations, where the front is dynamic, the requirement for small grid elements may extend over a large area, leading to prohibitively long run times. Adaptive meshing strategies, in which the most refined part of the model mesh evolves based on the location of the front at any given time, may offer efficiencies in this regard and is an area of research worth pursuing.

The modelling process represents the majority of the coastal Chalk aquifer as an equivalent porous medium (EPM) and with the exception of two fracture zones, does not explicitly represent the network of fractures and matrix blocks reported by Bloomfield (1996) and others in field observations of the Chalk. Although the true locations and characteristics of hydraulically significant fractures beneath the site cannot be measured, dual permeability modelling could

provide important insights into the residence time of saline water in the matrix of the Chalk following droughts and hence, the impacts of long-term climatic variations on the distribution of salinity within the aquifer. The close proximity of the saline front to the borehole in the current EPM model would suggest that the observed SP phenomena occur in a relatively small subset of coastal boreholes. Within a dual permeability or discrete fracture network (DFN) model, pockets of saline water in the matrix may persist over a much wider area and affect a greater number of boreholes, although the flow of fresh groundwater within the water column may create narrow pockets of low salinity water around the boreholes themselves.

SP monitoring allows the collection of data at a high frequency within a borehole of interest over a period of several months or years. This contrasts with traditional geophysical methods, such as electrical resistivity tomography (ERT), which provide greater spatial coverage across a coastal aquifer, but for financial and logistical reasons are less suitable for characterising the long-term evolution of a saline front. Future SP investigations may be enchanced by running field investigations in combination with ERT, to improve characterisation of the aquifer in both time and space and reduce non-uniqueness commonly associated with geophysical interpretations.

Bibliography

Allen, D., Brewerton, L., Coleby, L., Gibbs, B., Lewis, M., MacDonald, A., Wagstaff, S., and Williams, A. (1997). The physical properties of major aquifers in England and Wales. Report WD/97/034, British Geological Survey.

AMEC (2012). Lewes Winterbourne NEP investigation: Brighton and Worthing groundwater modelling study conceptual model report. Report, Environment and Infrastructure.

AMEC (2016). Lewes Winterbourne NEP investigation: Brighton and Worthing groundwater modelling study final model report. Report, Environment and Infrastructure.

Angelis, M. D. (2005). *Major Ions in Seawater*, pages 159–160. American Cancer Society.

Ataie-Ashtiani, B., Volker, R. E., and Lockington, D. A. (1999). Tidal effects on sea water intrusion in unconfined aquifers. *Journal of Hydrology*, 216(1-2):17–31.

Babu, D. S. S., Anish, M., Vivekanandan, K. L., Ramanujam, N., Murugan, K. N., and Ravindran, A. A. (2009). An account of submarine groundwater discharge from the SW Indian coastal zone. *Journal of Coastal Research*, 25(1):91–104.

Badon-Ghyben, W. (1888-1889). Nota in verband met de voorgenomen putboring nabij Amsterdam. *Koninklyk Instituut Ingenieurs Tijdschrift*, pages 8–22.

Bakhtyar, R., Barry, D. A., and Brovelli, A. (2012). Numerical experiments on interactions between wave motion and variable-density coastal aquifers. *Coastal Engineering*, 60:95–108.

Barlow, P. M. and Reichard, E. G. (2010). Saltwater intrusion in coastal regions of North America. *Hydrogeology Journal*, 18(1):247–260.

BGS (2017). Wireline log of TQ30SW3 Victoria Gardens Borehole. Copyright NERC. All rights reserved.

BGS (2018a). Geology of Britain viewer: Borehole scan of TQ30SE13. Accessed 10 january 2018. Available at: http://mapapps.bgs.ac.uk/geologyofbritain/home.htm.

BGS (2018b). World Data Centre for Geomagnetism (Edinburgh): Geomagnetic Data Master Catalogue - Minute Data for the Hartland Observatory. Accessed 21 February 2018. Available at: http://www.wdc.bgs.ac.uk/catalog/master.html.

Bindoff, N. L., Lilley, F. E. L., and Filloux, J. H. (1988). A separation of ionospheric and oceanic tidal components in magnetic fluctuation data. *Journal of Geomagnetism and Geoelectricity*, 40(12):1445–1467.

Bloomfield, J. (1996). Characterisation of hydrogeologically significant fracture distributions in the Chalk: An example from the Upper Chalk of southern England. *Journal of Hydrology*, 184(3-4):355–379.

Bloomfield, J. P., Brewerton, L. J., and Allen, D. J. (1995). Regional trends in matrix porosity and dry density of the Chalk of England. *Quarterly Journal of Engineering Geology and Hydrogeology*, 28(Supplement 2):S131–S142.

Bocanegra, E., Da Silva, G. C., Custodio, E., Manzano, M., and Montenegro, S. (2010). State of knowledge of coastal aquifer management in South America. *Hydrogeology Journal*, 18(1):261–267.

BODC (2015). UK tide gauge network. Accessed 8 June 2015. Available at: https://www.bodc.ac.uk/data/hosted_data_systems/sea_level/uk_tide_gauge_network/.

Bolève, A., Janod, F., Revil, A., Lafon, A., and Fry, J. J. (2011). Localization and quantification of leakages in dams using time-lapse self-potential measurements associated with salt tracer injection. *Journal of Hydrology*, 403(3-4):242–252.

Bresciani, E., Ordens, C., Werner, A., Batelaan, O., Guan, H., and Post, V. (2014). Spatial

variability of chloride deposition in a vegetated coastal area: Implications for groundwater recharge estimation. *Journal of Hydrology*, 519:1177 – 1191.

Butler, A. P. (1994). *Saline water dynamics in a shallow coastal aquifer : an experimental and modelling study*. PhD thesis, Imperial College London.

Butler, A. P., Hughes, A. G., Jackson, C. R., Ireson, A. M., Parker, S. J., Wheater, H. S., and Peach, D. W. (2012). Advances in modelling groundwater behaviour in Chalk catchments. *Geological Society, London, Special Publications*, 364(1):113–127.

Butler, A. P., Mathias, S. A., Gallagher, A. J., Peach, D. W., and Williams, A. T. (2009). Analysis of flow processes in fractured chalk under pumped and ambient conditions (UK). *Hydrogeology Journal*, 17(8):1849–1858.

Chave, A. and Jones, A. (2012). *The Magnetotelluric Method: Theory and Practice*. Cambridge University Press, UK.

Cherubini, C., Giasi, C., and Pastore, N. (2013). Fluid flow modeling of a coastal fractured karstic aquifer by means of a lumped parameter approach. *Environmental Earth Sciences*, 70(5):2055–2060.

Comte, J.-C. and Banton, O. (2007). Cross-validation of geo-electrical and hydrogeological models to evaluate seawater intrusion in coastal aquifers. *Geophysical Research Letters*, 34(10).

Cornell, R. M. and Aksoyoglu, E. S. (1991). Simultaneous determination of the cation-exchange capacity and the exchangeable cations on marl. *Clay Minerals*, 26(4):567–570.

Corwin, R. (1990). The self-potential method for environmental and engineering applications. *Geotechnical and Environmental Geophysics*, 1:127–145.

Custodio, E. (2010). Coastal aquifers of Europe: an overview. *Hydrogeology Journal*, 18(1):269–280.

Darcy, H. (1856). Les Fountaines Publiques de la Ville de Dijon. *Note D. Dalmont, Paris*.

Darling, T. (2005). *Well Logging and Formation Evaluation*. Elsevier. Online version available at: https://app.knovel.com/web/toc.v/cid:kpWLFE0006/viewerType:toc/root_slug:well-logging-and.

De Witte, L. (1948). A new method of interpretation of self-potential field data. *Geophysics*, 13(4):600–608.

Diersch, H. J. G. and Kolditz, O. (2002). Variable-density flow and transport in porous media: approaches and challenges. *Advances in Water Resources*, 25(8-12):899–944.

Dokou, Z. and Karatzas, G. P. (2012). Saltwater intrusion estimation in a karstified coastal system using density-dependent modelling and comparison with the sharp-interface approach. *Hydrological Sciences Journal*, 57(5):985–999.

Doodson, A. T. (1921). The harmonic development of the tide-generating potential. *Proceedings of the Royal Society of London A: Mathematical, Physical and Engineering Sciences*, 100(704):305–329.

DuCommun, J. (1828). On the cause of fresh water springs and fountains. *American Journal of Science*, 14:174–176.

EEA (1999). State and pressures of the marine and coastal Mediterranean environment. Report, European Environment Agency, Copenhagen.

Elder, J. (1967). Transient convection in a porous medium. *Journal of Fluid Mechanics*, 27:609–623.

Ernstson, K. and Scherer, H. U. (1986). Self-potential variations with time and their relation to hydrogeologic and meteorological parameters. *Geophysics*, 51(10):1967–1977.

Essaid, H. I. (1986). A comparison of the coupled fresh-water salt-water flow and the Ghyben-Herzberg sharp interface approaches to modeling of transient-behavior in coastal aquifer systems. *Journal of Hydrology*, 86(1-2):169–193.

Fay-Gomord, O., Soete, J., Katika, K., Galaup, S., Caline, B., Descamps, F., Lasseur, E., Fabricius, I. L., Saiag, J., Swennen, R., and Vandycke, S. (2016). New insight into the microtexture of chalks from NMR analysis. *Marine and Petroleum Geology*, 75:252–271.

Ferguson, G. and Gleeson, T. (2012). Vulnerability of coastal aquifers to groundwater use and climate change. *Nature Climate Change*, 2(5):342–345.

Fetter, C. (2001). *Applied Hydrogeology*. Prentice-Hall, New Jersey, 4th edition.

Fitterman, D. V. (2014). Mapping saltwater intrusion in the Biscayne Aquifer, Miami-Dade County, Florida using transient electromagnetic sounding. *Journal of Environmental and Engineering Geophysics*, 19(1):33–43.

Gallagher, A. J., Rutter, H. K., Buckley, D. K., and Molyneux, I. (2012). Lithostratigraphic controls on recharge to the Chalk aquifer of Southern England. *Quarterly Journal of Engineering Geology and Hydrogeology*, 45(2):161–172.

Gingerich, S. B. and Voss, C. I. (2005). Three-dimensional variable-density flow simulation of a coastal aquifer in southern Oahu, Hawaii, USA. *Hydrogeology Journal*, 13(2):436–450.

Glover, P. W. and Jackson, M. D. (2010). Borehole electrokinetics. *The Leading Edge*, 29(6):724.

Glover, P. W. J. (2009). What is the cementation exponent? A new interpretation. *Leading Edge*, 28:82–85.

Graf, T. and Therrien, R. (2008). A test case for the simulation of three-dimensional variable-density flow and solute transport in discretely-fractured porous media. *Advances in Water Resources*, 31(10):1352–1363.

Grillo, A., Logashenko, D., Stichel, S., and Wittum, G. (2010). Simulation of density-driven flow in fractured porous media. *Advances in Water Resources*, 33(12):1494–1507.

Gulamali, M. Y., Leinov, E., and Jackson, M. D. (2011). Self-potential anomalies induced by water injection into hydrocarbon reservoirs. *Geophysics*, 76(4):F283–F292.

Hassan, A., Pohlmann, K., and Chapman, J. (2001). Uncertainty analysis of radionuclide transport in a fractured coastal aquifer with geothermal effects. *Transport in Porous Media*, 43(1):107–136.

Henry, H. R. (1964). Effects of dispersion on salt encroachment in coastal aquifers, sea water in coastal aquifers. Report 1613-C.

Herzberg, A. (1901). Die Wasserversorgung einiger Nordseebäder [The water supply of some North Sea spas]. *Journal für Gasbeleuchtung und Wasserversorgung*, 44:815–819.

Hill, H. J. and Millburn, J. D. (1956). Effect of clay and water salinity on electrochemical behavior of reservoir rocks. *Journal Gasbeleuchtung und Wasserversorgung*, 44:815–819, 842–844.

Hunter, R. (1981). *Zeta Potential in Colloid Science: Principles and Applications*. Academic Press Ltd, London.

Ijioma, A. (2016). *Closed-loop feedback control of smart wells for production optimisation using self-potential measurements*. PhD thesis, Imperial College London.

Ikard, S. J., Revil, A., Jardani, A., Woodruff, W. F., Parekh, M., and Mooney, M. (2012). Saline pulse test monitoring with the self-potential method to nonintrusively determine the velocity of the pore water in leaking areas of earth dams and embankments. *Water Resources Research*, 48(4). W04201.

Ireson, A. M., Mathias, S. A., Wheater, H. S., Butler, A. P., and Finch, J. (2009). A model for flow in the chalk unsaturated zone incorporating progressive weathering. *Journal of Hydrology*, 365(3-4):244–260.

Jaafar, M. Z., Vinogradov, J., and Jackson, M. D. (2009). Measurement of streaming potential coupling coefficient in sandstones saturated with high salinity NaCl brine. *Geophysical Research Letters*, 36(21).

Jackson, M., Vinogradov, J., Saunders, J. H., and Jaafar, M. Z. (2010). Laboratory measurements and numerical modeling of streaming potential for downhole monitoring in intelligent wells. *SPE Journal*, 16(3):625–636.

Jackson, M. D. (2015). Tools and techniques: Self-potential methods. In Schubert, G., editor, *Treatise on Geophysics*, volume 11, book section 9, pages 261–293. 2nd edition.

Jackson, M. D., Butler, A. P., and Vinogradov, J. (2012a). Measurements of spontaneous potential in chalk with application to aquifer characterization in the southern UK. *Quarterly Journal of Engineering Geology and Hydrogeology*, 45(4):457–471.

Jackson, M. D., Gulamali, M. Y., Leinov, E., Saunders, J. H., and Vinogradov, J. (2012b). Spontaneous potentials in hydrocarbon reservoirs during waterflooding: Application to waterfront monitoring. *SPE JOURNAL*, 17:53–69.

Jacob, C. (1950). *Flow of ground water*, pages 321–386. John Wiley, New York.

Jardani, A., Dupont, J. P., and Revil, A. (2006). Self-potential signals associated with preferential groundwater flow pathways in sinkholes. *Journal of Geophysical Research*, 111(B9).

Jardani, A., Revil, A., Bolève, A., and Dupont, J. P. (2008). Three-dimensional inversion of self-potential data used to constrain the pattern of groundwater flow in geothermal fields. *Journal of Geophysical Research: Solid Earth*, 113(B9). B09204.

Jin, G., Torres-Verdín, C., Devarajan, S., Toumelin, E., and Thomas, E. (2007). Pore-scale analysis of the Waxman-Smits shaly-sand conductivity model. *Petrophysics*, 48(2):104–120.

Jones, B., Vengosh, A., Rosenthal, E., and Yechieli, Y. (1999). Geochemical investigations. In Bear, J., Cheng, A.-D., Sorek, S., Ouazar, D., and Herrera, I., editors, *Seawater Intrusion in Coastal Aquifers - Concepts, Methods and Practices*, Theory and Applications of Transport in Porous Media, pages 51–71. Kluwer Academic Publishers, Dordrecht, Netherlands.

Jones, H. K. and Robins, N. S. (1999). *The Chalk aquifer of the South Downs*. Hydrogeological Report Series of the British Geological Survey. British Geological Survey.

Jougnot, D., Linde, N., Haarderb, E. B., and Looms, M. C. (2015). Monitoring of saline tracer movement with vertically distributed self-potential measurements at the HOBE agricultural test site, Voulund, Denmark. *Journal of Hydrology*, 521:314–327.

Jouniaux, L., Maineult, A., Naudet, V., Pessel, M., and Sailhac, P. (2009). Review of self-potential methods in hydrogeophysics. *Comptes Rendus Geoscience*, 341(10-11):928–936.

Jouniaux, L. and Pozzi, J. P. (1995). Streaming potential and permeability of saturated sandstones under triaxial stress - consequences for electrotelluric anomalies prior to earthquakes. *Journal of Geophysical Research-Solid Earth*, 100(B6):10197–10209.

Kang, H. J., Cho, I. K., Kim, J. H., Yong, H. H., Song, S. H., and Park, Y. G. (2014). SP monitoring at a sea dike. *Near Surface Geophysics*, 12(1):83–92.

Konikow, L. F. (2011). The secret to successful solute-transport modeling. *Ground Water*, 49(2):144–159.

Korpi, G. and de Bruyn, P. (1972). Measurement of streaming potentials. *Journal of Colloid and Interface Science*, 40(2):263 – 266.

Lanteri, Y., Fievet, P., and Szymczyk, A. (2009a). Evaluation of the steric, electric, and dielectric exclusion model on the basis of salt rejection rate and membrane potential measurements. *Journal of Colloid and Interface Science*, 331(1):148–155.

Lanteri, Y., Szymczyk, A., and Fievet, P. (2009b). Membrane potential in multi-ionic mixtures. *Journal of Physical Chemistry B*, 113(27):9197–9204.

Leinov, E. and Jackson, M. D. (2014). Experimental measurements of the SP response to concentration and temperature gradients in sandstones with application to subsurface geophysical monitoring. *Journal of Geophysical Research: Solid Earth*, 119(9):6855–6876.

Li, X. Y., Hu, B. X., Burnett, W. C., Santos, I. R., and Chanton, J. P. (2009). Submarine ground water discharge driven by tidal pumping in a heterogeneous aquifer. *Ground Water*, 47(4):558–568.

Lomb, N. R. (1976). Least-squares frequency-analysis of unequally spaced data. *Astrophysics and Space Science*, 39(2):447–462.

MacAllister, D. (2015a). Hydrochemistry data from the English Channel and from the Balsdean observation borehole July 2013 - June 2014. Data provided by email on 30/06/15.

MacAllister, D. (2016). *Monitoring seawater intrusion into the fractured UK Chalk aquifer using measurements of self-potential (SP).* PhD thesis, Imperial College London.

MacAllister, D., Jackson, M., Butler, A., and Vinogradov, J. (2016). Tidal influence on self-potential measurements. *Journal of Geophysical Research: Solid Earth*, 121(12):8432–8452.

MacAllister, D., Jackson, M. D., Butler, A. P., and Vinogradov, J. (2018). Remote detection of saline intrusion in a coastal aquifer using borehole measurements of self-potential. *Water Resources Research*, 54(3):1669–1687.

MacAllister, D. J. (2015b). Self-potential, electrical conductivity and pressure data from the Saltdean observation borehole May 2013 - February 2015. Data provided by email on 15/06/15.

MacDonald, A. M. and Allen, D. J. (2001). Aquifer properties of the Chalk of England. *Quarterly Journal of Engineering Geology and Hydrogeology*, 34:371–384.

Maineult, A., Strobach, E., and Renner, J. (2008). Self-potential signals induced by periodic pumping tests. *Journal of Geophysical Research-Solid Earth*, 113(B1).

Malin, S. R. C. (1970). Separation of lunar daily geomagnetic variations into parts of ionospheric and oceanic origin. *Geophysical Journal International*, 21(5):447–455.

Martínez-Pagán, P., Jardani, A., Revil, A., and Haas, A. (2010). Self-potential monitoring of a salt plume. *Geophysics*, 75(4):Wa17–Wa25.

Mathias, S. (2005). *Modelling flow and transport in the Chalk unsaturated zone.* PhD thesis, Imperial College London.

McDonald, R., Russill, N., Miliorizos, M., and Thomas, J. (1998). A geophysical investigation of saline intrusion and geological structure beneath areas of tidal coastal wetland at Langstone Harbour, Hampshire, UK. In Robins, N. S., editor, *Groundwater Pollution, Aquifer Recharge and Vulnerability*, volume 130 of *Geological Society Special Publications*, pages 77–94. Geological Society, London.

Molyneux, I. (2012). *Hydrogeological characterisation of the Chalk: with specific reference to unsaturated zone behaviour*. PhD thesis, University of Brighton.

Morgan, L. K. and Werner, A. D. (2015). A national inventory of seawater intrusion vulnerability for Australia. *Journal of Hydrology Regional Studies*, 4:686–698.

MWH (2006). Drought management - deployable output water quality assessments of critical sources in Sussex: Balsdean desk study. Report prepared for Southern Water Ltd.

Nativ, R. and Fligelman, H. (1994). A field-test of the modified SP log interpretation method for estimating groundwater salinity. *Journal of Hydrology*, 161(1-4):133–144.

Nelson, P. H. (2009). Pore-throat sizes in sandstones, tight sandstones, and shales. *AAPG Bulletin*, 93(3):329–340.

Nunes, L. M., Dill, A. C., Ribeiro, L., and Vieira, J. (2003). Mixed analytical and numerical modelling of an oceanic peninsula using the Dupuit-Ghyben-Herzberg approach. *Calibration and Reliability in Groundwater Modelling: A Few Steps Closer to Reality*, (277):239–246.

Nutbrown, D. A., Downing, R. A., and Monkhouse, R. A. (1975). Use of a digital model in management of Chalk Aquifer in South Downs, England. *Journal of Hydrology*, 27(1-2):127–142.

OECD (1988). The international HYDROCOIN project - level 1: code verification report. Nuclear Energy Agency, Paris.

Patankar, S. V. (1980). *Numerical heat transfer and fluid flow*. Series in computational methods in mechanics and thermal sciences. Hemisphere Publishing, New York ; London.

Pezard, P. A., Gautier, S., Borgne, T. L., Legros, B., and Deltombe, J.-L. (2009). MuSET: A multiparameter and high precision sensor for downhole spontaneous electrical potential measurements. *Comptes Rendus Géoscience*, 341(10):957 – 964.

Pool, M. and Carrera, J. (2011). A correction factor to account for mixing in Ghyben-Herzberg and critical pumping rate approximations of seawater intrusion in coastal aquifers. *Water Resources Research*, 47.

Povich, T. J., Dawson, C. N., Farthing, M. W., and Kees, C. E. (2013). Finite element methods for variable density flow and solute transport. *Computational Geosciences*, 17(3):529–549.

Price, M. (1987). Fluid flow in the Chalk of England. In Goff, J. and Williams, B., editors, *Fluid Flow in Sedimentary Basins and Aquifers*, volume 34 of *Geology Society Special Publications*, pages 141–156. Geological Society, London.

Radhakrishna, I. (2001). Saline fresh water interface structure in Mahanadi delta region, Orissa, India. *Environmental Geology*, 40(3):369–380.

Revil, A. (1999). Ionic diffusivity, electrical conductivity, membrane and thermoelectric potentials in colloids and granular porous media: A unified model. *Journal of Colloid and Interface Science*, 212(2):503–522.

Revil, A. and Jardani, A. (2010). Stochastic inversion of permeability and dispersivities from time lapse self-potential measurements: A controlled sandbox study. *Geophysical Research Letters*, 37(11). L11404.

Revil, A. and Jougnot, D. (2008). Diffusion of ions in unsaturated porous materials. *Journal of Colloid And Interface Science*, 319(1):226–235.

Revil, A., Leroy, P., and Titov, K. (2005). Characterization of transport properties of argillaceous sediments: Application to the Callovo-Oxfordian argillite. *Journal of Geophysical Research-Solid Earth*, 110(B6).

Revil, A. and Linde, N. (2006). Chemico-electromechanical coupling in microporous media. *Journal of Colloid and Interface Science*, 302(2):682–694.

Rohling, E., Foster, G., Grant, K., Marino, G., Roberts, A., Tamisiea, M., and Williams, F. (2014). Sea-level and deep-sea-temperature variability over the past 5.3 million years. *Nature*, 508(7497):477–82.

Rosser, W. G. V. and Schlapp, D. M. (1990). Geomagnetic lunar variations due to the ocean dynamo measured at European observatories. *Geophysical Journal International*, 103(1):257–260.

Roubinet, D., Irving, J., and Pezard, P. (2018). Relating topological and electrical properties of fractured porous media: Insights into the characterization of rock fracturing. *Minerals*, 8(1).

Sandberg, S. K., Slater, L. D., and Versteeg, R. (2002). An integrated geophysical investigation of the hydrogeology of an anisotropic unconfined aquifer. *Journal of Hydrology*, 267(3-4):227–243.

Sato, M. and Mooney, H. (1960). The electrochemical mechanism of sulfide self-potentials. *Geophysics*, 25(1):226–249.

Saunders, J. H., Jackson, M. D., and Pain, C. C. (2008). Fluid flow monitoring in oilfields using downhole measurements of electrokinetic potential. *Geophysics*, 73(5):E165–E180.

Savitsky, A. and Golay, M. (1964). Smoothing and differentiation of data by simplified least squares procedures. *Analytical Chemistry*, 36(8):1627–1639.

Sawyer, A. H., David, C. H., and Famiglietti, J. S. (2016). Continental patterns of submarine groundwater discharge reveal coastal vulnerabilities. *Science*, 353(6300):705–707.

Scargle, J. D. (1982). Studies in Astronomical Time-Series Analysis. 2. Statistical Aspects of Spectral-Analysis of Unevenly Spaced Data. *Astrophysical Journal*, 263(2):835–853.

Schiavone, D. and Quarto, R. (1984). Self-potential prospecting in the study of water movements. *Geoexploration*, 22(1):47–58.

Schlapp, D. (1977). Lunar geomagnetic tides and the ocean dynamo. *Journal of Atmospheric and Terrestrial Physics*, 39(11):1453 – 1457.

Schlumberger (2010). Eclipse reservoir simulator, manual and technical description. ECLIPSE technical description, version 10. Technical report.

Schurch, M. and Buckley, D. (2002). Integrating geophysical and hydrochemical borehole-log measurements to characterize the Chalk aquifer, Berkshire, United Kingdom. *Hydrogeology Journal*, 10(6):610–627.

Sebben, M. L., Werner, A. D., and Graf, T. (2015). Seawater intrusion in fractured coastal aquifers: A preliminary numerical investigation using a fractured Henry problem. *Advances in Water Resources*, 85:93–108. Figure 3.4 reprinted from page 99 with permission from Elsevier.

Shi, L. and Jiao, J. J. (2014). Seawater intrusion and coastal aquifer management in China: a review. *Environmental Earth Sciences*, 72(8):2811–2819.

Sill, W. R. (1983). Self-potential modeling from primary flows. *Geophysics*, 48(1):76–86.

Simmons, C. T. (2005). Variable density groundwater flow: From current challenges to future possibilities. *Hydrogeology Journal*, 13(1):116–119.

Simmons, C. T., Bauer-Gottwein, P., Graf, T., Kinzelbach, W., Kooi, H., Li, L., Post, V., Prommer, H., Therrien, R., Voss, C. I., Ward, J., and Werner, A. (2010). *Variable density groundwater flow: from modelling to applications*. Groundwater Modelling in Arid and Semi-Arid Areas. Cambridge University Press.

Simmons, C. T., Narayan, K. A., and Wooding, R. A. (1999). On a test case for density-dependent groundwater flow and solute transport models: The salt lake problem. *Water Resources Research*, 35(12):3607–3620.

Small, C. and Nicholls, R. (2003). A global analysis of human settlement in coastal zones. *Journal of Coastal Research*, 19:584–599.

Soley, R., Power, T., Mortimore, R., Shaw, P., Dottridge, J., Bryan, G., and Colley, I. (2012). Modelling the hydrogeology and managed aquifer system of the Chalk across southern England. In Shepley, M., Whiteman, M., Hulme, P., and Grout, M., editors, *Groundwater*

Resources Modelling: A Case Study from the UK, volume 364 of *Geological Society Special Publications*, pages 129–154. Geological Society, London.

Somasundaran, P. and Kulkarni, R. (1973). A new streaming potential apparatus and study of temperature effects using it. *Journal of Colloid and Interface Science*, 45(3):591 – 600.

Southern Water (2015). Abstraction, pressure and electrical conductivity data for the Balsdean Pumping Station May 2013 - March 2015. Data provided by Mike Packman of Southern Water on 01/04/15.

Steyl, G. and Dennis, I. (2010). Review of coastal-area aquifers in Africa. *Hydrogeology Journal*, 18(1):217–225.

Stuart, M. (2005). Development of nitrate profiles database, British Geological Survey Report IR/05/058: accompanying dataset. Copyright NERC. Data provided by Marianne Stuart of the British Geological Survey on 18/05/16.

Sutter, E. and Ingham, M. (2017). Seasonal saline intrusion monitoring of a shallow coastal aquifer using time-lapse DC resistivity traversing. *Near Surface Geophysics*, 15(1):59–73.

Telford, W., Geldart, L., and Sheriff, R. (1990). *Applied Geophysics*. Cambridge University Press, UK, 2nd edition.

Trique, M., Perrier, F., Froidefond, T., Avouac, J. P., and Hautot, S. (2002). Fluid flow near reservoir lakes inferred from the spatial and temporal analysis of the electric potential. *Journal of Geophysical Research-Solid Earth*, 107(B10).

USGS (1999). Ground Water. U.s. geological survey general interest publication. available at: https://pubs.usgs.gov/gip/gw/.

van Reeuwijk, M., Mathias, S., Simmons, C. T., and Wards, J. D. (2009). Insights from a pseudospectral approach to the Elder problem. *Water Resources Research*, 45:W04416.

Vinogradov, J., Jaafar, M. Z., and Jackson, M. D. (2010). Measurement of streaming potential coupling coefficient in sandstones saturated with natural and artificial brines at high salinity. *Journal of Geophysical Research: Solid Earth*, 115(12).

Voss, C. I. and Provost, A. M. (2002). SUTRA, A model for saturated-unsaturated variable-density ground-water flow with solute or energy transport. US Geological Survey Water Resources Investigations Report 02-4231.

Walton, N. R. G. (1989). Electrical-conductivity and total dissolved solids - what is their precise relationship? *Desalination*, 72(3):275–292.

Wellings, S. R. (1984). Recharge of the Upper Chalk Aquifer at a site in Hampshire, England. 1. Water-balance and unsaturated flow. *Journal of Hydrology*, 69(1-4):259–273.

Werner, A. D., Bakker, M., Post, V. E. A., Vandenbohede, A., Lu, C. H., Ataie-Ashtiani, B., Simmons, C. T., and Barry, D. A. (2013). Seawater intrusion processes, investigation and management: Recent advances and future challenges. *Advances in Water Resources*, 51:3–26.

Werner, A. D. and Gallagher, M. R. (2006). Characterisation of sea-water intrusion in the Pioneer Valley, Australia using hydrochemistry and three-dimensional numerical modelling. *Hydrogeology Journal*, 14(8):1452–1469.

Westermann-Clark, G. and Christoforou, C. (1986). The exclusion-diffusion potential in charged porous membranes. *Journal of Electroanalytical Chemistry*, 198(2):19.

Williams, A., Bloomfield, J., Griffiths, K., and Butler, A. (2006). Characterising the vertical variations in hydraulic conductivity within the Chalk aquifer. *Journal of Hydrology*, 330(1-2):53–62.

Winston, R. (2014). Modifications made to ModelMuse to add support for the Saturated-Unsaturated Transport model (SUTRA). In *U.S. Geological Survey Techniques and Methods, Book 6, Chap. A49.*

Wurmstich, B. and Morgan, F. D. (1994). Modeling of streaming potential responses caused by oil-well pumping. *Geophysics*, 59(1):46–56.

WWAP (2014). United Nations World Water Development Report 2014. Technical report, United Nations World Water Assessment Programme.

Xin, P., Robinson, C., Li, L., Barry, D. A., and Bakhtyar, R. (2010). Effects of wave forcing on a subterranean estuary. *Water Resources Research*, 46.

Xu, Z. and Hu, B. X. (2016). Development of a discrete-continuum VDFST-CFP numerical model for simulating seawater intrusion to a coastal karst aquifer with a conduit system. *Water Resources Research*, 53(1):688–711.

Yungul, S. (1950). Interpretation of spontaneous polarization anomalies caused by spheroidal orebodies. *Geophysics*, 15(2):237–246.

Zaidman, M. D., Middleton, R. T., West, L. J., and Binley, A. M. (1999). Geophysical investigation of unsaturated zone transport in the Chalk in Yorkshire. *Quarterly Journal of Engineering Geology*, 32:185–198.

Zheng, C. and Bennett, G. D. (2002). *Applied Contaminant Transport Modeling*. John Wiley and Sons, New York, 2nd edition.

Zhou, P., Li, G., Lu, Y., and Li, M. (2013). Numerical modeling of the effects of beach slope on water-table fluctuation in the unconfined aquifer of Donghai Island, China. *Hydrogeology Journal*, 22(2):383–396.

Appendix A

Numerical method for the electrodynamic model

For simplicity, a description of the discretisation method is given for a single cell within a two-dimensional grid (Figure A.1), based on the approach described by Patankar (1980). In this example, it is assumed that V_{EK} is the sole contributor to SP and for clarity, the subscripts are removed from the terms V_{EK} and σ_s. Equation (2.19) is therefore written as follows:

$$\frac{\partial}{\partial x}\left(\sigma\frac{\partial V}{\partial x}\right)+\frac{\partial}{\partial y}\left(\sigma\frac{\partial V}{\partial y}\right)=J, \tag{A.1}$$

where J represents the electrokinetic source terms:

$$J\equiv-\frac{\partial}{\partial x}\left(\text{Ł}_{EK}\frac{\partial P_n}{\partial x}\right)-\frac{\partial}{\partial y}\left(\text{Ł}_{EK}\frac{\partial P_n}{\partial y}\right), \tag{A.2}$$

and the electrokinetic coupling term L_{EK} is given by Equations (2.2) and (4.8).

Considering only the first term on the left hand side of Equation (A.1) and integrating over a single control volume, as shown in Figure A.1 gives:

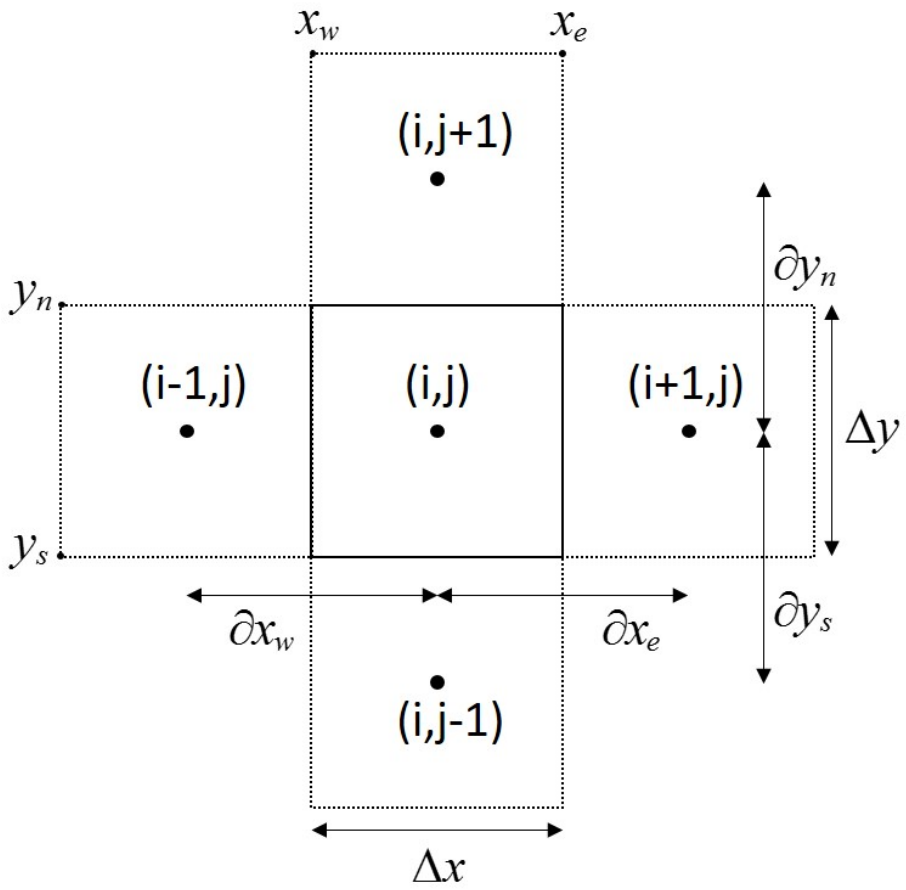

Figure A.1: Schematic of a single control volume in two dimensions.

$$\int_{y_s}^{y_n}\int_{x_w}^{x_e}\frac{\partial}{\partial x}(\sigma\frac{\partial V}{\partial x})dxdy = \int_{y_s}^{y_n}\left[(\sigma\frac{\partial V}{\partial x})_e - (\sigma\frac{\partial V}{\partial x})_w\right]dy \tag{A.3}$$

$$\approx \left[(\sigma\frac{\partial V}{\partial x})_e - (\sigma\frac{\partial V}{\partial x})_w\right]\Delta y \tag{A.4}$$

$$\approx \left[\sigma_e\frac{V_{i+1,j}-V_{i,j}}{\partial x_e} - \sigma_w\frac{V_{i,j}-V_{i-1,j}}{\partial x_w}\right]\Delta y. \tag{A.5}$$

Equation (A.4) assumes that the flux terms $(\sigma\frac{\partial V}{\partial x})_e$ and $(\sigma\frac{\partial V}{\partial x})_w$ remain constant over the length of the volume interface in the y direction, while Equation (A.5) invokes a central difference approximation. The terms $V_{i+1,j}$, $V_{i,j}$ and $V_{i-1,j}$ represent the nodal values of V, while σ_w and σ_e are the values of σ at the control volume interfaces. The method of interpolation for these interface values is described in Section A.

Similarly, the second term on the left hand side of Equation (A.1) is given by:

$$\int_{y_s}^{y_n}\int_{x_w}^{x_e}\frac{\partial}{\partial y}(\sigma\frac{\partial V}{\partial x})dydx \approx \big[\sigma_e\frac{V_{i,j+1}-V_{i,j}}{\partial y_n}-\sigma_w\frac{V_{i,j}-V_{i,j-1}}{\partial y_s}\big]\Delta x, \tag{A.6}$$

while integration of the source term gives:

$$\int_{y_s}^{y_n}\int_{x_w}^{x_e} J dxdy \approx J_{i,j}\Delta x\Delta y. \tag{A.7}$$

Combining Equations (A.5) to (A.7) with Equation (A.1) gives:

$$J_{i,j}\Delta x\Delta y = a_n V_{i,j+1} + a_e V_{i+1,j} + a_s V_{i,j-1} + a_w V_{i-1,j} + a_p V_{i,j}, \tag{A.8}$$

where

$$a_n = -\frac{\sigma_n \Delta x}{\partial y_n}, \tag{A.9}$$

$$a_e = -\frac{\sigma_e \Delta y}{\partial x_e}, \tag{A.10}$$

$$a_s = -\frac{\sigma_s \Delta x}{\partial y_s}, \tag{A.11}$$

$$a_w = -\frac{\sigma_w \Delta y}{\partial x_w}, \tag{A.12}$$

$$a_p = -(a_n + a_e + a_s + a_w). \tag{A.13}$$

Following a similar procedure for the source terms in Equation (A.2) and for clarity, removing the subscripts from P_n and L_{EK}, Equation (A.8) can be presented as follows:

$$a_n V_{i,j+1} + a_e V_{i+1,j} + a_s V_{i,j-1} + a_w V_{i-1,j} + a_p V_{i,j} = b_n P_{i,j+1} + b_e P_{i+1,j} + b_s P_{i,j-1} + b_w P_{i-1,j} + b_p P_{i,j}, \tag{A.14}$$

where

$$b_n = -\frac{L_n \Delta x}{\partial y_n}, \tag{A.15}$$

$$b_e = -\frac{L_e \Delta y}{\partial x_e}, , \tag{A.16}$$

$$b_s = -\frac{L_s \Delta x}{\partial y_s}, \tag{A.17}$$

$$b_w = -\frac{L_w \Delta y}{\partial x_w}, \tag{A.18}$$

$$b_p = -(b_n + b_e + b_s + b_w). \tag{A.19}$$

Equation (A.14) forms the basis for the sparse matrix equation used to solve the electrodynamic model:

$$\mathbf{Ax} = \mathbf{By}, \tag{A.20}$$

where $\mathbf{A}$ is an $mno \times mno$ matrix comprising all of the a terms in Equation (A.14) expanded into a third dimension to represent the m rows, n columns and o layers of the model domain, $\mathbf{x}$ is an $mno \times 1$ vector representing the electrical potential (effectively V_{EK} in this example) in each cell, $\mathbf{B}$ is an $mno \times mno$ matrix representing the b terms in Equation (A.14) in three

dimensions and $\mathbf{y}$ is an $mno \times 1$ vector representing the non-hydrostatic pressure in each cell. In three dimensions, the general form of the terms in matrix $\mathbf{A}$ are given by:

$$a_{\Gamma i} = -\frac{\sigma \Delta L1_i \Delta L2_i}{0.5(\Delta L3_i + \Delta L3_{i+1})} \tag{A.21}$$

for each boundary Γ of element i, where $\Delta L1 - 3_i$ are the dimensions of element i in the directions of the coordinate axes and:

$$a_{Pi} = -\sum_{\Gamma=1}^{6} a_{\Gamma i} \tag{A.22}$$

for the centre of each element. For matrix $\mathbf{B}$, the σ terms are replaced by the coupling term L_{EK}. A similar approach is implemented for the exclusion-diffusion potential, whereby $\mathbf{x}$ in Equation (A.20) represents V_{EED}, the coupling terms in $\mathbf{B}$ are based on the electrochemical coupling coefficient C_{EED} and $\mathbf{y}$ represents $ln(C_f)$.

In each case, a direct solution is found for $\mathbf{x}$ using the *mldivide* function in MATLAB and the total electrical potential is found by adding the solution vectors for V_{EK} and V_{EED}. As the SP signal is a potential difference between two points, the modelled SP is effectively the difference in potential between a given location and that of a reference electrode (in this case, at an elevation of -2.8 mAOD within the Saltdean OBH).

Conductivity and coupling terms

The conductivity σ and coupling term L_{EK} are assumed to be constant throughout each control volume and the values at each interface are defined based on an assumption of continuous flow across the boundaries, so that for σ at the right hand face of the control volume in Figure A.1:

$$\sigma_{i,j} \frac{\partial V}{\partial x} \mid_{x_{e-}} = \sigma_{i+1,j} \frac{\partial V}{\partial x} \mid_{x_{e+}} = \sigma_e \frac{\partial V}{\partial x} \mid_{x_e} . \tag{A.23}$$

In discretised form, this leads to:

$$\sigma_e \frac{V_{i+1,j} - V_{i,j}}{x_{i+1,j} - x_{i,j}} = \sigma_{i+1,j} \frac{V_{i+1,j} - V_e}{x_{i+1,j} - x_e}, \tag{A.24}$$

giving:

$$V_{i+1,j} - V_e = (V_{i+1,j} - V_{i,j})\big(\frac{x_{i+1,j} - x_e}{x_{i+1,j} - x_{i,j}}\big)\frac{\sigma_e}{\sigma_{i+1,j}} \tag{A.25}$$

and

$$\sigma_e \frac{V_{i+1,j} - V_{i,j}}{x_{i+1,j} - x_{i,j}} = \sigma_{i,j} \frac{V_e - V_{i,j}}{x_e - x_{i,j}}, \tag{A.26}$$

giving:

$$V_e - V_{i,j} = (V_{i+1,j} - V_{i,j})\big(\frac{x_e - x_{i,j}}{x_{i+1,j} - x_{i,j}}\big)\frac{\sigma_e}{\sigma_{i,j}}. \tag{A.27}$$

Adding Equations (A.25) and (A.27) gives:

$$V_{i+1,j} - V_{i,j} = \sigma_e\big(\frac{V_{i+1,j} - V_{i,j}}{x_{i+1,j} - x_{i,j}}\big)\big(\frac{x_{i+1,j} - x_e}{\sigma_{i+1,j}} + \frac{x_e - x_{i,j}}{\sigma_{i,j}}\big). \tag{A.28}$$

This ultimately leads to the following expression for electrical conductivity at the interface of the cells centred around (i,j) and (i+1,j):

$$\sigma_e = \frac{(x_{i+1,j} - x_{i,j})\sigma_{i,j}\sigma_{i+1,j}}{\sigma_{i,j}(x_{i+1,j} - x_e) + \sigma_{i+1,j}(x_e - x_{i,j})}. \tag{A.29}$$

A similar expression for the coupling term is obtained by substituting L_{EK} and P into Equations (A.23) to (A.29).

Appendix B

Sensitivity to electrodynamic grid design

B.1 Introduction

The requirement to implement small grid cells over a large extent within the hydrodynamic model was discussed in Sections 5.2 and 5.4.2 and there remains a balance to be struck between the accurate simulation of a relatively narrow saline front and the computational expense involved if this is to be achieved across a relatively large model domain. This is a subject that has received a great deal of attention in the literature (e.g. Diersch and Kolditz, 2002; Simmons et al., 2010; Voss and Provost, 2002), but there are few examples of grid sensitivity analyses in SP modelling as a whole and none that have been applied to a coastal aquifer.

B.2 Model extent

As discussed in Section 5.3, the electrodynamic model assumes no external sources or sinks of electrical current and hence allows no current flow across the domain boundaries. As the objective of the model is to simulate SP within the Saltdean OBH, it is important therefore

to ensure that the domain is large enough to avoid interfering with current flow, and hence electrical potential, at this location. The aim of this section is to investigate whether interference occurs, by varying the extent of the model domain and assessing any changes to the simulated SP gradient in the borehole.

This was done firstly by varying the extent of the grid in the direction of dip. As shown in Figure B.1, the simulated SP gradient in the borehole for the steady state model decreases as the domain extent is reduced, although the results are unaffected by an increase to the domain extent. Concentrations and pressures within the area of expansion were taken from the steady state regional model.

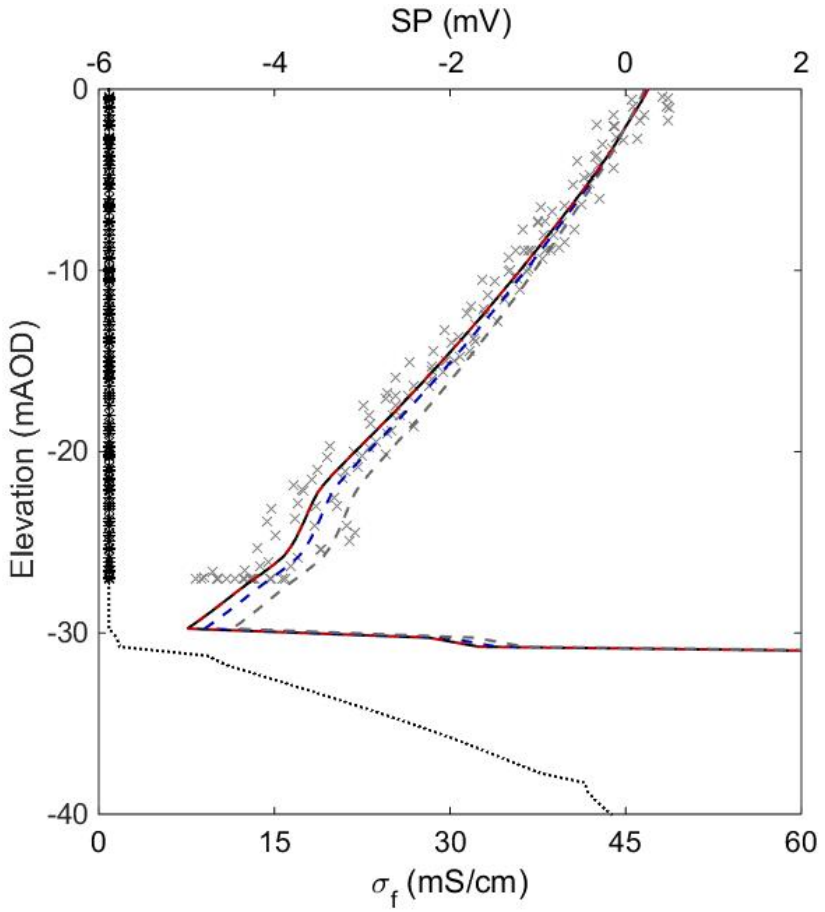

Figure B.1: Sensitivity of the initial BH SP gradient to the size of the model domain in the direction of dip. Results are shown for a model reduced by 50 m on each side (grey dashed line), by 25 m on each side (blue dashed line) and increased by 25 m (10 x 2.5 m cells) on each side (red dashed line). The original modelled SP (black solid line) and σ_f (black dotted line) are shown alongside the field SP (grey crosses) and σ_f (black asterisks) for comparison.

The importance of the model's vertical extent was investigated by removing 10 m from the base of the model (the lowest 2 rows of cells) and also by adding 2 rows of cells to the base of

the original model, each spanning 5 m in the z-direction. In each case, the SP profile in the borehole is barely distinguishable from that produced by the original model (Figure B.2).

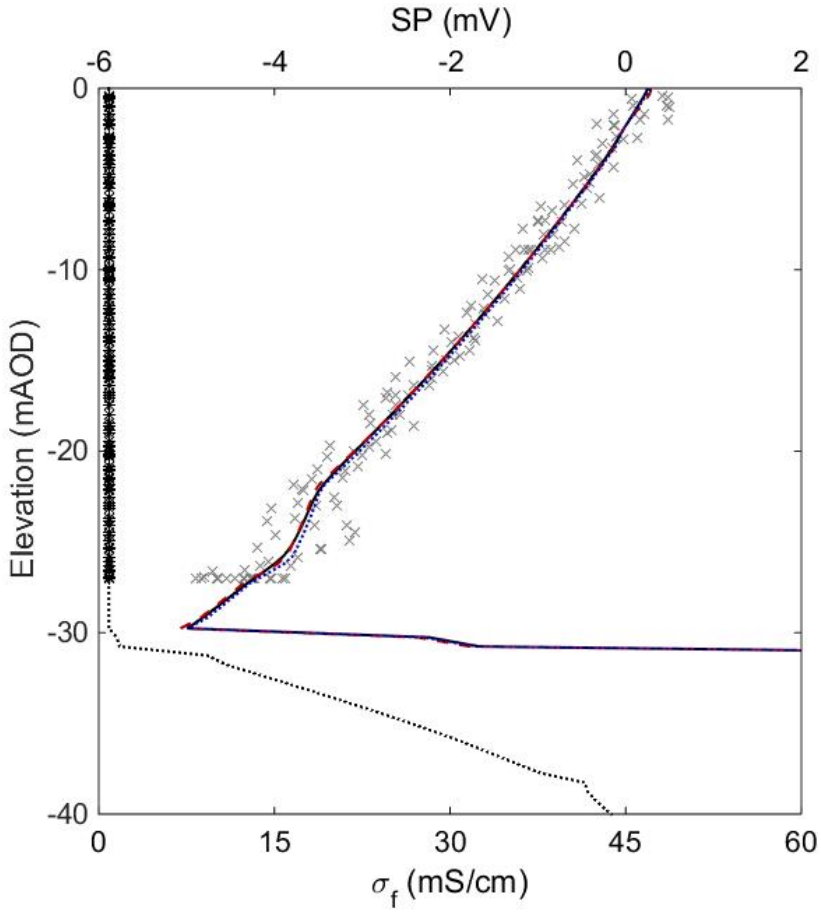

Figure B.2: Sensitivity of the initial BH SP gradient to the model's vertical extent. Results are shown for the original model (black solid line), for a model base elevation raised by 10 m (red dashed line) and a model base lowered by 10 m (blue dotted line). Field SP (grey crosses) and σ_f (black asterisks) observed on 15 August 2013 are shown for comparison.

Sensitivity to the domain extent parallel to the coast was assessed by removing the outer layer of grid cells at both edges of the model in the y-direction, thereby reducing the width of the domain from 64.5 m to 8.5 m. As shown in Figure B.3a, the results are not affected for the steady state model. As the boundary conditions for concentration and pressure do not vary in the y-direction of the model, this is unsurprising. However, prior to intrusion, the influence of the borehole creates three-dimensional effects and, as shown in Figure B.3b, a reduction in the domain extent produces a significant reduction in the modelled SP gradient at the borehole. A corresponding increase in the extent of the model domain (achieved by adding a single 28 m layer to each edge of the model in the y-direction) does not affect the results noticeably. This suggests that modelled SP in the borehole is not impacted by boundary effects in the original

model.

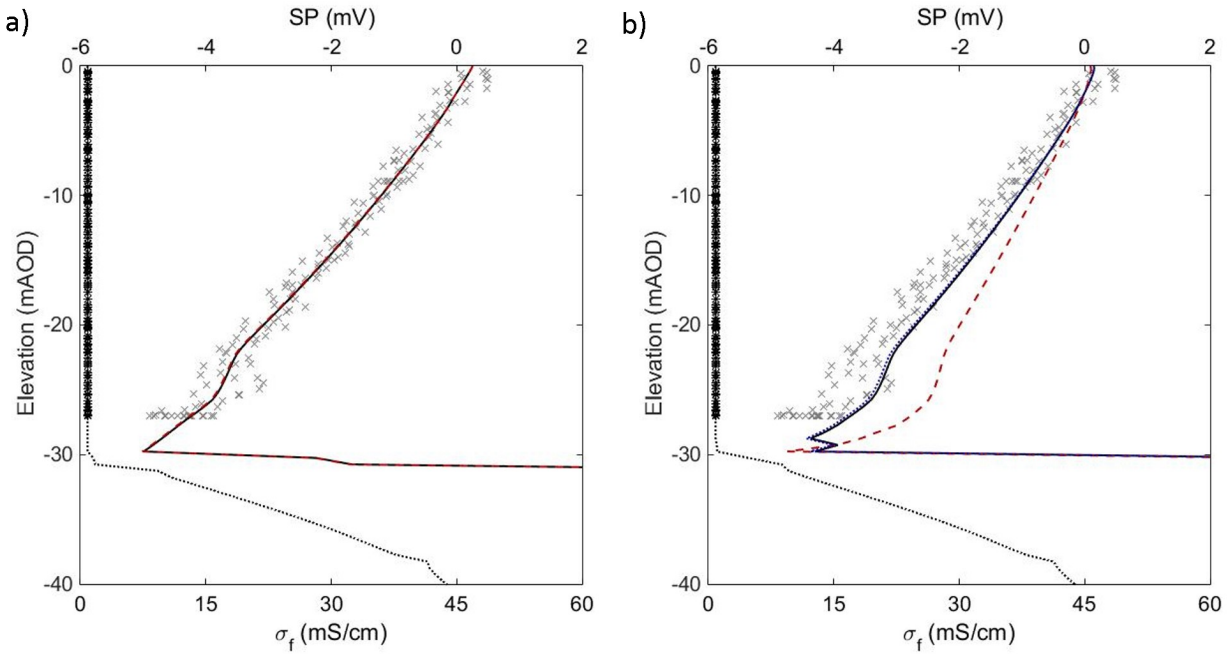

Figure B.3: Sensitivity of the BH SP gradient to the size of the model domain parallel to the coast. a) The SP results for the original steady state model (black solid line) are shown with those produced when the minimum and maximum extents of the model domain are reduced by 28 m in the y-direction (grey dashed line). b) The SP results from the original transient model 1 day prior to intrusion (black solid line) are compared to those produced by the reduced model domain (red dashed line) and those given by a model extended by a single 28 m wide layer in both directions along the y-axis (blue dotted line). Modelled σ_f (black dotted line) is shown alongside field σ_f (black asterisks) and SP (grey crosses) for comparison.

B.3 Grid refinement

The sensitivity of the model to grid cell size was assessed also. This was done firstly by halving the original cell dimensions in the x- and z-directions and then by doubling them. As shown in Figure B.4, implementing a coarser grid markedly changes the characteristics of the SP profile in the borehole. Additional grid refinement dampens the SP gradient, although the overall shape of the SP profile is similar.

Examination of the salinity gradient across lithological boundaries in the model provides some additional insight into these effects. In Figure B.5, the boundary between the Hope Gap Hardground and the overlying Chalk is used as an example. In the coarser model, the vertical

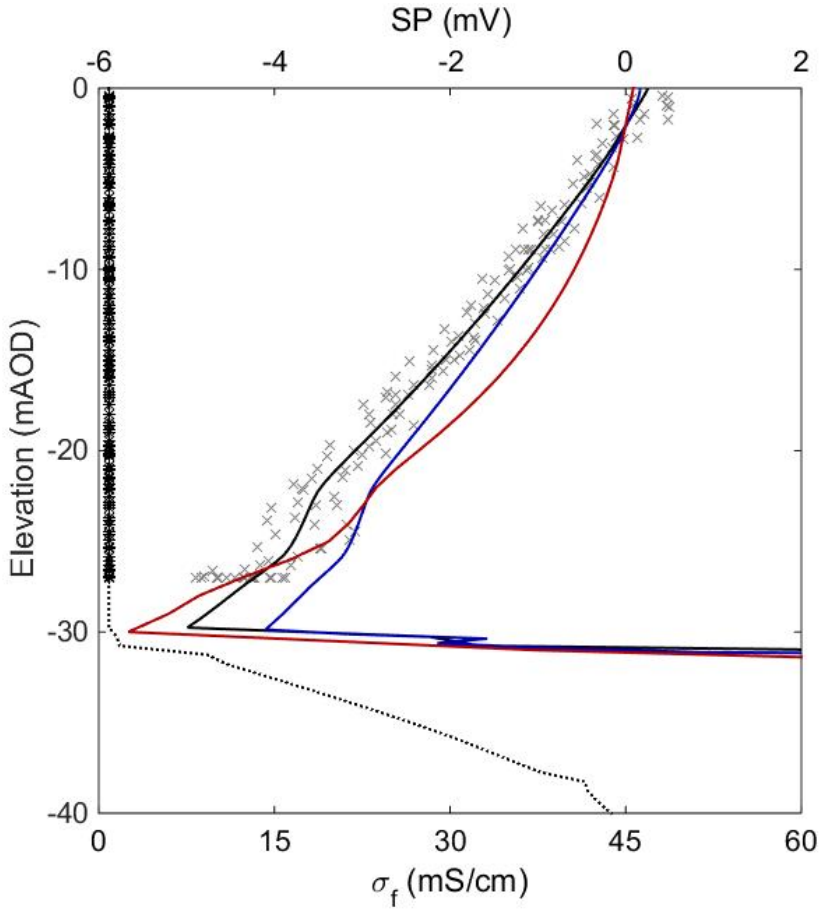

Figure B.4: Sensitivity of the BH SP gradient to grid cell size in the x- and z-directions, showing SP (black solid line) and σ_f (black dotted line) for the original model grid, SP for grid cells with half the original dimensions in the x- and z-directions (blue line) and SP for grid cells with twice the original dimensions in the x- and z-directions (red line). Observations of SP (grey crosses) and σ_f (black asterisks) from the Saltdean OBH on 15 August 2013 are shown for comparison.

gradient in C_f across the boundary is dampened significantly in comparison to the original model (Figure B.5a). Furthermore, the dimensions of the coarser grid cells fail to capture the scale of lithological variations throughout the conceptual and hydrodynamic models. As a result, average values for η have been applied.

By contrast, both the original and refined versions of the electrodynamic model are faithful to the conceptual model of geology. There is a modest change in the vertical gradient of C_f across the top of the Hope Gap Hardground (Figure B.5b) and, extrapolating this effect across other lithological boundaries, it is apparent that this leads to a slight change in the overall SP gradient.

Refinement of the grid in the y-direction by halving the original cell dimensions does not affect

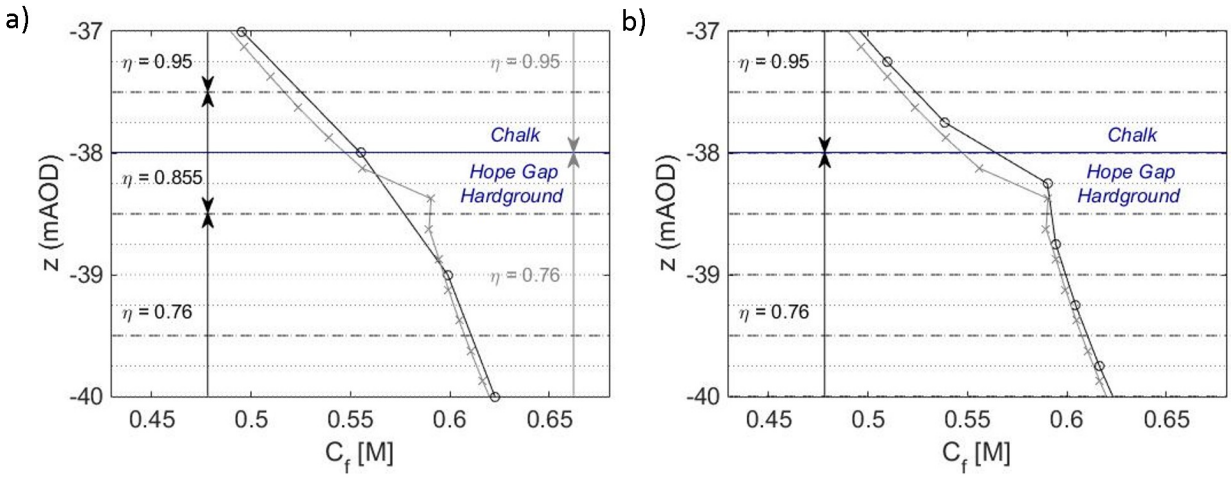

Figure B.5: Variations in C_f across the upper face of the Hope Gap Hardground at $x = 1800$m for a) the original model grid (grey lines with crosses at cell centres and dotted grey lines to indicate cell boundaries) and the coarse model grid (black lines with open circles at the cell centres and dashed black lines to indicate cell boundaries), with the η values in black applied to the coarse model and those in grey applied to the original model and b) the original model grid (black lines with open circles at cell centres and dashed black lines to indicate cell boundaries) and the refined model grid (grey lines with crosses at the cell centres and dotted grey lines to indicate cell boundaries), with the η values shown applied to both models. The boundary between the Hope Gap Hardground and the overlying Chalk as implemented in the hydrodynamic model is shown in blue.

the results significantly in the steady state model or immediately prior to intrusion in the transient model (Figure B.6).

B.4 Discussion on grid refinement

Intuitively, finer grid cells should produce a more faithful representation of the system, although this comes with considerable computational expense. Using parallel processing across 4 processors, the original electrodynamic model is solved for a single time step in 340 seconds. By doubling the number of cells in the x- and z-directions, this increases to 5100 seconds. It is unclear what effect further grid refinement would have and whether an optimal resolution exists below which finer discretisation will not change the model results. In hydrodynamic models of the well known Elder problem, commonly used as a benchmark for modelling software, Diersch and Kolditz (2002) show that refinement of even very fine model meshes can lead to substantial changes in the numerical solution. Paradoxically, for the more complex salt lake problem

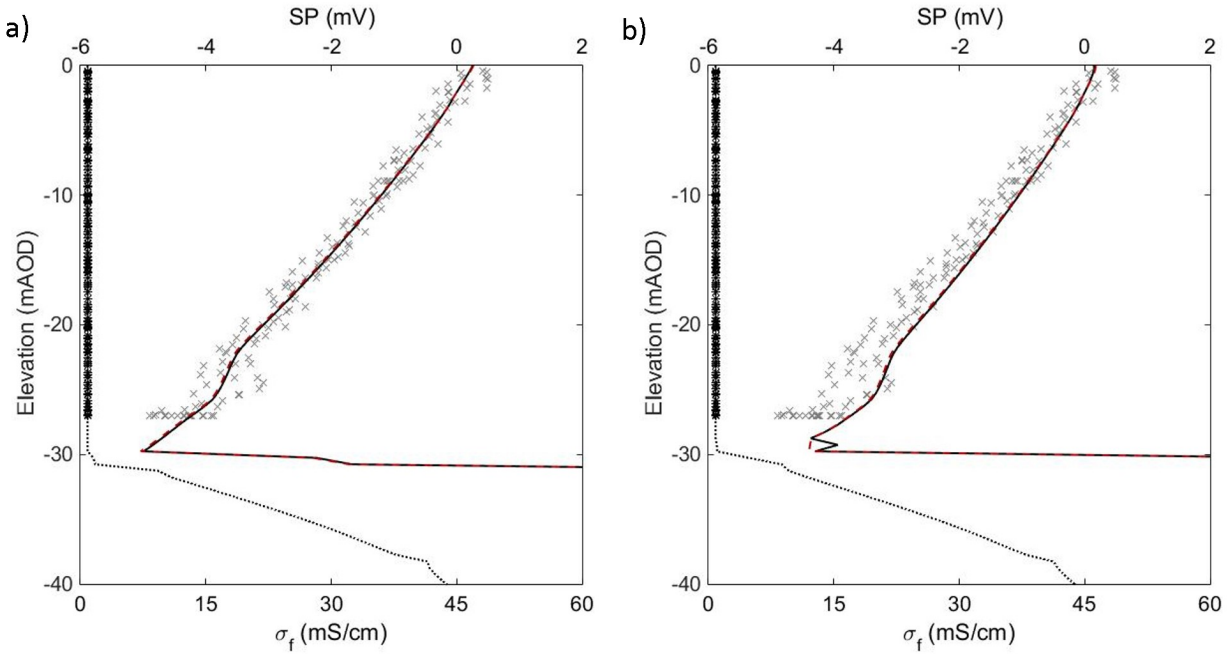

Figure B.6: Sensitivity of the BH SP gradient to grid cell size in the y-direction, showing a) steady state SP (black solid line) and σ_f (black dashed line) for the original model grid and SP for grid cells with half the original dimensions in the y-direction (red dashed line) and b) SP 1 day prior to intrusion in the original model (black solid line) and in the refined model (red dashed line). Observations of SP (grey crosses) and σ_f (black asterisks) from the Saltdean OBH on 15 August 2013 are shown for comparison.

developed by Simmons et al. (1999), model results appear to match laboratory observations more closely when a coarser grid is employed (Diersch and Kolditz, 2002). Clearly, there is a balance to be struck between model accuracy and run time, although in the absence of an analytical solution, the optimal level of discretisation remains unclear and is an area which requires further investigation.

B.5 Conclusions

Increasing the dimensions of the model domain does not lead to significant changes in the borehole SP profile, although reductions in the model extent substantially affect the results, suggesting that the original model extent is appropriate for simulating the field observations.

The model appears insensitive to further grid refinement parallel to the coast, although finer grid cells in the x-z plane reduce the magnitude, but not the shape, of the SP profile in the

borehole. The most significant gradients in pressure and salinity lie within this plane and the requirement for fine grid cells is perhaps unsurprising, although further refinements beyond those made in the current model would make the computational cost of calibration unfeasible.

Appendix C

Graphical results for each marl core experiment

In each of the following graphs, the data used to calculate ΔV_{EED} and η are shown by a light grey box. Longer term behaviour over 5 hour and 10 hourr periods are shown as insets to the main graph, showing voltages measured over the first 2 hours of the experiment.

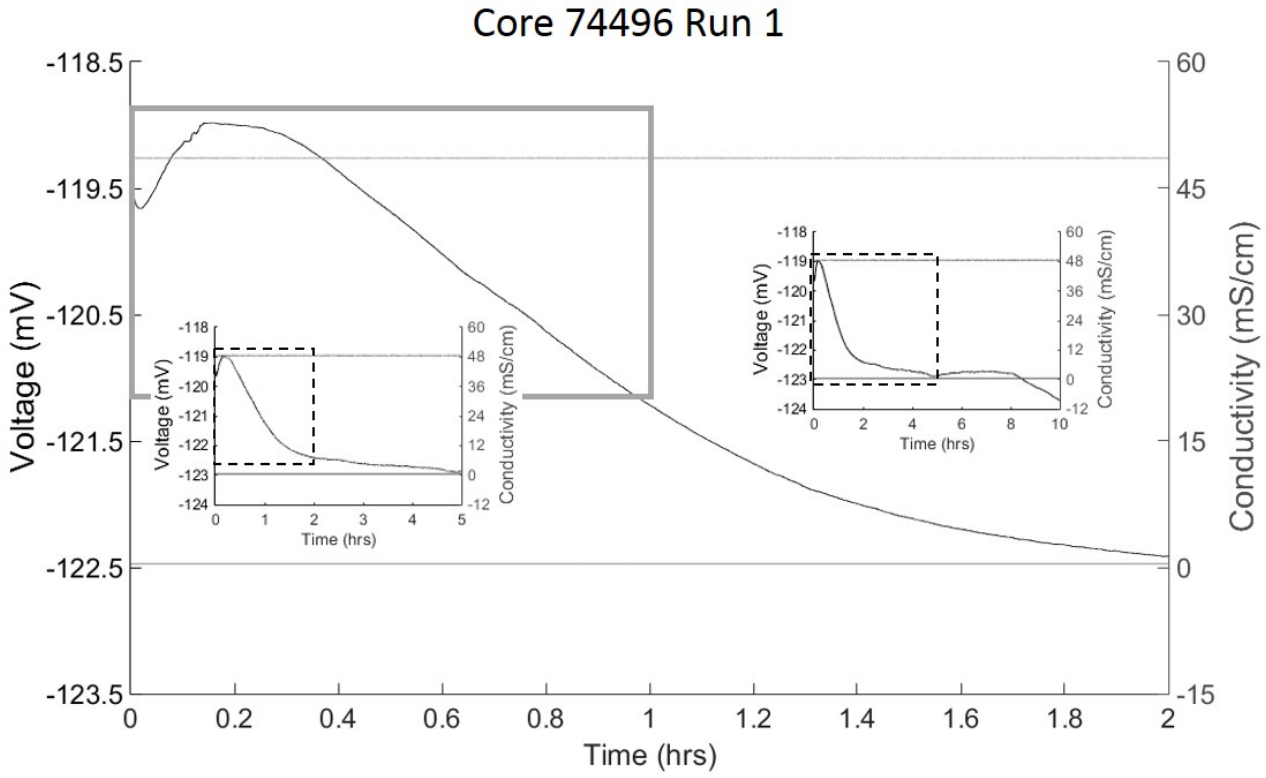
Core 74496 Run 1
Voltage (mV)
Conductivity (mS/cm)
Time (hrs)

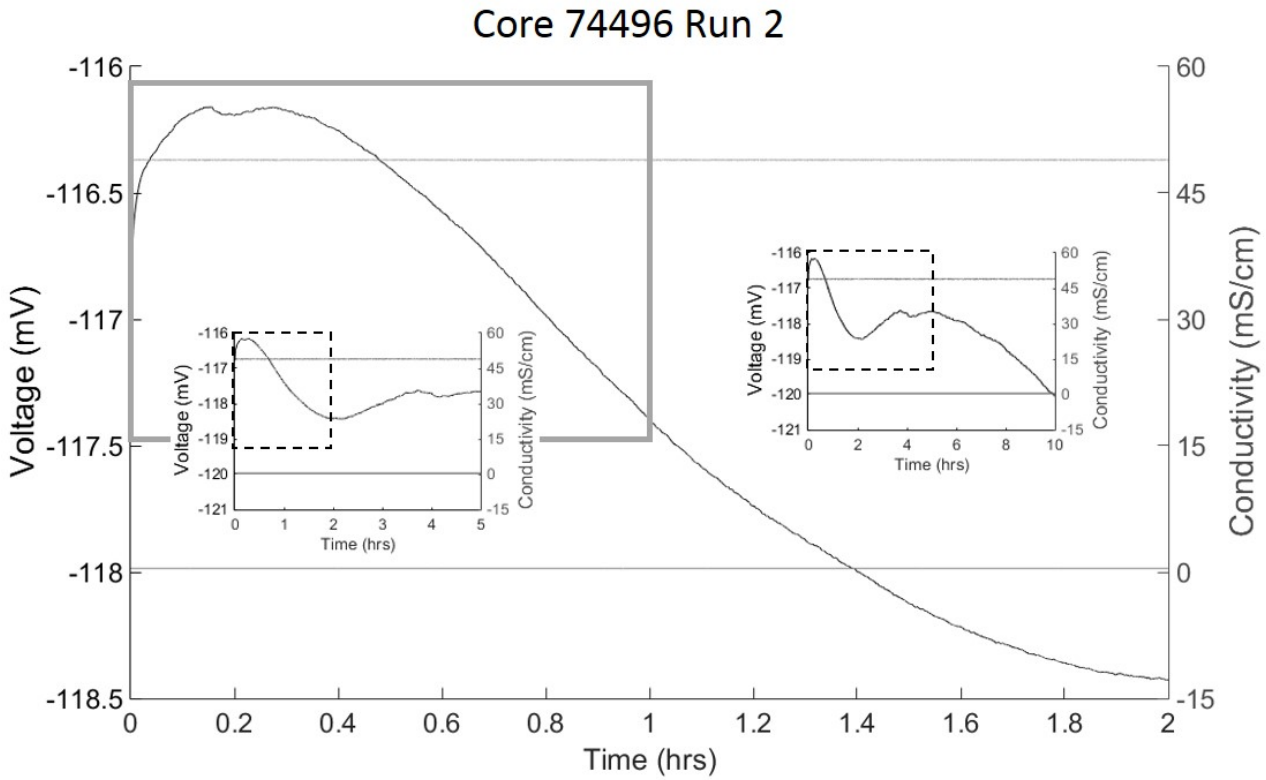
Core 74496 Run 2
Voltage (mV)
Conductivity (mS/cm)
Time (hrs)

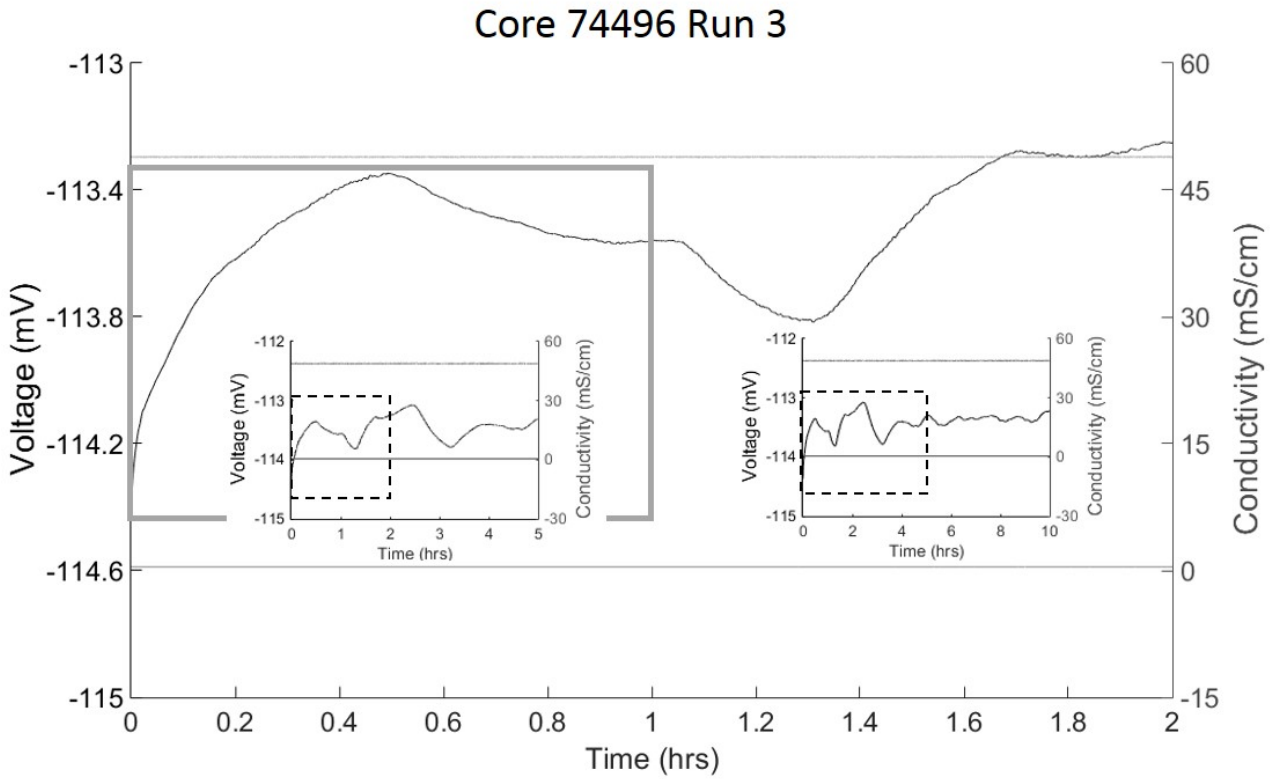
Core 74496 Run 3
Voltage (mV)
Conductivity (mS/cm)
Time (hrs)

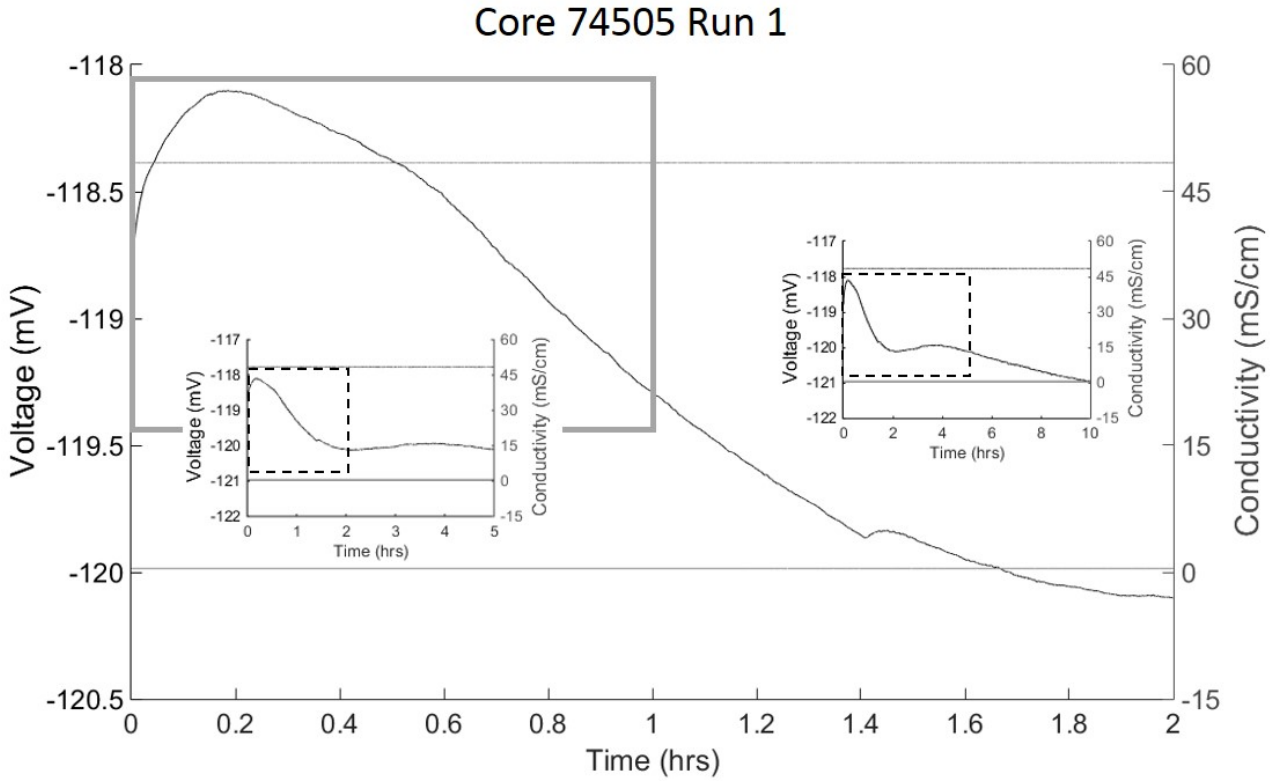
Core 74505 Run 1
Voltage (mV)
Conductivity (mS/cm)
Time (hrs)

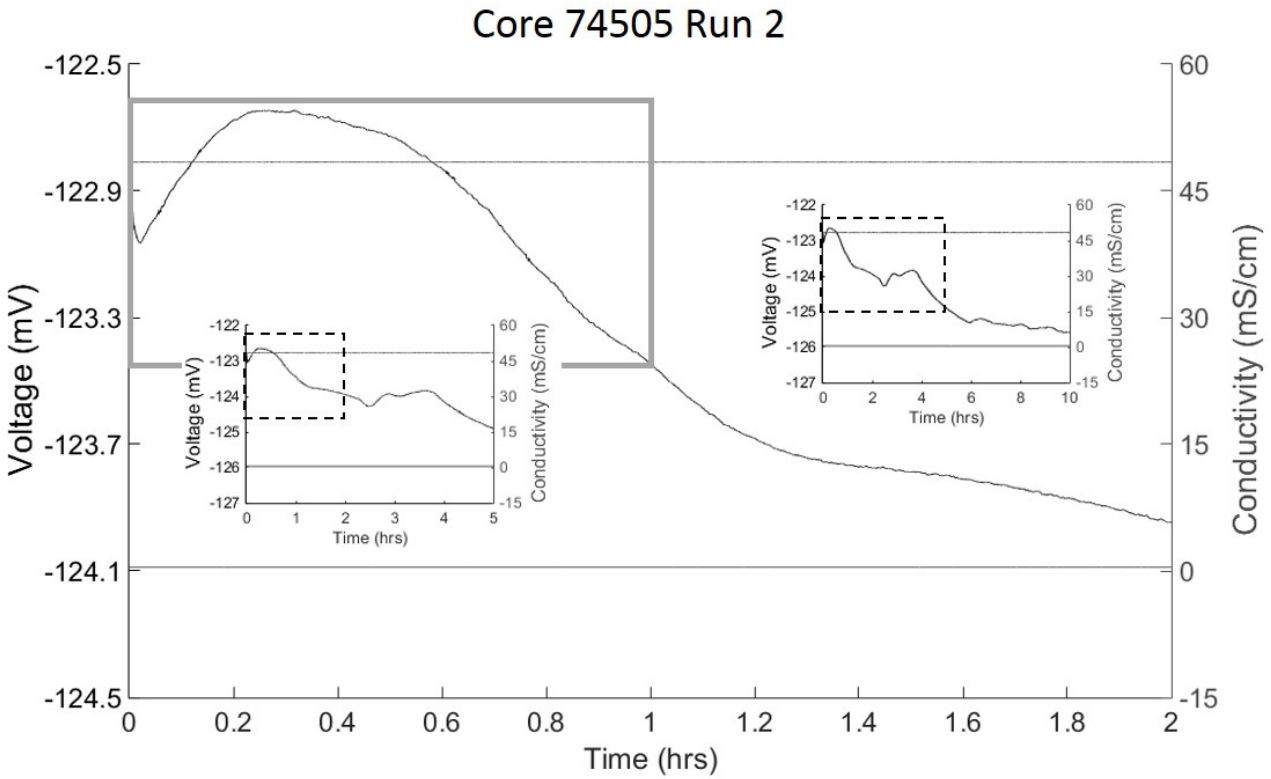
Core 74505 Run 2
Voltage (mV)
Conductivity (mS/cm)
Time (hrs)

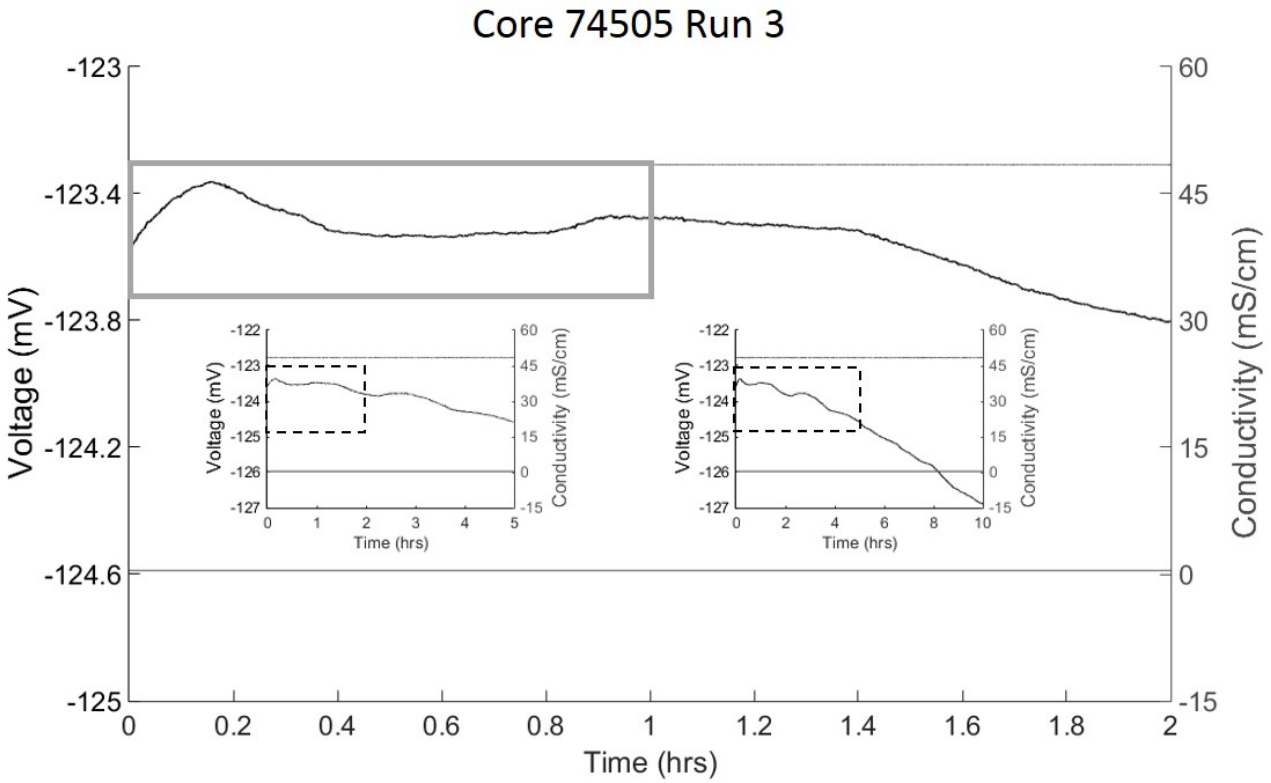
Core 74505 Run 3
Voltage (mV)
Conductivity (mS/cm)
Time (hrs)

Appendix D

Permissions for selected figures

Several figures in this thesis have been reproduced or adapted from previous published works and these have been cited accordingly. In the majority of instances, permissions exist to reproduce them under a Creative Commons licence or terms and conditions of use, as shown on the publishers' website. Table D.1 lists the figures which required express permission from the copyright holder and confirms the receipt of these permissions.

Table D.1: Summary of permissions to reproduce selected figures.

Page No.	Figure	Source	Copyright holder	Permission requested on	Granted (yes/no)	Permission note
36	Figure 2.2	Jackson, M., Vinogradov, J., Saunders, J. H., and Jaafar, M. Z. (2010). Laboratory measurements and numerical modeling of streaming potential for downhole monitoring in intelligent wells. SPE Journal, 16(3):625-636.	© SPE	28.06.18	yes	Written permission
45	Figure 2.4	As above.	© SPE	28.06.18	yes	Written permission
55	Figure 3.4	Sebben, M. L., Werner, A. D., and Graf, T. (2015). Seawater intrusion in fractured coastal aquifers: A preliminary numerical investigation using a fractured Henry problem. Advances in Water Resources, 85: page 99.	© Elsevier	28.06.18	yes	Written permission

SOCIETY OF PETROLEUM ENGINEERS LICENSE TERMS AND CONDITIONS

Jun 28, 2018

This Agreement between Imperial College London -- Malcolm Graham ("You") and Society of Petroleum Engineers ("Society of Petroleum Engineers") consists of your license details and the terms and conditions provided by Society of Petroleum Engineers and Copyright Clearance Center.

All payments must be made in full to CCC. For payment instructions, please see information listed at the bottom of this form.

License Number	4377630154814
License date	Jun 28, 2018
Licensed Content Publisher	Society of Petroleum Engineers
Licensed Content Publication	SPE Journal
Licensed Content Title	Spontaneous Potentials in Hydrocarbon Reservoirs During Waterflooding: Application to Water-Front Monitoring
Licensed Content Author	Matthew D. Jackson, Imperial College London;Murtaza Y. Gulamali, Imperial College London;Eli Leinov, Imperial College London et al
Licensed Content Date	Jan 1, 2012
Licensed Content Volume	17
Licensed Content Issue	01
Volume number	17
Issue number	01
Type of Use	Thesis/Dissertation
Requestor type	academic/educational
SPE member	no
Format	electronic
Portion	figures/tables/images
Number of figures/tables /images	2
Will you be translating?	no
Distribution	1
Order reference number	
Title of your thesis / dissertation	Modelling Self-Potentials as a Predictor of Seawater Intrusion in Coastal Groundwater Boreholes
Expected completion date	Jun 2018
Estimated size (number of pages)	193
Billing Type	Credit Card
Credit card info	Visa ending in 4926
Credit card expiration	04/2019
Requestor Location	Imperial College London Exhibition Road South Kensington London, SW7 2AZ United Kingdom

ELSEVIER LICENSE
TERMS AND CONDITIONS

Jun 28, 2018

This Agreement between Imperial College London -- Malcolm Graham ("You") and Elsevier ("Elsevier") consists of your license details and the terms and conditions provided by Elsevier and Copyright Clearance Center.

License Number	4377620861319
License date	Jun 28, 2018
Licensed Content Publisher	Elsevier
Licensed Content Publication	Advances in Water Resources
Licensed Content Title	Seawater intrusion in fractured coastal aquifers: A preliminary numerical investigation using a fractured Henry problem
Licensed Content Author	Megan L. Sebben,Adrian D. Werner,Thomas Graf
Licensed Content Date	Nov 1, 2015
Licensed Content Volume	85
Licensed Content Issue	n/a
Licensed Content Pages	16
Start Page	93
End Page	108
Type of Use	reuse in a thesis/dissertation
Intended publisher of new work	other
Portion	figures/tables/illustrations
Number of figures/tables /illustrations	1
Format	electronic
Are you the author of this Elsevier article?	No
Will you be translating?	No
Original figure numbers	Figure 4
Title of your thesis/dissertation	Modelling Self-Potentials as a Predictor of Seawater Intrusion in Coastal Groundwater Boreholes
Expected completion date	Jun 2018
Estimated size (number of pages)	193
Requestor Location	Imperial College London Exhibition Road South Kensington London, SW7 2AZ United Kingdom Attn: Imperial College London
Publisher Tax ID	GB 494 6272 12
Total	0.00 USD